Politecnico di Torino

ScuDo
Scuola di Dottorato ~ Doctoral School
WHAT YOU ARE, TAKES YOU FAR

Doctoral Dissertation
Doctoral Program in Aerospace Engineering (34^{th} cycle)

Low-Thrust Optimal Escape Trajectories from Lagrangian Points and Quasi-Periodic Orbits in a High-Fidelity Model

By

Luigi Mascolo

******

Supervisor:
Prof. Lorenzo Casalino

Doctoral Examination Committee:
Prof. Camilla Colombo, Politecnico di Milano, referee
Prof. Emmanuel Trélat, Sorbonne Université, referee
Prof. Manuela Battipede, Politecnico di Torino
Dr. Richard Epenoy, PhD, Centre National d'Etudes Spatiales
Prof. Carlo Novara, Politecnico di Torino

Politecnico di Torino
2023

Declaration

I hereby declare that, the contents and organization of this dissertation constitute my own original work and does not compromise in any way the rights of third parties, including those relating to the security of personal data.

Luigi Mascolo
2023

* This dissertation is presented in partial fulfillment of the requirements for the **Ph.D. degree in Aerospace Engineering** in the Graduate School of Politecnico di Torino (ScuDo).

To all the people of Planet Earth, may the space be your home.

Abstract

This thesis focuses on analyzing escape trajectories that use electric propulsion and depart from a Lagrangian point. Electric propulsion is a key technology for the exploration of the solar system due to the low propellant consumption, and the exploitation of Lagrangian points has become of great interest. Among the infinite possible trajectories for a specific mission, historically, those at minimum propellant request, in compliance with the other boundary conditions, have been identified as essential for maximizing the scientific return and minimizing the correlated costs. Namely, bringing less propellant on board, and thus being more efficient, means having more space available for the payload, which increases the scientific return to the same mission; at the same time, larger spacecraft structures are avoided to accommodate the extra-required space.

For this purpose, this thesis researches optimal space trajectories using electric propulsion in a higher fidelity model, aiming to minimize the propellant requests. The electric propulsion trajectory optimization is carried out with an indirect method based on the theory of optimal control and transforms the propellant minimization problem into a multipoint boundary value problem, solved with an iterative single-shooting procedure based on Newton's method. The problem considered here is a specific subclass of optimal control problems with discontinuous control law, named *bang-bang*. Techniques to address numerical issues and find proper tentative solutions, and an automated tool built over the user experience to autonomously generate tentative solutions, are explored. Issues regarding the handling of thrust discontinuities are also addressed, whereas the delicacy of the indirect method is tackled with specifically tailored strategies, such as the definition of an *a priori* thrust structure; the application of the Pontryagin's Maximum Principle allows to change a suboptimal solution when the thrust structure violates it in some arcs.

The dynamic model includes 4-body gravitation (spacecraft subject to the gravitational pull of the Earth, Moon, and Sun) and uses JPL's ephemerides to retrieve the gravitational bodies' states over time. The solar radiation pressure, a spherical harmonic model for the Earth, and the lunisolar gravitational effect are all included as additional perturbative effects. The delicate gravitational interaction between the Sun, Earth, and Moon dictates the dynamics in the neighborhood of the departure point, namely the Lagrangian point L_2 around the Sun-Earth and Earth-Moon binary systems. The proposed research aims to identify optimal trajectories among the sub-optimal ones in such a complex gravitational interdependency and seeks to provide a structured methodology to differentiate one from the others. Escape trajectories from Lagrangian points in both the Sun-Earth and Earth-Moon systems are the focus of this work. They are analyzed in detail in two different nuances; first, simple escape trajectories with a fixed time to escape and free terminal energy are sought, and then more complex escape trajectories with bounded terminal energy conditions are optimized. These solutions represent a starting point for both the transition into high-fidelity escape trajectories from quasi-periodic orbits (e.g., the Lyapunov orbits considered in this thesis) and for the analysis of interplanetary transfers (e.g., to Near-Earth Asteroids), and the effect that escape conditions have on their overall propellant consumption.

Contents

List of Figures

List of Tables

Acronyms

2BP	Two-Body Problem.
3BP	Three-Body Problem.
4BP	Four-Body Problem.
BC	Boundary Condition.
BCR4BP	Bi-Circular Restricted Four-Body Problem.
BVP	Boundary Value Problem.
CoV	Calculus of Variations.
CR3BP	Circular Restricted Three-Body Problem.
DC	Differential Corrector.
DCM	Direction Cosine Matrix.
DSG	Deep Space Gateway.
EM	Earth-Moon.
EME2000	Earth Mean Equator and Equinox of Epoch J2000.
EML_2	Earth-Moon Lagrangian Point L_2.
EOM	Equation of Motion.
EP	Electric Propulsion.
ER3BP	Circular Restricted Three-Body Problem.
FTDC	Fixed-Time Differential Correction.
H4BP	Hybrid Four-Body Problem.
HBVP	Hamiltonian Boundary Value Problem.
HE	Heliocentric Ecliptic.

HO	Halo Orbit.
ICRF	International Celestial Reference Frame.
IM	Indirect Method.
IMAGE	Indirect Method Automated Global Exploration.
JC	Jacobi Constant.
JD	Julian Day.
KSL	Kepler's Second Law.
L_1	Lagrangian Point L_1.
L_2	Lagrangian Point L_2.
L_3	Lagrangian Point L_3.
LEO	Low-Earth Orbit.
LHS	Left-Hand Side.
LLO	Lunar Low Orbit.
LO	Lyapunov Orbit.
LOP-G	Lunar Orbital Platform-Gateway.
LP	Lagrangian Point.
MJD	Modified Julian Day.
MOID	Minimum Orbit Intersection Distance.
MPBVP	Multi-Point Boundary Value Problem.
NAIF	Navigation and Ancillary Information Facility.
NBP	*n*-Body Problem.
NEA	Near-Earth Asteroid.
NL	Non Linear.
NRHO	Near Rectilinear Halo Orbit.
NSL	Newton's Second Law.
OC	Optimal Control.
OCP	Optimal Control Problem.
OCT	Optimal Control Theory.
ODE	Ordinary Differential Equation.

PMP	Pontryagin's Maximum Principle.
PO	Periodic Orbit.
QPLO	Quasi-Periodic Lyapunov Orbit.
QPNRHO	Quasi-Periodic Near Rectilinear Halo Orbit.
QPO	Quasi-Periodic Orbit.
R3BP	Restricted Three-Body Problem.
RF	Reference Frame.
RHS	Right-Hand Side.
RS	Reference System.
SC	Spacecraft.
SE	Sun-Earth.
SEL_2	Sun-Earth Lagrangian Point L_2.
SGP	Specific Gravitation Parameter.
SOI	Sphere Of Influence.
SRP	Solar Radiation Pressure.
STM	State Transition Matrix.
T_S	Thrust Structure.
TPBVP	Two-Point Boundary Value Problem.
UTC	Coordinated Universal Time.
VTDC	Variable-Time Differential Correction.
wrt	with respect to.
ZEN	Zenith-East-North.
ZVS	Zero-Velocity Surface.

Nomenclature

Symbol	Description	Value	Unit
a, $\mathbf{a}$	Acceleration	-	$\mathrm{km/s^2}$
a_p	Perturbing acceleration	-	$\mathrm{km/s^2}$
a_J	Earth asphericity effect	-	$\mathrm{km/s^2}$
a_{lsp}	Lunisolar effect	-	$\mathrm{km/s^2}$
a_{SRP}	Solar Radiation Pressure effect	-	$\mathrm{km/s^2}$
a	Semi-major axis (SMA)	-	km
a_h	Hohmann transfer SMA	-	km
A	CR3BP analytical orbit dimensions	-	-
A_x, A_y, A_z	SMA/sma/v-span	-	km
A_ξ, A_η, A_ζ	Nondimensional SMA/sma/v-span	-	-
AU	Astronomical unit	$1.49597870691 \times 10^8$	km
$\boldsymbol{A}$	Jacobian matrix	-	-
$\mathrm{c}(\cdot)$	$\cos(\cdot)$	-	-
c	Effective exhaust velocity	-	km/s
c	Speed of light	2.99792458×10^5	km/s
$\boldsymbol{c}$	OCP constants vector	-	-
C_{nm}	Spherical harmonic coefficients (order n, degree m)	-	-
$\mathscr{C}_3$	Characteristic energy	-	$(\mathrm{km/s})^2$
D, $\boldsymbol{D}$	Drag	-	N
e, $\boldsymbol{e}$, $\hat{\boldsymbol{e}}$	Eccentricity	-	-
E	Error	-	-
$\mathscr{E}$	Specific mechanical energy	-	$(\mathrm{km/s})^2$
$\mathcal{E}$	Epoch	-	UTC

Symbol	Description	Value	Unit
f	Family of solutions	-	-
g_0	Standard gravitational acceleration	9.80665	m/s^2
$\hat{\boldsymbol{g}}_1$, $\hat{\boldsymbol{g}}_2$, $\hat{\boldsymbol{g}}_3$	Heliocentric Ecliptic RF versors	-	-
G	Universal gravitational constant	$6.6743015 \times 10^{-20}$	$km^3/(kg \cdot s^2)$
h, $\boldsymbol{h}$, $\hat{\boldsymbol{h}}$	Specific angular momentum	-	-
$\mathcal{H}$	Hamiltonian	-	-
i	Inclination	-	rad
i	Imaginary number	-	-
I_{sp}	Specific impulse	-	s
$\hat{\boldsymbol{I}}$, $\hat{\boldsymbol{J}}$, $\hat{\boldsymbol{K}}$	EME2000 RF versors	-	-
J_C	Jacobi Constant (JC)	-	$(km/s)^2$
$\mathscr{J}_C$	CR3BP nondimensional JC	-	-
$\boldsymbol{J}$	CR3BP complete Jacobian matrix	-	-
$\mathcal{J}$	OCP Cost functional	-	-
$\mathcal{J}^*$	OCP Augmented Cost functional	-	-
$\mathcal{k}$	Boolean/relaxation factor	-	-
$\mathcal{k}_1$	OCP IM relaxation factor	-	-
$\mathcal{k}_2$	OCP IM max error increase factor	-	-
$\mathcal{k}_R$	Generic relaxation factor	-	-
ℓ^*	CR3BP characteristic length	-	km
L, $\boldsymbol{L}$	Lift	-	N
m	mass	-	kg
m^*	CR3BP characteristic mass	-	kg
M	Mean anomaly	-	rad
$\mathcal{M}_I$	Momentum integral (escape warning)	-	-
n	Mean motion	-	rad/s
p	Semiparameter	-	km

Symbol	Description	Value	Unit
p	Photon pressure	4.55682×10^{-6} (1AU)	$\mathrm{N/m^2}$
P_{nm}	Legendre functions (order n, degree m)	-	-
P	Power	-	W
$\mathcal{P}$	Solar constant (radiated power)	1367 (1AU)	$\mathrm{W/m^2}$
$\hat{\boldsymbol{p}}_{SC}$, $\hat{\boldsymbol{q}}_{SC}$, $\hat{\boldsymbol{w}}_{SC}$	Perifocal RF versors	-	-
r	Radius	-	km
r_E	Earth equatorial radius	6378.1363	km
r_H	Hill's sphere radius	-	km
r_{SOI}	SOI radius	-	km
$\boldsymbol{R}$	Direction Cosine Matrix	-	-
$\mathrm{s}(\cdot)$	$\sin(\cdot)$	-	-
S	Surface	-	$\mathrm{m^2}$
S_{nm}	Spherical harmonic coefficients (order n, degree m)	-	-
$\mathcal{S}_{\mathcal{F}}$	Switching function	-	-
t	time	-	s
t_ε	OCP IM nondimensional time	-	-
T	thrust	-	N
T_u, T_v, T_w	radial, tangential, out-of-plane T (ZEN RF)	-	N
$\mathscr{T}$	period	-	s
$\mathscr{T}_h$	Hohmann transfer period	-	s
$\mathscr{T}_{sid}$	Moon sideral period	27.32166	day
$\mathscr{T}_{syn}$	Moon synodic period	29.53059	day
$\mathscr{T}^*$	CR3BP characteristic period	-	s
u, v, w	radial, tangential, normal velocity (ZEN RF)	-	km/s
U	Potential function	-	$(\mathrm{km/s})^2$
$\mathscr{U}$	CR3BP nondimensional potential	-	-
u	Control variable	-	-
$\mathcal{U}$	Admissible controls	-	-
V, $\boldsymbol{V}$	Velocity	-	km/s

Symbol	Description	Value	Unit
V^*	CR3BP characteristic velocity	-	km/s
V_∞	Hyperbolic excess velocity	-	km/s
$\mathscr{V}$	Earth asphericity potential	-	$(\mathrm{km/s})^2$
x, y, z	Cartesian coordinates	-	km
$\boldsymbol{x}$, $\boldsymbol{X}$	State vector	-	-
$\hat{\boldsymbol{x}}_S$, $\hat{\boldsymbol{y}}_S$, $\hat{\boldsymbol{z}}_S$	Synodic RF versors	-	-
$\boldsymbol{y}$	OCP augmented state vector ($\boldsymbol{x}$, $\boldsymbol{\lambda}$)	-	-
$\boldsymbol{z}$	OCP complete state vector ($\boldsymbol{y}$, $\boldsymbol{c}$)	-	-
α_T	In-plane thrust angle	-	rad
β_T	Out-of-plane thrust angle	-	rad
γ_μ	EPH continuation parameter	-	-
ΔV	Change in velocity	-	km/s
η_R	Surface reflectivity	-	-
η_T	Thrust efficiency	-	-
$\eta_{sg,u}$, $\eta_{sg,v}$, $\overline{\eta_{sg}}$	Solar perturbation coefficients (radial, tangential, average)	-	-
ϑ	declination angle	-	rad
θ	Synodic RF angle	-	rad
λ, $\boldsymbol{\lambda}$	Adjoint variable/vector // eigenvalue	-	-
$\boldsymbol{\lambda}_r$	OCP position adjoint vector	-	-
$\boldsymbol{\lambda}_V$	OCP velocity adjoint vector (primer vector)	-	-
μ	Specific gravitation parameter (SGP)	-	$\mathrm{km}^3/\mathrm{s}^2$
μ_E	Earth	$3.98600441500 \times 10^5$	$\mathrm{km}^3/\mathrm{s}^2$
μ_ℓ	Moon	$4.90280107600 \times 10^3$	$\mathrm{km}^3/\mathrm{s}^2$
μ_S	Sun	$1.32712440018 \times 10^{11}$	$\mathrm{km}^3/\mathrm{s}^2$

Symbol	Description	Value	Unit
μ^*	CR3BP characteristic SGP	-	km^3/s^2
$\boldsymbol{\mu}$	OCP Lagrange multipliers	-	-
ν	True anomaly	-	rad
ξ, η, ζ	CR3BP synodic nondimensional coordinates	-	-
ρ	CR3BP nondimensional distance	-	-
σ_u, σ_v, σ	Solar perturbation proportionality terms (radial, tangential, comulative)	-	-
τ	CR3BP nondimensional time/period	2π	-
φ	Right ascension angle	-	rad
φ	OCP functional Mayer term	-	-
Φ	OCP functional Lagrange term	-	-
$\boldsymbol{\Phi}$, $\tilde{\boldsymbol{\Phi}}$	NBP/CR3BP State Transition Matrix	-	-
$\boldsymbol{\chi}$	Constraint vector	-	-
ω	Argument of periapsis	-	rad
ω_S	Synodic RF angular velocity	-	rad/s
Ω	Right ascension of the ascending node	-	rad

Chapter 1

Introduction

1.1 Preface

In 1492, a group of three sailing ships left the harbor of Palos de la Frontera in Spain. The *Pinta* and the *Niña*, two small caravels, were accompanied by the *Santa Maria*, the commanding carrack leading the navigation. A few days later, they all reached the main harbor of San Sebastián de La Gomera, where a few fixes to the boats were needed. The crew, led by the Pinzón brothers and Juan de la Cosa, took advantage of the stop to replenish the holds of the ships with all the necessary supplies for the long crossing through the Atlantic Ocean that they would have shortly had to do. Numerous years of navigation studies and calculations were needed to find the optimal course track to allow the three ships to take advantage of the Alisei (Trade Winds). On September 6, 1492, pushed by these favorable winds, the three ships started navigating along this narrow corridor that would have allowed them to cover the navigation in a shorter time. Almost at the end of the journey, an unknown phenomenon about the difference between the magnetic and geographical poles led the commanders to apply a real-time trajectory correction. On October 12, 1492, they managed to land on an island called Guanahani, in the modern Bahamas.

Carrying out a planning of the route, understanding whether the journey is feasible according to the resources that can be carried on, discovering if some paths provide advantages for a particular reason, and providing for the possibility of correcting any non-foreseen or non-predictable disturbing phenomena, are all factors at the basis of the modern space trajectory design and optimization. Indeed,

Cristoforo Colombo, in 1492, accomplished one of the most outstanding trajectory optimizations in history.

The fact that Colombo was *so* sure that he traveled to the East towards India, up to the point that he decided to proclaim all the indigenous people he encountered *indios* (and someone still calls them by that name) in what humanity universally recognize nowadays as America, is another story. A fun one, centuries later. But, honestly, that was simply a problem arising from selecting the wrong reference frame, and space trajectory optimization enthusiasts can surely relate to that.

Just as the transportation means of hundreds of years ago had their technological limitations, today, space *ships* must face various difficulties due to the clash with the often hostile space environment. While some requirements are somehow tradeable, sometimes, others narrow the range of possibilities substantially, separating feasible missions from unachievable ones. One of these stringent requirements is the available propellant and the fact that humans have not achieved building refueling stations out there in the solar system, *yet*. Since the early stages of the space exploration era, the questioning about the worthiness of a space mission was directly related to the amount of "useful" goods the spacecraft could carry on board; the payload. Maximizing the payload is undoubtedly a noble scope, namely having the maximum scientific return traded with the cost associated with the mission's ideation, design, and realization. However, maximizing the payload may lead to two different scenarios to accommodate it; a bigger spacecraft, or more free space in the same spacecraft. Actually, the first strategy is not entirely attainable -hold on a second on that-, and the second implies removing the only other tradeable quantity contained in the spacecraft itself, which is the propellant.

Understanding the amount of propellant a spacecraft can and should have on board is not as easy as it seems. Infinite propellant availability (or propellantless propulsion) would put an end to the story, making the space exploration a mere matter of *when* and *why* instead of *if* and *how*, and this thesis would not exist. Having more propellant to be used for the propulsive needs also means that the spacecraft is *bringing* that propellant while accelerating. Even a car consumes more gas with a full tank while, on the other hand, saving on gas to have a lighter car has the annoying effect of reducing the achievable mileage. However, there is an upper limit to the improvements a spacecraft can achieve by increasing the available propellant mass at the beginning of a mission.

1.2 Optimization Methods in Space Trajectories

In 1903, the archetype of the visionaries for propellant optimization, Konstantin Eduardovitch Tsiolkovsky, gifted humanity with his Rocket Equation in the "Exploration of the World Spaces by Reactive Devices".

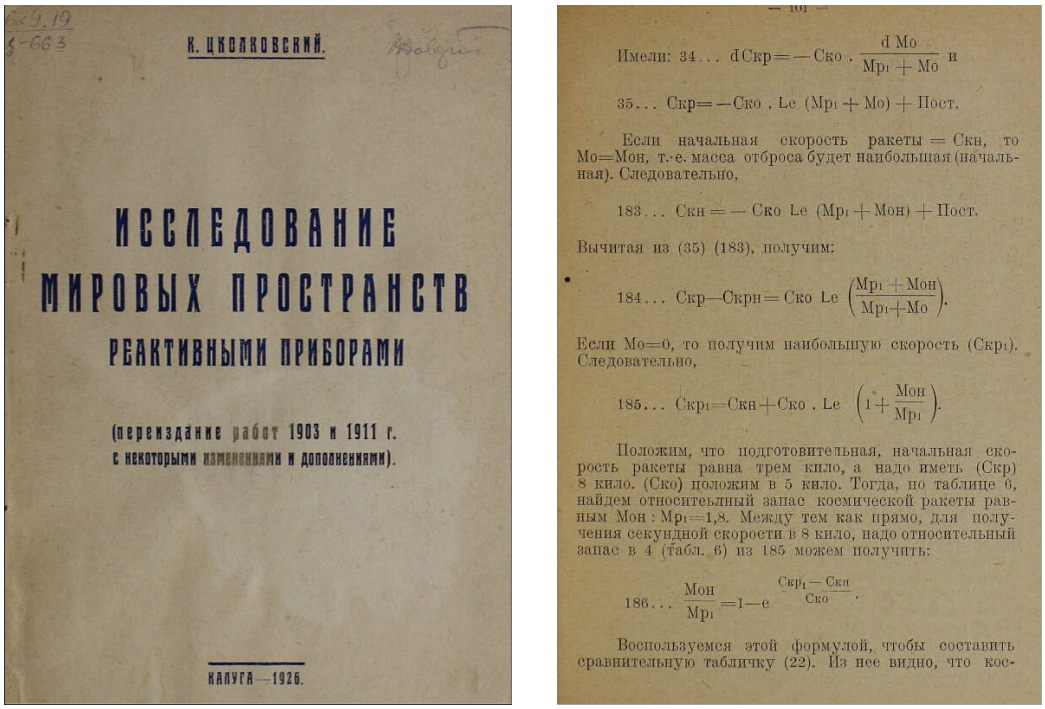

К. ЦИОЛКОВСКИЙ.

ИССЛЕДОВАНИЕ
МИРОВЫХ ПРОСТРАНСТВ
РЕАКТИВНЫМИ ПРИБОРАМИ

(переиздание работ 1903 и 1911 г.
с некоторыми изменениями и дополнениями).

КАЛУГА — 1926.

— 101 —

Имели: 34... $dCкр = -Cко \cdot \frac{d\,Mo}{Mp_1 + Mo}$ и

35... $Cкр = -Cко \cdot Le\,(Mp_1 + Mo) + Пост.$

Если начальная скорость ракеты = Скн, то Мо=Мон, т.-е. масса отброса будет наибольшая (начальная). Следовательно,

183... $Cкн = -Cко\ Le\,(Mp_1 + Mон) + Пост.$

Вычитая из (35) (183), получим:

184... $Cкр - Cкрн = Cко\ Le\left(\frac{Mp_1 + Mон}{Mp_1 + Mo}\right)$.

Если Мо=0, то получим наибольшую скорость ($Скр_1$). Следовательно,

185... $Скр_1 = Скн + Cко \cdot Le\left(1 + \frac{Мон}{Mp_1}\right)$.

Положим, что подготовительная, начальная скорость ракеты равна трем кило, а надо иметь (Скр) 8 кило. (Ско) положим в 5 кило. Тогда, по таблице 6, найдем относительный запас космической ракеты равным Мон : Mp_1=1,8. Между тем как прямо, для получения секундной скорости в 8 кило, надо относительный запас в 4 (табл. 6) из 185 можем получить:

186... $\frac{Мон}{Mp_1} = 1 - e^{-\frac{Скр_1 - Скн}{Cко}}$.

Воспользуемся этой формулой, чтобы составить сравнительную табличку (22). Из нее видно, что кос-

Fig. 1.1 *Exploration of the World Spaces by Reactive Devices*, 1903, Tsiolkovsky (reprint 1926) - front matter (left), first appearance of the Rocket Equation, p. 101 (right)

In Figure 1.1, the Tsiolkovsky equation appears in terms of the propellant fraction and assumes the following modern form:

$$\frac{m_p}{m_0} = 1 - \exp\left(-\frac{\Delta V}{I_{sp} g_0}\right).$$

Such concise, elegant formulation implies that the propellant request (m_p versus the initial spacecraft mass m_0) is a function of two parameters, besides the gravitational acceleration at sea level g_0; the change in velocity that the spacecraft has to provide to move from point A to point B, under specific dynamics (the ΔV), and the I_{sp} term, which is known as the specific impulse. The first one measures the cost of reaching the goal. The latter measures how efficiently a thruster is consuming the

propellant; the higher, the better or, more precisely, the higher, the less propellant for the same mission. Traditional chemical propulsion systems release a large quantity of energy in a very short amount of time, but they average an optimal specific impulse of about $250 \div 350$ s; for example, the Space Shuttle's solid rocket booster propellant had an I_{sp} of about 250 s, whereas its main liquid rocket engines provided an outstanding $I_{sp} = 450$ s. Physical limitations deny sensible improvements on I_{sp} in the foreseeable future for traditional propulsion. As missions became more demanding in terms of ΔV, the low I_{sp} of traditional propellants imposed an upper boundary on the achievable scenarios. However, there was, and there is, an alternative. As stated by Choueiri [1], electric propulsion systems have been the "prince in waiting" of spacecraft propulsion; as ready and tested in the previous decades, only in recent years has their use shifted from simple research and prototyping to real space applications. Electrical propulsion systems are capable of producing very high specific impulses; electrothermal, electrostatic, and electromagnetic propulsion systems respectively have I_{sp} in the order of $200 \div 1000$ s, up to 5000 s, and even beyond. The other side of the coin is that electric propulsion provides lower accelerations over time and ideally tends to require an effective ΔV greater than the ideal one, and thus the thrust phases of traditional rockets of few minutes are long gone; accelerations of hours, days, and weeks may be needed for the scope, and precisely oriented and adjusted over time. Additional constraints may arise, too; electric propulsion requires, *sic*, electricity, which may come from the Sun via solar panels; for example, if in an eclipse, the thruster may need to be turned off. Despite contingent reasons for which the thrust should or should not be applied, when and how to apply it in order to accomplish the same mission (from A to B) while minimizing the propellant request is the core of the present thesis.

Historically, two main branches of numerical methods have been applied to boundary value problems; direct and indirect methods [2]. They serve the same scope, namely solving the infinite-dimension time-continuous problem. Direct methods perform such operation by transcribing the original problem into subclasses that are subject to algebraic constraints; all continuous functions are discretized into a mesh, and the refinement level of this mesh provides the accuracy versus computational cost parameter of this class of numerical methods. Direct methods usually require a very high number of variables to describe the discretized problem adequately. Even with the advent of high-performing computers, some direct method optimizations are still computationally cumbersome in some cases. However, the

discretization reduces the problem's sensitivity to the initial guesses, making the model generally more robust compared to indirect methods. In some cases, direct methods can achieve a discrete optimality even without a complete understanding of the problem or of some boundary conditions; on the other hand, solutions may suffer from scarce accuracy and may require further refinement to jump into global minima.

On the other hand, indirect methods are generally faster because they require a vastly smaller set of variables and, when opportunely started, produce very accurate optimal solutions or provide tools to understand how such potentially suboptimal solutions can be improved. An indirect method introduces additional quantities, namely adjoint variables and Lagrange multipliers, to produce an augmented problem. Necessary conditions for optimality are derived and define a boundary value problem. The necessary conditions have to be retrieved case-to-case; therefore, a deeper understanding of the problem is mandatory. Moreover, given their high sensitivity to initial conditions, they may suffer from poor convergence, and an *a priori* knowledge (or reasonable guess) of the correct control strategy should be outlined in advance. Some of these drawbacks are inherently rooted in the indirect method (as the computational cost for direct methods), whereas others may be tackled and minimized.

A comprehensive comparison between direct and indirect methods is provided in Bett's work [2] and is beyond the scope of this thesis. However, it is worth mentioning that, in general, direct methods have been preferred for the most complex problems [3–5], both in terms of the dynamic model and constraints complexity, but the applicability of indirect methods has grown and similar problems are now treated with indirect methods [6–9]. Further details and examples will be given in the following Chapters.

1.3 Motivations and Objectives

The nuance of the trajectory design and optimization treated in this thesis is the minimization of the propellant request for a specific mission with the use of electric propulsion in a higher fidelity model, also known as the solar system model.

The selected scenario considers escape trajectories from Lagrangian Points and from orbits in their vicinity. The reasons behind this specific scenario may explain why Lagrangian points have gained significant interest in the last few decades. They represent equilibrium positions in the three-body dynamics, and a spacecraft positioned in a Lagrangian point remains locked in the reference frame that rotates with the two primaries, maintaining a relative fixed position; these positions offer highly advantageous strategic locations for both logistic purposes and the study and analysis of deep space. The scientific community is showing great interest in visiting such Lagrangian points and, in the near future, numerous space missions are planned towards them.

For example, among other initiatives, the European Space Agency is planning the Vigil mission [10], formerly known as Lagrange [11], to observe and monitor interplanetary space and solar activity, with two spacecraft in the Sun-Earth Lagrangian Points L_1 and L_5. Furthermore, multiple missions are foreseen in the Sun-Earth Lagrangian Point L_2 (SEL_2), such as PLATO [12] and EUCLID [13]. On the other hand, as missions are planned towards Lagrangian Points, other missions will be planned to depart from them; for example, such points could also be used as departure locations for interplanetary missions. For instance, a recent contribution [14] showed how departures from either Sun-Earth Lagrangian Points L_4 or L_5 might be extremely favorable for missions to Near-Earth Asteroids (NEAs) that have small Minimum Orbit Intersection Distance (MOID), in particular when the target asteroid passes relatively close to the Earth. Likewise, the Comet Interceptor [15] will be launched in 2029 towards SEL_2 as a piggyback on the Ariel mission [16]. The Comet Interceptor will then depart from SEL_2 to visit a yet-to-be-discovered Long Period Comet (LPC) or interstellar object as it approaches Earth's orbit.

In a similar way, a joint effort between NASA, CSA, ESA, and JAXA, aims to place the future Lunar Orbital Platform-Gateway (LOP-G, formerly named Deep Space Gateway, DSG) close to the Moon, on a stable orbit around, even though quite far from, the Earth-Moon Lagrangian Point L_2 (EML_2). This orbiting platform will be used to simplify some deep space operations greatly, produce a more practical handling of lunar resources, and act as a supply hub for other spacecraft, such as the Deep Space Transport, traveling to and from distant destinations [17–19]. Again, interesting scenarios arise by analyzing departure trajectories from this strategic location; moreover, the propulsive requirements to depart on low energy trajectories are minimal and, therefore, very appetible to be accomplished via electric propulsion.

In recent literature, Ref. [20] considered evasion from the SEL_2 in the Circular Restricted Three-Body Problem (CR3BP). Impulsive maneuvers were first considered and then extended to finite low-thrust electric propulsion, using direct collocation and a nonlinear programming optimization scheme. The analysis presented in this thesis additionally takes orbit eccentricity and Moon gravity into account. Ref. [21] implemented low-fidelity impulsive escape trajectories in the CR3BP domain from SEL_2 towards NEAs while using Four-Body Problem (4BP) dynamics to propagate the initial parking orbit and the NEAs trajectories. In a specular way, another recent effort [22] computed via a genetic algorithm impulsive and low-thrust trajectories towards NEAs departing from periodic Lissajous orbits around SEL_1 and SEL_2 in the CR3BP, transitioning only these suboptimal outbound trajectories into a higher-fidelity model via a direct optimization solver, the General Purpose Optimal Control Software (GPOPS-II [23]), implemented with IPOPT [24]. The present analysis extends the overall fidelity by transitioning the Periodic Orbits (POs) of the CR3BP to higher-fidelity Quasi-Periodic Orbits (QPOs), thus accurately representing the epoch-dependent dynamics. Furthermore, this thesis exploits and leverages the use of an indirect optimization method and its advanced theoretical tools for the accurate determination of optimal escape solutions in a complete 4BP dynamics with perturbations.

On the other hand, in the Earth-Moon system, recent contributions studied the access to Lagrangian Points [25, 26], but the emphasis was not on low-thrust escape trajectories. Impulsive escape trajectories from the EML_2 were analyzed in Ref. [27] in the Sun-Earth-Moon Bi-Circular Restricted Four-Body Problem (BCR4BP), either for direct escape or via Earth swing-by; the Sun gravitational perturbation and the relative Moon angular position were both considered. The scenario proposed in this thesis is further refined by implementing the use of electric propulsion, the JPL's DE430 ephemerides, and a higher fidelity model for direct escape trajectories.

Several perturbing accelerations influence motion close to Lagrangian Points. For this reason, the dynamic model adopted in this thesis considers 4-body gravitation. Thus, the spacecraft is subject to Earth, Moon, and Sun gravity; JPL's ephemerides are used to retrieve the states of the gravitational bodies over time. Perturbations and gravitational effects, such as the solar radiation pressure, a spherical harmonic model for the Earth, and the lunisolar gravitational effect, are included and analyzed. The selected scenario, from which optimal escape trajectories will be computed, has as a departure point the Lagrangian point L_2 around the Sun-Earth and Earth-

Moon binary systems. The dynamics in the vicinity of such Lagrange points is characterized by a complex gravitational interaction between Sun, Earth, and Moon.

In such intricate gravitational interdependency, the proposed research aims at finding optimal trajectories among the suboptimal ones and tries to provide a general framework to distinguish the ones from the others. In order to analyze and optimize the time-continuous problem domain, the choice of the appropriate numerical method is of utmost importance, namely, a numerical model able to provide theoretical insights regarding *how* suboptimal solutions can be improved would be very useful for the scope.

In this thesis, the optimization of electric propulsion trajectories is carried out with an indirect method based on the theory of optimal control and transforms the propellant minimization problem into a multipoint boundary value problem. The boundary value problem is then solved with an iterative single-shooting procedure based on Newton's method. The problem considered here is a specific subclass of optimal control problems with discontinuous control law, named *bang-bang*; extensive discussion about this topic will be provided later in the thesis. Techniques to address numerical issues and find proper tentative solutions will be introduced, and a tool built over the user experience will be provided to produce initial neighborhood guesses via a continuation method. The optimization method finds local optima with computational efficiency and convergence robustness, which enables the identification of the most relevant local optima and ultimately the selection of the global optimum among them. Escape trajectories from Lagrangian Points in both the Sun-Earth and Earth-Moon systems are analyzed as a starting point and then transitioned into high-fidelity escape trajectories from quasi-periodic orbit.

The main objectives of this thesis are the following:

- Unify and improve previous research efforts and define a framework for the successful application of indirect methods to escape trajectories from Lagrangian Points and Quasi-Periodic Orbits in a high-fidelity model, including perturbation effects and real planetary ephemerides, and merging different detached efforts in literature into a unified approach

- Create a tool for automatically building and transitioning from Periodic Orbits to Quasi-Periodic Orbits in an n-body model with perturbations, allowing for realistic and correct time-dependent Quasi-Periodic Orbits to be used as

departure points for escape trajectories and the option to easily modify the model fidelity by adding or removing gravitational bodies

- Address issues related to the handling of thrust discontinuities and definition of suitable initial guesses for the optimization process
- Develop an automated global search algorithm that leverages the benefits of indirect methods, including the ability to compute initial guesses, and find hundreds of escape trajectories with self-recovery and corrective techniques robustly
- Analyze the characteristics of escape trajectories from the Sun-Earth L_2, Earth-Moon L_2, and Quasi-Periodic Orbits in the vicinity of these points, with a focus on the effects of perturbations and optimal escape conditions
- Provide fast and easy evaluation of escape trajectories to assist in the design and planning of interplanetary missions with departures from Lagrangian Points and Quasi-Periodic Orbits towards heliocentric destinations such as Near-Earth Asteroids.

1.4 Dissertation overview

Here a brief overview of the thesis contents is outlined.

Chapter 2 discusses the dynamical model in which the spacecraft moves over time. A concise description of the main reference systems is outlined, followed by some concepts of basic astrodynamics. The three-body problem and the n-body problem domains are extensively discussed in their differences and distinctive aspects, and techniques to transpose a problem from one system to the other are proposed and discussed. Epoch-dependent considerations are introduced, and the principal perturbing accelerations acting in the higher fidelity model are explicitly derived.

Chapter 3 deals with all the processes required to compute periodic and quasi-periodic orbits, respectively, in the three-body and n-body problems. Single-shooting methods and differential correction strategies are described here to account for the nonlinearities that may prevent the periodicity or the quasi-stability of quasi-periodic orbits. A novel algorithm to transition from the three-body domain to the higher fidelity one, and *vice versa*, is discussed in its main aspects.

Chapter 4 introduces the optimal control theory and defines the multi-point value problem subject to optimization. The numerical tools to solve the optimization problem are introduced, and theoretical insights provided by the indirect methods are extensively analyzed in their specific features. Here specific algorithms and manipulations to improve the convergence of the method are discussed, and then the optimal control theory is applied to the spacecraft trajectory optimization domain.

Chapter 5 analyzes the solutions for optimal escape trajectories from the Sun-Earth and Earth-Moon Lagrangian point L_2 in the so-called Hybrid 4 Body Problem. Detailed analysis of the switching function defining the optimal thrust phases is performed. Different cases are presented, spanning a whole lunar month and with different constraints on the desired mission duration and terminal energy. Strategies to comply with the optimality conditions and the fulfillment of the Pontryagin's Maximum Principle are here outlined in detail, with a comprehensive discussion regarding optimal thrust arcs, thrust strategies, optimal thrust directions, and favorable exploitation of the lunisolar perturbation.

In Chapter 6, selected trajectories are transitioned into the complete high-fidelity 4 Body Problem. Planar Lyapunov orbits are computed in the n-body domain and

rendered quasi-stable in order to be used as departure locations for such escape missions. Differences in performances in this domain are also detailed.

Chapter 7, in conclusion, presents a summary of the most significant contributions and proposes future research directions and topics.

Chapter 2

Dynamic models

Chapter 2 describes the dynamic model implemented for the whole analysis. A significant part of the research bases its assumptions on the use of the n-body Equations of Motion (EOMs) in a higher fidelity model; indeed, a comprehensive discussion will be given to detailing perturbing accelerations. Nonetheless, preliminary considerations in the Three-Body Problem (3BP) are helpful for preliminary analyses and the generation of guess seeds to create the QPOs.

The first part of the Chapter introduces the reference systems used for the ephemeris model and the description of the Spacecraft (SC) motion. A brief introduction to classical orbital parameters is also provided, in the framework of orbital plane motion. Although a complete definition of these topics, including the Two-Body Problem (2BP), Kepler's laws, conic sections, primary assumptions, and special types of orbits, as well as the derivation of the most useful vectorial quantities, is undoubtedly interesting, such information is beyond the scope of this thesis. Therefore, only the most relevant details that are necessary for the later sections of this thesis will be provided. For example, each SC state can be defined completely using six quantities, such as position and velocity vectors, or orbital elements that also provide direct information on the orbit shape. Some examples of orbital elements include Keplerian elements, equinoctial elements, two-line element sets, Delaunay variables, and Poincaré variables. For further information and more in-depth analysis, reference can be made to well-known textbooks on orbital mechanics, such as [28–38]. The last part of the Chapter introduces the dynamic models referred to the CR3BP and n-Body Problem (NBP), thoroughly detailed in their main assumptions.

Please note that, while there are more accurate models and analyses than the CR3BP (such as the Elliptical Restricted Three-Body Problem, the Bi-Circular Four-Body Problem (BC4BP), and so on [39]), their exploitation was superseded by the development of an improved robust method for transitioning directly CR3BP states to the high-fidelity NBP, avoiding to perform further intermediate transitions.

The following notation, unless otherwise specified, will be used throughout the thesis to have a clear and concise expression of formula and equations; vectors will be presented in lowercase bold fonts ($\boldsymbol{x}$), with the exceptions of known quantities (e.g., velocity $\boldsymbol{V}$), and will be column vectors; unit vectors are bold lowercase letters with a hat ($\hat{\boldsymbol{x}}$); matrices are identified via uppercase bold fonts ($\boldsymbol{A}$); quantities derived over time will be marked with one or multiple dots, for both scalars and vectors ($\dot{x}$, $\ddot{x}$, $\dot{\boldsymbol{x}}$, $\ddot{\boldsymbol{x}}$). Greek letters and Chancery fonts refer to quantities that have undergone some mathematical manipulations such as nondimensionalization. If such characters have the same graphical symbology with their corresponding Latin characters, thus being similar in the two versions (dimensional and non-dimensional), a tilde or a breve superscript will be used ($\tilde{x}$,$\dot{\tilde{x}}$, $\ddot{\tilde{x}}$, $\tilde{\boldsymbol{x}}$,$\dot{\tilde{\boldsymbol{x}}}$, $\ddot{\tilde{\boldsymbol{x}}}$ or $\breve{x}$,$\dot{\breve{x}}$, $\ddot{\breve{x}}$, $\breve{\boldsymbol{x}}$,$\dot{\breve{\boldsymbol{x}}}$, $\ddot{\breve{\boldsymbol{x}}}$)[1].

[1]The notation showing dots above superscripts is preferred for clarity. Look how happy are they!

2.1 Reference systems

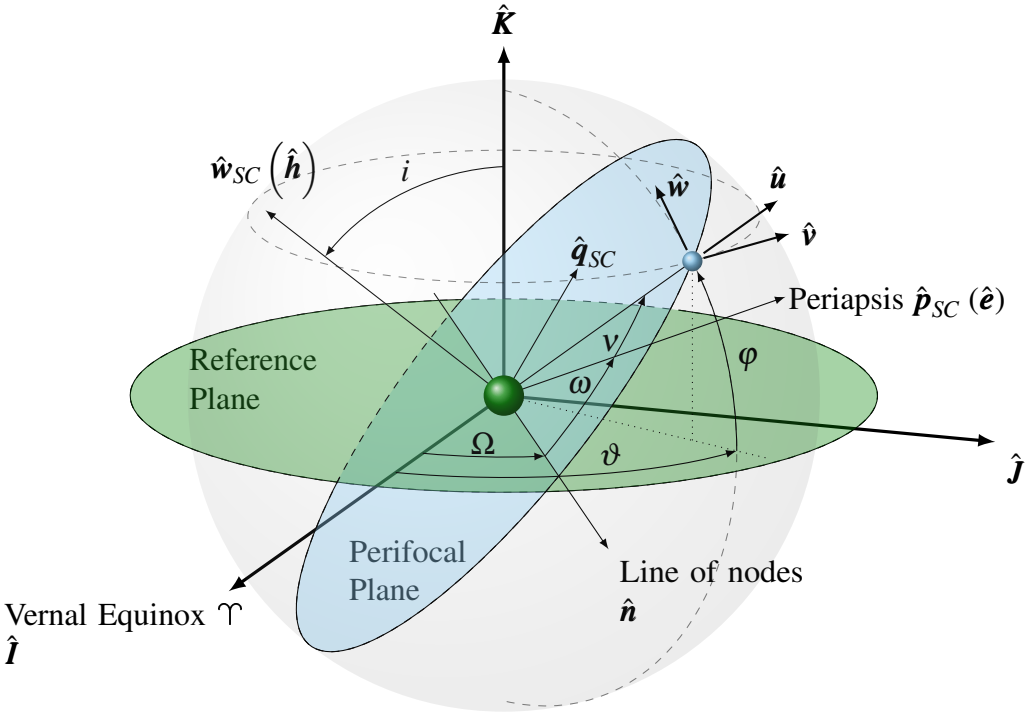

Fig. 2.1 EME2000 $\{\hat{I}, \hat{J}, \hat{K}\}$, perifocal $\{\hat{p}_{SC}, \hat{q}_{SC}, \hat{w}_{SC}\}$, and ZEN $\{\hat{u}, \hat{v}, \hat{w}\}$ RSs

A generic Reference System (RS) is uniquely defined by its origin, a fundamental plane, and an orthonormal right-handed triad which composes the Reference Frame (RF). Depending on the specific analysis, it may be more convenient to implement an inertial or non-inertial RS. The main difference between the two lies in the presence or absence of additional pseudo-accelerations due to relative observations, such as the Coriolis effect in rotating RFs. The motion of a satellite or a celestial body with respect to the Earth, for example, is easily described in an inertial RS in different sets of coordinates, such as cartesian or polar.

In the present thesis, the geocentric-equatorial RS coincides with the so-called Earth Mean Equator and Equinox of Epoch J2000 (EME2000). JPL ephemerides pertaining to the DE4xx series, such as the JPL DE430 used in this analysis, are provided in the International Celestial Reference Frame (ICRF) and include nutations and librations [40]. These wobbling effects historically granted the EME2000 RF, also known as J2000, the quasi-inertial definition. However, since the rotational offset between the ICRF and the dynamical EME2000 has a magnitude of a hundredth

of arcsecond [41], the EME2000 RF is henceforth considered inertial. Such RF is represented in Figure 2.1; its origin is at the Earth's center, the reference plane is the equatorial plane, and its unit vectors $\{\hat{\boldsymbol{I}},\ \hat{\boldsymbol{J}},\ \hat{\boldsymbol{K}}\}$ have $\hat{\boldsymbol{I}}$ aligned towards the direction of the Vernal equinox, $\hat{\boldsymbol{K}}$ normal to the reference plane, $\hat{\boldsymbol{J}}$ completing the triad.

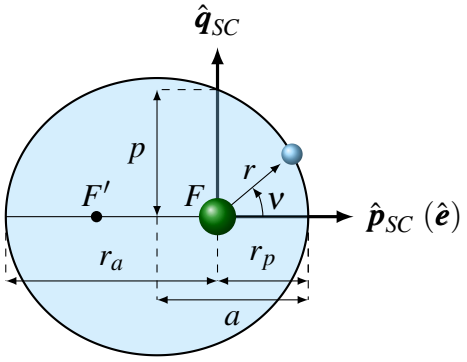

Fig. 2.2 Perifocal RF - orbit with eccentricity $e = 0.4$

The perifocal RF contains the satellite motion. The origin of this RF is at the center of the gravitational body in the primary focus and has unit vectors $\{\hat{\boldsymbol{p}}_{SC},\ \hat{\boldsymbol{q}}_{SC},\ \hat{\boldsymbol{w}}_{SC}\}$. The $\hat{\boldsymbol{p}}_{SC}$ unit vector coincides with the eccentricity vector direction $\hat{\boldsymbol{e}}$, $\hat{\boldsymbol{w}}_{SC}$ is normal to the orbital plane - with direction matching the specific angular momentum vector $\hat{\boldsymbol{h}}$, as in Figure 2.1-, and $\hat{\boldsymbol{q}}_{SC}$ completes the triad. Under the assumption of no external perturbations, a SC in this RF would follow a conic indefinitely, provided that the path is closed, according to Kepler's First Law. The shape and orientation of a conic in space can be described using a set of parameters, such as the classical Keplerian ones. The Keplerian set $\{a, e, i, \Omega, \omega, \nu\}$ uniquely defines the orbit's geometry and orientation in space and also identifies the spacecraft's location. However, a subset of these parameters is sufficient for the perifocal RF representation; in the case of a closed orbit, its dimension and shape depend respectively on the semi-major axis (sma) a, i.e., the half distance between the SC's periapsis r_p and apoapsis r_a, and on the eccentricity e, measuring the deviation of the orbit from a circle. These two Keplerian elements, often interconnected by the semiparameter (or semilatus rectum) $p = a\left(1-e^2\right)$, suffice to draw the orbit in Figure 2.2 via the well-known conic equation [28–38]:

$$r = \frac{a\left(1-e^2\right)}{1+e\cos\left(\nu\right)}\,. \tag{2.1}$$

The true anomaly, ν, identifies the angular position of the SC from the periapsis in the perifocal RF. The mean anomaly, M, can also be used. Therefore, the three Keplerian elements $\{a, e, \nu\}$, fully define the SC's location on a specific orbit in the perifocal RF.

To orient the perifocal plane in the three-dimensional space (with respect to the EME2000 RF in Figure 2.1), the other remaining three Keplerian elements are required. In particular, the orbital plane may be inclined relative to the reference plane (equator) by a generic angle i. Such plane intersects the reference plane by creating an intersecting line called line of nodes $\hat{\boldsymbol{n}}$, which marks the SC's passage from the southern to the northern hemispheres, respectively at the ascending and descending node. The principal direction of $\hat{\boldsymbol{n}}$ coincides with the ascending node and is measured from the $\hat{\boldsymbol{I}}$ axis in the EME2000 RF via the right ascension of the ascending node (RAAN) Ω. For non-circular orbits, the location of the periapsis is identified by the argument of periapsis ω, measured from the line of nodes, for non-equatorial orbits, or from the $\hat{\boldsymbol{I}}$ axis otherwise, when Ω is not defined.

Positioned in the SC's center of mass, there is the Zenith-East-North (ZEN) RF. Such topocentric, rotating, non-inertial frame, identified by the triad $\{\hat{\boldsymbol{u}},\ \hat{\boldsymbol{v}},\ \hat{\boldsymbol{w}}\}$, conveniently describes the SC's velocity components in the radial, tangential, and normal directions, respectively. The radial direction is obtained by prolonging the position vector of the SC from the Earth's center. The tangential and normal directions coincide with the directions of a parallel and a meridian of a celestial sphere. As shown in Figure 2.1, in general the velocity components are neither parallel nor coincident with the orbital SC velocity vector, namely the vector tangent to the orbital plane.

The choice of a convenient RF may facilitate the analysis and resolution of a specific problem. Indeed, the same object in space can be described via multiple RSs; the SC in Figure 2.1 has perifocal characteristic quantities $\{a, e, i, \Omega, \omega, \nu\} = \{r,\ 0.01,\ 50^\circ,\ 30^\circ,\ 30^\circ,\ 20^\circ\}$, but may be described as well in the EME2000 RF in polar coordinates $\{r,\ \vartheta,\ \varphi\} = \{r,\ 67.45^\circ,\ 35.93^\circ\}$ or in cartesian coordinates $\{x, y, z\} = r \cdot \{0.34,\ 0.82,\ 0.65\}$. Which set of quantities is more suitable depends on the specific analysis.

The state of a SC is described by the following set of Ordinary Differential Equations (ODEs) in an inertial RS centered in the primary celestial body, for example the EME2000. Such equations describe the state evolution of the SC,

namely how its position and velocity vectors, $\boldsymbol{r}$ and $\boldsymbol{V}$, and its mass m change over time and under different influences and perturbations [42]

$$\frac{\mathrm{d}\boldsymbol{r}}{\mathrm{d}t} = \boldsymbol{V} \tag{2.2a}$$

$$\frac{\mathrm{d}\boldsymbol{V}}{\mathrm{d}t} = \boldsymbol{g} + \frac{\boldsymbol{T}}{m} + \frac{\boldsymbol{D}}{m} + \frac{\boldsymbol{L}}{m} + \mathbf{a}_p \tag{2.2b}$$

$$\frac{\mathrm{d}m}{\mathrm{d}t} = -\frac{T}{c}, \tag{2.2c}$$

where the last equation, (2.2c), represents the decrease in mass due to the propulsive effort. The implemented propulsive systems are two low-thrust Electric Propulsion (EP) thrusters with different but constant specific impulse I_{sp}. Moreover, in the present discussion, all the trajectories will be far enough from the Earth's atmosphere so that all aerodynamic forces, such as the drag $\boldsymbol{D}$ and the lift $\boldsymbol{L}$, shall be considered negligible. The term $\boldsymbol{g}$ is the gravitational acceleration

$$\boldsymbol{g} = -\frac{\mu}{r^2}\frac{\boldsymbol{r}}{r} \tag{2.3}$$

and, if only such force is present without any external perturbation or further gravitational attraction, such quantities can be integrated analytically in the 2BP domain. Two interesting quantities from such simplification are useful for the discussion. Please refer to any of [29, 31, 38] for a more detailed analysis.

The first vital information from the 2BP formulation is that the specific mechanical energy is constant for any orbit in such domain, namely

$$\mathscr{E} = \frac{V^2}{2} - \frac{\mu}{r}, \tag{2.4}$$

where the first term refers to the specific kinetic energy and the latter to the specific potential energy. Equation (2.4) is historically known as *vis-viva*. Further considerations provide that the SC specific energy is related to the shape of the orbit:

$$\mathscr{E} = -\frac{\mu}{2a}. \tag{2.5}$$

The passage from negative to positive values of $\mathscr{E}$ distinguishes closed orbits (ellipses, $\mathscr{E} < 0$) from open orbits ($\mathscr{E} \geq 0$, for parabolas ($=$) and hyperbolae ($>$)). The SC can reach an infinite distance from the central body when on an open orbit.

In practice, the concept of Sphere Of Influence (SOI) is employed, namely the region of space in which a smaller body, such as a SC, can be considered under the gravitational attraction of a single central body, while the gravity of other bodies can be neglected at a first approximation.

The second useful quantity in the 2BP is the specific angular momentum h,

$$\boldsymbol{h} = \boldsymbol{r} \times \boldsymbol{V}\,, \tag{2.6}$$

which is conserved for every specified orbit. From such information, multiple milestones arise such as the Kepler's laws and closed form equations for transfer orbits and orbit determination. For example, being the specific mechanical energy $\mathscr{E}$ preserved throughout any orbit, one can compare two different statuses of an orbit to stem further considerations, i.e. from periapsis to apoapsis

$$\mathscr{E} = \frac{V_p^2}{2} - \frac{\mu}{r_p} = \frac{V_a^2}{2} - \frac{\mu}{r_a}\,. \tag{2.7}$$

A trajectory reaching an infinite distance from the central body at its apoapsis has a corresponding null velocity, leading to the minimum escape velocity V_e formula

$$V_e = \sqrt{\frac{2\mu}{r}}\,, \tag{2.8}$$

for any departing radius r value. Similarly, for more energetic orbits, one can assume that at the SOI there will be an excess velocity in the corresponding hyperbola, which is known as hyperbolic excess velocity V_∞, namely

$$\mathscr{E} = \frac{V^2}{2} - \frac{\mu}{r} = \frac{V_\infty^2}{2} - \cancel{\frac{\mu}{r_\infty}} \implies V_\infty = \sqrt{V^2 - \frac{2\mu}{r}} = \sqrt{V^2 - V_e^2}\,. \tag{2.9}$$

A common quantity used in preliminary interplanetary studies is the characteristic energy $\mathscr{C}_3$ which measures directly such specific excessive energy. Its values is simply the specific mechanical energy doubled

$$\mathscr{C}_3 = 2\mathscr{E} = V^2 - \frac{2\mu}{r} = -\frac{\mu}{a} \tag{2.10}$$

and, for orbits having an hyperbolic excess, the $\mathscr{C}_3 = V_\infty^2$ formulation is valid. The $\mathscr{C}_3$ information is synergically connected to the SOI concept just introduced. Although the SOI has characteristic shapes depending on the complex interaction among other gravitational bodies, under suitable simplifying assumptions it can be considered a perfect sphere whose radius is approximately equal to

$$r_{SOI,ij} \approx r_{ij} \left(\frac{m_j}{m_i} \right)^{2/5}, \tag{2.11}$$

where $r_{ij} = r_j - r_i$ is the position vector of the smaller j-th gravitational body with respect to the bigger i-th gravitational body. Although more complex dynamics and concepts will be used throughout the thesis, the patched-conic approximation, which is often used in preliminary analysis, uses the 2BP approximate value of the SOI's radius to split a complex trajectory into simpler 2BPs.

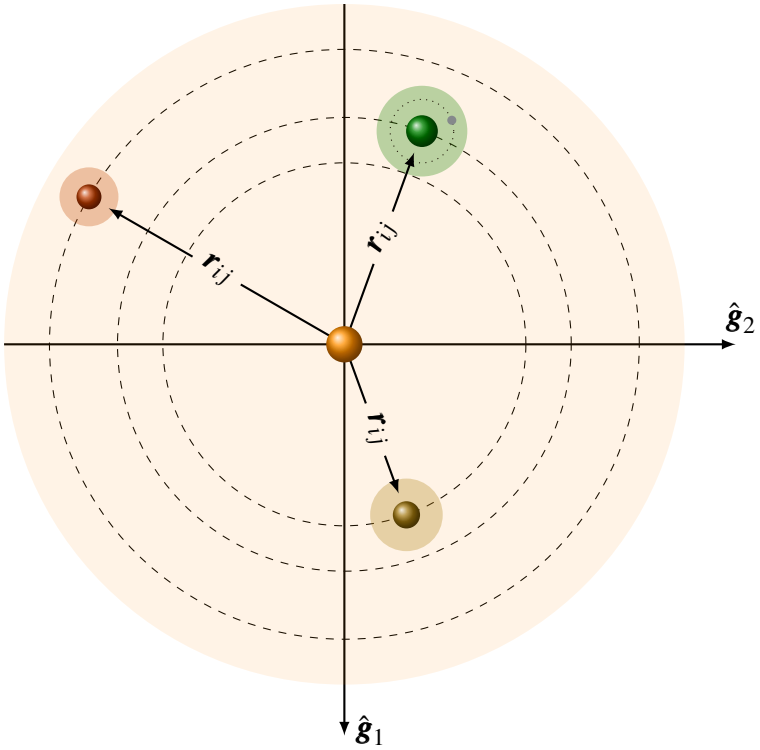

Fig. 2.3 Schematic representation of Spheres of Influence in the Heliocentric Ecliptic RF

For example, in the Heliocentric Ecliptic (HE) RF, defined through the triad $\{\hat{\boldsymbol{g}}_1, \hat{\boldsymbol{g}}_2, \hat{\boldsymbol{g}}_3\}$ centered in the Sun and lying on the ecliptic plane, all the j-th planets in the solar system have their own SOI depending on their mutual distance with

respect to the Sun and proportional to their mutual mass ratio, as per Equation (2.11). Figure 2.3 shows in light orange the Sun's SOI, which comprises all the planets, and a superimposed SOI referred to each planet. Every body orbiting inside a planet's SOI, in the 2BP formulation, can be supposed to experience only that planet gravitational attraction, as per the Moon around the Earth.

Table 2.1 shows the SOIs radii and escape velocities, computed with departures at the planet's surface, for the four inner planets.

	r_{SOI} [10^6 km]	V_e [km/s]
Mercury	0.112392	4.2500
Venus	0.616227	10.3613
Earth	0.924647	11.1799
Mars	0.527973	5.0222

Table 2.1 Escape quantities

In the present discussion, it has been imposed that a complete escape took place if a SC reached a distance from the central body close to three times its SOI's radius. For the Earth's gravitational pull combined to the Moon's one, such escape limit has been imposed to 3 millions km from Earth's center.

2.2 Three Body Problem

The CR3BP is the first approximate representation whose fidelity to the n-body dynamic model considered in this thesis is close enough to be able to carry out preliminary considerations closely related to the real scenario. The CR3BP dynamic model deals with studying the interaction between three bodies, including two main gravitational bodies and one of negligible mass, with the addition of some hypotheses that simplify the discussion deriving directly from the 3BP dynamical model.

While the 2BP presents (elegant) closed-form analytical solutions that are conics, by adding a third body in the gravity model no closed-form solutions for the EOMs have been found up to date. Such consideration keeps being true even with further simplifications that transition the 3BP to the simplified CR3BP.

Specifically, the 3BP referred to a generic binary system is analyzed here. The main bodies, with masses m_1 and m_2 respectively for the bigger and smaller pri-

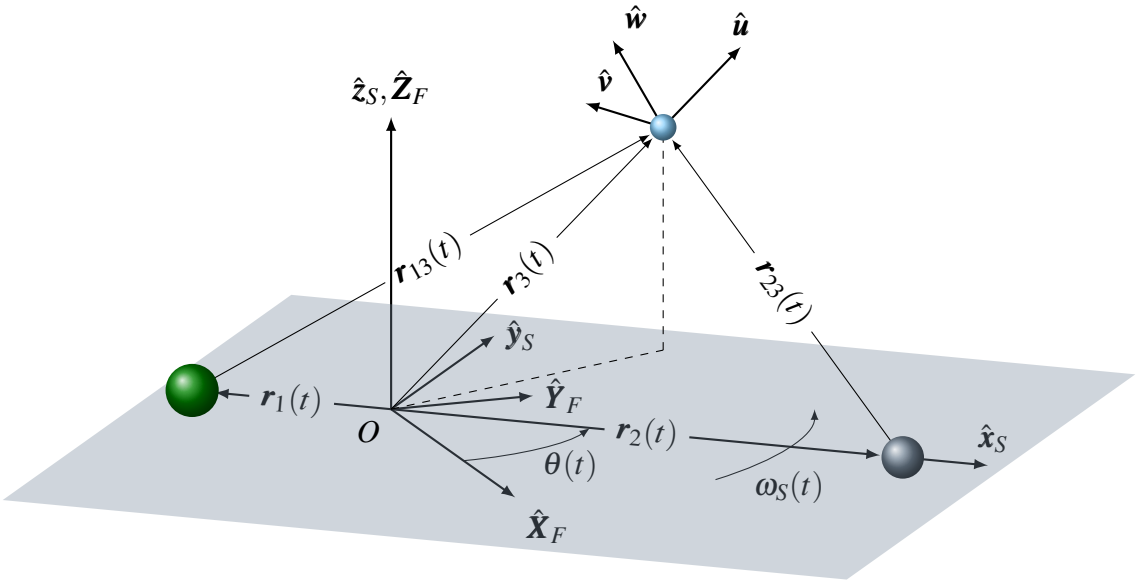

Fig. 2.4 Synodic reference system - not to scale

mary, revolve around their barycenter. When observed from an inertial RS, such as the $\{\hat{\boldsymbol{X}}_F, \hat{\boldsymbol{Y}}_F, \hat{\boldsymbol{Z}}_F\}$ represented in Figure 2.4, their mutual angular speed is $\omega_S(t)$. The non-inertial, rotating RF centered in the barycenter is also called synodic RF, $\{\hat{\boldsymbol{x}}_S, \hat{\boldsymbol{y}}_S, \hat{\boldsymbol{z}}_S\}$, and follows the main bodies' path; the $\hat{\boldsymbol{x}}_S$ axis lies on the line joining the two primaries, the $\hat{\boldsymbol{z}}_S$ axis is normal to the plane on which the orbits of the primaries lie and $\hat{\boldsymbol{y}}_S$ completes the right triad. The third body can move in the 3D space freely under the mutual influence of both the primary bodies; up to this point, the description of this system may resemble the Sun-Earth-Moon three-body system, being Sun and Earth the primary bodies and the Moon the third one; however, in such scenario, even if Moon's gravitational influence would clearly be orders of magnitude lower than those of the two more massive bodies, it would still be experienced and would influence the relative motion. Therefore, if the mass of the third body is supposed to be negligible, being the third body a much smaller object such as a SC, the Restricted Three-Body Problem (R3BP) hypotheses arise, namely, the third body does not influence nor exerts accelerations on the primaries, but is influenced by both of them [28, 31, 35].

The rotation rate $\omega_S(t)$ depends on the distance between the two primaries $\boldsymbol{r}_{12}(t)$. A generic vector with double subscript $\boldsymbol{r}_{ij}$ is a position vector from the i-th to the j-th body such as

$$\boldsymbol{r}_{ij}(t) = \boldsymbol{r}_i(t) - \boldsymbol{r}_j(t)\,, \tag{2.12}$$

where, rigorously, $\boldsymbol{r}_i(t) = \boldsymbol{r}_{Oi}(t)$, with respect to the origin O. The dimensional mean motion for the binary system is then

$$n(t) = \sqrt{\frac{\mu_1 + \mu_2}{r_{12}(t)^3}} = \sqrt{\frac{\mu^*}{r_{12}(t)^3}}\,, \tag{2.13}$$

where μ^* is the sum of the specific gravitational parameters of the primaries. Therefore, the angle between the inertial and the synodic RSs at epoch can be computed as

$$\theta(t) = n(t)t\,, \tag{2.14}$$

where t is the dimensional elapsed time in seconds. Such angle θ and the mean motion n generally imply roto-pulsating behaviors as long as the generic distance between the primaries is not constant. Indeed, such quantities are time-dependent if planetary ephemerides are used in the computation or if the eccentricity of Keplerian orbits is taken into consideration. If the primaries revolve around their common barycenter on circular Keplerian orbits, then such further hypothesis completes the CR3BP assumptions. Under these simplifying hypotheses, the primaries position vectors have constant module $r_i(t) = r_i$ for all times. Thus, their relative distance and the mean motion n become constant, leading to a constant prograde swept angle θ with constant angular velocity ω_S. Both for a historical convention in literature [43–45] and numerical precision, the quantities of the CR3BP are usually nondimensionalized with respect to some characteristic values. Specifically these nondimensionalizations are:

$$\begin{cases} \ell^* = r_1 + r_2 & \text{(2.15a)} \\ m^* = m_1 + m_2 & \text{(2.15b)} \\ \mathscr{T}^* \triangleq \sqrt{\dfrac{(\ell^*)^3}{Gm^*}} & \text{(2.15c)} \end{cases}$$

The characteristic length ℓ^* is the fixed mean distance between the two primaries; the characteristic mass m^* is the sum of the primaries masses; the characteristic time $\mathscr{T}^*$ is not directly imposed but is the result of imposing that the nondimensional universal gravitational constant equals the unity in the Kepler's third law formulation, and therefore is implicitly derived. Such characteristic quantities are included in the Nomenclature at the beginning of this document.

Therefore, the nondimensional quantities for distances, masses, and times, under the CR3BP assumptions, are

$$\begin{cases} \rho_{12} = \dfrac{r_{12}}{\ell^*} = 1 & \text{(2.16a)} \\ \mu \triangleq \dfrac{m_2}{m^*} & \text{(2.16b)} \\ \tau = \dfrac{\mathscr{T}}{\mathscr{T}^*} = 2\pi & \text{(2.16c)} \end{cases}$$

With simple mathematical steps the nondimensional mass ratios are

$$\mu \triangleq \frac{\mu_2}{\mu^*}, \qquad \frac{\mu_1}{\mu^*} = 1 - \mu \tag{2.17}$$

and, similarly, the barycenter position with respect to the bigger primary is easily derived

$$\rho_{CG} = \frac{\sum \rho_i \mu_i}{\sum \mu_i} = \mu\,. \tag{2.18}$$

Therefore

$$\rho_1 = \frac{r_1}{\ell^*} = -\mu \tag{2.19a}$$

$$\rho_2 = \frac{r_2}{\ell^*} = 1 - \mu\,. \tag{2.19b}$$

2.2.1 Equations of motion

From Newton's Second Law (NSL) the compact dimensional form of the EOMs is

$$\ddot{\boldsymbol{r}} = -\frac{\mu_1}{r_{12}^2}\frac{\boldsymbol{r}_{13}}{r_{13}} - \frac{\mu_2}{r_{23}^2}\frac{\boldsymbol{r}_{23}}{r_{23}}, \tag{2.20}$$

where, again, $\boldsymbol{r}_{13}$ and $\boldsymbol{r}_{23}$ are the position vectors from the primaries to the SC

$$\boldsymbol{r}_{i3} = \boldsymbol{r}_3 - \boldsymbol{r}_i\,, \qquad i = 1,2\,. \tag{2.21}$$

Given the "restricted" assumption of the CR3BP, the primaries influence the SC motion but are not affected by the SC itself. Henceforth, from now on the subscript

3 for the sole SC is dropped for the sake of clarity, and its coordinates are simply given by $\{x, y, z\}$ values.

By projecting the EOMs into the synodic RF cardinal directions one has

$$\ddot{x} = -\frac{\mu_1}{r_{13}^3}(x - x_1) - \frac{\mu_2}{r_{23}^3}(x - x_2) \tag{2.22a}$$

$$\ddot{y} = -\frac{\mu_1}{r_{13}^3} y - \frac{\mu_2}{r_{23}^3} y \tag{2.22b}$$

$$\ddot{z} = -\frac{\mu_1}{r_{13}^3} z - \frac{\mu_2}{r_{23}^3} z, \tag{2.22c}$$

where the relative position vectors are

$$r_{i3} = \sqrt{(x - x_i)^2 + y^2 + z^2}, \qquad i = 1, 2. \tag{2.23}$$

It is useful to project the EOMs in the interial RF. In order to do so, the total differentiation of the position vector $\boldsymbol{r}$ in the inertial RF is provided as the sum of the differentiation of the same vector in the synodic frame plus the transport component. In general, the transport theorem for a generic quantity $*$ provides

$$^F\frac{\mathrm{d}*}{\mathrm{d}t} = {}^R\frac{\mathrm{d}*}{\mathrm{d}t} + {}^{R/F}\boldsymbol{\omega} \times {}^R* \tag{2.24}$$

where the prescripts F or R indicate the corresponding fixed and synodic RFs, as in Figure 2.4, and R/F implies that such quantity is measured in the rotating RF with respect to the inertial RF. Therefore the inertial velocity can be computed as [35]

$$^F\dot{\boldsymbol{r}} = {}^F\frac{\mathrm{d}\boldsymbol{r}}{\mathrm{d}t} = {}^R\frac{\mathrm{d}\boldsymbol{r}}{\mathrm{d}t} + {}^{R/F}\boldsymbol{\omega_S} \times {}^R\boldsymbol{r}. \tag{2.25}$$

At the same time, the inertial acceleration shows multiple correction parameters to account for the coordinate system rotation. Indeed,

$$
\begin{aligned}
{}^{F}\ddot{\boldsymbol{r}} &= {}^{F}\frac{\mathrm{d}\dot{\boldsymbol{r}}}{\mathrm{d}t} = {}^{R}\frac{\mathrm{d}\,{}^{F}\dot{\boldsymbol{r}}}{\mathrm{d}t} + {}^{R/F}\boldsymbol{\omega}_S \times {}^{F}\dot{\boldsymbol{r}} \\
&= {}^{R}\frac{\mathrm{d}}{\mathrm{d}t}\left({}^{R}\dot{\boldsymbol{r}} + {}^{R/F}\boldsymbol{\omega}_S \times {}^{R}\boldsymbol{r}\right) + {}^{R/F}\boldsymbol{\omega}_S \times \left({}^{R}\dot{\boldsymbol{r}} + {}^{R/F}\boldsymbol{\omega}_S \times {}^{R}\boldsymbol{r}\right) \\
&= {}^{R}\ddot{\boldsymbol{r}} + {}^{R/F}\dot{\boldsymbol{\omega}}_S \times {}^{R}\boldsymbol{r} + {}^{R/F}\boldsymbol{\omega}_S \times {}^{R}\dot{\boldsymbol{r}} + {}^{R/F}\boldsymbol{\omega}_S \times {}^{R}\dot{\boldsymbol{r}} + {}^{R/F}\boldsymbol{\omega}_S \times \left({}^{R/F}\boldsymbol{\omega}_S \times {}^{R}\boldsymbol{r}\right) \\
{}^{F}\ddot{\boldsymbol{r}} &= \ddot{\boldsymbol{r}} + \dot{\boldsymbol{\omega}}_S \times \boldsymbol{r} + 2\boldsymbol{\omega}_S \times \dot{\boldsymbol{r}} + \boldsymbol{\omega}_S \times (\boldsymbol{\omega}_S \times \boldsymbol{r})\,,
\end{aligned}
\tag{2.26}
$$

where in the last line the prescripts R and R/F are dropped for clarity, given all the terms are referred to the rotating RF. Moreover,

$$
\boldsymbol{\omega}_S = \omega_S \hat{\boldsymbol{z}}_S \tag{2.27}
$$

and, from the Keplerian motion definition,

$$
\omega_S = \frac{\mu_1 + \mu_2}{r_{12}^3}\,. \tag{2.28}
$$

The first term in the Right-Hand Side (RHS) of equation (2.26) is the rotating acceleration in the synodic reference frame, whereas the other three terms have historically been known as tangential, centripetal, and Coriolis acceleration. By using the CR3BP simplification, one immediately notices that no variation over time of ω_S arises, and therefore no tangential acceleration can happen on circular orbits; similarly, also the centripetal acceleration cannot take place for circular orbits, given no change in position vector norm happens. The sole Coriolis acceleration is always present for any rotating frame. However, explicitly expanding quantities in equation (2.26) for the most generic case in the 3BP, the velocity shows components

$$
\begin{aligned}
{}^{F}\dot{\boldsymbol{r}} &= (\dot{x}\hat{\boldsymbol{x}}_S + \dot{y}\hat{\boldsymbol{y}}_S + \dot{z}\hat{\boldsymbol{z}}_S) + \begin{vmatrix} \hat{\boldsymbol{x}}_S & \hat{\boldsymbol{y}}_S & \hat{\boldsymbol{z}}_S \\ 0 & 0 & \omega_S \\ x & y & z \end{vmatrix} \\
&= (\dot{x}\hat{\boldsymbol{x}}_S + \dot{y}\hat{\boldsymbol{y}}_S + \dot{z}\hat{\boldsymbol{z}}_S) + [(-y\omega_S)\hat{\boldsymbol{x}}_S - (-x\omega_S)\hat{\boldsymbol{y}}_S + (0)\hat{\boldsymbol{z}}_S] \\
{}^{F}\dot{\boldsymbol{r}} &= (\dot{x} - y\omega_S)\hat{\boldsymbol{x}}_S + (\dot{y} + x\omega_S)\hat{\boldsymbol{y}}_S + \dot{z}\hat{\boldsymbol{z}}_S\,,
\end{aligned}
\tag{2.29}
$$

whereas the acceleration

$$
\begin{aligned}
{}^{F}\ddot{\boldsymbol{r}} &= \ddot{\boldsymbol{r}} + \dot{\boldsymbol{\omega}}_S \times \boldsymbol{r} + 2\boldsymbol{\omega}_S \times \dot{\boldsymbol{r}} + \boldsymbol{\omega}_S \times (\boldsymbol{\omega}_S \times \boldsymbol{r}) \\
&= \ddot{\boldsymbol{r}} + \begin{vmatrix} \hat{\boldsymbol{x}}_S & \hat{\boldsymbol{y}}_S & \hat{\boldsymbol{z}}_S \\ 0 & 0 & \dot{\omega}_S \\ x & y & z \end{vmatrix} + 2 \begin{vmatrix} \hat{\boldsymbol{x}}_S & \hat{\boldsymbol{y}}_S & \hat{\boldsymbol{z}}_S \\ 0 & 0 & \omega_S \\ \dot{x} & \dot{y} & \dot{z} \end{vmatrix} + \boldsymbol{\omega} \times \begin{vmatrix} \hat{\boldsymbol{x}}_S & \hat{\boldsymbol{y}}_S & \hat{\boldsymbol{z}}_S \\ 0 & 0 & \omega_S \\ x & y & z \end{vmatrix} \\
&= (\ddot{x} - 2\dot{y}\omega_S - y\dot{\omega}_S)\,\hat{\boldsymbol{x}}_S + (\ddot{y} + \dot{x}\omega_S + x\dot{\omega}_S) + (\ddot{z})\,\hat{\boldsymbol{z}}_S + \begin{vmatrix} \hat{\boldsymbol{x}}_S & \hat{\boldsymbol{y}}_S & \hat{\boldsymbol{z}}_S \\ 0 & 0 & \omega_S \\ -y\omega_S & x\omega_S & 0 \end{vmatrix} \\
&= \left(\ddot{x} - 2\dot{y}\omega_S - y\dot{\omega}_S - x\omega_S^2\right)\hat{\boldsymbol{x}}_S + \left(\ddot{y} + \dot{x}\omega_S + x\dot{\omega}_S - y\omega_S^2\right)\hat{\boldsymbol{y}}_S + \ddot{z}\hat{\boldsymbol{z}}_S\,. \qquad (2.30)
\end{aligned}
$$

By equalling equations (2.22) and (2.30) component by component

$$\ddot{x} - 2\dot{y}\omega_S - y\dot{\omega}_S - x\omega_S^2 = -\frac{\mu_1}{r_{13}^3}(x - x_1) - \frac{\mu_2}{r_{23}}(x - x_2) \qquad (2.31a)$$

$$\ddot{y} + 2\dot{x}\omega_S + x\dot{\omega}_S - y\omega_S^2 = -\frac{\mu_1}{r_{13}^3}y - \frac{\mu_2}{r_{23}^3}y \qquad (2.31b)$$

$$\ddot{z} = -\frac{\mu_1}{r_{13}^3}z - \frac{\mu_2}{r_{23}^3}z \qquad (2.31c)$$

and by applying the nondimensionalization and the hypotheses of the CR3BP, namely that there are no roto-pulsating behaviors, i.e. the angular velocity $\omega_S = 1$ and thus $\dot{\omega}_S = 0$, the full system of nondimensional ODEs for the cartesian components in the CR3BP dynamical model is obtained

$$\ddot{\xi} - 2\dot{\eta} - \xi = -\frac{1-\mu}{\rho_{13}^3}(\xi - \mu) - \frac{\mu}{\rho_{23}^3}[\xi - (1-\mu)] \qquad (2.32a)$$

$$\ddot{\eta} + 2\dot{\xi} - \eta = -\frac{1-\mu}{\rho_{13}^3}\eta - \frac{\mu}{\rho_{23}^3}\eta \qquad (2.32b)$$

$$\ddot{\zeta} = -\frac{1-\mu}{\rho_{13}^3}\zeta - \frac{\mu}{\rho_{23}^3}\zeta\,. \qquad (2.32c)$$

2.2.2 Jacobian Integral

Among the historical and modern challenges that the CR3BP poses in order to solve analytically its EOMs, which could not even be possible as discussed extensively in Szebehely's work [28], a spark comes from the Jacobi integral. Such quantity is a

pseudo-integral of motion existing in the CR3BP in the rotating synodic RF and is particularly useful to understand stability and accessible regions in the binary system. Its derivation starts for an inertial RF by defining a positive potential function U as

$$^{F}U = \sum_{i=1}^{2} \frac{\mu_i}{r_{i3}}, \tag{2.33}$$

where j indicates the SC and each i-th body is a gravitational attractor. In the 3BP rotating RF, such potential is modified to account also of the centrifugal potential and becomes

$$^{R}U = \frac{\mu_1}{r_{13}} + \frac{\mu_2}{r_{23}} + \frac{1}{2}\omega_S \left(x^2 + y^2\right) \tag{2.34}$$

or, in nondimensional form,

$$^{R}\mathscr{U} = \frac{1-\mu}{\rho_{13}} + \frac{\mu}{\rho_{23}} + \frac{1}{2}\left(\xi^2 + \eta^2\right). \tag{2.35}$$

Such quantity is defined as pseudopotential in the CR3BP domain. By taking the nondimensional derivative of $\mathscr{U}$ with respect to the nondimensional coordinates,

$$\frac{\partial \mathscr{U}}{\partial \xi} = \xi - \frac{1-\mu}{\rho_{13}^3}(\xi - \mu) - \frac{\mu}{\rho_{23}^3}\left[\xi - (1-\mu)\right] \tag{2.36a}$$

$$\frac{\partial \mathscr{U}}{\partial \eta} = \eta - \frac{1-\mu}{\rho_{13}^3}\eta - \frac{\mu}{\rho_{23}^3}\eta \tag{2.36b}$$

$$\frac{\partial \mathscr{U}}{\partial \zeta} = -\frac{1-\mu}{\rho_{13}^3}\zeta - \frac{\mu}{\rho_{23}^3}\zeta. \tag{2.36c}$$

Equations (2.32) and (2.36) can be combined to produce the following

$$\ddot{\xi} - 2\dot{\eta} = \frac{\partial \mathscr{U}}{\partial \xi} \tag{2.37a}$$

$$\ddot{\eta} + 2\dot{\xi} = \frac{\partial \mathscr{U}}{\partial \eta} \tag{2.37b}$$

$$\ddot{\zeta} = \frac{\partial \mathscr{U}}{\partial \zeta}. \tag{2.37c}$$

Moreover, by multiplying respectively each of the dimensional equations in (2.31) by $2\dot{x}$, $2\dot{y}$, $2\dot{z}$, and by summing them, one obtains

$$2\ddot{x}\dot{x} + 2\ddot{y}\dot{y} + 2\ddot{z}\dot{z} - 2\omega_S^2 (\dot{x}x + \dot{y}y) = 2\dot{x}\frac{\partial U}{\partial x} + 2\dot{y}\frac{\partial U}{\partial y} + 2\dot{z}\frac{\partial U}{\partial z} = 2\frac{\mathrm{d}U}{\mathrm{d}t} \tag{2.38}$$

which, once integrated, provides the Jacobian integral equation

$$\dot{x}^2 + \dot{y}^2 + \dot{z}^2 = V^2 = 2U - J_C\,. \tag{2.39}$$

The term on the Left-Hand Side (LHS) is the velocity squared V^2 in the synodic RF, whereas in the RHS the pseudopotential U contains the integrated term $\omega_S^2\left(x^2+y^2\right)$. The Jacobi Constant J_C can be seen as an inverse energy-like quantity as in the *vis-viva* equation in the 2BP (2.4), where the total specific mechanical energy $\mathscr{E}$ is the sum of the kinetic $V^2/2$ and the potential $-\mu/r$ specific energies. The greater J_C is, the less energy the SC has in the synodic RF. Indeed, such quantity is preferibly computed in its nondimensional synodic form $\mathscr{J}_C$, providing

$$\dot{\xi}^2 + \dot{\eta}^2 + \dot{\zeta}^2 = v^2 = 2\mathscr{U} - \mathscr{J}_C\,. \tag{2.40}$$

2.2.3 Equilibrium Points

In 1772, Joseph-Louis Lagrange published in his *Essay sur le Problème des Trois Corps* [46] a comprehensive demonstration on the motion of three gravitational bodies, including many mathematical strategies still implemented nowadays such as nondimensionalization and restrictions.

In his one hundred pages treaty, Lagrange demonstrated that in the CR3BP there are analytical solutions, or equilibrium points, that nowadays are called Lagrangian Points (LPs) in his honor.

Despite no analytical solution has been found up to date for the complete system of ODEs in equation (2.37), useful theoretical insigths can be retrieved by manipulating them and retracing Lagrange's steps.

By setting the vector gradient of the pseudopotential function to zero,

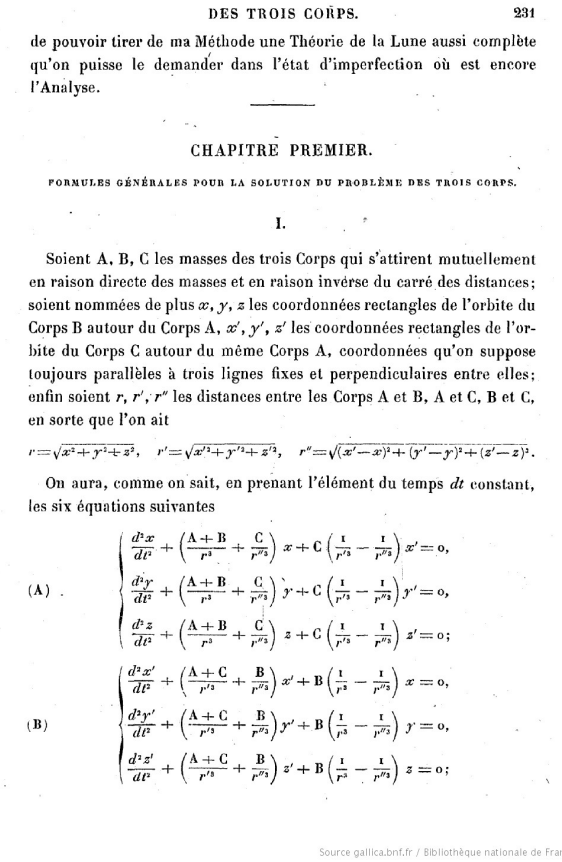

DES TROIS CORPS. 231

de pouvoir tirer de ma Méthode une Théorie de la Lune aussi complète qu'on puisse le demander dans l'état d'imperfection où est encore l'Analyse.

CHAPITRE PREMIER.

FORMULES GÉNÉRALES POUR LA SOLUTION DU PROBLÈME DES TROIS CORPS.

I.

Soient A, B, C les masses des trois Corps qui s'attirent mutuellement en raison directe des masses et en raison inverse du carré des distances; soient nommées de plus x, y, z les coordonnées rectangles de l'orbite du Corps B autour du Corps A, x', y', z' les coordonnées rectangles de l'orbite du Corps C autour du même Corps A, coordonnées qu'on suppose toujours parallèles à trois lignes fixes et perpendiculaires entre elles; enfin soient r, r', r'' les distances entre les Corps A et B, A et C, B et C, en sorte que l'on ait

$$r=\sqrt{x^2+y^2+z^2},\quad r'=\sqrt{x'^2+y'^2+z'^2},\quad r''=\sqrt{(x'-x)^2+(y'-y)^2+(z'-z)^2}.$$

On aura, comme on sait, en prenant l'élément du temps dt constant, les six équations suivantes

$$(A)\quad \begin{cases} \frac{d^2x}{dt^2}+\left(\frac{A+B}{r^3}+\frac{C}{r''^3}\right)x+C\left(\frac{1}{r'^3}-\frac{1}{r''^3}\right)x'=0,\\ \frac{d^2y}{dt^2}+\left(\frac{A+B}{r^3}+\frac{C}{r''^3}\right)y+C\left(\frac{1}{r'^3}-\frac{1}{r''^3}\right)y'=0,\\ \frac{d^2z}{dt^2}+\left(\frac{A+B}{r^3}+\frac{C}{r''^3}\right)z+C\left(\frac{1}{r'^3}-\frac{1}{r''^3}\right)z'=0; \end{cases}$$

$$(B)\quad \begin{cases} \frac{d^2x'}{dt^2}+\left(\frac{A+C}{r'^3}+\frac{B}{r''^3}\right)x'+B\left(\frac{1}{r^3}-\frac{1}{r''^3}\right)x=0,\\ \frac{d^2y'}{dt^2}+\left(\frac{A+C}{r'^3}+\frac{B}{r''^3}\right)y'+B\left(\frac{1}{r^3}-\frac{1}{r''^3}\right)y=0,\\ \frac{d^2z'}{dt^2}+\left(\frac{A+C}{r'^3}+\frac{B}{r''^3}\right)z'+B\left(\frac{1}{r^3}-\frac{1}{r''^3}\right)z=0; \end{cases}$$

Fig. 2.5 Excerpt from the *Essay sur le Problème des Trois Corps*, J. L. Lagrange, 1772

$$\nabla\mathscr{U}=\mathbf{0}, \tag{2.41}$$

which implies setting accelerations and velocities in the rotating RF equal to zero, a specific set of coordinates in the form $\{\xi_i,\eta_i,\zeta_i\}$, with $i=1,\ldots,5$ per each LP, can be retrieved to satisfy these relations, specifically

$$\frac{\partial\mathscr{U}}{\partial\xi}=0=\xi-\frac{1-\mu}{\rho_{13}^3}(\xi-\mu)-\frac{\mu}{\rho_{23}^3}[\xi-(1-\mu)] \tag{2.42a}$$

$$\frac{\partial\mathscr{U}}{\partial\eta}=0=\eta-\frac{1-\mu}{\rho_{13}^3}\eta-\frac{\mu}{\rho_{23}^3}\eta \tag{2.42b}$$

$$\frac{\partial\mathscr{U}}{\partial\zeta}=0=-\frac{1-\mu}{\rho_{13}^3}\zeta-\frac{\mu}{\rho_{23}^3}\zeta\,. \tag{2.42c}$$

The last equation (2.42c) is immediately satisfied by imposing $\zeta = 0$, meaning that such equilibrium coordinates lie in the $\hat{\boldsymbol{\xi}}_S - \hat{\boldsymbol{\eta}}_S$ plane. Then, the two remaining equations (2.42a) and (2.42b) can be solved via substitution. Three roots are computed numerically in the derived quintic equation that is retrieved when imposing $\eta = \zeta = 0$; such solutions exist on the $\hat{\boldsymbol{\xi}}_S$ axis and are named collinear libration points; other two roots can be found by setting the primaries distances with respect to the SC equal to unity, i.e. $\rho_{13} = \rho_{23} = 1$, retrieving the triangular libration points at the vertices.

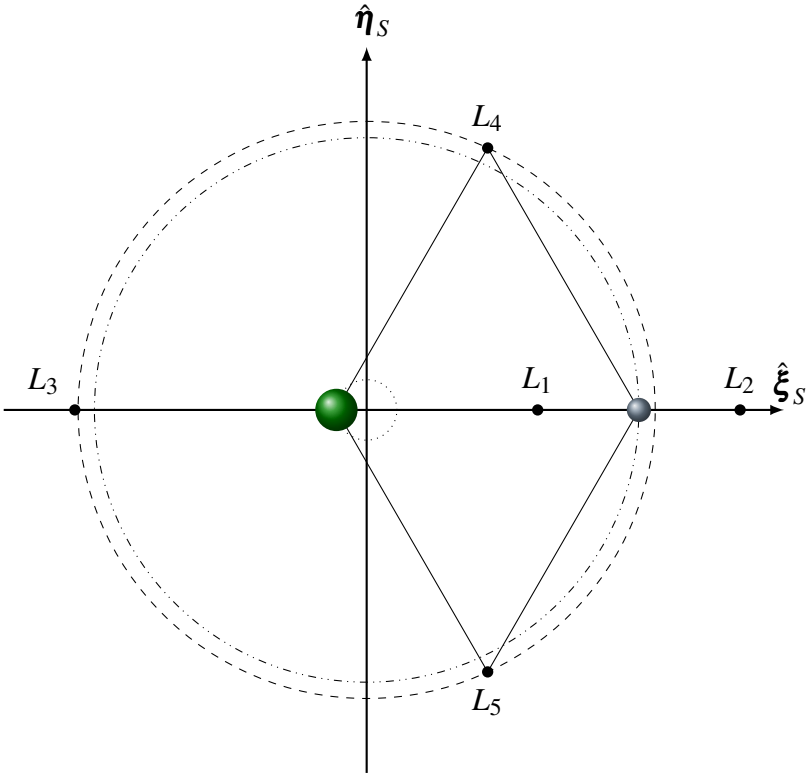

Fig. 2.6 Lagrangian points in a generic synodic RS with $\mu = 0.1$

Figure 2.6 shows a generic binary system in which LPs are computed by considering a system's mass ratio of $\mu = 0.1$, which is almost ten times greater than the Earth-Moon (EM) one. The collinear points lie on the $\hat{\boldsymbol{\xi}}_S$ axis, whereas the triangular ones at the vertices of the equilateral triangle having as base the primaries distance. The dashed circle represents the radial positioning of such triangular LPs; L_3 lies just outside this region in this configuration, and L_1 and L_2 distances are approximately the same with respect to the smaller primary -L_2 is slightly farther away-. The dash-dot-dot and dotted circles, instead, represent the circular orbits of

the primaries with respect to (wrt) the system barycenter when observed from an inertial RF.

Some approximate formulations for the quintic equation deriving from (2.42) are available for the computation of LPs locations via the perturbation theory [47]. While the complete form to be solved numerically for the collinear LPs is

$$\xi^5 \mp (3-\mu)\,\xi^4 + (3-2\mu)\,\xi^3 - \mu\xi^2 \pm 2\mu\xi - \mu = 0\,, \tag{2.43}$$

by supposing that the smaller primary is orders of magnitude smaller than the bigger primary, the first two LPs are approximately at the same distance from the smaller primary close to the Hill's sphere radius, namely

$$x_{Li} \approx \mp r_{12} \sqrt[3]{\frac{\mu_2}{3\mu_1}}\,, \qquad\qquad i = 1,2\,. \tag{2.44}$$

2.2.4 Zero Velocity Surfaces

A useful result deriving from imposing in the $\mathscr{J}_C$ that the relative velocity in the synodic RF is zero, $v = 0$, is the Zero-Velocity Surface (ZVS) concept. Such a constraint, given a specific value for the constant, provides the equation of a surface which is the extremal value of all the potential limit apogee-like locations

$$\mathscr{J}_C = 2\mathscr{U} = 2\left(\frac{1-\mu}{\rho_1} + \frac{\mu}{\rho_2}\right) + \left(\xi^2 + \eta^2\right). \tag{2.45}$$

By inverting signs in (2.40), thus resembling the energy quantities in the *vis-viva*, the representation of these surfaces comes closer to the expected understanding of potential energy, as in the 2BP. These surfaces are represented in Figure 2.7

If a SC lies in the vicinity of a primary and has an initial velocity close to the orbital one, its apogee-like condition (the maximum apogee it could reach if all the orbit's energy is converted in altitude) will be confined in the gravitational well of the primary itself. The shape of this confinement close to the primaries in the EM ZVS representation in Figure 2.7 resembles a circle; ample discussion of approximate ZVSs shapes stemming from approximations of equation (2.45) is provided in Vallado's work [31]. Increasing its initial energy (both kinetic and/or potential), the SC widens its accessible regions and encounters its first surfaces

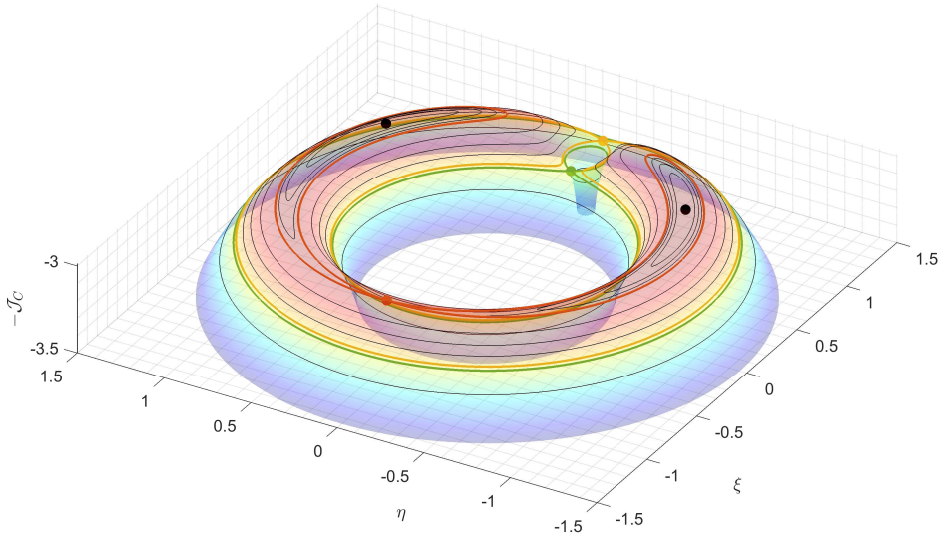

Fig. 2.7 3D Earth-Moon ZVSs at LPs energy

intersecting point at L_1, whose ZVS level is represented in green, followed by L_2, in yellow. It is noteworthy that the yellow energy level has a lower absolute value of $\mathcal{J}_C$, even by being positioned at "graphically higher" locations, thus having reduced forbidden regions of motion. By increasing the SC energy, which in turn implies a lower positive $\mathcal{J}_C$, the SC widens further its accessible regions, including all those beyond the Moon. Technically, a SC able to cross the L_2 ZVS from the inner regions has enough energy to evade from the EM binary system for specific trajectories exploiting the primaries gravitational pulls. L_3, with a red contour, is almost at the top of the surfaces; if a SC can access L_4 or L_5, depicted in black dots, then it has enough energy to cross all ZVSs and, thus, show no forbidden regions of motion.

Similarly, in Figure 2.8, all white regions have $\mathcal{J}_C > \mathcal{J}_{C,L1}$; orange regions have $\mathcal{J}_{C,L2} < \mathcal{J}_C < \mathcal{J}_{C,L1}$; yellow regions $\mathcal{J}_{C,L3} < \mathcal{J}_C < \mathcal{J}_{C,L2}$; red regions $\mathcal{J}_{C,L4} = \mathcal{J}_{C,L5} < \mathcal{J}_C < \mathcal{J}_{C,L3}$.

Tables 2.2 and 2.3 show the locations and corresponding Jacobi Constant values for each LPs in the two binary systems implemented in the analysis, the Earth-Moon and Sun-Earth ones.

The order in which such LPs are named comes from the values of the Jacobi Constant $\mathcal{J}_C$ in decreasing order, which incidentally corresponds to the order in

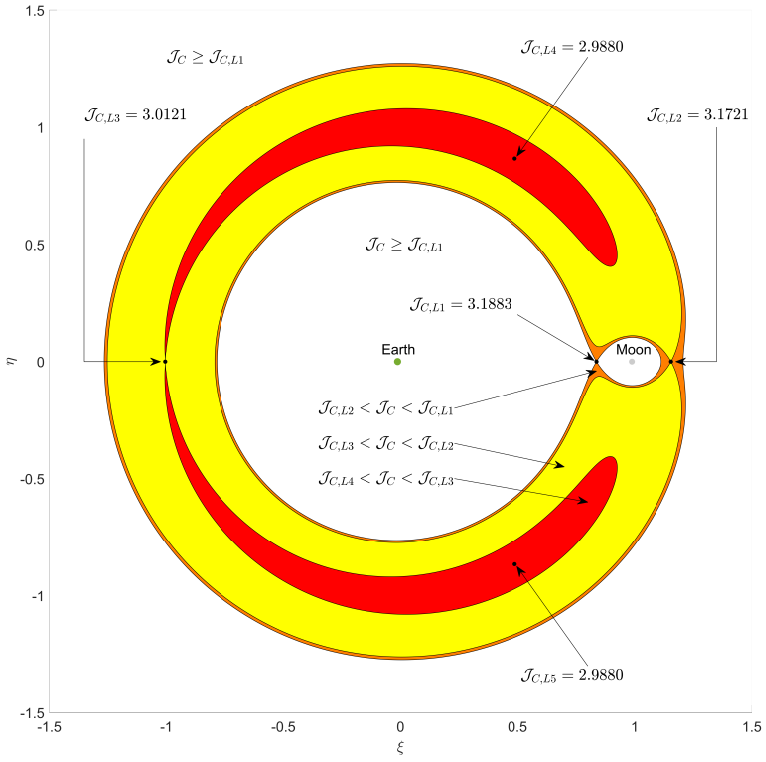

Fig. 2.8 Earth-Moon ZVSs at LPs energy

	ξ	η	ζ	$\mathcal{J}_C$
L_1	0.83740242	0.00000000	0.00000000	3.188326
L_2	1.15618808	0.00000000	0.00000000	3.172147
L_3	−1.00506193	0.00000000	0.00000000	3.012145
L_4	0.48785136	0.86602540	0.00000000	2.987999
L_5	0.48785136	−0.86602540	0.00000000	2.987999

Table 2.2 Earth-Moon Lagrangian Points positions and Jacobi Constants, synodic RF

which they become accessible. Indeed, both for the EM and Sun-Earth (SE) scenario, the highest value of the nondimensional $\mathcal{J}_C$, which implies the first accessible zone at SC lower energy, is the first LP, followed by the others in order. Specifically, L_4 and L_5 show the same value of the $\mathcal{J}_C$, which is the lowest; if a SC has enough energy to reach such LPs, then all the regions of space in the CR3BP are accessible.

	ξ	η	ζ	$\mathscr{J}_C$
L_1	0.99002661	0.00000000	0.00000000	3.000891
L_2	1.01003433	0.00000000	0.00000000	3.000887
L_3	−1.00000125	0.00000000	0.00000000	3.000003
L_4	0.49999700	0.86602540	0.00000000	2.999997
L_5	0.49999700	−0.86602540	0.00000000	2.999997

Table 2.3 Sun-Earth Lagrangian Points positions and Jacobi Constants, synodic RF

2.3 N-body problem

In order to compute a comprehensive and high-fidelity trajectory optimization, a dynamical system closer to the real solar system one is required to take into account all the effects and perturbations due to other bodies and phenomena in the solar system. As anticipated in Section 2.1, JPL DE430 planetary ephemerides in the NBP dynamical system are employed, and the dynamical model considers 4-body gravitation (Sun, Earth, Moon, and the SC itself), accounting also for multiple perturbations and effects that will be discussed in detail in Section 2.6.

For the NBP, the use of a non-rotating RS proves to be more useful and straightforward to derive the EOMs and to stem further considerations. Indeed, in such dynamical model, n different bodies evolve in their states mutually influencing all the others. The present discussion deals with trajectories in the ephemeris model computed with respect to the Earth as the central body. The RS is the EME2000 and such central body is the k-th one among the n. Moreover, each other gravitational body may be considered the j-th with the exception of the SC itself, which is denoted as i, as represented in Figure 2.9.

The acceleration experienced by the SC in such dynamical model with respect to a generic inertial frame is written from NSL as

$$\ddot{\boldsymbol{r}}_i = -\sum_{\substack{j=1 \\ j\neq i}}^{n} \frac{\mu_j}{r_{ji}^3} \boldsymbol{r}_{ji}\,. \tag{2.46}$$

However, a more convenient formulation is obtained when the SC and all the perturbing bodies states are computed with respect to a particular reference gravitational body. As anticipated, in the present discussion the Earth is chosen as central

body in the EME2000 RF, and thus the acceleration exerted on the SC under the influence of each j-th perturbing body with respect to the k-th central body takes the form of the following second-order ODE

$$\ddot{\boldsymbol{r}}_{ki} = -\frac{(\mu_i + \mu_k)}{r_{ki}^3}\boldsymbol{r}_{ki} + \sum_{\substack{j=1 \\ j\neq i,\, k}}^{n} \mu_j \left(\frac{\boldsymbol{r}_{ij}}{r_{ij}^3} - \frac{\boldsymbol{r}_{kj}}{r_{kj}^3} \right) . \tag{2.47}$$

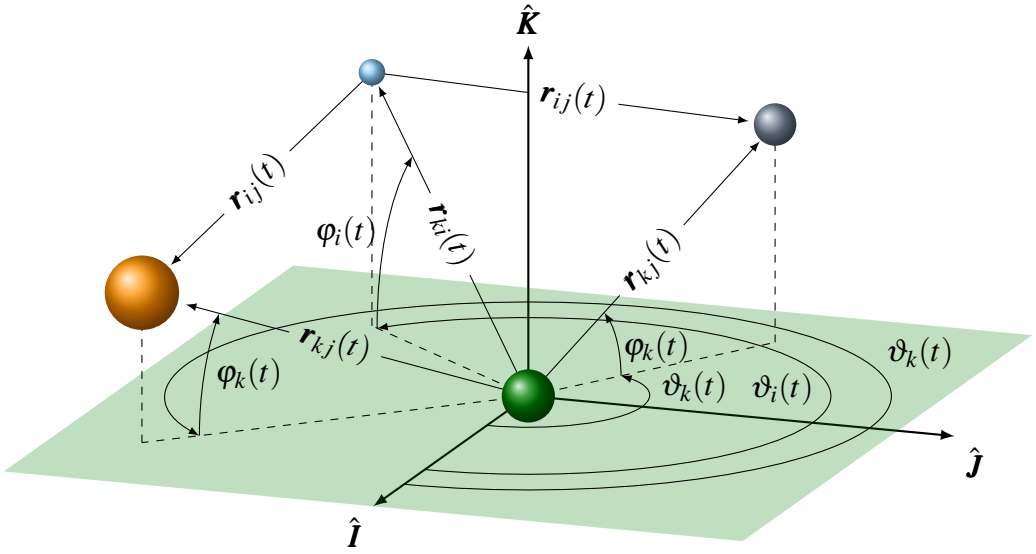

Fig. 2.9 Schematic representation of the EME2000 RF

While the position vector for the SC $\boldsymbol{r}_{ki}$ is computed while performing the trajectory analysis, all the other position vectors $\boldsymbol{r}_{kj}$ with respect to the Earth are known and retrieved from the DE430 JPL ephemerides [40], provided by the JPL's Navigation and Ancillary Information Facility (NAIF). These position vectors are given in rectangular coordinates x_{kj}, y_{kj}, z_{kj} with respect to the Earth in the ICRF, i.e. $\boldsymbol{r}_{kj} = x_{kj}\hat{\boldsymbol{I}} + y_{kj}\hat{\boldsymbol{J}} + z_b\hat{\boldsymbol{K}}$, as shown in Figure 2.9. Polar coordinates are also represented for completeness, and their representation with only positive values is only for graphical purposes. As anticipated in Section 2.1, the small differences between ICRF and EME2000 are neglected, and the latter is used in the present analysis. Relative position vectors $\boldsymbol{r}_{ij}$ to compute the perturbations due to other gravitational bodies are obtained via vector subtraction,

$$\boldsymbol{r}_{ij}(t) = \boldsymbol{r}_{kj}(t) - \boldsymbol{r}_{ki}(t) . \tag{2.48}$$

For the sake of brevity, henceforth is implied that all states in the NBP, including positions and velocities, are time-dependent and thus the notation (t) describing their time dependency is dropped from all equations in the NBP.

A common mathematical strategy follows the considerations made in the CR3BP discussion, namely regarding the nondimensionalization for numerical accuracy purposes. Lengths and masses are nondimensionalized with respect to specific characteristic quantities, providing more manageable numbers to compute mathematical operations.

Quantity	Earth-Moon	Sun-Earth
ℓ^*	r_{EM}	r_{SE}
μ^*	$\mu_E + \mu_M$	$\mu_S + \mu_E$
Derived		
$\mathscr{T}^*$	$\sqrt{(\ell^*)^3/\mu^*}$	
V^*	$\ell^*/\mathscr{T}^*$	

Table 2.4 Characteristic quantities in the n-body problem

Times, velocities, and other derived quantities are nondimensionalized accordingly. By identifying with a breve superscript $\breve{x}$ nondimensionalized quantities in the NBP, the relative formulation of the n-body EOMs from equation (2.47) becomes

$$\ddot{\breve{\boldsymbol{r}}}_{ki} = -\frac{(\breve{\mu}_i + \breve{\mu}_k)}{\breve{r}_{ki}^3}\breve{\boldsymbol{r}}_{ki} + \sum_{\substack{j=1 \\ j\neq i,\, k}}^{n} \breve{\mu}_j \left(\frac{\breve{\boldsymbol{r}}_{ij}}{\breve{r}_{ij}^3} - \frac{\breve{\boldsymbol{r}}_{kj}}{\breve{r}_{kj}^3} \right), \tag{2.49}$$

where the generic position vector is nondimensionalized from the ephemerides as follows

$$\breve{\boldsymbol{r}}_{kj} = \frac{\boldsymbol{r}_{kj}}{\ell^*} = \breve{x}_{kj}\hat{\boldsymbol{I}} + \breve{y}_{kj}\hat{\boldsymbol{J}} + \breve{z}_{kj}\hat{\boldsymbol{K}}. \tag{2.50}$$

2.3.1 Equation of motion in spherical coordinates

The EOMs presented in the set of equations (2.2) should be expanded in cardinal directions for further considerations. Two different choices are made for positions and velocities; positions are expressed in polar coordinates in the EME2000 RF, thus

being defined by the SC radius r and its longitude and latitude, ϑ and φ respectively. Velocities, instead, are projected in the ZEN RF, thus being composed by the radial (Zenith), tangential (East), and normal (North) components [42], namely

$$\frac{\mathrm{d}r}{\mathrm{d}t} = u \tag{2.51a}$$

$$\frac{\mathrm{d}\vartheta}{\mathrm{d}t} = \frac{v}{r\cos\varphi} \tag{2.51b}$$

$$\frac{\mathrm{d}\varphi}{\mathrm{d}t} = \frac{w}{r} \tag{2.51c}$$

$$\frac{\mathrm{d}u}{\mathrm{d}t} = -\frac{\mu}{r^2} + \frac{v^2}{r} + \frac{w^2}{r} + \frac{T_u}{m} + (\mathrm{a}_p)_u \tag{2.51d}$$

$$\frac{\mathrm{d}v}{\mathrm{d}t} = -\frac{uv}{r} + \frac{vw}{r}\tan\varphi + \frac{T_v}{m} + (\mathrm{a}_p)_v \tag{2.51e}$$

$$\frac{\mathrm{d}w}{\mathrm{d}t} = -\frac{uw}{r} - \frac{v^2}{r}\tan\varphi + \frac{T_w}{m} + (\mathrm{a}_p)_w \tag{2.51f}$$

$$\frac{\mathrm{d}m}{\mathrm{d}t} = -\frac{T}{c}\,, \tag{2.51g}$$

where a_p are perturbing accelerations of different nature and the projections of the thrust vector T are

$$T_u = T\sin\alpha_T \tag{2.52a}$$

$$T_v = T\cos\alpha_T\cos\beta_T \tag{2.52b}$$

$$T_w = T\cos\alpha_T\sin\beta_T\,. \tag{2.52c}$$

Here α_T is the in-plane thrust angle in the ZEN RF, whereas β_T is the out-of-plane thrust angle. Further comments regarding the importance of the optimal thrust angles will be given in Section 4.5.

2.4 Time-invariant coordinate transformation

Simple elementary rotational matrices are implemented to switch between two different RFs. Such matrices are composed by a series of elementary Direction Cosine Matrix (DCM) that are, for a generic positive rotation of $(\cdot)$, in the form

$$\boldsymbol{R}_1(\cdot) = \begin{bmatrix} 1 & 0 & 0 \\ 0 & \mathrm{c}\cdot & \mathrm{s}\cdot \\ 0 & -\mathrm{s}\cdot & \mathrm{c}\cdot \end{bmatrix}, \boldsymbol{R}_2(\cdot) = \begin{bmatrix} \mathrm{c}\cdot & 0 & \mathrm{s}\cdot \\ 0 & 1 & 0 \\ -\mathrm{s}\cdot & 0 & \mathrm{c}\cdot \end{bmatrix}, \boldsymbol{R}_3(\cdot) = \begin{bmatrix} \mathrm{c}\cdot & \mathrm{s}\cdot & 0 \\ -\mathrm{s}\cdot & \mathrm{c}\cdot & 0 \\ 0 & 0 & 1 \end{bmatrix}. \quad (2.53)$$

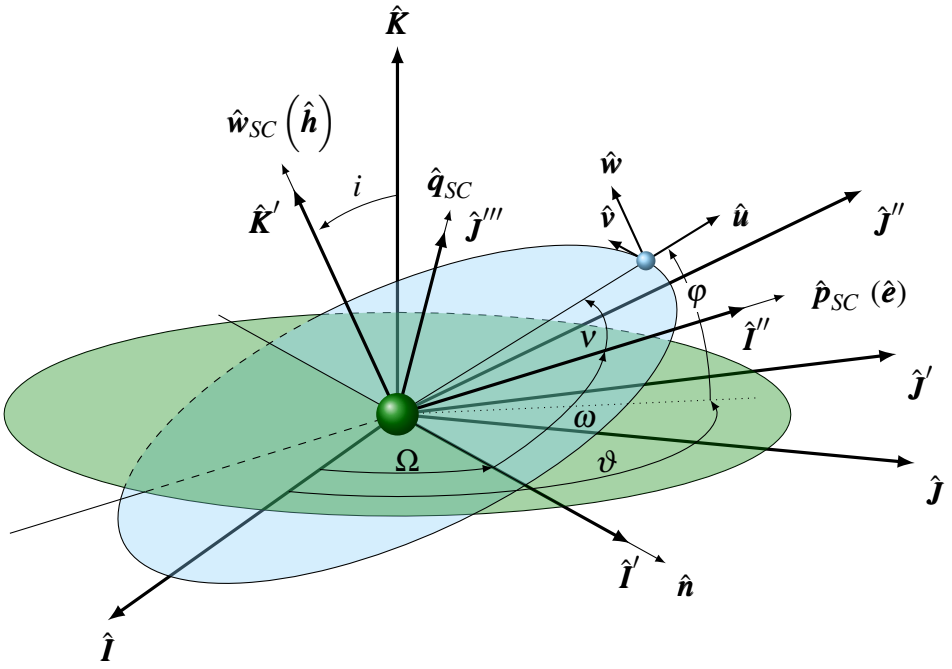

Fig. 2.10 Transformation steps from the EME2000 RF $\{\hat{\boldsymbol{I}}, \hat{\boldsymbol{J}}, \hat{\boldsymbol{K}}\}$ to the perifocal RF $\{\hat{\boldsymbol{p}}_{SC}, \hat{\boldsymbol{q}}_{SC}, \hat{\boldsymbol{w}}_{SC}\}$

The following notation is used for a complete transformation between two RFs. Taking into consideration, for example, the EME2000 RF and the perifocal RF in Figure 2.10, in order to perform a transformation from the first to the latter one has to compute an elementary rotation about the third $\hat{\boldsymbol{Z}}$ axis of Ω,

$$\boldsymbol{r}_{I'J'K} = \boldsymbol{R}_3(\Omega)\,\boldsymbol{r}_{IJK}, \quad (2.54)$$

from which the rotated $\hat{\boldsymbol{I}}'$ axis coincide with the line of nodes $\hat{\boldsymbol{n}}$, then an elementary rotation about the rotated first $\hat{\boldsymbol{I}}'$ axis of i,

$$\boldsymbol{r}_{I''J''K'} = \boldsymbol{R}_1(i)\,\boldsymbol{r}_{I'J'K}, \quad (2.55)$$

making the rotated $\hat{\boldsymbol{K}}'$ axis coincide with the $\hat{\boldsymbol{w}}_{SC}$ versor, and finally an elementary rotation about the rotated third $\hat{\boldsymbol{K}}'$ axis of ω,

$$\boldsymbol{r}_{pqw} = \boldsymbol{R}_3(\omega)\,\boldsymbol{r}_{I''J''K'}\,, \tag{2.56}$$

letting $\hat{\boldsymbol{I}}''$ coincide with $\hat{\boldsymbol{p}}_{SC}$ and $\hat{\boldsymbol{J}}'''$ with $\hat{\boldsymbol{q}}_{SC}$. The order of the rotation provides a 313 elementary rotation, but as elementary operations are applied singularly, in reality the complete rotational matrix follows the Euler sequence notation, namely

$$\boldsymbol{R}_{313}(\omega, i, \Omega)\,, \tag{2.57}$$

given that

$$\boldsymbol{r}_{pqw} = \boldsymbol{R}_3(\omega)\,\boldsymbol{r}_{I''J''K'} = \boldsymbol{R}_3(\omega)\,\boldsymbol{R}_1(i)\,\boldsymbol{r}_{I'J'K} = \boldsymbol{R}_3(\omega)\,\boldsymbol{R}_1(i)\,\boldsymbol{R}_3(\Omega)\,r_{IJK}\,. \tag{2.58}$$

Henceforth, transformation matrices between two RFs will have the following notation; a subscript composed by a number of single digits equal to the number of elementary rotations applied, and a parentheses including the respective elementary angles used for the rotations. With a similar procedure, the following principal rotation between RFs are presented

$$\begin{aligned} \boldsymbol{r}_{pqw} &= \boldsymbol{R}_{313}(\omega, i, \Omega)\,\boldsymbol{r}_{IJK}\,, \\ \boldsymbol{r}_{ZEN} &= \boldsymbol{R}_{23}(\varphi, \vartheta)\,\boldsymbol{r}_{IJK}\,. \end{aligned} \tag{2.59}$$

Inverse rotations are computed easily with the transposed DCMs, being them orthonormal.

2.5 Time-dependant coordinate transformation

2.5.1 Rotating frame to inertial frame

An important coordinate frame transformation that will be used extensively is the transformation between the CR3BP RF and the EME2000 RF, in the framework of

producing QPOs and similar topics. Being the CR3BP a rotating frame, one has to be able to convert quantities in an inertial RF. Moreover, more complex operations are required when the inertial RF is the EME2000's one, because planetary ephemerides are required to know its exact position.

In Figure 2.11 there are the EM synodic RS and a generic inertial RS centered at the barycenter of the binary system. They share the same fundamental plane, which are the nondimensional $\left\{\hat{\boldsymbol{\xi}}_S, \hat{\boldsymbol{\eta}}_S\right\}$ and $\left\{\hat{\boldsymbol{X}}_F, \hat{\boldsymbol{Y}}_F\right\}$ planes. Also the inertial RF has been nondimensionalized with respect to the characteristic quantities in the CR3BP for ease of calculation.

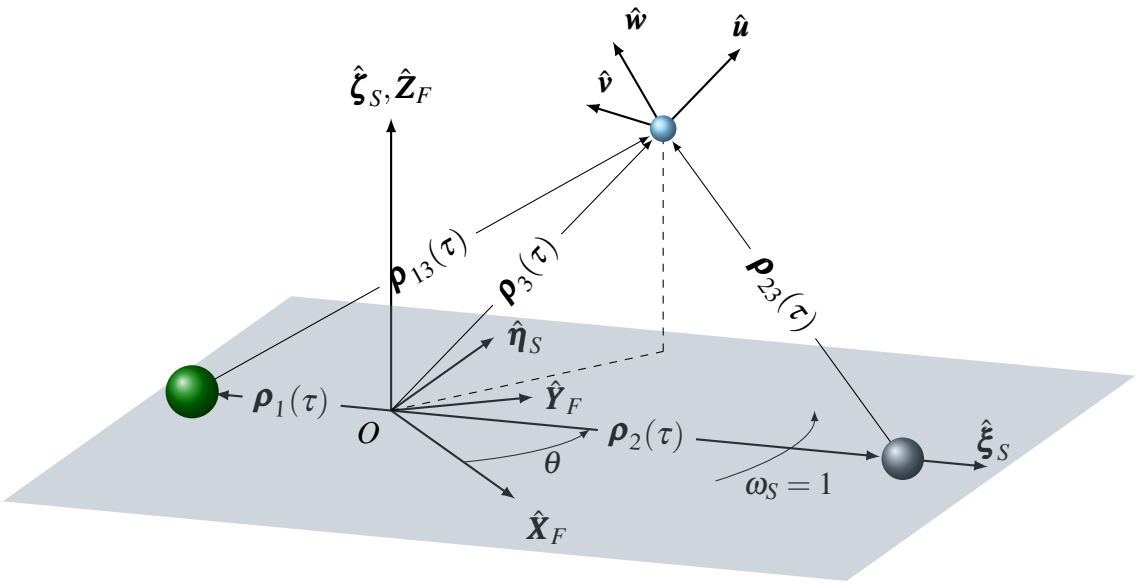

Fig. 2.11 Earth-Moon synodic RS - not to scale

The position vector of the SC in the rotating RF is easily transposed in the inertial RF with elementary DCM procedures, as seen in Section 2.4, specifically

$$^F\boldsymbol{\rho} = \boldsymbol{R}_3^T(\theta)\,{}^R\boldsymbol{\rho}\,, \tag{2.60}$$

where the transpose matrix is required due to a negative rotation of θ from the synodic to the intertial RF.

However, the velocity vector has to be corrected for the system's angular velocity, even if the CR3BP's hypotheses impose it to be equal to a constant value of one.

Therefore, by recalling the basic kinematic equation (2.29) and by nondimensionalizing it,

$$ {}^{R}\boldsymbol{\dot{\rho}} = \left(\dot{\xi} - \eta\right)\hat{\boldsymbol{\xi}}_S + \left(\dot{\eta} + \xi\right)\hat{\boldsymbol{\eta}}_S + \dot{\zeta}\hat{\boldsymbol{\zeta}}_S \,. \tag{2.61} $$

By defining with $\tilde{\boldsymbol{X}}$ the complete nondimensional state of the SC, one then has

$$ {}^{F}\tilde{\boldsymbol{X}} = \boldsymbol{R}_{R/F}\,{}^{R}\tilde{\boldsymbol{X}} = \left[\begin{array}{c|c} \boldsymbol{R}_3^T(\theta) & \boldsymbol{0} \\ \hline \boldsymbol{R}_\theta(\theta) & \boldsymbol{R}_3^T(\theta) \end{array}\right] {}^{R}\tilde{\boldsymbol{X}} \,, \tag{2.62} $$

where

$$ \boldsymbol{R}_\theta(\theta) = \begin{bmatrix} -\mathrm{s}\theta & -\mathrm{c}\theta & 0 \\ \mathrm{c}\theta & -\mathrm{s}\theta & 0 \\ 0 & 0 & 0 \end{bmatrix} . \tag{2.63} $$

Please note that the uppercase $\tilde{\boldsymbol{X}}$ letter, here, is used to avoid confusion with the first vector component (in dimensional form, $\boldsymbol{X} = \{x, y, z, \dot{x}, \dot{y}, \dot{z}\}^T$).

2.5.2 Rotating frame to J2000

This rotation is particularly useful when preliminary computations of POs in the CR3BP have to be transitioned to the NBP dynamical model. Usually, during convergence and calculations, the transformation between these two dynamical models happens back and forth multiple times. Therefore, a good understanding of the underlying procedures and an efficient routine prove to be particularly useful.

The main procedure requires transforming the state vector of the SC between the principal RS in the CR3BP to the principal one in the NBP. In particular, in the NBP, planetary ephemerides are implemented and, therefore, all the roto-pulsating behaviors that are neglected in simpler dynamical models such as the CR3BP have to be accounted for. For this reason, usually all transformations happen at the centrobaric point of a primary in a binary system. A schematic representation of the procedures is contained in the flowchart in Figure 2.12 for a complete transformation from a nondimensional CR3BP state, ${}^{R/CG}\tilde{\boldsymbol{X}}$, to a nondimensional NBP state, ${}^{F/E}\breve{\boldsymbol{X}}$, and *vice versa*. Please note that the selected primary for transformation is chosen to

be the Earth for both the EM and SE binary systems, even if in the SE scenario the Earth happens to be the smaller primary.

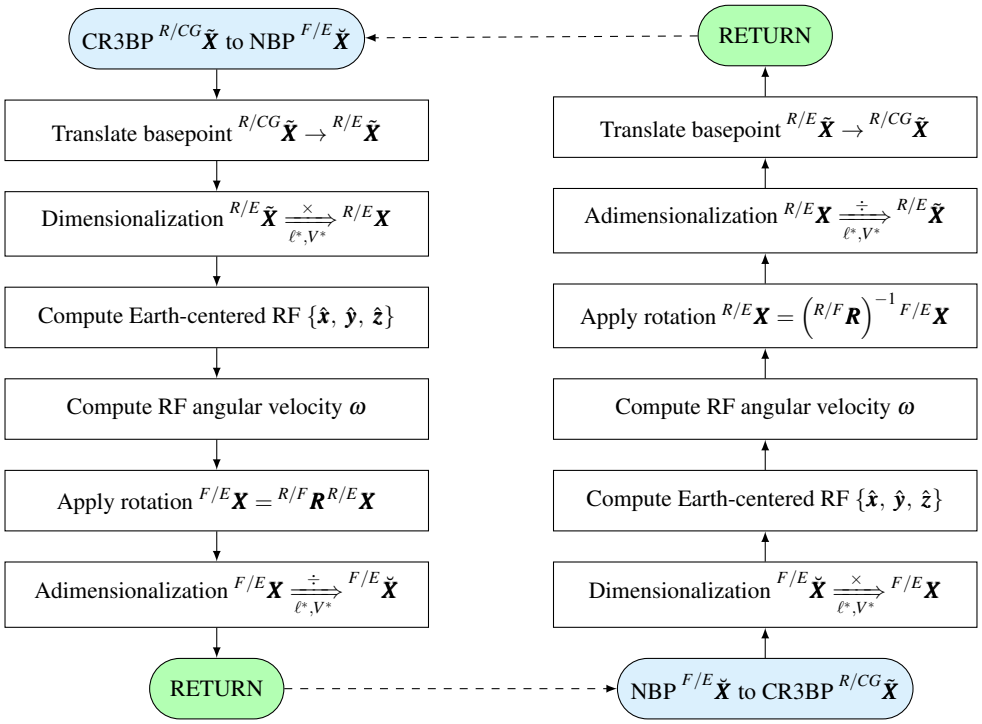

Fig. 2.12 Flowchart representation for CR3BP RF to NBP RF transformation, and *vice versa*

Below are presented the main notations used for the various state vectors depicted in the flowchart in figure 2.12 and their corresponding unit vectors

$$ {}^{R/CG}\tilde{\boldsymbol{X}} = \left\{\xi \quad \eta \quad \zeta \quad \dot{\xi} \quad \dot{\eta} \quad \dot{\zeta}\right\}^T_S \qquad \left\{\hat{\boldsymbol{\xi}}_S,\ \hat{\boldsymbol{\eta}}_S,\ \hat{\boldsymbol{\zeta}}_S\right\} \tag{2.64a} $$

$$ {}^{R/E}\tilde{\boldsymbol{X}} = \left\{\xi \quad \eta \quad \zeta \quad \dot{\xi} \quad \dot{\eta} \quad \dot{\zeta}\right\}^T_R \qquad \left\{\hat{\boldsymbol{\xi}}_R,\ \hat{\boldsymbol{\eta}}_R,\ \hat{\boldsymbol{\zeta}}_R\right\} \tag{2.64b} $$

$$ {}^{R/E}\boldsymbol{X} = \left\{x \quad y \quad z \quad \dot{x} \quad \dot{y} \quad \dot{z}\right\}^T_R \qquad \{\hat{\boldsymbol{x}}_R,\ \hat{\boldsymbol{y}}_R,\ \hat{\boldsymbol{z}}_R\} \tag{2.64c} $$

$$ {}^{F/E}\boldsymbol{X} = \left\{x \quad y \quad z \quad \dot{x} \quad \dot{y} \quad \dot{z}\right\}^T_F \qquad \left\{\hat{\boldsymbol{I}},\ \hat{\boldsymbol{J}},\ \hat{\boldsymbol{K}}\right\} \tag{2.64d} $$

$$ {}^{F/E}\breve{\boldsymbol{X}} = \left\{\breve{x} \quad y \quad z \quad \dot{\breve{x}} \quad \dot{y} \quad \dot{z}\right\}^T_F \qquad \left\{\hat{\boldsymbol{\breve{x}}}_F,\ \hat{\boldsymbol{y}}_F,\ \hat{\boldsymbol{z}}_F\right\}. \tag{2.64e} $$

First of all, quantities have to be translated in the Earth's barycenter,

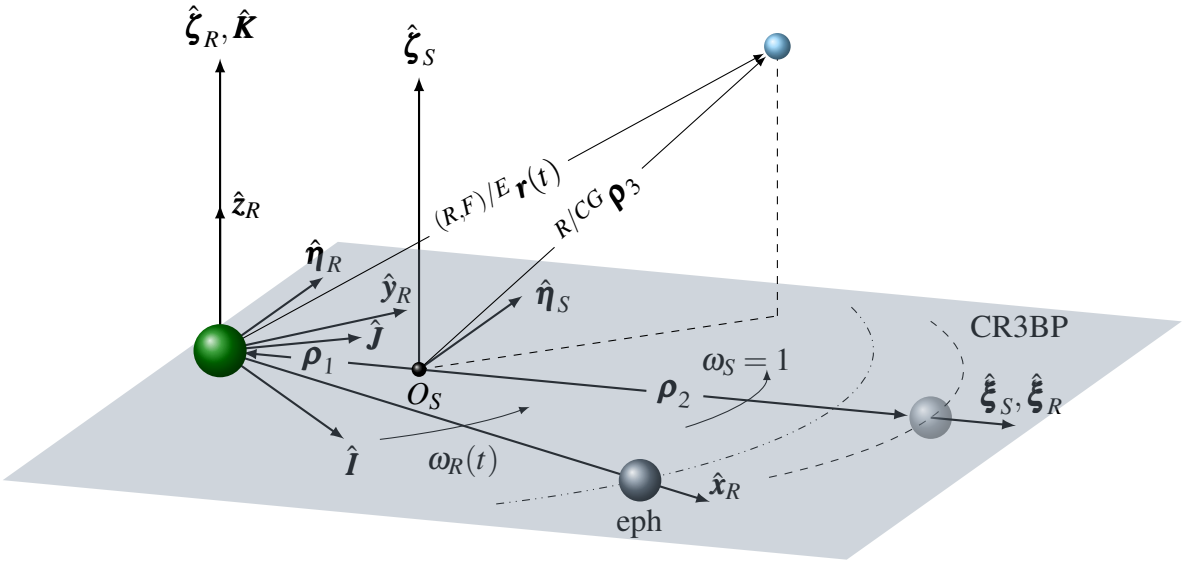

Fig. 2.13 CR3BP synodic RF to J2000 RF transformation - EM RF - not to scale

$$^{R/E}\tilde{\boldsymbol{X}} = {}^{R/CG}\tilde{\boldsymbol{X}} + \begin{Bmatrix} \mu - \mathcal{k}(1+2\mu) \\ 0 \\ 0 \\ 0 \\ 0 \\ 0 \end{Bmatrix}, \qquad \mathcal{k} = \begin{cases} 0 & \text{EM} \\ 1 & \text{SE} \end{cases}, \tag{2.65}$$

where the factor $\mathcal{k}$ takes into account the translation to the closest bigger primary (of $+\mu$) in the EM binary system or to the farther smaller primary (of $-(1-\mu)$) for the SE binary system, in order to have all the subsequent RSs in the Earth's center.

The rotating RF centered in the Earth's barycenter (or a generic primary) has unit axes $\left\{\hat{\boldsymbol{\xi}}_R,\ \hat{\boldsymbol{\eta}}_R,\ \hat{\boldsymbol{\zeta}}_R\right\}$; the first axes coincide, namely $\hat{\boldsymbol{\xi}}_S = \hat{\boldsymbol{\xi}}_R$, whereas the other two are mutually parallel to each other $\hat{\boldsymbol{\eta}}_S \parallel \hat{\boldsymbol{\eta}}_R$, $\hat{\boldsymbol{\zeta}}_S \parallel \hat{\boldsymbol{\zeta}}_R$. As shown in figure 2.13, the synodic RF preserves its constant angular speed $\omega_S = 1$ in nondimensional values.

When transitioned in the rotating RF centered in Earth's barycenter, quantities in the SC state vector have to be dimensionalized with respect to characteristic values for the position vector ($\boldsymbol{\rho} \to \boldsymbol{r}$) and velocity vector ($\boldsymbol{v} \to \boldsymbol{V}$), namely

$$
{}^{R/E}\boldsymbol{X} = {}^{R/E}\tilde{\boldsymbol{X}}\left[\ell^* \;\middle|\; V^*\right] = \begin{Bmatrix} \xi_R \ell^* \\ \eta_R \ell^* \\ \zeta_R \ell^* \\ \dot{\xi}_R V^* \\ \dot{\eta}_R V^* \\ \dot{\zeta}_R V^* \end{Bmatrix} = \begin{Bmatrix} x_R \\ y_R \\ z_R \\ \dot{x}_R \\ \dot{y}_R \\ \dot{z}_R \end{Bmatrix}. \tag{2.66}
$$

The dimensional state ${}^{R/E}\boldsymbol{X}$ now identifies the SC in a rotating frame centered in Earth's barycenter and with constant angular velocity, as per the CR3BP hypotheses. Please note that all the j-th gravitational bodies, such as the Moon (in transparency) and the Sun, are still positioned at the same Keplerian state in this phase. However, in order to compute the SC state in an inertial RF centered in Earth's barycenter, namely the J2000, planetary ephemerides have to be taken into account and the instantaneous unit vectors of such rotating RF have to be computed

$$
\begin{cases}
\hat{\boldsymbol{x}}_R = \dfrac{\boldsymbol{r}_{12}}{\|\boldsymbol{r}_{12}\|} & = \begin{Bmatrix} \hat{x}_I & \hat{x}_J & \hat{x}_K \end{Bmatrix}^T & \text{(2.67a)} \\
\hat{\boldsymbol{y}}_R = \hat{\boldsymbol{z}} \times \hat{\boldsymbol{x}} & = \begin{Bmatrix} \hat{y}_I & \hat{y}_J & \hat{y}_K \end{Bmatrix}^T & \text{(2.67b)} \\
\hat{\boldsymbol{z}}_R = \dfrac{\boldsymbol{r}_{12} \times \boldsymbol{V}_{12}}{\|\boldsymbol{r}_{12} \times \boldsymbol{V}_{12}\|} & = \begin{Bmatrix} \hat{z}_I & \hat{z}_J & \hat{z}_K \end{Bmatrix}^T. & \text{(2.67c)}
\end{cases}
$$

The rotating RF $\{\hat{\boldsymbol{x}}_R,\ \hat{\boldsymbol{y}}_R,\ \hat{\boldsymbol{z}}_R\}$ is centered in the primary body used to retrieve ephemerides, the Earth. Therefore, its origin is the Earth's barycenter and its first unit vector, $\hat{\boldsymbol{x}}_R$, points to the actual position of the j-th gravitational body that was the other primary in the CR3BP. In Figure 2.13 the Moon's ephemerides place the smaller primary in a different position compared to the simplified one in the CR3BP; for ease of representation, its orbital plane has been kept coincident with the synodic one, but in general has three-dimensional position states over time. Similarly, the EME2000 RF $\hat{\boldsymbol{I}} - \hat{\boldsymbol{J}}$ plane is made coincident with the synodic one. Its unit vectors $\left\{\hat{\boldsymbol{I}},\ \hat{\boldsymbol{J}},\ \hat{\boldsymbol{K}}\right\}$ can be expressed in terms of projections of $\{\hat{\boldsymbol{x}}_R,\ \hat{\boldsymbol{y}}_R,\ \hat{\boldsymbol{z}}_R\}$, or *vice versa*, given that the latter is computed via ephemerides retrieved with respect to the J2000 RS itself. For example, the $\hat{\boldsymbol{I}}$ unit vector is composed of all the first components of the rotating unit vectors. Therefore, the rotating Earth-centered RF unit vectors $\{\hat{\boldsymbol{x}}_R,\ \hat{\boldsymbol{y}}_R,\ \hat{\boldsymbol{z}}_R\}$ can be related to their inertial equivalent $\left\{\hat{\boldsymbol{I}},\ \hat{\boldsymbol{J}},\ \hat{\boldsymbol{K}}\right\}$ in the inertial

EME2000 RF via the ${}^{F/R}\boldsymbol{R} \in \mathbb{R}^{3\times3}$ rotational matrix ${}^{F/R}\boldsymbol{R} = \begin{bmatrix} \hat{\boldsymbol{x}}_R & \hat{\boldsymbol{y}}_R & \hat{\boldsymbol{z}}_R \end{bmatrix}$,

$$\begin{Bmatrix} \hat{\boldsymbol{I}} \\ \hat{\boldsymbol{J}} \\ \hat{\boldsymbol{K}} \end{Bmatrix} = \begin{bmatrix} \hat{x}_I & \hat{y}_I & \hat{z}_I \\ \hat{x}_J & \hat{y}_J & \hat{z}_J \\ \hat{x}_K & \hat{y}_K & \hat{z}_K \end{bmatrix} \begin{Bmatrix} \hat{\boldsymbol{x}}_R \\ \hat{\boldsymbol{y}}_R \\ \hat{\boldsymbol{z}}_R \end{Bmatrix} \qquad \begin{Bmatrix} \hat{\boldsymbol{x}}_R \\ \hat{\boldsymbol{y}}_R \\ \hat{\boldsymbol{z}}_R \end{Bmatrix} = \begin{bmatrix} \hat{x}_I & \hat{x}_J & \hat{x}_K \\ \hat{y}_I & \hat{y}_J & \hat{y}_K \\ \hat{z}_I & \hat{z}_J & \hat{z}_K \end{bmatrix} \begin{Bmatrix} \hat{\boldsymbol{I}} \\ \hat{\boldsymbol{J}} \\ \hat{\boldsymbol{K}} \end{Bmatrix}. \tag{2.68}$$

As per the CR3BP, velocities have to be corrected via the transport theorem. Recalling the equation (2.29) and including the appropriate transformations from equation (2.68), one has

$$\begin{aligned} {}^{F}\dot{\boldsymbol{r}} &= (\dot{x} - y\omega_R)\,\hat{\boldsymbol{x}}_R + (\dot{y} + x\omega_R)\,\hat{\boldsymbol{y}}_R + \dot{z}\hat{\boldsymbol{z}}_R \\ &= (\dot{x} - y\omega_R)\left(x_I\hat{\boldsymbol{I}} + x_J\hat{\boldsymbol{J}} + x_K\hat{\boldsymbol{K}}\right) + (\dot{y} + x\omega_R)\left(y_I\hat{\boldsymbol{I}} + y_J\hat{\boldsymbol{J}} + y_K\hat{\boldsymbol{K}}\right) + \\ &+ \dot{z}\left(z_I\hat{\boldsymbol{I}} + z_J\hat{\boldsymbol{J}} + z_K\hat{\boldsymbol{K}}\right) \\ {}^{F}\dot{\boldsymbol{r}} &= \left[(\dot{x} - y\omega_R)\,\hat{x}_I + (\dot{y} + x\omega_R)\,\hat{y}_I + \dot{z}\hat{z}_I\right]\hat{\boldsymbol{I}} + \\ &+ \left[(\dot{x} - y\omega_R)\,\hat{x}_J + (\dot{y} + x\omega_R)\,\hat{y}_J + \dot{z}\hat{z}_J\right]\hat{\boldsymbol{J}} + \\ &+ \left[(\dot{x} - y\omega_R)\,\hat{x}_K + (\dot{y} + x\omega_R)\,\hat{y}_K + \dot{z}\hat{z}_K\right]\hat{\boldsymbol{K}}. \end{aligned} \tag{2.69}$$

All the quantities x, y, z and their derivatives are here referred to the rotating frame and the epoch-dependent istantaneous angular velocity is computed via the 2BP definition. The instantaneous value of the specific angular momentum is equal to

$$h = \|\boldsymbol{r}_{12} \times \boldsymbol{V}_{12}\|, \tag{2.70}$$

and therefore

$$\omega_R(t) = \frac{h}{\|\boldsymbol{r}_{12}\|^2}. \tag{2.71}$$

The complete transformation matrix from the SC state in the rotating Earth-centered RF ${}^{R/E}\boldsymbol{X} = \begin{Bmatrix} x_R & y_R & z_R & \dot{x}_R & \dot{y}_R & \dot{z}_R \end{Bmatrix}^T$ to the fixed EME2000 RF ${}^{F/E}\boldsymbol{X} = \begin{Bmatrix} x_F & y_F & z_F & \dot{x}_F & \dot{y}_F & \dot{z}_F \end{Bmatrix}^T$ is therefore

$$\begin{Bmatrix} x_F \\ y_F \\ z_F \\ \dot{x}_F \\ \dot{y}_F \\ \dot{z}_F \end{Bmatrix} = \begin{bmatrix} \hat{x}_I & \hat{y}_I & \hat{z}_I & 0 & 0 & 0 \\ \hat{x}_J & \hat{y}_J & \hat{z}_J & 0 & 0 & 0 \\ \hat{x}_K & \hat{y}_K & \hat{z}_K & 0 & 0 & 0 \\ \omega_R y_I & -\omega_R x_I & 0 & \hat{x}_I & \hat{y}_I & \hat{z}_I \\ \omega_R y_J & -\omega_R x_J & 0 & \hat{x}_J & \hat{y}_J & \hat{z}_J \\ \omega_R y_K & -\omega_R x_K & 0 & \hat{x}_K & \hat{y}_K & \hat{z}_K \end{bmatrix} \begin{Bmatrix} x_R \\ y_R \\ z_R \\ \dot{x}_R \\ \dot{y}_R \\ \dot{z}_R \end{Bmatrix}, \tag{2.72}$$

or, in short notation,

$${}^{F/E}\boldsymbol{X} = \boldsymbol{R}_{R/F}\,{}^{R/E}\boldsymbol{X} = \left[\begin{array}{c|c} \boldsymbol{R}_{\{\hat{\boldsymbol{x}},\,\hat{\boldsymbol{y}},\,\hat{\boldsymbol{z}}\}} & \boldsymbol{0} \\ \hline \boldsymbol{R}_{\omega_R}(\omega_R) & \boldsymbol{R}_{\{\hat{\boldsymbol{x}},\,\hat{\boldsymbol{y}},\,\hat{\boldsymbol{z}}\}} \end{array}\right] {}^{R/E}\boldsymbol{X}\,, \tag{2.73}$$

where

$$\boldsymbol{R}_{\omega_R}(\omega_R) = \begin{bmatrix} \omega_R y_I & -\omega_R x_I & 0 \\ \omega_R y_J & -\omega_R x_J & 0 \\ \omega_R y_K & -\omega_R x_K & 0 \end{bmatrix}. \tag{2.74}$$

2.6 Perturbing accelerations

The dynamical model includes three main perturbing effects on the bodies' motion. The perturbing acceleration caused by Moon and Sun's gravity, the perturbing acceleration due to the Earth's non-sphericity, and the perturbation that accounts for the solar radiation pressure. Therefore, the vectorial form of the cumulative combined perturbing acceleration from the system in equation (2.51) is

$$\mathbf{a}_p = \mathbf{a}_{lsp} + \mathbf{a}_J + \mathbf{a}_{SRP}\,. \tag{2.75}$$

Such formulation of the perturbing acceleration has been discussed recently [48], and further analyses can be retrieved in textbooks [31, 33, 35] or presented in recent literature under different nuances. For example, some studies implemented such perturbation to study the stability and de-orbit behavior of a SC in highly-elliptical orbits [49, 50]. Other research focused the attention on the analytical expansion of the lunisolar effect [51], while others implemented in optimal control problems the J_2 [52] and the atmospheric drag [53] effects. There is no general, analytical

solution for predicting the long-term effects of orbital perturbation. Instead, numerical techniques (special perturbation methods) or approximate analytical solutions (general perturbation methods) must be used to estimate these effects. Further on each perturbation is discussed singularly in the following three Sections.

2.6.1 Lunisolar effect

Third-body perturbation and gravitational perturbations have been subjects of extensive studies in recent literature due to their importance in predicting how specific orbits, such as highly-elliptical or distant retrograde ones, deviate from expected behaviors over time [49, 50, 54, 55]. Incidentally, the third-body perturbation is one of the main reasons behind the discovery of Neptune. Since Galileo's time, in the 17th Century, Neptune was indeed observed, but due to its low apparent magnitude and characteristic light blue color, it was often misinterpreted as a small fixed blue star. When access to telescopes became easier, Friedrick William Hershel discovered Uranus in 1781, and astronomers could accurately predict its orbital parameters, including its orbital period of about 84 years. For a shorter period, Uranus followed mathematical predictions with great accuracy; however, around 50 years after its discovery, Alexis Bouvard disclosed that predictions of Uranus' ephemeris had positioning errors with the same order of magnitude as the planet's radius itself. Such declaration implied that computations were incongruent with the gravitational effects of all the other celestial bodies known to be present in the solar system, namely the six orbiting at semi-major axes below Uranus' one. Only a few years later, with John Couch Adams' computations in 1843, followed by further research by Urbain Le Verrier in 1846, the small blue dot in the sky was correctly labeled as a planet and given the name Neptune. Divergences in Uranus' orbit were ultimately corrected by adding the additional third-body perturbation of Neptune.

For what concerns the dynamical system of interest, the third-body position components in the SC-centered topocentric frame with respect to the EME2000 RF, with subscript $b = s, \ell$ for Sun and Moon respectively, are retrieved from DE430 JPL ephemerides [40]. If subscript b is used to indicate a generic body, its position vector $\boldsymbol{r}_{Eb}$ is given in rectangular coordinates x_{Eb}, y_{Eb}, z_{Eb} with respect to the Earth in the ICRF, i.e. $\boldsymbol{r}_{Eb} = x_{Eb}\hat{\boldsymbol{I}} + y_{Eb}\hat{\boldsymbol{J}} + z_{Eb}\hat{\boldsymbol{K}}$. Again, ICRF and EME2000 are used

indistinctly due to the absence of nutations and precession.

$$\boldsymbol{r}_{ZEN} = \boldsymbol{R}_{23}(\varphi, \vartheta)\, \boldsymbol{r}_{IJK}$$

$$(r_{Eb})_u = x_b \cos\vartheta \cos\varphi + y_b \sin\vartheta \cos\varphi + z_b \sin\varphi \tag{2.76a}$$

$$(r_{Eb})_v = -x_b \sin\vartheta + y_b \cos\vartheta \tag{2.76b}$$

$$(r_{Eb})_w = -x_b \cos\vartheta \sin\varphi - y_b \sin\vartheta \sin\varphi + z_b \cos\varphi\,. \tag{2.76c}$$

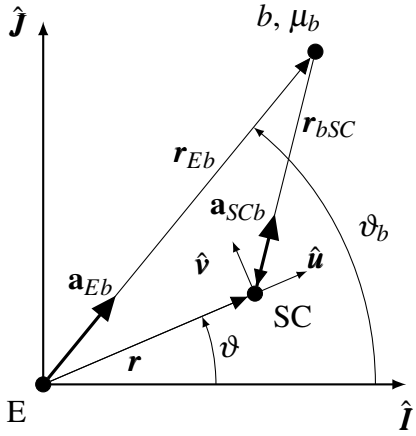

Fig. 2.14 Schematic representation of third body gravitational perturbation in EME2000 RF

The gravitational perturbation caused by the third body of gravitational parameter μ_b and position vector with respect to the Earth $\boldsymbol{r}_{Eb}$ on the SC, $\mathbf{a}_{bg}$, is obtained as the difference of the gravitational accelerations on SC, $\mathbf{a}_{SCb}$, and Earth, $\mathbf{a}_{Eb}$,

$$\mathbf{a}_{bg} = \mathbf{a}_{SCb} - \mathbf{a}_{Eb} = -\frac{\mu_b}{r_{bSC}^3}\boldsymbol{r}_{bSC} - \frac{\mu_b}{r_{Eb}^3}\boldsymbol{r}_{Eb}\,. \tag{2.77}$$

The SC position with respect to the third body is written as $\boldsymbol{r}_{bSC} = \boldsymbol{r} - \boldsymbol{r}_{Eb}$. The acceleration is projected onto the topocentric frame at epoch to easily obtain the perturbing components. Thus the gravitational effect becomes (same formal

expression for Sun and Moon)

$$(\mathrm{a}_b)_u = \frac{\mu_b}{r_{bSC}^3}\left[(r_{Eb})_u - r\right] - \frac{\mu_b}{r_{Eb}^3}(r_{Eb})_u \tag{2.78a}$$

$$(\mathrm{a}_b)_v = \frac{\mu_b}{r_{bSC}^3}(r_{Eb})_v - \frac{\mu_b}{r_{Eb}^3}(r_{Eb})_v \tag{2.78b}$$

$$(\mathrm{a}_b)_w = \frac{\mu_b}{r_{bSC}^3}(r_{Eb})_w - \frac{\mu_b}{r_{Eb}^3}(r_{Eb})_w\,, \tag{2.78c}$$

with dependence on r, ϑ and φ. The SC distance from the Sun or from the Moon is $r_{bSC} = \sqrt{[r-(r_{Eb})_u]^2 + (r_{Eb})_v^2 + (r_{Eb})_w^2}$.

When the perturbing body is very far compared to the Earth-SC distance (i.e., when $\boldsymbol{r}_{Eb} \gg \boldsymbol{r}$ as it happens for the Sun) and coplanarity is assumed, a simple expression of the tangential and radial components of the perturbation can be derived (please refer to Refs. [48, 49] for further details)

$$(\mathbf{a}_{SCs} - \mathbf{a}_{Es}) \cdot \hat{\boldsymbol{u}} = \frac{3}{2}\frac{\mu_s}{r_{Es}^3}\left\{1 + \cos\left[2\left(\vartheta_s - \vartheta\right)\right]\right\} \tag{2.79a}$$

$$(\mathbf{a}_{SCs} - \mathbf{a}_{Es}) \cdot \hat{\boldsymbol{v}} = \frac{3}{2}\frac{\mu_s}{r_{Es}^3}\sin\left[2\left(\vartheta_s - \vartheta\right)\right], \tag{2.79b}$$

where $\hat{\boldsymbol{u}}$ and $\hat{\boldsymbol{v}}$ are, respectively, the radial and tangential unit vectors in the VNB (ZEN) RF.

The SC velocity has main components along tangential and radial directions, so these terms can be used to estimate the positive or negative effects of solar perturbation during the escape. The two quantities contained in equation (2.79) will be analyzed extensively in Chapter 5 in the design and optimization of escape trajectories from EM and SE LPs.

2.6.2 Earth asphericity

The first perturbation is computed via the Earth Gravitational Model EGM2008 [56]. The Tide Free system is implemented in the present analysis and extensive details about the model can be found in [57]. The dimensional potential $\mathscr{V}$ due to the Earth asphericity of an object positioned at a geocentric distance r, with longitude ϑ_{Lo} and latitude φ, can be expressed as [31, 48, 49]

$$\mathscr{V} = -\frac{\mu_E}{r}\left\{1+\sum_{n=2}^{N}\left(\frac{r_E}{r}\right)^n \sum_{m=0}^{n}\left[C_{nm}\cos\left(m\vartheta_{Lo}\right)+S_{nm}\sin\left(m\vartheta_{Lo}\right)\right]P_{nm}\sin\left(\varphi\right)\right\}. \tag{2.80}$$

Harmonics of order 8 and degree 8 are implemented along the associated legendre functions P_{nm} and spherical harmonic coefficients, C_{nm} and S_{nm}. Since nutation and precession are neglected, Earth's rotation is assumed constant. Moreover, declination and latitude coincide. The terrestrial longitude is obtained as

$$\vartheta_{Lo}(t) = \vartheta - \vartheta_G(t) = \vartheta - \left[\vartheta_{Gref} + \omega_E\left(t - t_{ref}\right)\right]. \tag{2.81}$$

The reference time t_{ref} is the J2000 epoch, January 1, 2000 at 12:00:00 UTC (51544.5 MJD), and $\vartheta_{G0} = 280.46061837504$ deg; ω_E is evaluated assuming the sidereal day equal to 86164.098903690351 s (no precession is considered). The perturbing acceleration due to Earth's non-sphericity is the gradient of $\Phi = \mathscr{V} + \mu_E/r$, and its components in the topocentric frame, as per equations (2.51d) to (2.51f), are thus evaluated as

$$\left(\mathrm{a}_J\right)_u = \frac{\partial\Phi}{\partial r} \tag{2.82a}$$

$$\left(\mathrm{a}_J\right)_v = \frac{\partial\Phi}{\partial\vartheta}\frac{1}{r\cos\varphi} \tag{2.82b}$$

$$\left(\mathrm{a}_J\right)_w = \frac{\partial\Phi}{\partial\varphi}\frac{1}{r}. \tag{2.82c}$$

Derivation with respect to r and ϑ is straightforward; derivatives with respect to φ require the derivatives of the associated Legendre functions, which are obtained recursively, exploiting the properties of Legendre polynomials.

Please note that the escape trajectories optimized in the present thesis will depart from the EML_2 point and QPOs in both the EM and SE binary system. Therefore, the influence of the Earth's gravitational model is indeed minimal and could be, in theory, neglected. However, it has been chosen to implement the Earth's aspherical harmonics nevertheless to have the capability of treating these perturbations when needed in future studies, without modifying the code and preserving the desired

fidelity. In the present scenario, therefore, the effect is actually negligible both on results and computational speed.

2.6.3 Solar Radiation Pressure

The Solar Radiation Pressure (SRP) is the third perturbation taken into account in the dynamical model. Since the early days of the first radiometers, such as the Crookes' radiometer, experiments on the light's wave-particle duality exhibited how light can exert a net momentum when hitting a surface. Photons emitted from the Sun possess momentum and travel at the speed of light c. Although the SC is considered massless in some dynamical models, it indeed has specific physical properties. The one used in the analysis has the characteristics shown in Table 2.5.

Quantity		Value	
Mass	m_0	850	kg
Cross-section Surface	S	5.7	m^2
Surface reflectivity	η_R	0.7	

Table 2.5 SC characteristic values

The photon pressure p at a generic distance r from the Sun, considered a point source of light which emits spherical wavefronts, is

$$p = \frac{\mathcal{P}}{4\pi r^2} c\,, \tag{2.83}$$

where $\mathcal{P} = 1367\ \mathrm{W/m^2}$ is the radiated power, also called solar constant or solar irradiance, which scales with the inverse squared distance from the Sun in AU. The photon pressure at $r^* = 1$ AU equals $p^* = 4.55682 \times 10^{-6}\ \mathrm{N/m^2}$. By defining the quantity

$$\Gamma = (1 + \eta_R)\, pS\,, \tag{2.84}$$

the acceleration on a spherical body of mass m and surface S at a distance from the Sun r_{sSC} is

$$(\mathrm{a}_{srp})_u = -\frac{\Gamma}{m r_{sSC}^3}\left[(r_{Es})_u - r\right] \tag{2.85a}$$

$$(\mathrm{a}_{srp})_v = -\frac{\Gamma}{m r_{sSC}^3}(r_{Es})_v \tag{2.85b}$$

$$(\mathrm{a}_{srp})_w = -\frac{\Gamma}{m r_{sSC}^3}(r_{Es})_w\,. \tag{2.85c}$$

Again, the SRP is function of r, ϑ and φ, but also depends on the mass of the SC itself, m, which varies along the trajectory while thrusting. The formulation presented here is a partially simplified one in which the SC's surface is supposed to be equally facing the Sun at all times, therefore neglecting changes in perspective and effective area [33].

Chapter 3

Periodic and quasi-periodic orbits

Chapter 3 describes the processes that allow the construction and validation of Periodic Orbits (POs), in the Circular Restricted Three-Body Problem (CR3BP), and Quasi-Periodic Orbits (QPOs), in the n-Body Problem (NBP).

The CR3BP provides a time-invariant system, namely a set of epoch-independent, autonomous equations that can be linearized in order to perform differential corrections; the concepts of single-shooting methods and State Transition Matrix (STM) are introduced, which result, in the CR3BP domain, in the existence of exact periodic motion for specific families of orbits. Two main types of POs are analyzed; the Lyapunov Orbits (LOs), namely those POs sharing the same orbital plane with the two primaries, and Halo Orbits (HOs), which bifurcates from the Lyapunov ones in three dimensions.

On the other hand, the high-fidelity NBP requires the implementation of the ephemerides, which render the Non Linear (NL) set of Ordinary Differential Equations (ODEs) time-dependent and non-autonomous. A gradual numerical transition from the CR3BP POs to specific NBP QPOs is performed with continuation strategies, relaxations, and gradual perturbation methods.

The first three Sections describe the procedure to obtain such POs in the CR3BP, from analytical approximations to the ones obtained via Differential Corrector (DC) strategies and single-shooting methods. The last Section outlines how such POs are transitioned into QPOs in the NBP.

3.1 Trajectory construction in the Circular-Restricted Three-Body Problem

The study of the existence and stability of POs near the Lagrangian Points (LPs) and QPOs in the regions close to such quasi-stable equilibrium points has received significant attention in the literature. Since Farquar's early research [58], many studies explored different aspects including long-term stability [59, 60] and trajectory design [61–63], and multiple textbooks extensively covered these topics [28, 31, 35, 64–66]. In this dissertation, the construction of POs and QPOs serves as a foundation and precursor for the main focus: optimizing low-thrust escape trajectories. Therefore, this Chapter is confined to the purpose of obtaining QPOs from POs in the ephemeris full force model through analytical or iterative computations, with the goal to increase the fidelity of the trajectories presented later in the thesis.

To explore how a Spacecraft (SC) behaves close to LPs is useful to linearize the Equations of Motion (EOMs), from equation (2.37), in their vicinity. By applying a Taylor series expansion to the Right-Hand Side (RHS) of equation (2.37), and by imposing that

$$\frac{\partial^2 \mathscr{U}}{\partial \xi \, \partial \eta} \triangleq \mathscr{U}_{\xi\eta} \tag{3.1}$$

indicates the second partial derivative of $\mathscr{U}$ with respect to ξ and η, one has

$$\ddot{\xi} - 2\dot{\eta} = \mathscr{U}_{\xi\xi}\big|_{LP}\,\xi + \mathscr{U}_{\xi\eta}\big|_{LP}\,\eta + \mathscr{U}_{\xi\zeta}\big|_{LP}\,\zeta \tag{3.2a}$$

$$\ddot{\eta} + 2\dot{\xi} = \mathscr{U}_{\eta\xi}\big|_{LP}\,\xi + \mathscr{U}_{\eta\eta}\big|_{LP}\,\eta + \mathscr{U}_{\eta\zeta}\big|_{LP}\,\zeta \tag{3.2b}$$

$$\ddot{\zeta} = \mathscr{U}_{\zeta\xi}\big|_{LP}\,\xi + \mathscr{U}_{\zeta\eta}\big|_{LP}\,\eta + \mathscr{U}_{\zeta\zeta}\big|_{LP}\,\zeta\,. \tag{3.2c}$$

This set of equations -known as variational equations- and the *LP* subscript refer to the partials computed at the equilibrium points. For brevity, this notation is dropped in the current Chapter. All equilibrium points lie in the $\left\{\hat{\boldsymbol{\xi}}_S, \hat{\boldsymbol{\eta}}_S\right\}$ plane, so mixed partial derivatives containing ζ are null by definition, $\mathscr{U}_{\xi\zeta} = \mathscr{U}_{\eta\zeta} = 0$. Thus, the acceleration $\ddot{\zeta}$ produces an out-of-plane motion ζ whose variation has a linear, negligible influence on the in-plane motion in the ξ and η directions. Indeed, they are decoupled ODEs, and the last equation (3.2c) is an harmonic in the $\hat{\boldsymbol{\zeta}}_S$ direction

$$\ddot{\zeta} = \mathscr{U}_{\zeta\zeta}\,\zeta\,, \qquad \zeta = A_\zeta \cos\left(\omega_\zeta \tau\right) + B_\zeta \sin\left(\omega_\zeta \tau\right), \tag{3.3}$$

with A_ζ, B_ζ constants depending on the initial conditions. The out-of-plane frequency is computed as

$$\omega_\zeta^2 = -\mathscr{U}_{\zeta\zeta}\,. \tag{3.4}$$

The first two equations (3.2a) and (3.2b) represent a coupled system of two second-order ODEs that can be transformed in a set of four first-order ODEs

$$\begin{Bmatrix} \dot{\xi} \\ \dot{\eta} \\ \ddot{\xi} \\ \ddot{\eta} \end{Bmatrix} = \begin{bmatrix} 0 & 0 & 1 & 0 \\ 0 & 0 & 0 & 1 \\ \mathscr{U}_{\xi\xi} & \mathscr{U}_{\xi\eta} & 0 & 2 \\ \mathscr{U}_{\eta\xi} & \mathscr{U}_{\eta\eta} & -2 & 0 \end{bmatrix} \begin{Bmatrix} \xi \\ \eta \\ \dot{\xi} \\ \dot{\eta} \end{Bmatrix}, \tag{3.5}$$

or, in matricial form,

$$\dot{\tilde{\boldsymbol{X}}} = \tilde{\boldsymbol{A}}\tilde{\boldsymbol{X}}\,, \tag{3.6}$$

which is the baseline representation of an homogeneous state equation in which $\tilde{\boldsymbol{A}}$ represents the nondimensional Jacobian matrix and $\tilde{\boldsymbol{X}}$, here, represents the (planar reduced) nondimensional state of the SC.

The first and second derivatives of the pseudopotential function are explicitly computed in Appendix A. However, by studying their sign with respect to a changing μ parameter, one notices that $\mathscr{U}_{\xi\xi} > 0$, $\mathscr{U}_{\eta\eta} < 0$ and $\mathscr{U}_{\xi\eta} = 0$ for all three collinear points, respectively for equations (A.2a), (A.2b) and (A.2e), as shown in Figure 3.1.

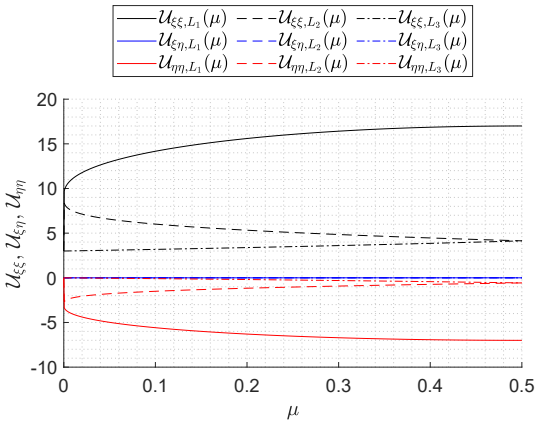

Fig. 3.1 Second partial derivatives of the pseudopotential function $\mathscr{U}$ at the three collinear Lagrangian points as a function of the specific binary mass ratio μ

Therefore, when looking at the determinant, which produces four different roots,

$$\lambda^4 + \left(4 - \mathscr{U}_{\xi\xi} - \mathscr{U}_{\eta\eta}\right)\lambda^2 + \left(\mathscr{U}_{\xi\xi}\mathscr{U}_{\eta\eta} - \mathscr{U}_{\xi\eta}^2\right) = 0\,, \tag{3.7}$$

the procedure followed in Szebehely [28] can be implemented so that the equation (3.7) can be rewritten in the following form to find the two roots $\Lambda_{1/2}$

$$\left.\begin{aligned} \Lambda &= \lambda^2 \\ \beta_1 &= 2 - \frac{\mathscr{U}_{\xi\xi} + \mathscr{U}_{\eta\eta}}{2} \\ \beta_2 &= \sqrt{-\mathscr{U}_{\xi\xi}\mathscr{U}_{\xi\eta}} \end{aligned}\right\} \quad \Longrightarrow \Lambda_{1/2} = -\beta_1 \pm \sqrt{\beta_1^2 + \beta_2^2}\,. \tag{3.8}$$

The eigenvalues are

$$\lambda_{1/2} = \pm\sqrt{\Lambda_1} \tag{3.9a}$$

$$\lambda_{3/4} = \pm\sqrt{\Lambda_2}\,. \tag{3.9b}$$

The first two eigenvalues in equation (3.9a) are real ones, whereas the third and fourth in equation (3.9b) are pure imaginary. The first imaginary solution provides the in-plane frequency of the linearized PO, namely

$$\omega_3 = -i\lambda_3\,. \tag{3.10}$$

The solutions for ξ and η as a function of the nondimensional time τ are coupled and include aperiodic exponential instabilities and aperiodic decays. The first-order approximation sought for the following analysis is a mere aperiodic structure. With further mathematical manipulation and by setting all the aperiodic exponential instabilities to zero, a much simpler set of EOMs is obtained in the form [67]

$$\begin{cases} \xi(\tau) = A_\xi \cos(\omega_3\tau + \phi) & \text{(3.11a)} \\ \eta(\tau) = -c_2 A_\xi \sin(\omega_3\tau + \phi) & \text{(3.11b)} \\ \zeta(\tau) = A_\zeta \cos\left(\omega_\zeta\tau + \psi\right) & \text{(3.11c)} \\ \dot{\xi}(\tau) = -A_\xi\omega_3 \sin(\omega_3\tau + \phi) & \text{(3.11d)} \\ \dot{\eta}(\tau) = -c_2 A_\xi\omega_3 \cos(\omega_3\tau + \phi) & \text{(3.11e)} \\ \dot{\zeta}(\tau) = -A_\zeta\omega_\zeta \sin\left(\omega_\zeta\tau + \psi\right) & \text{(3.11f)} \end{cases}$$

where A_ξ is the initial amplitude in the ξ direction and resembles a semimajor axis, whereas the semiminor axis A_η can be computed as

$$A_\eta = c_2 A_\xi \,. \tag{3.12}$$

Trajectories computed via the set of equations in (3.11) can be used as initial seeds for the differential correction procedure. Indeed, by taking as initial state $\tilde{\boldsymbol{X}}^a(\tau_0) = \left\{\xi_0, \eta_0, \zeta_0, \dot{\xi}_0, \dot{\eta}_0, \dot{\zeta}_0\right\}^T$, an analytical propagation provides a indefinitely stable elliptical orbit. If $\tilde{\boldsymbol{X}}^a(\tau_0)$ is used as the initial state for the NL integration of the CR3BP EOMs, nonlinearities arise that excite divergent behaviors. The smaller the dimension of the analytical orbit, the more plausible that the integrated one will remain stable for longer. In literature, there are many methods and contributions on how to predict the evolution and stability of CR3BP POs [68, 69]. For example, in this research's early stages, the use of the momentum integral, also known as the escape integral, proved to be particularly useful. Such integral is essentially a line integral computed over the integrated state of a SC in the CR3BP from τ_0 to τ_f and is capable of predicting with a sufficient margin when nonlinearities are inducing an undesired escape. The momentum integral has the following form:

$$\mathcal{M}_I = \int_{\tau_0}^{\tau_f} \left[\xi(\tau)\,\dot{\xi}(\tau) + \eta(\tau)\,\dot{\eta}(\tau) + \zeta(\tau)\,\dot{\zeta}(\tau)\right] \mathrm{d}\tau \,. \tag{3.13}$$

A Lyapunov analytical orbit with $A_y = 5 \times 10^5$ km, centered at the Sun-Earth Lagrangian Point L_2 (SEL_2), is plotted in Figure 3.2 and the same initial guess is seeded as starting point for the integration of the EOMs for multiple revolutions. After two complete revolutions, the nonlinear integration shows divergence with respect to the analytical orbit, providing an escape a few moments later.

The escape integral, depicted in Figure 3.3, shows that after two complete revolutions, an escape "warning" is issued, namely, the first point in which $\mathcal{M}_I > 0$. Indeed, the third complete revolution is not completed, and divergence is observed both in the escape integral and the trajectory.

This technique is particularly useful for all the stationkeeping strategies that have to be analyzed in order to guarantee stability for a SC that has to remain stable for long periods around POs and QPOs. Such domain goes beyond the scope of this thesis, but further interesting details can be found, for example, in [69]. However,

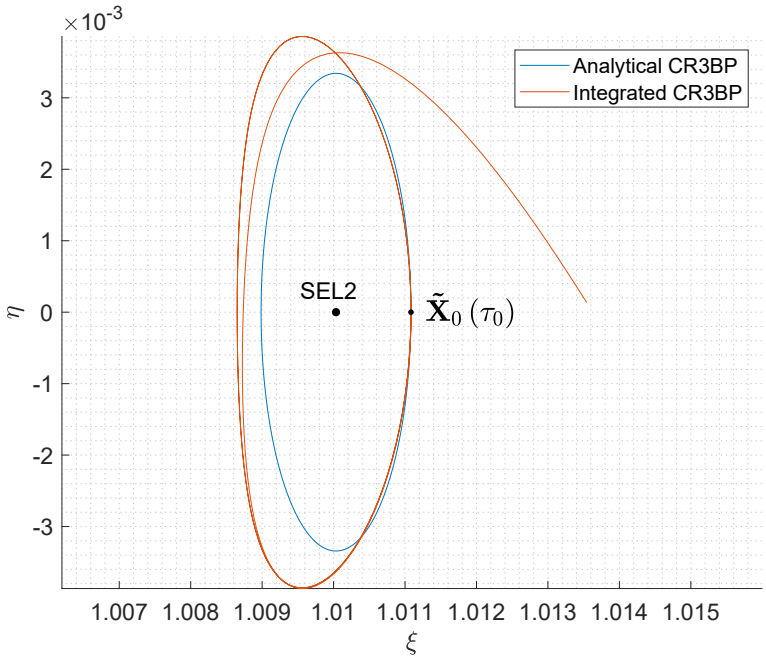

Fig. 3.2 Analytical propagation vs nonlinear integration - Sun-Earth Lyapunov orbit

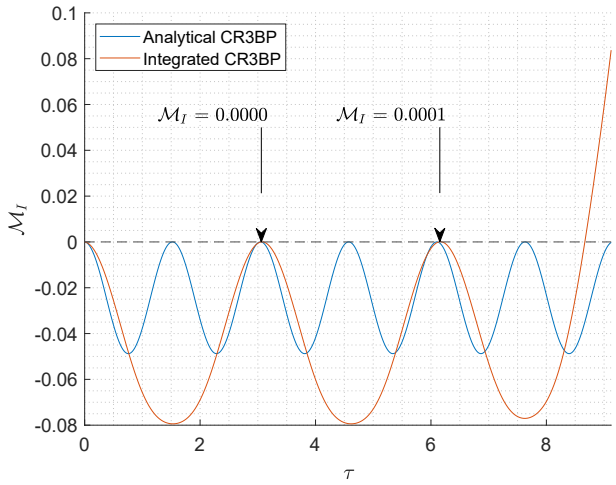

Fig. 3.3 Momentum integral (escape warning)

the escape integral will be used to verify the stability of the generated QPOs in the ephemeris model, further validating the escape trajectories.

3.2 Differential correctors

The scope of the present thesis is to perform a trajectory optimization in a higher fidelity model of escape trajectories starting from LPs in the Earth-Moon (EM) and Sun-Earth (SE) binary systems, followed by a more thorough analysis of fuel-optimal low-thrust escape trajectories from QPOs around such LPs. Therefore, the study of the stability of POs and QPOs is not itself a requisite, as long as the baseline departure trajectory remains for a reasonable time in its initial configuration. Such reasonable time can be assessed in having stability for *at least* a single complete orbit. Therefore, more complex methods and strategies to guarantee long-term stability around CR3BP POs and NBP QPOs, such as multi-shooting methods and station-keeping techniques, are beyond the scope and utility of this work. Simpler strategies, such as single-shooting methods, are implemented here to tackle the initial stability requirements and to improve the simple guesses that can be obtained via analytical methods, as presented in Section 3.1. Two types of periodic and quasi-periodic orbits are of interest; planar Lyapunov orbits and three-dimensional Near Rectilinear Halo Orbits (NRHOs).

A simple but "blind" method to finding a specified path from an initial state $\tilde{\boldsymbol{X}}(\tau_0)$ to a desired final state $\tilde{\boldsymbol{X}}\left(\tilde{\boldsymbol{X}}(\tau_0),\tau_f\right)$, or $\boldsymbol{X}(t_0)$ to $\boldsymbol{X}\left(\boldsymbol{X}(t_0),t_f\right)$ in dimensional quantities, is to select a reasonable initial guess for the initial state and integrate it for a specified duration, changing its initial quantities, randomly or discretely, until an integrated final state lies close to the desired one. Such *brute-force* trial-and-error approach bets on chances and has no methods of understanding if a specific change in the initial values is actually improving the convergence.

Another procedure, which is more robust and provides theoretical insights about the evolution of the associated state over time, is to understand *how* an initial state $\boldsymbol{X}(t_0)$ should be changed and corrected to produce a desired final state $\boldsymbol{X}\left(\boldsymbol{X}(t_0),t_f\right)$. Namely, correcting a baseline trajectory to have specific terminal conditions implies understanding how initial and terminal conditions are related along the trajectory. Such a scenario is the classic framework of a Two-Point Boundary Value Problem (TPBVP).

Figure 3.4 shows in green a planar Lyapunov orbit in the EM binary system as the targeted desired trajectory. Such orbit is defined by an initial state $\tilde{\boldsymbol{X}}^*(\tau_0)$ which produces, after a complete orbit, the final state $\tilde{\boldsymbol{X}}^*\left(\tilde{\boldsymbol{X}}^*(\tau_0),\tau_f\right)$. Please note

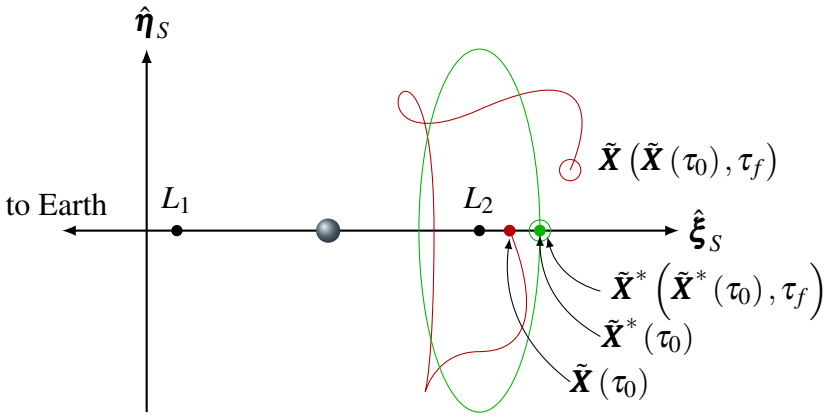

Fig. 3.4 Single shooting differential correction procedure from a generic state $\tilde{X}$ to a desired reference state $\tilde{X}^*$ for a planar Lyapunov orbit in the CR3BP domain

the final state dependency on the initial state itself. The trajectory in red, however, is a non-converged tentative solution to obtain the same Lyapunov orbit; its initial guess $\tilde{X}(\tau_0)$ has a departing point in the wrong position along the $\hat{\xi}_S$ axis and also velocities are highly likely to be corrected; such discrepancies in the initial state lead to a final state $\tilde{X}\left(\tilde{X}(\tau_0),\tau_f\right)$ far from the desired one. As per the equation (3.6), the aim is to understand how *sensible* are initial and final conditions due to changes in the one or in the other. Similarly, the aim is to understand what is the *variation* between the desired and actual final states. The (hopefully small) discrepancy, or perturbation state, can be described as

$$\delta\tilde{X}(\tau_f) = \tilde{X}\left(\tilde{X}(\tau_0),\tau_f\right) - \tilde{X}^*\left(\tilde{X}^*(\tau_0),(\tau_f)\right). \tag{3.14}$$

The differential correction procedure aims at nullifying the differences between the two states. Such a result can be obtained by noticing that a specific correction in the initial state, say $\delta\tilde{X}(\tau_0)$, should produce the desired initial state as

$$\tilde{X}^*(\tau_0) = \tilde{X}(\tau_0) + \delta\tilde{X}(\tau_0). \tag{3.15}$$

Therefore, equation (3.14) can be expanded and linearized as

$$\begin{aligned}
\delta\tilde{\boldsymbol{X}}\left(\tau_f\right) &= \tilde{\boldsymbol{X}}\left(\tilde{\boldsymbol{X}}\left(\tau_0\right),\tau_f\right) - \tilde{\boldsymbol{X}}^*\left(\tilde{\boldsymbol{X}}^*\left(\tau_0\right),\tau_f\right) \\
&= \tilde{\boldsymbol{X}}\left(\tilde{\boldsymbol{X}}\left(\tau_0\right) + \delta\tilde{\boldsymbol{X}}\left(\tau_0\right),\tau_f\right) - \tilde{\boldsymbol{X}}^*\left(\tilde{\boldsymbol{X}}^*\left(\tau_0\right),\tau_f\right) \\
&= \frac{\partial\tilde{\boldsymbol{X}}\left(\tau_f\right)}{\partial\tilde{\boldsymbol{X}}\left(\tau_0\right)}\delta\tilde{\boldsymbol{X}}\left(\tau_0\right), \\
\delta\tilde{\boldsymbol{X}}\left(\tau_f\right) &= \tilde{\boldsymbol{\Phi}}\left(\tau_f,\tau_0\right)\delta\tilde{\boldsymbol{X}}\left(\tau_0\right).
\end{aligned} \tag{3.16}$$

The first term in the RHS of equation (3.16) is the partial derivative of all state quantities at a specified final time τ_f with respect to all the same state quantities computed at the initial time. Such linear mapping between initial and final states is known as STM and denoted with the symbol $\tilde{\boldsymbol{\Phi}}\left(\tau_f,\tau_0\right)$, in its nondimensional form in the CR3BP domain. A more general formulation of this linear mapping includes a generic time $\tau \geq \tau_0$ in place of a specified final time τ_f. Such STM is expressed explicitly as

$$\tilde{\boldsymbol{\Phi}}\left(\tau,\tau_0\right) = \begin{bmatrix}
\frac{\partial\xi}{\partial\xi_0} & \frac{\partial\xi}{\partial\eta_0} & \frac{\partial\xi}{\partial\zeta_0} & \frac{\partial\xi}{\partial\dot{\xi}_0} & \frac{\partial\xi}{\partial\dot{\eta}_0} & \frac{\partial\xi}{\partial\dot{\zeta}_0} \\
\frac{\partial\eta}{\partial\xi_0} & \frac{\partial\eta}{\partial\eta_0} & \frac{\partial\eta}{\partial\zeta_0} & \frac{\partial\eta}{\partial\dot{\xi}_0} & \frac{\partial\eta}{\partial\dot{\eta}_0} & \frac{\partial\eta}{\partial\dot{\zeta}_0} \\
\frac{\partial\zeta}{\partial\xi_0} & \frac{\partial\zeta}{\partial\eta_0} & \frac{\partial\zeta}{\partial\zeta_0} & \frac{\partial\zeta}{\partial\dot{\xi}_0} & \frac{\partial\zeta}{\partial\dot{\eta}_0} & \frac{\partial\zeta}{\partial\dot{\zeta}_0} \\
\frac{\partial\dot{\xi}}{\partial\xi_0} & \frac{\partial\dot{\xi}}{\partial\eta_0} & \frac{\partial\dot{\xi}}{\partial\zeta_0} & \frac{\partial\dot{\xi}}{\partial\dot{\xi}_0} & \frac{\partial\dot{\xi}}{\partial\dot{\eta}_0} & \frac{\partial\dot{\xi}}{\partial\dot{\zeta}_0} \\
\frac{\partial\dot{\eta}}{\partial\xi_0} & \frac{\partial\dot{\eta}}{\partial\eta_0} & \frac{\partial\dot{\eta}}{\partial\zeta_0} & \frac{\partial\dot{\eta}}{\partial\dot{\xi}_0} & \frac{\partial\dot{\eta}}{\partial\dot{\eta}_0} & \frac{\partial\dot{\eta}}{\partial\dot{\zeta}_0} \\
\frac{\partial\dot{\zeta}}{\partial\xi_0} & \frac{\partial\dot{\zeta}}{\partial\eta_0} & \frac{\partial\dot{\zeta}}{\partial\zeta_0} & \frac{\partial\dot{\zeta}}{\partial\dot{\xi}_0} & \frac{\partial\dot{\zeta}}{\partial\dot{\eta}_0} & \frac{\partial\dot{\zeta}}{\partial\dot{\zeta}_0}
\end{bmatrix} = \left[\begin{array}{c|c} \tilde{\boldsymbol{\Phi}}_{\rho\rho} & \tilde{\boldsymbol{\Phi}}_{\rho v} \\ \hline \tilde{\boldsymbol{\Phi}}_{v\rho} & \tilde{\boldsymbol{\Phi}}_{vv} \end{array}\right], \tag{3.17}$$

where the subscript 0 is used as a short notation for the (τ_0) expression and the generic time τ is omitted at the numerator for the sake of conciseness and readiness. As shown in the last part of equation (3.17), the STM is a $\tilde{\boldsymbol{\Phi}} \in \mathbb{R}^{6\times 6}$ matrix composed by four square submatrices 3×3 of partial derivatives; the first pedice indicates

the numerator, the second the denominator, where position quantities are described by the vector $\boldsymbol{\rho}$ and velocities by $\boldsymbol{v}$. Each element of the STM is denoted as φ_{ij} for brevity. To avoid burdening the notation, the following shortenings are also introduced:

$$\tilde{\boldsymbol{X}}_f \triangleq \tilde{\boldsymbol{X}}\left(\tilde{\boldsymbol{X}}\left(\tau_0\right), \tau_f\right), \tag{3.18a}$$

$$\tilde{\boldsymbol{X}}_0 \triangleq \tilde{\boldsymbol{X}}\left(\tau_0\right). \tag{3.18b}$$

Given its role in linearly mapping small changes between subsequent states in time, such STM is often denoted as sensitivity matrix, since it measures how much variations in the final state are sensible to perturbations and changes in the initial state. The STM, therefore, evolves over the trajectory in the same manner as the trajectory itself, and thus has its own 36 ODEs describing this evolution. Therefore,

$$\begin{aligned}
\dot{\tilde{\boldsymbol{\Phi}}}\left(\tau, \tau_0\right) &= \frac{\mathrm{d}}{\mathrm{d}\tau}\tilde{\boldsymbol{\Phi}}\left(\tau, \tau_0\right) = \frac{\mathrm{d}}{\mathrm{d}\tau}\left(\frac{\partial \tilde{\boldsymbol{X}}}{\partial \tilde{\boldsymbol{X}}_0}\right) \\
&= \frac{\partial}{\partial \tilde{\boldsymbol{X}}_0}\left(\frac{\mathrm{d}\tilde{\boldsymbol{X}}}{\mathrm{d}\tau}\right) \\
&= \frac{\partial \dot{\tilde{\boldsymbol{X}}}}{\partial \tilde{\boldsymbol{X}}}\frac{\partial \tilde{\boldsymbol{X}}}{\partial \tilde{\boldsymbol{X}}_0}, \\
\dot{\tilde{\boldsymbol{\Phi}}}\left(\tau, \tau_0\right) &= \tilde{\boldsymbol{A}}\left(\tau\right)\tilde{\boldsymbol{\Phi}}\left(\tau, \tau_0\right).
\end{aligned} \tag{3.19}$$

The state evolution of the STM is governed by an ODE composed by a complete Jacobian matrix $\tilde{\boldsymbol{A}}\left(\tau\right)$ and the STM itself. The Jacobian matrix carries out the same task of the one in equation (3.6). However, in the full CR3BP state equation, $\tilde{\boldsymbol{A}} \in \mathbb{R}^{6\times 6}$ is composed by four square 3×3 submatrices, similarly to the STM,

$$\tilde{\boldsymbol{A}}\left(\tau\right) = \left[\begin{array}{c|c} \boldsymbol{0} & \boldsymbol{I} \\ \hline \boldsymbol{U} & \boldsymbol{\Omega} \end{array}\right], \tag{3.20}$$

or, in explicit form,

$$\tilde{\boldsymbol{A}}(\tau) = \begin{bmatrix} 0 & 0 & 0 & 1 & 0 & 0 \\ 0 & 0 & 0 & 0 & 1 & 0 \\ 0 & 0 & 0 & 0 & 0 & 1 \\ \mathscr{U}_{\xi\xi} & \mathscr{U}_{\xi\eta} & \mathscr{U}_{\xi\zeta} & 0 & 2 & 0 \\ \mathscr{U}_{\eta\xi} & \mathscr{U}_{\eta\eta} & \mathscr{U}_{\eta\zeta} & -2 & 0 & 0 \\ \mathscr{U}_{\zeta\xi} & \mathscr{U}_{\zeta\eta} & \mathscr{U}_{\zeta\zeta} & 0 & 0 & 0 \end{bmatrix}. \tag{3.21}$$

In general, $\tilde{\boldsymbol{A}}(\tau)$ is a function of the state of the reference trajectory. To verify the matrix elements, one can simply double-check the set of equations (3.2). The explicit form of the second partial derivatives of the pseudopotential is omitted here for brevity, but are derived and presented in Appendix A.

3.3 Single shooting procedure

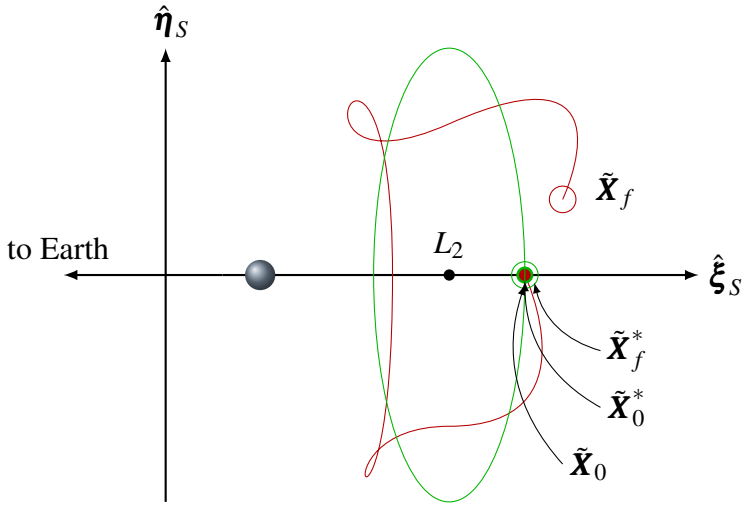

Fig. 3.5 Single shooting DC procedure from a generic state $\tilde{\boldsymbol{X}}$ to a desired reference state $\tilde{\boldsymbol{X}}^*$ for a planar Lyapunov orbit in the CR3BP domain - erroneous initial velocities

As anticipated, the "shooting" procedure is nothing more than adjusting some initial conditions until a targeted set of specified end conditions is respected, in the

form of a TPBVP. This recursive method requires cyclically targeting the desired final state and, while possibly computing corrections for undesired terminal deviations, updating the initial state at each r-th step. However, not all the initial values may be allowed to vary, and some final conditions may be allowed to acquire any feasible value. For example, the non-converged tentative Lyapunov in Figure 3.5 has been modified to have the initial guess with an initial position already coinciding with the desired one. Therefore, the divergence between the desired final state $\tilde{\boldsymbol{X}}_f^*$ and the actual one $\tilde{\boldsymbol{X}}_f$ should be imputed to the initial guesses for the sole velocities, and thus only these should be allowed to vary during the correction, keeping the initial position components as fixed.

Therefore, the free-variable vector $\tilde{\boldsymbol{X}}_0 \in \mathbb{R}^{n\times 1}$ is in the form

$$\tilde{\boldsymbol{X}}_0 = \{X_1, X_2, \ldots, X_n\}^T \tag{3.22}$$

and may contain state elements, such as position, velocity, and integration times. The constraint vector, on the other hand, targets the desired final quantities. For the purposes of the present analysis, the targeted quantities are all those referred to producing the POs in the CR3BP, and therefore $\boldsymbol{\chi}\left(\tilde{\boldsymbol{X}}_f\right) \in \mathbb{R}^{m\times 1}$ accounts the differences between actual and desired final states. A complete constraint vector is

$$\boldsymbol{\chi}\left(\tilde{\boldsymbol{X}}_f\right) = \{\chi_1, \chi_2, \ldots, \chi_m\}^T = \begin{Bmatrix} \xi - \xi^* \\ \eta - \eta^* \\ \zeta - \zeta^* \\ \dot{\xi} - \dot{\xi}^* \\ \dot{\eta} - \dot{\eta}^* \\ \dot{\zeta} - \dot{\zeta}^* \end{Bmatrix}. \tag{3.23}$$

The correction method now shifts to search for a specified initial state $\tilde{\boldsymbol{X}}_0^*$ that satisfies all constraints, $\boldsymbol{\chi}\left(\tilde{\boldsymbol{X}}_f^*\right) = \boldsymbol{0}$. A first order Taylor expansion of the constraint vector is performed to understand how to update the free-variable vector. Specifically, this process allows determining the change in the constraint vector resulting from a given change in the design vector. Let $\tilde{\boldsymbol{X}}$ be the terminal state vector at a generic time $\tau \geq \tau_0$, then

$$\boldsymbol{\chi}\left(\tilde{\boldsymbol{X}}\right) = \boldsymbol{\chi}\left(\tilde{\boldsymbol{X}}_0\right) + \frac{\partial \boldsymbol{\chi}\left(\tilde{\boldsymbol{X}}_0\right)}{\partial \tilde{\boldsymbol{X}}}\left(\tilde{\boldsymbol{X}} - \tilde{\boldsymbol{X}}_0\right), \tag{3.24}$$

where the partial derivatives of the constraints with respect to the forward-in-time free-variable vector quantities form again a Jacobian matrix $\tilde{\boldsymbol{J}}\left(\boldsymbol{\chi}\left(\tilde{\boldsymbol{X}}_0\right),\tilde{\boldsymbol{X}}\right)\in\mathbb{R}^{m\times n}$,

$$\frac{\partial\boldsymbol{\chi}\left(\tilde{\boldsymbol{X}}_0\right)}{\partial\tilde{\boldsymbol{X}}}=\tilde{\boldsymbol{J}}\left(\boldsymbol{\chi}\left(\tilde{\boldsymbol{X}}_0\right),\tilde{\boldsymbol{X}}\right)=\begin{bmatrix}\dfrac{\partial\chi_1}{\partial\tilde{X}_1} & \dfrac{\partial\chi_1}{\partial\tilde{X}_2} & \cdots & \dfrac{\partial\chi_1}{\partial\tilde{X}_n}\\ \dfrac{\partial\chi_2}{\partial\tilde{X}_1} & \dfrac{\partial\chi_2}{\partial\tilde{X}_2} & \cdots & \dfrac{\partial\chi_2}{\partial\tilde{X}_n}\\ \vdots & \vdots & \ddots & \vdots\\ \dfrac{\partial\chi_m}{\partial\tilde{X}_1} & \dfrac{\partial\chi_m}{\partial\tilde{X}_2} & \cdots & \dfrac{\partial\chi_m}{\partial\tilde{X}_n}\end{bmatrix}. \tag{3.25}$$

Such definition closely resembles the one seen in equation (3.17) for the STM. The Taylor expansion can be written in an iterative form in which the subsequent step $r+1$ is function of the previous r-th one, namely

$$\boldsymbol{\chi}\left(\tilde{\boldsymbol{X}}_{r+1}\right)=\boldsymbol{\chi}\left(\tilde{\boldsymbol{X}}_r\right)+\frac{\partial\boldsymbol{\chi}\left(\tilde{\boldsymbol{X}}_r\right)}{\partial\tilde{\boldsymbol{X}}_{r+1}}\left(\tilde{\boldsymbol{X}}_{r+1}-\tilde{\boldsymbol{X}}_r\right). \tag{3.26}$$

Shortenings are introduced also in this case to avoid burdening the notation:

$$\boldsymbol{\chi}_r\triangleq\boldsymbol{\chi}\left(\tilde{\boldsymbol{X}}_r\right), \tag{3.27a}$$

$$\tilde{\boldsymbol{J}}\left(\boldsymbol{\chi}_r\right)\triangleq\tilde{\boldsymbol{J}}\left(\boldsymbol{\chi}\left(\tilde{\boldsymbol{X}}_r\right),\tilde{\boldsymbol{X}}_{r+1}\right). \tag{3.27b}$$

If a solution exists, then $\boldsymbol{\chi}_{r+1}=\boldsymbol{0}$ and an iterative solution takes the form

$$\boldsymbol{\chi}_r+\left[\tilde{\boldsymbol{J}}\left(\boldsymbol{\chi}_r\right)\right]\left(\tilde{\boldsymbol{X}}_{r+1}-\tilde{\boldsymbol{X}}_r\right)=\boldsymbol{0}. \tag{3.28}$$

Therefore one can compute at each iteration the state of the design vector $\tilde{\boldsymbol{X}}_r$ and the updated value of the constraint vector $\boldsymbol{\chi}_r$ derived directly from integrating all EOMs from $\tilde{\boldsymbol{X}}_r$, as in the following:

$$\tilde{\boldsymbol{X}}_{r+1}=\tilde{\boldsymbol{X}}_r-\left[\tilde{\boldsymbol{J}}\left(\boldsymbol{\chi}_r\right)\right]^{-1}\boldsymbol{\chi}_r. \tag{3.29}$$

If there are more variables than constraints $n>m$, the minimum norm update equation is used in place of equation (3.29), namely

$$\tilde{\boldsymbol{X}}_{r+1} = \tilde{\boldsymbol{X}}_r - \left[\tilde{\boldsymbol{J}}(\boldsymbol{\chi}_r)\right]^T \left[\tilde{\boldsymbol{J}}(\boldsymbol{\chi}_r)\tilde{\boldsymbol{J}}(\boldsymbol{\chi}_r)^T\right]^{-1} \boldsymbol{\chi}_r, \tag{3.30}$$

which guides the next solution to be as close as possible to the initial guess $\tilde{\boldsymbol{X}}_r$ among the infinite possible ones. A relaxation parameter κ_R aids the convergence, allowing smaller corrections to be performed at each iteration. For planar LOs a $\kappa_R \approx 0.5$ is sufficient, whereas more complex trajectories such as NRHOs are robustly computed with a single-shooting method with $\kappa_R \approx 0.2$. Therefore the modified iterative update processes, including relaxation parameters, are

$$\tilde{\boldsymbol{X}}_{r+1} = \tilde{\boldsymbol{X}}_r - \kappa_R \cdot \left[\tilde{\boldsymbol{J}}(\boldsymbol{\chi}_r)\right]^{-1} \boldsymbol{\chi}_r, \qquad \text{if } n = m, \tag{3.31a}$$

$$\tilde{\boldsymbol{X}}_{r+1} = \tilde{\boldsymbol{X}}_r - \kappa_R \cdot \left[\tilde{\boldsymbol{J}}(\boldsymbol{\chi}_r)\right]^T \left[\tilde{\boldsymbol{J}}(\boldsymbol{\chi}_r)\tilde{\boldsymbol{J}}(\boldsymbol{\chi}_r)^T\right]^{-1} \boldsymbol{\chi}_r, \qquad \text{if } n > m. \tag{3.31b}$$

3.3.1 Variable-time vs fixed-time correction scheme

As anticipated, the design vector $\tilde{\boldsymbol{X}}_0$ comprises state variables and may include the integration time. In the case of interest, such integration time would be the period to complete a whole revolution about a specific PO, which may be imposed (requested/known) or guessed. A complete free-variable vector has the form of

$$\tilde{\boldsymbol{X}}_0 = \left\{\xi \quad \eta \quad \zeta \quad \dot{\xi} \quad \dot{\eta} \quad \dot{\zeta} \quad \tau\right\}^T, \tag{3.32}$$

where τ, specifically for this analysis, is the nondimensional period of the PO, which coincides also with the following definition

$$\tau = \tau_f - \tau_0. \tag{3.33}$$

A complete constraint vector coincides with the one in equation (3.23); indeed, it is not helpful to include the time constraint in this vector, since it would be enough to avoid including it in the free-variable vector and specify the period of the PO directly. By using such values one has, for the Jacobian, the derivative of state variables with respect to other state variables; therefore, there are seven free variables and six constraints, which lead to a further column from the Jacobian in equation (3.25), making $\tilde{\boldsymbol{J}} \in \mathbb{R}^{6\times 7}$ in its complete form

$$\tilde{\boldsymbol{J}}\left(\boldsymbol{\chi}\left(\tilde{\boldsymbol{X}}_0\right),\tilde{\boldsymbol{X}}_f\right)=\begin{bmatrix}\frac{\partial\xi_f}{\partial\xi_0} & \frac{\partial\xi_f}{\partial\eta_0} & \frac{\partial\xi_f}{\partial\zeta_0} & \frac{\partial\xi_f}{\partial\dot{\xi}_0} & \frac{\partial\xi_f}{\partial\dot{\eta}_0} & \frac{\partial\xi_f}{\partial\dot{\zeta}_0} & \frac{\partial\xi_f}{\partial\tau}\\ \frac{\partial\eta_f}{\partial\xi_0} & \frac{\partial\eta_f}{\partial\eta_0} & \frac{\partial\eta_f}{\partial\zeta_0} & \frac{\partial\eta_f}{\partial\dot{\xi}_0} & \frac{\partial\eta_f}{\partial\dot{\eta}_0} & \frac{\partial\eta_f}{\partial\dot{\zeta}_0} & \frac{\partial\eta_f}{\partial\tau}\\ \frac{\partial\zeta_f}{\partial\xi_0} & \frac{\partial\zeta_f}{\partial\eta_0} & \frac{\partial\zeta_f}{\partial\zeta_0} & \frac{\partial\zeta_f}{\partial\dot{\xi}_0} & \frac{\partial\zeta_f}{\partial\dot{\eta}_0} & \frac{\partial\zeta_f}{\partial\dot{\zeta}_0} & \frac{\partial\zeta_f}{\partial\tau}\\ \frac{\partial\dot{\xi}_f}{\partial\xi_0} & \frac{\partial\dot{\xi}_f}{\partial\eta_0} & \frac{\partial\dot{\xi}_f}{\partial\zeta_0} & \frac{\partial\dot{\xi}_f}{\partial\dot{\xi}_0} & \frac{\partial\dot{\xi}_f}{\partial\dot{\eta}_0} & \frac{\partial\dot{\xi}_f}{\partial\dot{\zeta}_0} & \frac{\partial\dot{\xi}_f}{\partial\tau}\\ \frac{\partial\dot{\eta}_f}{\partial\xi_0} & \frac{\partial\dot{\eta}_f}{\partial\eta_0} & \frac{\partial\dot{\eta}_f}{\partial\zeta_0} & \frac{\partial\dot{\eta}_f}{\partial\dot{\xi}_0} & \frac{\partial\dot{\eta}_f}{\partial\dot{\eta}_0} & \frac{\partial\dot{\eta}_f}{\partial\dot{\zeta}_0} & \frac{\partial\dot{\eta}_f}{\partial\tau}\\ \frac{\partial\dot{\zeta}_f}{\partial\xi_0} & \frac{\partial\dot{\zeta}_f}{\partial\eta_0} & \frac{\partial\dot{\zeta}_f}{\partial\zeta_0} & \frac{\partial\dot{\zeta}_f}{\partial\dot{\xi}_0} & \frac{\partial\dot{\zeta}_f}{\partial\dot{\eta}_0} & \frac{\partial\dot{\zeta}_f}{\partial\dot{\zeta}_0} & \frac{\partial\dot{\zeta}_f}{\partial\tau}\end{bmatrix}. \tag{3.34}$$

As presented, the 6×6 submatrix in equation (3.34) starting from the first row and column coincides exactly with the definition of the STM in equation (3.17). The last column contains the derivative of the state quantities, namely velocities and accelerations. Such values are determined by evaluating the EOMs at the final state along the integrated trajectory, namely $\tilde{\boldsymbol{X}}_f$. A compact form for Jacobian in equation (3.34) uses the STM notation as follows

$$\tilde{\boldsymbol{J}}\left(\boldsymbol{\chi}\left(\tilde{\boldsymbol{X}}_0\right),\tilde{\boldsymbol{X}}_f\right)=\begin{bmatrix}\varphi_{11} & \varphi_{12} & \varphi_{13} & \varphi_{14} & \varphi_{15} & \varphi_{16} & \dot{\xi}_f\\ \varphi_{21} & \varphi_{22} & \varphi_{23} & \varphi_{24} & \varphi_{25} & \varphi_{26} & \dot{\eta}_f\\ \varphi_{31} & \varphi_{32} & \varphi_{33} & \varphi_{34} & \varphi_{35} & \varphi_{36} & \dot{\zeta}_f\\ \varphi_{41} & \varphi_{42} & \varphi_{43} & \varphi_{44} & \varphi_{45} & \varphi_{46} & \ddot{\xi}_f\\ \varphi_{51} & \varphi_{52} & \varphi_{53} & \varphi_{54} & \varphi_{55} & \varphi_{56} & \ddot{\eta}_f\\ \varphi_{61} & \varphi_{62} & \varphi_{63} & \varphi_{64} & \varphi_{65} & \varphi_{66} & \ddot{\zeta}_f\end{bmatrix}. \tag{3.35}$$

Such a correction scheme is named variable-time shooting method and evaluates, along the state evolution itself, the influence of the integration time on the final state. The procedure is also known as Variable-Time Differential Correction (VTDC). If the integration time is not a free-variable quantity, then the Jacobian coincides in its full form with the STM and the correction method is indicated as fixed-time, or Fixed-Time Differential Correction (FTDC).

3.3.2 CR3BP planar Lyapunov orbit computation

Before expressing the underlying procedures to compute POs, two useful preliminary considerations are noteworthy. First off, as anticipated, the CR3BP dynamical model is autonomous and, therefore, time-invariant. Such consideration implies that a correct initial state $\tilde{\boldsymbol{X}}_0^*$ integrated over a whole period forward in time τ provides the same terminal conditions when integrated backward in time $-\tau$, by opportunely inverting the correct velocity non-null components.

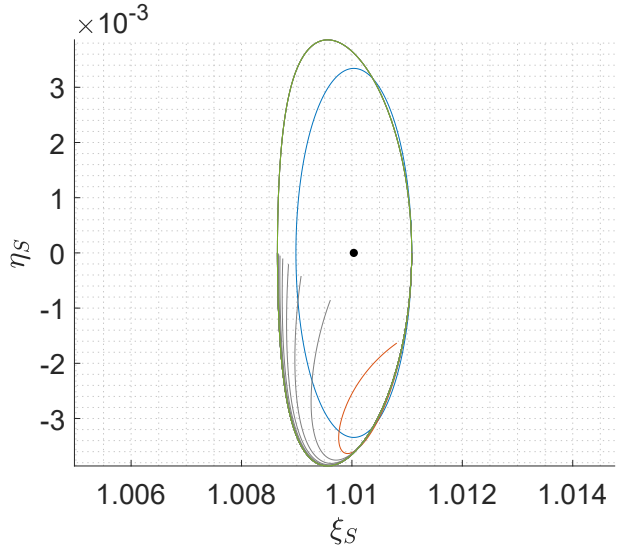

Fig. 3.6 SEL2 Lyapunov orbit convergence steps in the CR3BP

On the other hand, another important observation comes from the work of Roy [34] on the mirror theorem; POs in the CR3BP dynamical model that cross a specific plane perpendicularly twice possess symmetrical configurations with respect to this specific plane. For example, Figure 3.6 shows the convergence process for a SEL_2 LO from the analytical approximation (with $A_y = 5 \times 10^5$ km), in blue, to the converged CR3BP LO, in green. The red trajectory is the non-converged NL integration having as initial state, $\tilde{\boldsymbol{X}}_0$, the analytical approximate one, $\tilde{\boldsymbol{X}}_0^a$. All the black trajectories are iterations referred to the first half of the LO to guarantee convergence. Once the half LO is computed, which clearly shows symmetric properties with respect to the $\hat{\boldsymbol{\xi}}_S - \hat{\boldsymbol{\zeta}}_S$ plane at the initial time, the complete orbit is readily obtained in a single iteration by doubling the integration time.

These two observations imply that implementing the shooting method only for half-period is an accepted and efficient procedure to compute the complete PO.

For the simple computation of a periodic LO in the CR3BP, the design vector and the constraint vector have to be constructed accordingly to the information that such PO provides. A LO lies on the $\hat{\boldsymbol{\xi}}_S - \hat{\boldsymbol{\eta}}_S$ plane in the CR3BP synodic Reference System (RS), and therefore does not have quantities in the out-of-plane direction, nor for position ζ nor for velocity $\dot{\zeta}$. Due to the abovementioned considerations, when the LO crosses the $\hat{\boldsymbol{\xi}}_S - \hat{\boldsymbol{\zeta}}_S$ it shall not have also velocities along the $\hat{\boldsymbol{\xi}}_S$ direction, thus $\dot{\tilde{\boldsymbol{\xi}}}_0 = \dot{\tilde{\boldsymbol{\xi}}}_{\tau_f/2} = 0$. Therefore, a simple targeting scheme would require to check if, after half orbit, the plane crossing is again perpendicular. The constraint vector is therefore simply

$$\boldsymbol{\chi}\left(\tilde{\boldsymbol{X}}_f\right) = \begin{Bmatrix} \eta \\ \dot{\xi}_f \end{Bmatrix} = \mathbf{0}, \tag{3.36}$$

whereas the only free-variable quantities allowed to change and be corrected are the starting position along the $\hat{\boldsymbol{\xi}}_S$ axis, the initial velocity along the $-\hat{\boldsymbol{\eta}}_S$ direction (for initial ξ_0 positions laying on the positive side of Lagrangian Point L_2 (L_2)) and, if needed, the integration time,

$$\tilde{\boldsymbol{X}}_0 = \begin{Bmatrix} \xi \\ \dot{\eta} \\ \tau \end{Bmatrix}. \tag{3.37}$$

The Jacobian can be directly computed by calculating the associated partial derivatives or can be extracted from the complete one in equation (3.35) by taking the appropriate rows and columns. In particular, for the planar Lyapunov case, rows $\{2,4\}$ corresponding to $\left\{\eta_f, \dot{\xi}_f\right\}$ shall be extracted and then reduced only to the columns $\{1,5,7\}$, corresponding to $\{\xi_0, \dot{\eta}_0, \tau\}$

$$\tilde{\boldsymbol{J}} = \begin{bmatrix} \varphi_{21} & \varphi_{25} & \dot{\eta}_f \\ \varphi_{41} & \varphi_{45} & \ddot{\xi}_f \end{bmatrix}. \tag{3.38}$$

Figure 3.7 shows a complete LO family which has been computed by a continuation strategy, both for the Earth-Moon Lagrangian Point L_2 (EML_2) and SEL_2 binary system, respectively to the left and to the right. After computing the analytical LOs with $A_y = \left\{1 \times 10^4, 1 \times 10^5\right\}$ km (elliptical black shapes centered in L_2), respectively, the ξ_0 position is increased by a small finite step $d\xi$ and is kept fixed

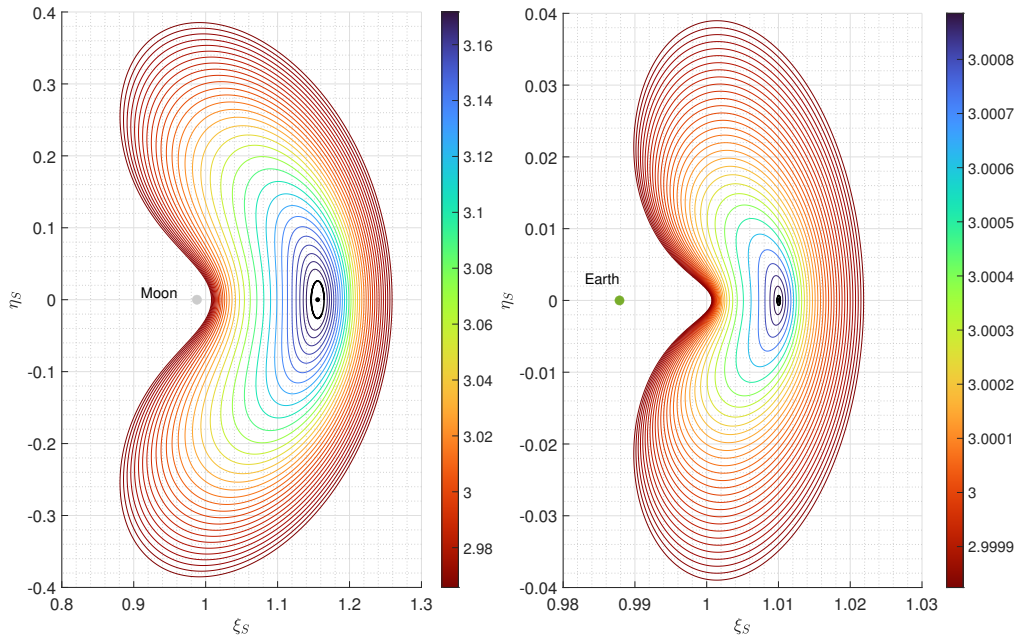

Fig. 3.7 Lyapunov orbits family centered in L_2 - EM (left), SE (right) binary system

during the DC procedure, allowing only the initial velocity along the $\hat{\boldsymbol{\eta}}_S$ axis and the integration time τ to vary. Due to nonlinearities, the convergence robustness is improved when the varying ξ_0 point is the one that provides smaller variations while increasing the orbit shape, namely the positive coordinate ξ beyond L_2. The LOs show decreasing values of the $\mathscr{J}_C$ the further they depart from L_2 itself. Indeed, greater energy is required to move on more complex geometries. At the same time, smaller LOs closely resemble the analytical one, in an ellipse-like shape, whereas larger ones show their distinctive cashew shape.

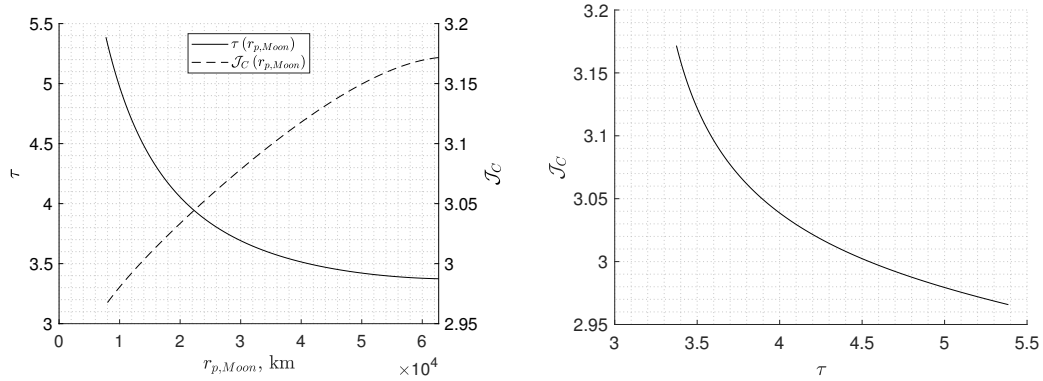

Fig. 3.8 EML2 LOs family period τ and Jacobi Constant $\mathscr{J}_C$ as a function of their minimum periapsis-like distance with respect to the Moon (left); EML2 LOs τ vs $\mathscr{J}_C$ (right)

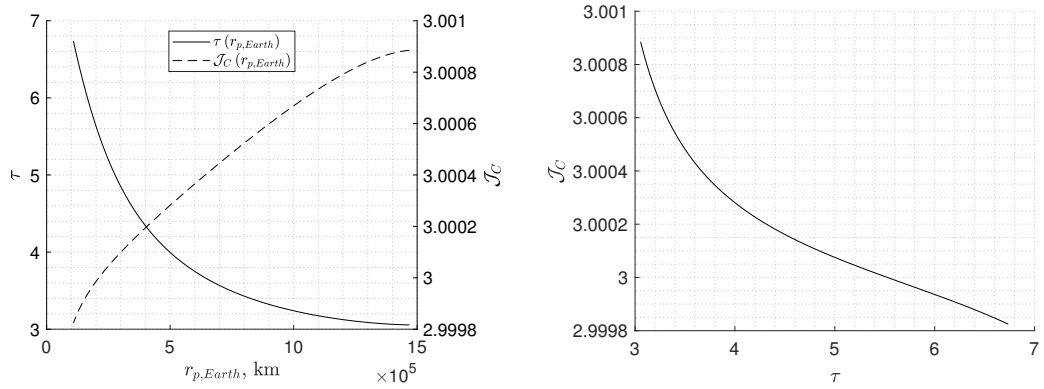

Fig. 3.9 SEL2 LOs family period τ and Jacobi Constant $\mathscr{J}_C$ as a function of their minimum periapsis-like distance with respect to the Earth (left); SEL2 LOs τ vs $\mathscr{J}_C$ (right)

Figures 3.8 and 3.9, instead, represent specific characteristics for each of the represented LOs. Both Figures show, on the left, the nondimensional period τ and the Jacobi Constant $\mathscr{J}_C$ plotted versus the minimum distance with respect to the closest primary, namely the periapsis-like distance with respect to the Moon in the EML_2 scenario and the Earth in the SEL_2. Here smaller LOs, those farther from the primary and therefore closer to L_2, show a smaller period, as intuitively foreseeable from the Two-Body Problem (2BP) background, and have the highest value for the Jacobi Constant. On the other hand, larger LOs show longer periods and lower values of $\mathscr{J}_C$; indeed, a SC on such higher orbits would have greater mechanical energy compared to the ones close to L_2 itself. Please note, however, that bigger LOs require greater initial velocities in their initial state $\tilde{\boldsymbol{X}}_0$, in contrast with the Keplerian trend.

3.3.3 CR3BP three-dimensional NRHO computation

Robert W. Farquhar, in his Ph.D. dissertation in 1966 [58], first used the term Halo to define the particular shape that such three-dimensional POs, in the CR3BP domain, had with respect to the closest primary when seen in perspective. As per the LOs, also these three-dimensional HOs are characterized by a periodic behavior in the CR3BP and complete families can be computed. HOs derive from a bifurcation from the planar Lyapunov POs at specific Jacobi Constant levels depending on the binary system in consideration [70]. Among all those HOs, the NRHOs [71] are of particular interest in this thesis due to their potential use in future spaceflight application [48]. For example, the future Lunar Orbital Platform-Gateway (LOP-

G), formerly named Deep Space Gateway (DSG), is expected to be placed close to the Moon, on a quasi-stable orbit around, even though quite far from, EML_2. The selected potential operational orbit is a Southern L2 NRHO with 9:2 Lunar Synodic Resonance, which minimizes the required station-keeping maneuvers while eliminating eclipses almost completely [72].

The synodic resonance (S_R) is an important characteristic for such NRHOs; an $x : y$ synodic resonance, for example, implies that a SC on such 3D PO completes x revolutions while the closest primary performs y complete periods. In the EM system, the Moon synodic month, i.e. the time in which the Moon returns at the same relative position with respect to the Earth and the Sun, is equal to $\mathscr{T}_{syn} = 29.53059$ days [73]. On the other hand, the Moon's period with respect to a fixed star is the sidereal month, which is easily computed via the 2BP definition for the orbital period, spanning

$$\mathscr{T}_{sid} = 2\pi\sqrt{\frac{(\ell^*)^3}{\mu_E + \mu_\ell}} = 27.32166 \text{ days}\,. \tag{3.39}$$

The targeting scheme for an HO requires to include the third dimension both in the design vector and in the constraint vector. Namely, the planar bifurcation happens because the initial position has a positive or negative out-of-plane component ζ_0, respectively for northern and southern HOs, where however the out-of-plane velocity is constrained to be null. These two additions imply that, for a generic HO, the constraint vector is

$$\boldsymbol{\chi}\left(\tilde{\boldsymbol{X}}_f\right) = \begin{Bmatrix} \eta \\ \dot{\xi}_f \\ \dot{\zeta}_f \end{Bmatrix} = \boldsymbol{0}\,, \tag{3.40}$$

whereas the only free-variable quantities allowed to change and be corrected are the starting position along the $\hat{\boldsymbol{\xi}}_S$ axis, the initial velocity along the $-\hat{\boldsymbol{\eta}}_S$ direction and, if needed, the integration time

$$\tilde{\boldsymbol{X}}_0 = \begin{Bmatrix} \xi \\ \zeta \\ \dot{\eta} \\ \Delta\tau \end{Bmatrix}. \tag{3.41}$$

The Jacobian gains a further row and column with respect to the Lyapunov case in equation (3.38)

$$\tilde{\boldsymbol{J}} = \begin{bmatrix} \varphi_{21} & \varphi_{23} & \varphi_{25} & \dot{\eta}_f \\ \varphi_{41} & \varphi_{43} & \varphi_{45} & \ddot{\xi}_f \\ \varphi_{61} & \varphi_{63} & \varphi_{65} & \ddot{\zeta}_f \end{bmatrix} . \tag{3.42}$$

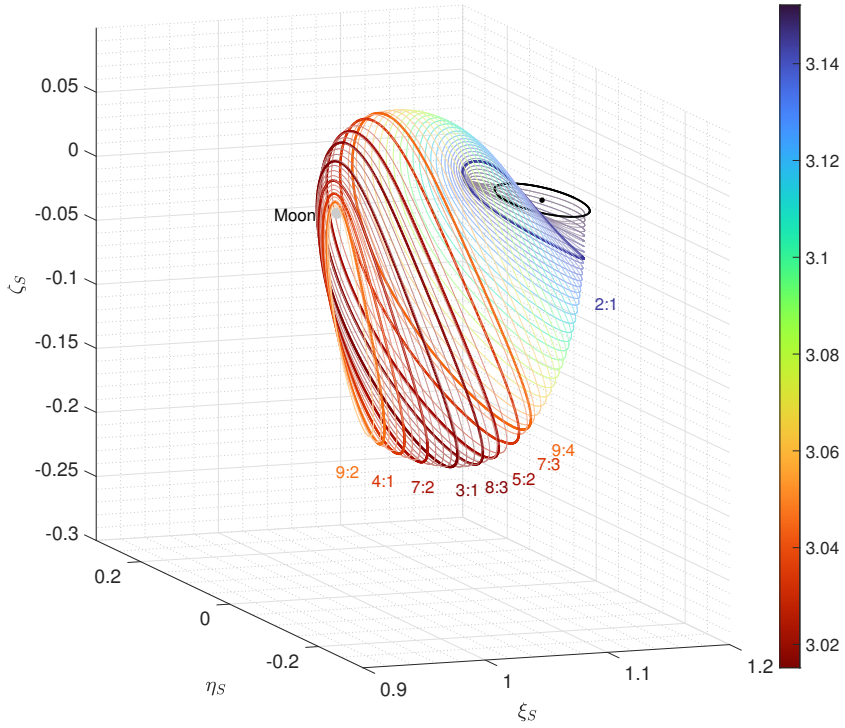

Fig. 3.10 EML2 NRHOs family

Figure 3.10 shows a complete family of HOs starting from the planar bifurcation, from a LO with approximately $A_y \approx 3 \times 10^4$ km, up to the closest possible NRHO (with minimum periselenium allowable value). Here the continuation strategy has to follow separate steps to improve convergence. For the NRHOs, it could be more convenient to increase the out-of-plane position ζ_0 by a small fixed step size $\delta\zeta$, allowing the VTDC to find the corresponding ξ_0 and τ. On the other hand, when the HO reaches a particularly vertical configuration and shows larger changes in the $\hat{\boldsymbol{\xi}}_S$ axial direction compared to the changes in the out-of-plane direction $\hat{\boldsymbol{\zeta}}_S$ (around $\mathscr{J}_C \approx 3.02 \div 3.05$ in Figure 3.10), the search should fix the ξ_0 as per the Lyapunov case and allow the convergence with ζ_0 in the free-variable vector. Some orbits are highlighted to indicate their particular synodic resonance, from the lowest one

(2:1) to the highest one (9:2). Differently from the Lyapunov case, the values for the Jacobi constant do not show a monotonic trend; HOs close to EML_2 have the lowest level of energy, showing high $\mathscr{J}_C$ values; the more the HOs evolve in their three-dimensional shape, detaching from EML_2 and reducing their periselenium, the lower the Jacobi Constant become, showing its minimum value with initial state

$$\tilde{\boldsymbol{X}}_0 = \{1.082893,\ 0.000000,\ -0.202320,\ 0.000000,\ -0.200962,\ 0.000000\}^T\ ,$$
$$\tau = 2.382552\,,\ \mathscr{J}_C = 3.015178\,.$$

Incidentally, such $\tilde{\boldsymbol{X}}_0$ is really close to the 3:1 synodic resonance condition. After this point, by further reducing the periselenium, the Jacobi Constant increases again, showing that, for example, 7:2, 4:1, and 9:2 synodic resonant orbits are slightly less energy-demanding than the 3:1 one. The HOs with increasing $\mathscr{J}_C$ value while decreasing their nondimensional period are named NRHOs.

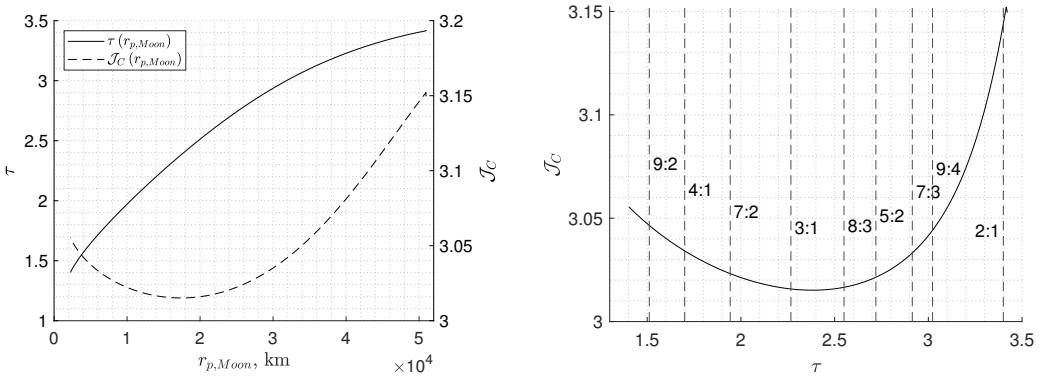

Fig. 3.11 EML2 NRHOs family period τ and Jacobi Constant $\mathscr{J}_C$ as a function of their minimum periapsis-like distance to the Moon (left); EML2 NRHOs τ vs $\mathscr{J}_C$ (right)

The same considerations are provided in Figure 3.11. The Jacobi constant trend is shown on the left, showing that HOs have shorter periods the lower their periselenium is. Table 3.1 provides the $\mathscr{J}_C$ and τ pairs for each specific S_R. Even if such values may diverge among studies even only due to minimal differences in a gravitational parameter, the underlying values for the 9:2 S_R case, for example, well match the NASA NRHO reference [72] and a similar research [74].

Figures 3.12 and 3.13 show a top-view and 3D view of LOs and HOs families with their respective Jacobi Contsant contours, whereas Figure 3.14 depicts their period and Jacobi constant trends by showing the bifurcation behaviors. Figures 3.12 and 3.13 use bolded contours to show all the S_R in Table 3.1.

Table 3.1 Integer to integer synodic resonance S_R for Lyapunov (left) and Halo (right) orbits in the EML2 scenario - corresponding Jacobi constants and nondimensional periods

S_R	$\mathscr{J}_C$	τ	S_R	$\mathscr{J}_C$	τ
2:1	3.158891	3.400199	2:1	3.144110	3.400199
9:5	3.064890	3.777999	9:4	3.044273	3.022399
7:4	3.050875	3.885941	7:3	3.033007	2.914456
5:3	3.031240	4.080238	5:2	3.021451	2.720159
8:5	3.017894	4.250248	8:3	3.016577	2.550149
3:2	3.000502	4.533598	3:1	3.015768	2.266799
7:5	2.985168	4.857427	7:2	3.023184	1.942971
4:3	2.975631	5.100298	4:1	3.034181	1.700099
9:7	2.968995	5.289198	9:2	3.046491	1.511199

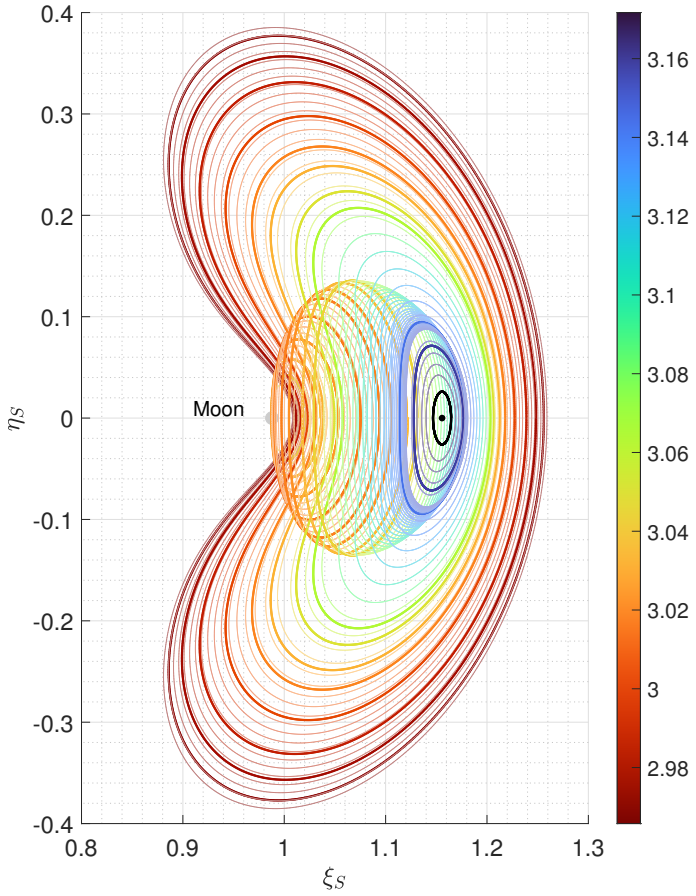

Fig. 3.12 EML2 LOs and NRHOs family

Table 3.1 conveniently shows that the 2:1 S_R is the only one shared between the Lyapunov and the Halo families within a reasonable[1] integer to integer ratio. Indeed,

[1] Other higher integer to integer pairs of synodic resonances are shared between the two families, such as 499:250, 333:167, up to 500:251, for example.

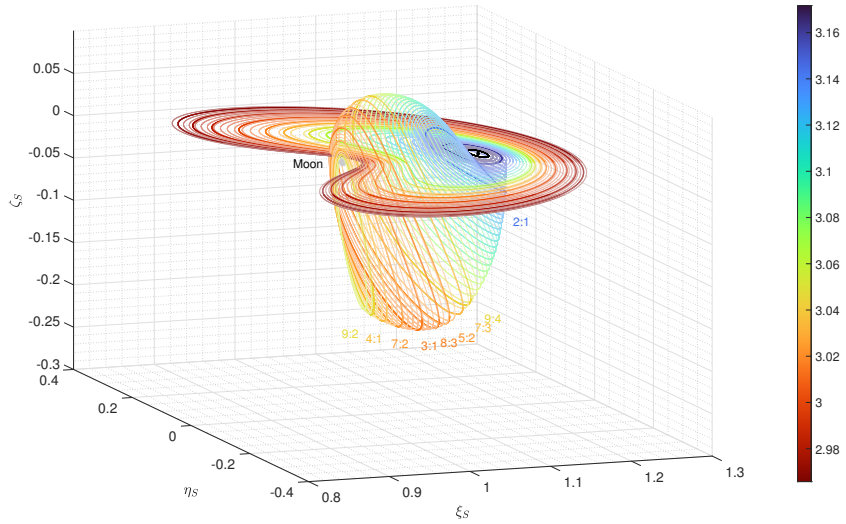

Fig. 3.13 EML2 LOs and NRHOs family - 3D view

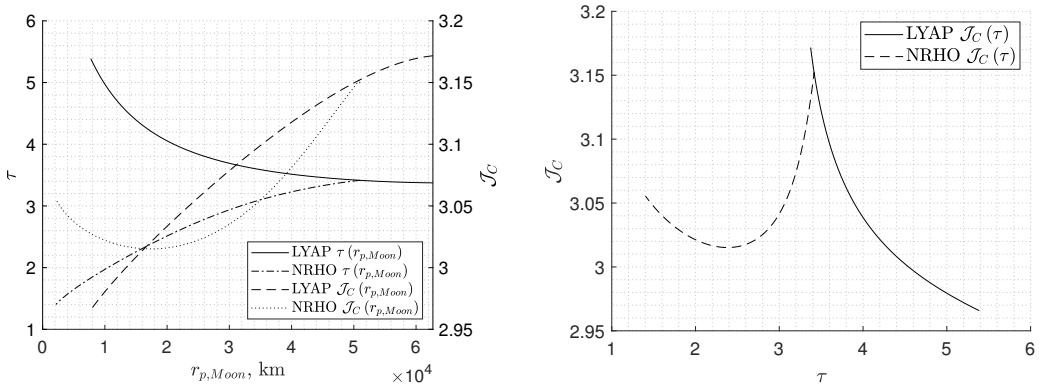

Fig. 3.14 EML2 LOs and NRHOs families period τ and Jacobi Constant $\mathcal{J}_C$ as a function of their minimum periapsis-like distance with respect to the Moon (left); EML2 LOs and NRHOs τ vs $\mathcal{J}_C$ (right)

as per Figure 3.14, HOs monotonically reduce their nondimensional period after bifurcating from the planar case, thus increasing their resonance value up to the 9:2 S_R, whereas Lyapunov orbits monotonically increase their nondimansional periods moving towards lower synodic resonance ratios such as 3:2, 4:3, and so on.

Although beyond the scope of the present thesis, the following paragraph outlines a brief representation of the bifurcation phenomenon from the planar LOs towards the HOs. In particular, Figure 3.15 shows, for both the planar and three-dimensional cases, the state evolution of a SC on a specific PO, identified by its specific key-colored Jacobi value. The x-axis contains the SC distance from the Moon in the

EM synodic Reference Frame (RF), whereas the y-axis shows the SC velocity in the same frame.

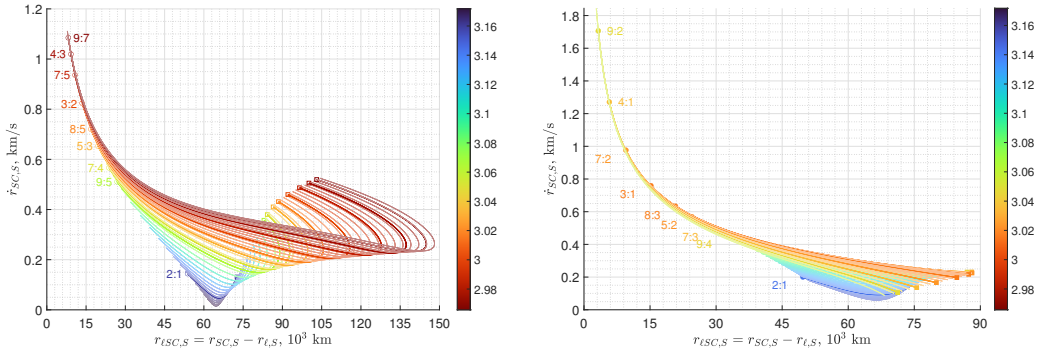

Fig. 3.15 EML2 phase space representation of LOs (left) and HOs (right)

The square marks, respectively hollow and filled for LOs and HOs, represent the τ_0 condition when $\eta = 0$, whereas the dots identify the conditions after half PO, when again $\eta = 0$. When a PO matches a reasonable integer to integer S_R, the corresponding line is bolded and the $x : y$ S_R is depicted alongside. A merged view of the two phase space representations is provided in Figure 3.16, showing again a maximum higher energy level for LOs with a particularly reduced periselenium compared to the HOs one. However, NRHOs show a peak velocity close to the periselenium that is unmatched against LOs.

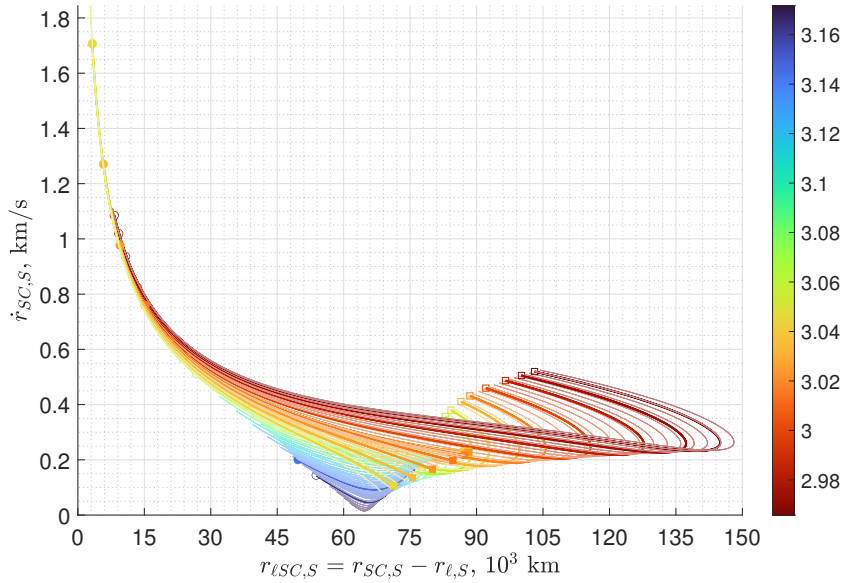

Fig. 3.16 EML2 phase space joint representation of LOs and HOs

Figure 3.17 shows the trend of the initial and half-orbit phase space conditions for the two families. Here the bifurcation phenomenon is particularly visible, and happens at specific values of distance and velocity (which, in turn, correspond to specific synodic initial conditions).

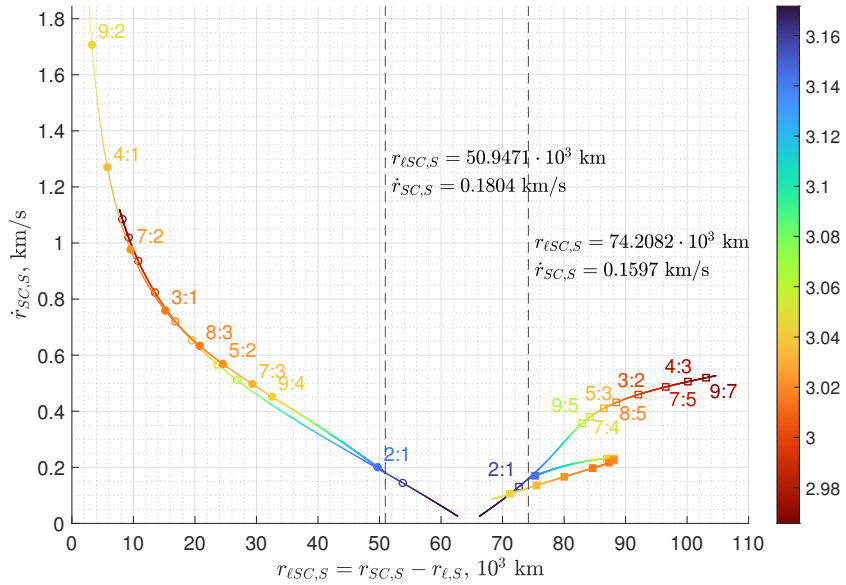

Fig. 3.17 EML2 phase space joint representation of LOs and HOs - detailed analysis of initial and half-period conditions

3.4 Trajectory construction in the Ephemeris Model

The generation of QPOs in the ephemeris model requires taking into account further perturbations and influences beyond the POs convergence procedures just observed. POs computed in the CR3BP are transitioned in the higher fidelity model via transformation routines depicted in Section 2.5.2. If such a trajectory is integrated in the NBP as it is, it would highly likely diverge from the expected behavior. Moreover, the concept of "periodicity" itself is not viable nor really exists anymore in the NBP. Therefore, specific strategies to tackle the highly nonlinear behavior during convergence are implemented. The current Section delivers an overview of the algorithm implemented for such scope and strategies. Please note that what follows is a step-by-step explanation of the procedure presented in figure 3.18, to make the methodology clear and more easily reproducible.

The QPOs generation starts indeed from the analytical approximation of POs in the CR3BP, with guess initial state $\tilde{\boldsymbol{X}}_0^a$. Via DC strategies, the analytical orbit is transitioned and rendered periodic in its medium-fidelity counterpart PO in the CR3BP, with initial desired conditions ${}^{R/CG}\tilde{\boldsymbol{X}}_0^*$. At this point, the transition to the NBP dynamic happens, and by doing so dimensional ephemerides have to be retrieved. Due to its non-autonomous characteristic, the NBP transition also requires defining a starting epoch, t_0, and a generic final epoch, t. Let $\mathscr{T}_0 = t - t_0$ be the first guess integration time (namely, the guess period of the QPO) and let N_E be the total number of discrete subintervals in which the integration time is divided. Thus the dimensional ephemerides $\boldsymbol{X}_{kj} \in \mathbb{R}^{6\times N_E}$, retrieved from JPL's DE430 binaries, are

$$\boldsymbol{X}_{kj}(\mathscr{T}_0) = \begin{bmatrix} \boldsymbol{r}_{kj} \\ \boldsymbol{V}_{kj} \end{bmatrix} = \begin{bmatrix} x_{kj}(t_0) & x_{kj}(t_0+dt) & x_{kj}(t_0+2dt) & \dots & x_{kj}(t) \\ y_{kj}(t_0) & y_{kj}(t_0+dt) & y_{kj}(t_0+2dt) & \dots & y_{kj}(t) \\ z_{kj}(t_0) & z_{kj}(t_0+dt) & z_{kj}(t_0+2dt) & \dots & z_{kj}(t) \\ \dot{x}_{kj}(t_0) & \dot{x}_{kj}(t_0+dt) & \dot{x}_{kj}(t_0+2dt) & \dots & \dot{x}_{kj}(t) \\ \dot{y}_{kj}(t_0) & \dot{y}_{kj}(t_0+dt) & \dot{y}_{kj}(t_0+2dt) & \dots & \dot{y}_{kj}(t) \\ \dot{z}_{kj}(t_0) & \dot{z}_{kj}(t_0+dt) & \dot{z}_{kj}(t_0+2dt) & \dots & \dot{z}_{kj}(t) \end{bmatrix}, \quad (3.43)$$

where the reference k-th body is the Earth, at which center is positioned the Earth Mean Equator and Equinox of Epoch J2000 (EME2000) RF, whereas the other j-th gravitational bodies are the Moon and the Sun, in all similarity to the concepts presented in Section 2.3. Given the particular structure of the code, whose principal mechanics and strategies are addressed in the flowchart in Figure 3.18, the addition of further gravitational bodies, e.g. Jupiter, is straightforward and readily available. In particular, each additional j-th body perturbation is added gradually with a transitioning parameter $\gamma_{\mu_j,r} \in [0,1]$ during the FTDC or VTDC r-th step, until all the considered total n_b gravitational bodies have been included.

The correction procedure implements the same single-shooting iterative process of Section 3.3, equation (3.31). The required NBP reduced Jacobian $\boldsymbol{J}\left(\chi(\boldsymbol{X}_0), \boldsymbol{X}_f\right)$ takes from the complete NBP Jacobian the rows and columns corresponding to the requested free-design vector quantities and the selected terminal constraints. The complete NBP Jacobian matrix $\boldsymbol{A}(t) \in \mathbb{R}^{6\times 6}$ is composed by four submatrices 3×3 as in the following

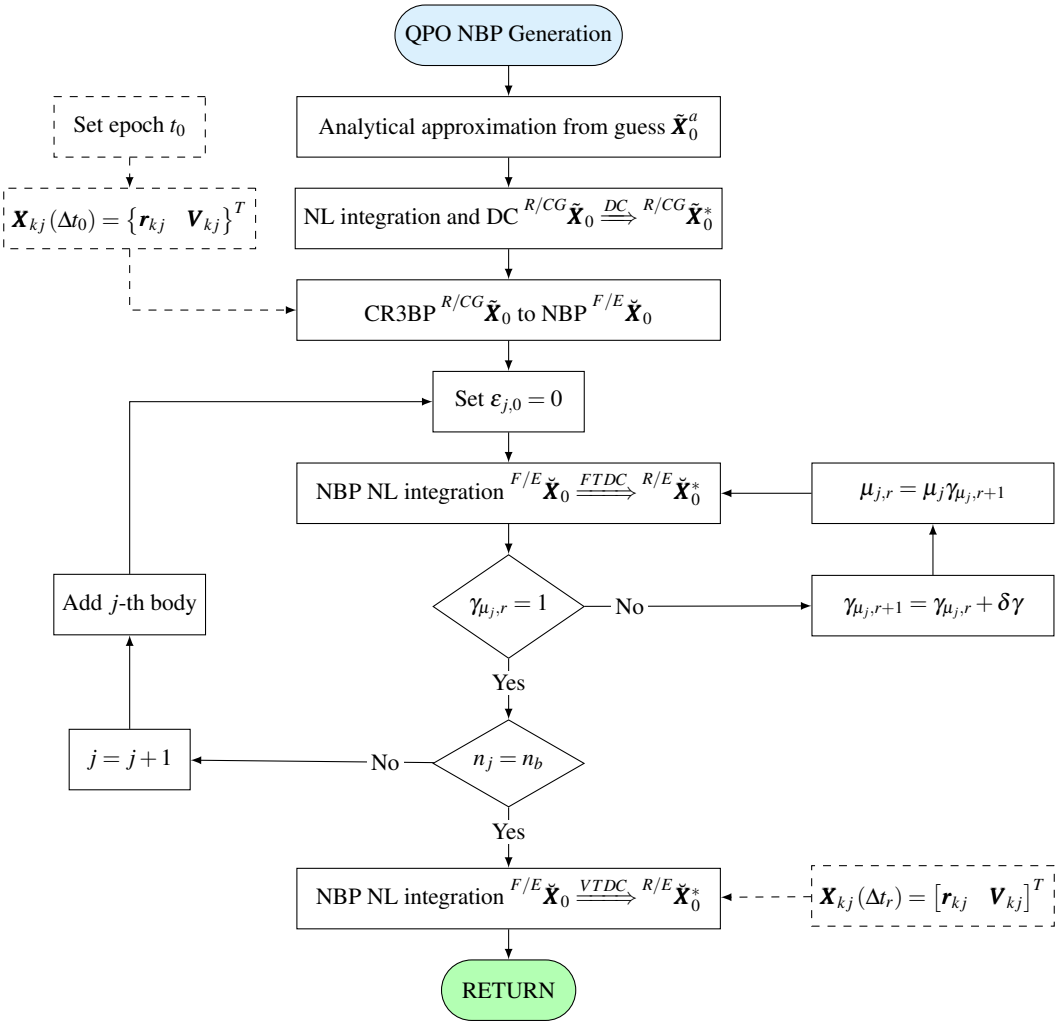

Fig. 3.18 Flowchart representation for the QPOs construction in the Ephemeris Model

$$\boldsymbol{A}(t) = \left[\begin{array}{c|c} \boldsymbol{0} & \boldsymbol{I} \\ \hline \boldsymbol{U} & \boldsymbol{0} \end{array}\right], \tag{3.44}$$

or, in explicit form,

$$\boldsymbol{A}(t) = \begin{bmatrix} 0 & 0 & 0 & 1 & 0 & 0 \\ 0 & 0 & 0 & 0 & 1 & 0 \\ 0 & 0 & 0 & 0 & 0 & 1 \\ U_{xx} & U_{xy} & U_{xz} & 0 & 0 & 0 \\ U_{yx} & U_{yy} & U_{yz} & 0 & 0 & 0 \\ U_{zx} & U_{zy} & U_{zz} & 0 & 0 & 0 \end{bmatrix}. \tag{3.45}$$

The submatrix $\boldsymbol{U} \in \mathbb{R}^{3\times3}$ is composed by the second partial derivatives of the potential function for the NBP. They are basically the first partial derivatives of the relative form of the NBP EOMs as in equation (2.47), omitted here for the sake of brevity but derived and presented in Appendix B. The correction procedure iteratively follows the same conceptual steps of the CR3BP, namely, after computing $\boldsymbol{A}(t_r)$ at the r-th step, the 36 ODEs for the NBP STM are implemented and integrated with the 6 ODEs of the trajectory itself,

$$\dot{\boldsymbol{\Phi}}(t,t_0) = \boldsymbol{A}(t)\,\boldsymbol{\Phi}(t,t_0)\,, \tag{3.46}$$

from which the DC procedure allows the single-shooting method to finely correct design variables with one of the following

$$\boldsymbol{X}_{r+1} = \boldsymbol{X}_r - \kappa_R \cdot [\boldsymbol{J}(\boldsymbol{\chi}_r)]^{-1}\boldsymbol{\chi}_r\,, \qquad \text{if } n = m\,, \tag{3.47a}$$

$$\boldsymbol{X}_{r+1} = \tilde{\boldsymbol{X}}_r - \kappa_R \cdot [\boldsymbol{J}(\boldsymbol{\chi}_r)]^{T}\left[\boldsymbol{J}(\boldsymbol{\chi}_r)\boldsymbol{J}(\boldsymbol{\chi}_r)^{T}\right]^{-1}\boldsymbol{\chi}_r\,, \qquad \text{if } n > m\,. \tag{3.47b}$$

where a suitable relaxation parameter of $\kappa_R \approx 0.1 \div 0.2$ increases the robustness of the single-shooting method in both the highly nonlinear FTDC and VTDC procedures.

Please note that for both the CR3BP to NBP transition and the gradual addition of further gravitational bodies, the ephemerides are retrieved only once to increase the convergence robustness, thus using a FTDC strategy. Once all the gravitational bodies have been added and the QPO has terminal conditions within a reasonable error from the initial ones, then a further VTDC is implemented to actually target and "close" the trajectory. As anticipated, the requirements for this thesis lie in the generation of a QPO which remains reasonably in place for at least a single orbit; therefore, more complex strategies and long-term stability are not sought.

Chapter 4

Optimal Control Theory

"All roads lead to Rome" may be considered a strong truth in the spacecraft trajectory domain, as long as a specific sought terminal condition does not have to account for all the subtle details that distinguish sub-optimal (or non-optimal) and optimal solutions. Until *sci-fi* unlimited propellant availability or in-orbit refueling strategies will become a consolidated reality, computing low-thrust trajectories and optimizing the requests needed to perform a certain mission will remain of utmost importance in the astrodynamics research field.

An Optimal Control Problem (OCP) researches the control law that extremizes a specific merit index. Here the concept of extremal value may indicate a maximization or a minimization. The optimal trajectory is the one that minimizes the propellant consumption during a complete transfer from an initial state to a final one or, equivalently, maximizes the final mass given the initial mass. In this thesis, the maximization of the final mass is preferred. Therefore, the terms "extremization" and "maximization" are here sometimes used interchangeably. The key concept is that specific parameters influencing the accomplishment of specific final objectives have to be opportunely controlled over the whole trajectory to find the optimal time-history of control variables able to satisfy constraints and maximize the performance index. The set of optimal control variables can be grouped in the term "optimal control law"; in this thesis, the Optimal Control Theory (OCT) is used to determine the necessary conditions that distinguish an optimal solution.

Chapter 4 is therefore outlined as follows. The first Section briefly describes that OCPs can be solved with two principal numerical methods, the indirect and direct

ones; their differences and the main reasons behind the choice of the indirect method in the present thesis will be outlined. Section 2 describes a general OCP as a Two-Point Boundary Value Problem (TPBVP), detailing the main results and conditions for optimality. Section 3 transforms such a problem in a Multi-Point Boundary Value Problem (MPBVP). Section 4 delineates how such MPBVP is solved via a single shooting method and how it is actually implemented in the algorithm used in this thesis. Section 5, in the end, applies the OCT to the spacecraft trajectory optimization domain, explicitly showing how to solve the actual Hamiltonian Boundary Value Problem (HBVP) implemented in the high-fidelity scenario.

4.1 Direct versus Indirect Numerical Methods

The scope of numerical methods is to decompose a generally complex problem as a sequence of smaller, more manageable finite sub-problems. The considered low-thrust trajectory optimization OCP is a continuous one, and the scope is to convert, with numerical methods, the infinite-dimensional problem into an approximate set of finite-dimensional sub-problems. Such procedure is also known as *transcription* and aims at converting the set of governing Ordinary Differential Equations (ODEs) into a problem with a finite, hopefully small, number of variables. Numerical methods are generally divided into two main branches; direct and indirect. A comprehensive detailing of such methods is provided in the recent opera by Betts [2], and a complete analysis is beyond the scope of this thesis. However, further details on the specific application and differences for the analyzed OCP can be found in [42] and omitted here for brevity.

Different research groups often gravitate towards using either direct or indirect optimization methods. An example of this natural tendency has been noticed in the various editions of the Global Trajectory Optimization Challenge (GTOC), a competition instituted and organized in 2005 under the leadership of Dario Izzo of the Advanced Concept Team (ACT) at ESA [75]. Ultimately, both direct and indirect methods have their strengths and weaknesses, and the ongoing "rivalry" between the two serves to push the boundaries of optimization techniques. Indeed, results of the GTOC over the previous years showed that both "direct methods teams" and "indirect methods teams" can successfully solve very complex problems related to the space trajectory optimization domain. In this framework, ref. [76] provides

an exceptional survey of the state-of-the-art in numerical methods to solve OCPs related to the low-thrust trajectory optimization field, continuing and updating the efforts of other research that, over the decades, attempted to categorize the available numerical techniques [77–80]. Such work encompasses an outstanding collection of the most widespread and well-known, public or private, *seventy-seven* software that use direct (i.e., COPERNICUS [81] from Texas University, the open-source NASA GMAT [82], or the commercial AGI STK [83]) or indirect methods (i.e., NASA JPL's GA-SEPTOP [84] and BNDSCO [85] from Hamburg University) to solve the low-thrust trajectory optimization OCP. Moreover, it provides a very useful insight regarding the different historical preference and use among the two methods; in recent times, roughly two of every three references implement direct methods, whereas the remaining one out of three refers to indirect ones.

Indeed, over the last decades, direct methods have been generally preferred due to their more straightforward implementation with respect to a generic OCP. Indeed, direct methods are generally robust and can treat complex problems. They perform a parametric optimization of the generic time-continuous problem, transforming it into a finite-dimension approximate one via the discretization of both the state and the optimal controls. In order to obtain a precise optimal solution, however, the mesh defining the domain discretization has to be particularly dense, which, in turn, requires a significant number of discrete points, or nodes, increasing the computational cost. In some instances, even refining the domain further, direct methods may still suffer from scarce accuracy, and solution refinement techniques may be needed. Modern computers can easily withstand the high computational cost of such discretization; therefore, one of the historical drawbacks of direct methods is nowadays superseded. However, understanding whether an analytical approximation is optimal is a complex task, given that the numerical nature of the solution does not usually offer theoretical insights.

On the other hand, solutions provided by Indirect Methods (IMs) are very accurate and usually come at a minimal computational cost and time compared to direct methods, although characterized by more convergence issues. IMs provide invaluable theoretical insights that help to understand the examined problem and guide the user toward the globally optimal solution, or at least provide information regarding how a tentative solution may be changed and, thus, improved towards the optimal one. In the past, indirect methods implementations suffered difficulties arising from the need to derive case-specific optimality, adjoint, and control equa-

tions. There are a few reasons that still nowadays may induce researchers to detract from an indirect method in practice. Indeed, to solve an OCP with indirect methods, specific problem-dependent quantities have to be manually computed via the OCT, and solutions are very sensitive to the initial conditions, requiring an expert user to at least "start" the process. Even Lawden's early efforts in the 1950s [86–89] among other contemporary fellow researchers [90, 91] attained to obtain optimal analytical solutions to these optimization problems to laid the foundation for the modern space trajectory optimization with IMs. Despite these difficulties, IMs have been profitably used in the past years in many different space trajectory applications [2, 37, 92–95].

Over the previous years, extensive studies and publications have been made at Politecnico di Torino discussed henceforth. Early research at Politecnico di Torino defined a very efficient framework for applying the OCT to space trajectories [96, 97]. The main feature is the definition of internal boundaries to handle constraints and discontinuities, converting a TPBVP into a MPBVP. Using proper numerical techniques allows this approach to improve the robustness of the IM. The increased robustness allowed for the application of IMs to complex problems, which were historically treated almost exclusively with the more robust direct methods. Initially, the IM was implemented to solve a finite-thrust orbital transfer TPBVP. Further implementations showed that the indirect optimization method was also well suited to manage impulsive maneuvers [98–100], demonstrating its high flexibility towards multiple scenarios with specific management of thrust phases. Since then, numerous subsequent studies and improvements have been made on optimal low-thrust trajectories using Electric Propulsion (EP) and gravity assists [101, 102]. The present research starts with such heritage.

The handy theoretical insights of IMs are undoubtedly a powerful tool for searching for optimal solutions in the space trajectories optimization domain. Thanks to all the previous contributions in the indirect spacecraft trajectory optimization field, the present work implements a further developed algorithm introducing several improvements and showing significant robustness and adaptability to different mission scenarios. Moreover, thanks to the distinctive theoretical insights, suboptimal solutions can be easily transitioned towards optimal ones. These reasons, as well as the significant practical applications from a space engineering perspective -further discussed in Chapters 5 and 6-, suggest that the use of IMs for optimizing escape trajectories from Lagrangian Points (LPs) and then Quasi-Periodic Orbits (QPOs) is well motivated.

4.2 Optimal control theory

The OCT applied to space trajectories OCPs has been extensively analyzed in the literature, starting from Lawden's formulation of optimal trajectories for space navigation [86], and following with Kirk's, Bryson's, and Burghes' treatises on Optimal Control (OC) [103–105]. While the main principles of the OCT, based on the Calculus of Variations (CoV), are solid milestones in literature, in recent times many authors adapted them in different nuances, given the increasing availability of much more performant calculators and more complex numerical methods [2, 36, 76, 106–109]. The OCT is indeed an extension of the CoV. The name "CoV" dates back to 1766 to Euler in his *Elementa Calculi Variationum* [110, 111]. The formulations and results in sections 4.2, 4.2.1 and 4.2.2 are well-documented in the previously cited references and are not signaled at each step for brevity. Furthermore, the following declination of the OCP is tailored for the spacecraft trajectory optimization domain.

As anticipated, an OCP aims at maximizing a specific merit index by establishing the optimal control law, among the admissible ones, that satisfies all the constraints for a trajectory that evolves in its dynamical model from an initial to a final state.

Therefore, the OCP defines a set of first-order ODEs $\dot{\boldsymbol{x}}$ to describe the evolution of n state variables over time. Such ODEs are function of the state vector $\boldsymbol{x}(t) \in \mathbb{R}^n$ itself between the initial and final time and depend also on a specific control vector $\boldsymbol{u}(t) \in \mathbb{R}^m$, containing m different control variables. Please note that the time t is the independent variable. An optimal solution requires finding the optimal trajectory $\boldsymbol{x}^*(t)$, subject to the optimal controls $\boldsymbol{u}^*(t)$, that maximizes the merit index. The ODE system can be generically written as

$$\dot{\boldsymbol{x}}(t) = \boldsymbol{f}(\boldsymbol{x}(t), \boldsymbol{u}(t), t) . \tag{4.1}$$

In general, a trajectory may be defined by conditions at the initial and final time, and the problem in equation (4.1) is a TPBVP. The extremal boundary conditions, at the beginning and at the end of the trajectory, namely at t_0 and t_f, are called external boundaries. The optimal trajectory is usually bounded to respect specific boundaries of different types; constraints on the state quantities at the external boundaries and, if required, on the epochs themselves may be imposed. Such Boundary Conditions

(BCs) are grouped in the constraint vector

$$\boldsymbol{\chi}\left(\boldsymbol{x}_0, \boldsymbol{x}_f, t_0, t_f\right) = \mathbf{0}\,, \tag{4.2}$$

where $\boldsymbol{\chi} : [\mathbb{R}^n, \mathbb{R}^n, \mathbb{R}, \mathbb{R}] \to \mathbb{R}^q$ contains all the q different constraints.

The control vector $\boldsymbol{u}$ may also be constrained; some of its quantities may be bounded in a specific range of admissible controls, or minimum and maximum values. The admissibility criterion $\boldsymbol{u} \in \boldsymbol{\mathcal{U}}$ and details on the control vector $\boldsymbol{u}$ are introduced later on in the discussion.

The optimality of the OCP is evaluated by means of a merit index $\mathcal{J}$ for which extremal values (relative maximums or minimums) have to be found, as per

$$\mathcal{J} = \varphi\left(\boldsymbol{x}_0, \boldsymbol{x}_f, t_0, t_f\right) + \int_{t_0}^{t_f} \left[\Phi\left(\boldsymbol{x}\left(t\right), \boldsymbol{u}\left(t\right), t\right)\right] \, \mathrm{d}t\,. \tag{4.3}$$

The merit index $\mathcal{J}$, or functional, presents two main scalar terms. On the one hand, the first function φ is dependent on the values that variables and times have at the extremal boundaries, thus depending on the specific final state, among the admissible ones, that is reached. On the other hand, the integral of the function Φ depends on the values that state variables, controls, and the time itself have over time, and therefore it quantifies *how* the solution evolved to reach the final state from the initial one. By introducing opportune auxiliary variables, the equation (4.15) can be rewritten or in the Lagrange's formulation, with $\varphi = 0$, or in the Mayer formulation, with $\Phi = 0$. The problem just described, in equations (4.1) to (4.3), is a classical CoV OCP, named Bolza's problem, which aims to optimize a time-continuous set of ODEs between two extremal states and under specific BCs.

The following notation is introduced for the sake of brevity:

$$\varphi \triangleq \varphi\left(\boldsymbol{x}_0, \boldsymbol{x}_f, t_0, t_f\right)\,, \tag{4.4a}$$

$$\boldsymbol{\chi} \triangleq \boldsymbol{\chi}\left(\boldsymbol{x}_0, \boldsymbol{x}_f, t_0, t_f\right)\,. \tag{4.4b}$$

Here a fundamental manipulation is introduced, namely the IM's principles are introduced henceforth. The optimality conditions are found by imposing an augmented merit function $\mathcal{J}^*$ that includes a measure of how much constraints and state quantities, with respect to the ODEs of the evolving dynamical model, are

respected. This action is performed by respectively introducing the adjoint variables, collected in the adjoint vector $\boldsymbol{\lambda}(t)$ and associated with the state variables, and the Lagrange multipliers, $\boldsymbol{\mu}$, linked to the BCs. It follows that $\boldsymbol{\lambda} \in \mathbb{R}^n$ and $\boldsymbol{\mu} \in \mathbb{R}^m$. Therefore, the augmented merit index has the form

$$\mathcal{J}^* = \varphi + \boldsymbol{\mu}^T \boldsymbol{\chi} + \int_{t_0}^{t_f} \left[\Phi + \boldsymbol{\lambda}^T (\boldsymbol{f} - \dot{\boldsymbol{x}}) \right] \, \mathrm{d}t \,. \tag{4.5}$$

Both of the functionals in equations (4.3) and (4.5) are a function of the state variables $\boldsymbol{x}(t)$, thus their derivatives $\dot{\boldsymbol{x}}(t)$, and the control variables $\boldsymbol{u}(t)$. For a generic non-converged solution, namely when $\boldsymbol{\chi} \neq \mathbf{0}$, equation (4.1) is not respected and $\dot{\boldsymbol{x}} \neq \boldsymbol{f}$. If both BCs and state equations are respected, then $\boldsymbol{\chi} = \mathbf{0}$ and $\boldsymbol{f} = \dot{\boldsymbol{x}}$ and, therefore, $\mathcal{J} = \mathcal{J}^*$. It follows that solving the augmented problem posed with the merit index in equation (4.5) is mathematically equivalent to solve the one in equation (4.3), once provided that all the constraints are fulfilled.

Time derivatives of the state variables $\dot{\boldsymbol{x}}$ are integrated while performing the trajectory optimization and ideally unknown. Therefore, it is useful to eliminate them by integrating the $-\boldsymbol{\lambda}^T \dot{\boldsymbol{x}}$ term in equation (4.5) by part

$$\int_{t_0}^{t_f} -\left(\boldsymbol{\lambda}^T \dot{\boldsymbol{x}} \right) \, \mathrm{d}t = -\left(\boldsymbol{\lambda}_f^T \boldsymbol{x}_f \right) + \left(\boldsymbol{\lambda}_0^T \boldsymbol{x}_0 \right) + \int_{t_0}^{t_f} \left(\dot{\boldsymbol{\lambda}}^T \boldsymbol{x} \right) \, \mathrm{d}t \,. \tag{4.6}$$

Therefore, by substituting equation (4.6) into equation (4.5), one has

$$\mathcal{J}^* = \varphi + \boldsymbol{\mu}^T \boldsymbol{\chi} + \left(\boldsymbol{\lambda}_0^T \boldsymbol{x}_0 - \boldsymbol{\lambda}_f^T \boldsymbol{x}_f \right) + \int_{t_0}^{t_f} \left(\Phi + \boldsymbol{\lambda}^T \boldsymbol{f} - \dot{\boldsymbol{\lambda}}^T \boldsymbol{x} \right) \, \mathrm{d}t \,. \tag{4.7}$$

An useful quantity appears in equation (4.7), the system's Hamiltonian $\mathcal{H}$

$$\mathcal{H} \triangleq \Phi + \boldsymbol{\lambda}^T \boldsymbol{f} \,. \tag{4.8}$$

Maximizing (or minimizing) the merit index $\mathcal{J}^*$ implies respecting the necessary condition for the optimality, namely that the $\mathcal{J}^*$ has to be stationary at the optimal point, which implies that its first order variation must be null. With some

mathematical steps, the first order differentiation $\delta\mathcal{J}^*$ is obtained

$$\delta\mathcal{J}^* = \left(\frac{\partial\varphi}{\partial t_0} + \boldsymbol{\mu}^T\frac{\partial\boldsymbol{\chi}}{\partial t_0} - \mathcal{H}_0\right)\delta t_0 + \tag{4.9a}$$

$$+\left(\frac{\partial\varphi}{\partial t_f} + \boldsymbol{\mu}^T\frac{\partial\boldsymbol{\chi}}{\partial t_f} + \mathcal{H}_f\right)\delta t_f + \tag{4.9b}$$

$$+\left(\frac{\partial\varphi}{\partial \boldsymbol{x}_0} + \boldsymbol{\mu}^T\frac{\partial\boldsymbol{\chi}}{\partial \boldsymbol{x}_0} + \boldsymbol{\lambda}_0^T\right)\delta\boldsymbol{x}_0 + \tag{4.9c}$$

$$+\left(\frac{\partial\varphi}{\partial \boldsymbol{x}_f} + \boldsymbol{\mu}^T\frac{\partial\boldsymbol{\chi}}{\partial \boldsymbol{x}_f} - \boldsymbol{\lambda}_f^T\right)\delta\boldsymbol{x}_f + \tag{4.9d}$$

$$+\int_{t_0}^{t_f}\left[\left(\frac{\partial\mathcal{H}}{\partial\boldsymbol{x}} + \dot{\boldsymbol{\lambda}}^T\right)\delta\boldsymbol{x} + \frac{\partial\mathcal{H}}{\partial\boldsymbol{u}}\delta\boldsymbol{u}\right]\mathrm{d}t\,, \qquad j = 1,\ldots,n_p\,. \tag{4.9e}$$

An adequate choice of adjoint variables $\boldsymbol{\lambda}$ and Lagrange multipliers $\boldsymbol{\mu}$ can nullify $\delta\mathcal{J}^*$ for any choice of δt_0, δt_f, $\delta\boldsymbol{x}_0$, $\delta\boldsymbol{x}_f$, $\delta\boldsymbol{x}$, and $\delta\boldsymbol{u}$, by nullifying their respective multiplying coefficients. Different sets of conditions descend from each specific term in equation (4.9); when the multiplying coefficients in lines (4.9a) and (4.9b) are null, two algebraic equations arise at the initial and final times, called *transversality conditions*; lines (4.9c) and (4.9d) provide $2n$ algebraic equations, one per each state quantity both at initial and final bounds, named *optimality conditions*. The last two multiplying coefficients produce two important results, namely n Euler-Lagrange ODEs for the adjoint variables and m algebraic equations for the control.

4.2.1 Boundary Conditions for Optimality

The boundary conditions for optimality are composed by the set of ODEs that control how times (2 transversality conditions) and states ($2n$ optimality conditions) at the trajectory extremal points should behave. By nullifying the coefficients of δt_0, δt_f,

$\delta \boldsymbol{x}_0$, and $\delta \boldsymbol{x}_f$ in the set of equations (4.9), one obtains

$$\frac{\partial \varphi}{\partial t_0} + \boldsymbol{\mu}^T \frac{\partial \boldsymbol{\chi}}{\partial t_0} - \mathcal{H}_0 = 0 \tag{4.10a}$$

$$\frac{\partial \varphi}{\partial t_f} + \boldsymbol{\mu}^T \frac{\partial \boldsymbol{\chi}}{\partial t_f} + \mathcal{H}_f = 0 \tag{4.10b}$$

$$\frac{\partial \varphi}{\partial \boldsymbol{x}_0} + \boldsymbol{\mu}^T \frac{\partial \boldsymbol{\chi}}{\partial \boldsymbol{x}_0} - \boldsymbol{\lambda}_0^T = \mathbf{0} \tag{4.10c}$$

$$\frac{\partial \varphi}{\partial \boldsymbol{x}_f} + \boldsymbol{\mu}^T \frac{\partial \boldsymbol{\chi}}{\partial \boldsymbol{x}_f} + \boldsymbol{\lambda}_f^T = \mathbf{0}\,. \tag{4.10d}$$

From the two tranversality equations (4.10a) and (4.10b), if the time does not appear nor in the function φ nor is constrained, the Hamiltonian is null at that point, both for initial and final times, and the values for the time are dependent on the optimization. On the other hand, if the time is constrained, namely in $\boldsymbol{\chi}$ there are equations of the type $t_0 = a$ and/or $t_f = b$, then the corresponding Hamiltonian is free and its value is dependent on the optimization. For example, missions with a fixed duration Δt do have both an assigned initial epoch t_0 and a consequentially assigned final epoch $t_f = t_0 + \Delta t$; in such a scenario, $\mathcal{H}_0 \neq 0$ and $\mathcal{H}_f \neq 0$. For a mission with unconstrained final time, t_0 is assigned and therefore $\mathcal{H}_0 \neq 0$, whereas the final time t_f is unbounded and subject to optimization, and therefore $\mathcal{H}_f = 0$.

Similarly, the optimality conditions in equations (4.10c) and (4.10d) state that if a specific i-th state variable x_i appears neither in the function φ nor in any constraint, its associated adjoint variable $\lambda_{x_i} = 0$ at the same point. Otherwise, if x_i is imposed, then its corresponding adjoint variable is unconstrained at the same point. For example, a simple Hohmann transfer from a lower radius r_0 to a higher radius r_f requires that both the radii are imposed at initial and final times, thus their corresponding adjoint vectors $\lambda_{r_0} \neq 0$ and $\lambda_{r_f} \neq 0$. On the other hand, for example, if the initial radius r_0 is subject to optimization, then $\lambda_{r_0} = 0$.

This practical set of rules for the transversality and optimality conditions is summarized in a schematic flowchart in Figure 4.1.

4.2.2 Equations for adjoint and control variables

The set of ODEs obtained by nullifying the multiplying coefficients in the last line (4.9e) of equation (4.9) describes how adjoint variables and controls evolve over time. By nullifying the coefficient of $\boldsymbol{\delta x}$ one retrieves the Euler-Lagrange equations for the adjoint variables

$$\frac{\mathrm{d}\boldsymbol{\lambda}}{\mathrm{d}t} = -\left(\frac{\partial \mathcal{H}}{\partial \boldsymbol{x}}\right)^T . \tag{4.11}$$

Given that adjoint variables are uniquely linked one-to-one to their associate state variable, $\dot{\boldsymbol{\lambda}} \in \mathbb{R}^n$. On the other hand, by nullifying the coefficient of $\boldsymbol{\delta u}$, a total of m algebraic equations for the controls are found, namely

$$\left(\frac{\partial \mathcal{H}}{\partial \boldsymbol{u}}\right)^T = 0 . \tag{4.12}$$

In the most general form, as anticipated, one or more elements of the control vector $\boldsymbol{u}$ may be bounded to specified limits of admissibility, say $\boldsymbol{\mathcal{U}}$. In general, $\boldsymbol{u}(\boldsymbol{x}(t),t)$, thus the specific control may be dependent on state variables and on the time itself. In the present scenario, only explicit constraints are considered; for example, a specific control quantity u shall be kept within the limits $\mathcal{U}_{min} \leq u \leq \mathcal{U}_{max}$. In the presence of explicit admissibility constraints, the optimal control $\boldsymbol{u}^* \in \boldsymbol{\mathcal{U}}$ for the desired trajectory is the one that, per each point in the trajectory, extremizes the Hamiltonian in equation (4.8) in that specific point. Such a concept is known as Pontryagin's Maximum Principle (PMP) (for a maximization problem, otherwise it is known as Pontryagin's minimum Principle, PmP). The PMP does not strictly imply that a control must be bounded to the extremes of its admissibility range; the generic optimal control value is the one provided by equation (4.12) if $\mathcal{U}_{min} < u < \mathcal{U}_{max}$, thus being unbounded, otherwise it is set to the extremes of $\mathcal{U}$.

However, equation (4.12) cannot hold if the Hamiltonian in equation (4.8) is linear, or affine, with respect to the bounded control. Two cases arise

$$\frac{\partial \mathcal{H}}{\partial u_i} = \begin{cases} k_{u_i} & \text{if } \mathcal{H} \text{ affine wrt } u_i \\ f(u_i) & \text{otherwise} \end{cases} \tag{4.13}$$

where k_{u_i} is a constant. If the Hamiltonian is affine to the control, the equation (4.13) cannot be fulfilled (except for $k_{u_i} = 0$), given that u_i cannot explicitly appear in

the calculation. In such scenario, the strategy to be sought is dependent upon the remaining coefficient k_{u_i} that the derivation provides. Specifically, if $k_{u_i} \neq 0$, then $\mathcal{H}$ is maximized by imposing that the control shall acquire the maximum admissible value, $u_i = \mathcal{U}_{i,max}$ if $k_{u_i} > 0$, or the minimum admissible value, $u_i = \mathcal{U}_{i,min}$ if $k_{u_i} < 0$. Such condition is known as *bang-bang* control and is precisely the case arising in the implemented OCP; the Hamiltonian is linear to the selected control variable -the thrust T-, under specific assumptions that will be detailed in Section 4.5, and additional considerations regarding the switch between the two extremal bounds for T_{min} (i.e., 0) and T_{max} will play a major role in the optimal trajectory definition. If $k_{u_i} = 0$ during a finite time interval, a different strategy has to be sought. Such operation is described in [112] and implies the presence of singular arcs. In the present thesis, such scenario never arises and therefore is omitted for the sake of brevity.

These specific rules for the control equations in the OCP complete the ones provided in section 4.2.1 and are included in Figure 4.1.

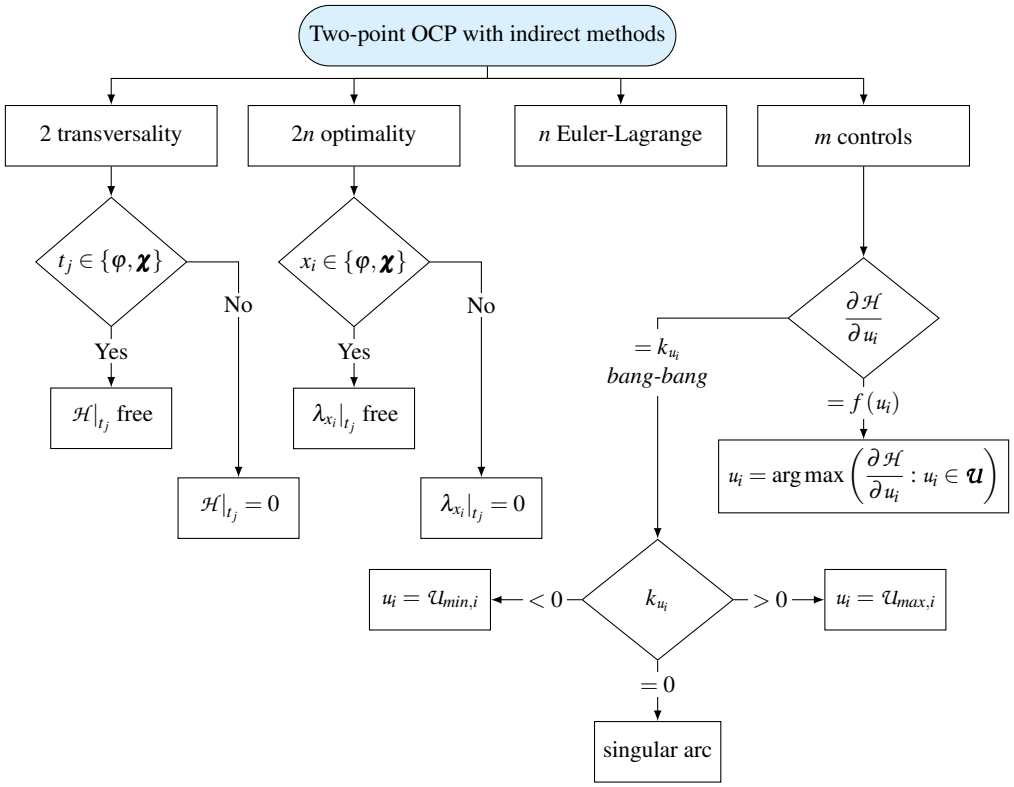

Fig. 4.1 Schematic flowchart representation of a two-point OCP

As such a TPBVP is presented, with the imposed m boundary conditions $\boldsymbol{\chi} = \mathbf{0}$, one has $2 + 2n + m$ equations, respectively from transversality (equations (4.10a) and (4.10b)), optimality (equations (4.10c) and (4.10d)), and control (equation (4.12)) relations, which implicitly determine 2 times (t_0 and t_f), the initial state values for the $2n$ state ODEs (for $\boldsymbol{x}$ and $\boldsymbol{\lambda}$), and m adjoint constants ($\boldsymbol{\mu}$).

4.3 Multi-Point Optimal Control Problem

A MPBVP arises when constraints are imposed in internal points along the trajectory (e.g., if a flyby occurs en route to the target of an interplanetary mission). The trajectory may be divided into a number of n_p of subintervals, that are called indistinctly phases or arcs, also to improve the code robustness and aid the convergence. Variables are continuous along each arc, but may present discontinuities at the internal boundaries, i.e. the junction points between two distinct adjacent arcs. Such implementation renders the problem presented in equations (4.1) to (4.3) a MPBVP. Each j-th arc starts at $t_{(j-1)_+}$ and terminates at t_{j_-}, with extremal state variable vectors in the form $\boldsymbol{x}_{(j-1)_+}$ and $\boldsymbol{x}_{j_-}$, respectively. A schematic representation of the generic MPBVP is presented in Figure 4.2, where the shortening $\boldsymbol{x}\left(t_j\right) \triangleq \boldsymbol{x}_j$ is introduced to avoid burdening the notation. Each j-th arc spans over a generic duration Δt_j, usually unknown and subject to optimization, which may be different among all the arcs.

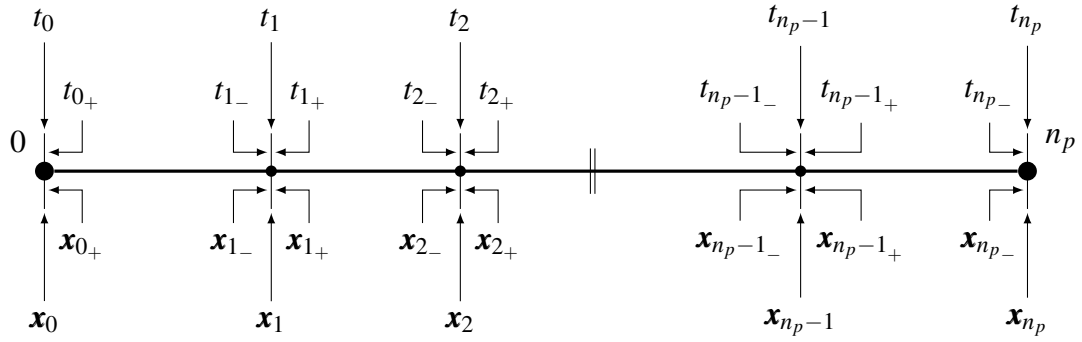

Fig. 4.2 Schematic representation of a MPBVP trajectory composed by n_p arcs

The BCs are again generally Non Linear (NL) and mixed and, in the MPBVP, can be imposed at the internal boundaries in addition to the external boundaries seen in equation (4.2). They may be function of both the state variables and the

independent time variable and assume the form of

$$\boldsymbol{\chi}\left(\boldsymbol{x}_{(j-1)_+},\boldsymbol{x}_{j_-},t_{(j-1)_+},t_{j_-}\right)=\mathbf{0}\,,\qquad j=1,\ldots,n_p\,. \tag{4.14}$$

The OC MPBVP functional $\mathcal{J}$ is, therefore,

$$\mathcal{J}=\varphi\left(\boldsymbol{x}_{(j-1)_+},\boldsymbol{x}_{j_-},t_{(j-1)_+},t_{j_-}\right)+\sum_{j=1}^{n_p}\int_{t_{(j-1)_+}}^{t_{j_-}}\Phi\left(\boldsymbol{x}(t),\boldsymbol{u}(t),t\right)\,\mathrm{d}t\,. \tag{4.15}$$

Here, φ is dependent on the values that variables and times have at every boundary, both for the complete trajectory, from $j=0$ to $j=n_p$, and for each arc. The sum of all the integrals of the function Φ still depends on the evolution over time of state variables, controls, and the time itself, but now accounts for how the solution evolves arc-by-arc. The MPBVP augmented merit index has the form

$$\mathcal{J}^*=\varphi+\boldsymbol{\mu}^T\boldsymbol{\chi}+\sum_{j=1}^{n_p}\int_{t_{(j-1)_+}}^{t_{j_-}}\left[\Phi+\boldsymbol{\lambda}^T\left(\boldsymbol{f}-\dot{\boldsymbol{x}}\right)\right]\,\mathrm{d}t \tag{4.16}$$

and, after integrating by part,

$$\mathcal{J}^*=\varphi+\boldsymbol{\mu}^T\boldsymbol{\chi}+\sum_{j=1}^{n_p}\left(\boldsymbol{\lambda}_{(j-1)_+}^T\boldsymbol{x}_{(j-1)_+}-\boldsymbol{\lambda}_{j_-}^T\boldsymbol{x}_{j_-}\right)+\sum_{j=1}^{n_p}\int_{t_{(j-1)_+}}^{t_{j_-}}\left(\Phi+\boldsymbol{\lambda}^T\boldsymbol{f}-\dot{\boldsymbol{\lambda}}^T\boldsymbol{x}\right)\,\mathrm{d}t\,. \tag{4.17}$$

The first order differentiation $\delta\mathcal{J}^*$ now is expressed per each arc as

$$\delta\mathcal{J}^*=\left(\frac{\partial\varphi}{\partial t_{(j-1)_+}}+\boldsymbol{\mu}^T\frac{\partial\boldsymbol{\chi}}{\partial t_{(j-1)_+}}-\mathcal{H}_{(j-1)_+}\right)\delta t_{(j-1)_+}+ \tag{4.18a}$$

$$+\left(\frac{\partial\varphi}{\partial t_{j_-}}+\boldsymbol{\mu}^T\frac{\partial\boldsymbol{\chi}}{\partial t_{j_-}}+\mathcal{H}_{j_-}\right)\delta t_{j_-}+ \tag{4.18b}$$

$$+\left(\frac{\partial\varphi}{\partial\boldsymbol{x}_{(j-1)_+}}+\boldsymbol{\mu}^T\frac{\partial\boldsymbol{\chi}}{\partial\boldsymbol{x}_{(j-1)_+}}+\boldsymbol{\lambda}_{(j-1)_+}^T\right)\delta\boldsymbol{x}_{(j-1)_+}+ \tag{4.18c}$$

$$+\left(\frac{\partial\varphi}{\partial\boldsymbol{x}_{j_-}}+\boldsymbol{\mu}^T\frac{\partial\boldsymbol{\chi}}{\partial\boldsymbol{x}_{j_-}}-\boldsymbol{\lambda}_{j_-}^T\right)\delta\boldsymbol{x}_{j_-}+ \tag{4.18d}$$

$$+\sum_{j=1}^{n_p}\int_{t_{(j-1)_+}}^{t_{j_-}}\left[\left(\frac{\partial\mathcal{H}}{\partial\boldsymbol{x}}+\dot{\boldsymbol{\lambda}}\right)\delta\boldsymbol{x}+\frac{\partial\mathcal{H}}{\partial\boldsymbol{u}}\delta\boldsymbol{u}\right]\,\mathrm{d}t\,,\qquad j=1,\ldots,n_p\,. \tag{4.18e}$$

Optimality and transversality conditions, in the MPBVP domain, are more conveniently expressed in terms of the j-th boundary itself. Therefore, instead of considering a single j-th arc from $t_{(j-1)_+}$ to t_{j_-}, the boundary itself is considered and values immediately before and after the boundary are written as

$$\frac{\partial \varphi}{\partial t_{j_+}} + \boldsymbol{\mu}^T \frac{\partial \boldsymbol{\chi}}{\partial t_{j_+}} - \mathcal{H}_{j_+} = 0, \qquad j = 0, \ldots, n_p - 1 \tag{4.19a}$$

$$\frac{\partial \varphi}{\partial t_{j_-}} + \boldsymbol{\mu}^T \frac{\partial \boldsymbol{\chi}}{\partial t_{j_-}} + \mathcal{H}_{j_-} = 0, \qquad j = 1, \ldots, n_p \tag{4.19b}$$

$$\frac{\partial \varphi}{\partial \boldsymbol{x}_{j_+}} + \boldsymbol{\mu}^T \frac{\partial \boldsymbol{\chi}}{\partial \boldsymbol{x}_{j_+}} + \boldsymbol{\lambda}_{j_+}^T = \mathbf{0}, \qquad j = 0, \ldots, n_p - 1 \tag{4.19c}$$

$$\frac{\partial \varphi}{\partial \boldsymbol{x}_{j_-}} + \boldsymbol{\mu}^T \frac{\partial \boldsymbol{\chi}}{\partial \boldsymbol{x}_{j_-}} - \boldsymbol{\lambda}_{j_-}^T = \mathbf{0}, \qquad j = 1, \ldots, n_p. \tag{4.19d}$$

Considerations on Euler-Lagrange equations for the adjoints and control equations stand identically true in the MPBVP domain.

4.4 The implemented Boundary Value Problem

This section describes the implementation, under the OCT, of the Boundary Value Problem (BVP). A spacecraft trajectory subject to low-thrust EP under the gravitational influence of the high-fidelity Four-Body Problem (4BP) requires a very precise control and optimization. When using indirect methods, particular attention must be given to the code robustness and the high sensitivity of the solution with respect to a variation of initial conditions. The 4BP is highly NL and numerical issues may prevent convergence. The handling of the thrust magnitude control is of particular relevance. Great improvements are obtained if the trajectory is split into phases with assigned control law, as described in Section 4.5. As presented in Section 4.2 and extended in the MPBVP fashion in Section 4.3, the OCT converts the original BVP in an augmented new one in which some of the initial state values may be unknown. The solution of such augmented BVP aims at finding the optimal initial state $\boldsymbol{y}_0^* = \left\{ (\boldsymbol{x}^*)^T \quad \left(\boldsymbol{\lambda}^*\right)^T \right\}^T$ that allows reaching the desired final condition $\boldsymbol{y}_f^*$ while satisfying all BCs, both the imposed and the optimality ones. The selected numerical method is again the single-shooting one presented in Section 3.3, which

is preferred for its straightforward implementation and its computational cost and speed.

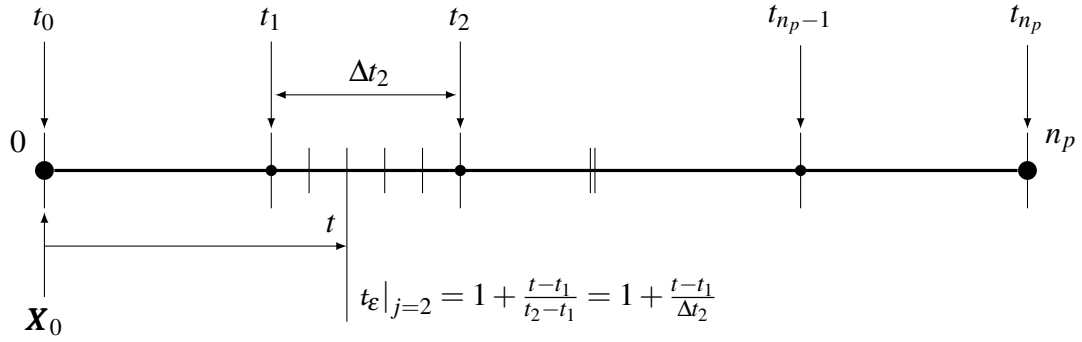

Fig. 4.3 Schematic representation of nondimensional time t_ε in the j-th arc

Figure 4.3 shows a schematic representation of a specific arc subdivided into n_E equally spaced subarc elements. One of the main drawbacks of indirect methods derives from the consideration of arc boundaries; given that their duration Δt is unknown, consistent numerical difficulties may arise if such nonlinearity is not taken into account, leading to a very ill-conditioned problem. In order to avoid such a problem, only for the set of ODEs that have to be integrated, a new independent non-dimensional time variable is introduced

$$t_\varepsilon = j - 1 + \frac{t - t_{j-1}}{t_j - t_{j-1}} = j - 1 + \frac{t - t_{j-1}}{\Delta t_j}\,, \tag{4.20}$$

where

$$\Delta t_j \triangleq t_j - t_{j-1}\,, \qquad j = 1, \ldots, n_p\,. \tag{4.21}$$

While Δt_j is still unknown and subject to optimization, the use of t_ε fixes the boundaries at integer values; for example, the second arc has boundaries $t_\varepsilon = [1,2]$, which are independent on the actual value of the arc duration. This particular introduction makes the resolution incredibly more robust and flexible.

The general method can be described as follows; the general form of the complete set of ODEs for the indirect method is

$$\dot{\boldsymbol{y}} = \boldsymbol{f}\left(\boldsymbol{y}(t), t\right), \tag{4.22}$$

or, in nondimensional quantities,

$$\dot{\check{\boldsymbol{y}}} = \boldsymbol{f}\left(\check{\boldsymbol{y}}\left(t_\varepsilon\right), t_\varepsilon\right), \tag{4.23}$$

where $\check{\boldsymbol{y}}$ now comprises state and adjoint variables, and the check accent is used to identify quantities that are function of the nondimensional time. However, the OCP may contain also some constant variables. A new vector $\boldsymbol{z} = \left\{\boldsymbol{y}^T \quad \boldsymbol{c}^T\right\}^T$ can be used to account also for constants vector $\boldsymbol{c}$. By introducing the new independent variable t_ε in place of t, the following set of ODEs arises

$$\dot{\check{\boldsymbol{z}}} = \frac{\mathrm{d}\check{\boldsymbol{z}}}{\mathrm{d}t_\varepsilon} = \boldsymbol{f}\left(\check{\boldsymbol{z}}\left(t_\varepsilon\right), t_\varepsilon\right), \tag{4.24}$$

where

$$\dot{\check{\boldsymbol{y}}} = \frac{\mathrm{d}\check{\boldsymbol{y}}}{\mathrm{d}t_\varepsilon} = \Delta t_j \frac{\mathrm{d}\boldsymbol{y}(t)}{\mathrm{d}t} \tag{4.25a}$$

$$\dot{\check{\boldsymbol{c}}} = \frac{\mathrm{d}\check{\boldsymbol{c}}}{\mathrm{d}t_\varepsilon} = \boldsymbol{0}. \tag{4.25b}$$

The new complete set of BCs, comprising both imposed and optimal ones, is

$$\boldsymbol{\chi}\left(\check{\boldsymbol{s}}\right) = \boldsymbol{0}, \tag{4.26}$$

where $\check{\boldsymbol{s}}$ is a vector containing all the values that variables have at each internal or external boundary, e.g. at $t_\varepsilon = 0, 1, \ldots, n_p$, namely

$$\check{\boldsymbol{s}} = \left\{\check{\boldsymbol{y}}_0^T \quad \check{\boldsymbol{y}}_1^T \quad \ldots \quad \check{\boldsymbol{y}}_{n_p-1}^T \quad \check{\boldsymbol{y}}_{n_p}^T \quad \check{\boldsymbol{c}}^T\right\}^T. \tag{4.27}$$

Now the problem needs to focus on finding the optimal initial values for the design vector that produce the desired final conditions while complying with all the constraints. A single shooting method is implemented to find the optimal initial state $\check{\boldsymbol{q}}_0^*$ which satisfies BCs $\boldsymbol{\chi}\left(\check{\boldsymbol{q}}^*\right) = \boldsymbol{0}$, in all similarity with the process seen in Section 3.3. The iterative process starts by defining a guess initial vector $\check{\boldsymbol{q}}_r = \check{\boldsymbol{z}}_0$ for the unknowns; here, the general formulation, in which all initial values are unknown, is described. Per each j-th boundary, the error on BCs at the r-th iteration is computed as $\boldsymbol{\chi}\left(\check{\boldsymbol{q}}_r\right)$. The BCs at the following iteration are a function of the values

assumed by BCs and state vector at the previous r-th one, namely, with a Taylor expansion of the first order,

$$\boldsymbol{\chi}\left(\check{\boldsymbol{q}}_{r+1}\right) = \boldsymbol{\chi}\left(\check{\boldsymbol{q}}_{r}\right) + \frac{\partial \boldsymbol{\chi}\left(\check{\boldsymbol{q}}_{r}\right)}{\partial \check{\boldsymbol{q}}_{r+1}}\left(\check{\boldsymbol{q}}_{r+1} - \check{\boldsymbol{q}}_{r}\right), \tag{4.28}$$

where the partial derivatives of the constraint vector with respect to the forward-in-time free-variable vector quantities compose the Jacobian matrix $\check{\boldsymbol{J}}$

Let the following shortenings be introduced to avoid burdening the notation:

$$\check{\boldsymbol{\chi}}_{r} \triangleq \boldsymbol{\chi}\left(\check{\boldsymbol{q}}_{r}\right), \tag{4.29a}$$

$$\check{\boldsymbol{J}}\left(\check{\boldsymbol{\chi}}_{r}\right) \triangleq \check{\boldsymbol{J}}\left(\check{\boldsymbol{\chi}}\left(\check{\boldsymbol{q}}_{r}\right), \check{\boldsymbol{q}}_{r+1}\right). \tag{4.29b}$$

If a solution exists, then $\check{\boldsymbol{\chi}}_{r+1} = \boldsymbol{0}$ and an iterative solution takes the form

$$\check{\boldsymbol{\chi}}_{r} + \left[\check{\boldsymbol{J}}\left(\check{\boldsymbol{\chi}}_{r}\right)\right]\left(\check{\boldsymbol{q}}_{r+1} - \check{\boldsymbol{q}}_{r}\right) = \boldsymbol{0}. \tag{4.30}$$

Therefore one can compute at each iteration the state of the design vector $\check{\boldsymbol{q}}_{r}$ and the updated value of the constraint vector $\boldsymbol{\chi}_{r}$

$$\check{\boldsymbol{q}}_{r+1} = \check{\boldsymbol{q}}_{r} - \left[\check{\boldsymbol{J}}\left(\check{\boldsymbol{\chi}}_{r}\right)\right]^{-1}\check{\boldsymbol{\chi}}_{r} \tag{4.31}$$

In this case, the Jacobian matrix is computed via two matrices multiplication

$$\check{\boldsymbol{J}}\left(\check{\boldsymbol{\chi}}_{r}\right) = \frac{\partial \check{\boldsymbol{\chi}}_{r}}{\partial \check{\boldsymbol{q}}_{r+1}} = \frac{\partial \check{\boldsymbol{\chi}}_{r}}{\partial \check{\boldsymbol{s}}_{r}}\frac{\partial \check{\boldsymbol{s}}_{r}}{\partial \check{\boldsymbol{q}}_{r+1}}. \tag{4.32}$$

The first one is easily computed, given that it comprises the constrained quantities derived by the quantities contained in the $\boldsymbol{s}$ vector (which contains all of them). The second matrix contains the partial derivatives of all the variables at each boundary with respect to initial values. Such a condition can be described again with a State Transition Matrix (STM), which linearly maps the subsequent states at the step $r+1$ related to the ones at the previous r-th step, as per equation (3.16). Let t_{ε_0} be the initial nondimensional time and $t_{\varepsilon} \geq t_{\varepsilon_0}$ a generic forward-in-nondimensional-time value. The STM here has the form

$$\frac{\partial \check{\boldsymbol{z}}_r}{\partial \check{\boldsymbol{q}}_{r+1}} = \check{\boldsymbol{\Phi}}\left(t_\varepsilon, t_{\varepsilon_0}\right). \tag{4.33}$$

Such STM has its own set of ODEs describing its evolution, which is defined as

$$\begin{aligned}
\dot{\check{\boldsymbol{\Phi}}}\left(t_\varepsilon, t_{\varepsilon_0}\right) &= \frac{\mathrm{d}}{\mathrm{d}t_\varepsilon}\check{\boldsymbol{\Phi}}\left(t_\varepsilon, t_{\varepsilon_0}\right) = \frac{\mathrm{d}}{\mathrm{d}t_\varepsilon}\left(\frac{\partial \check{\boldsymbol{z}}}{\partial \check{\boldsymbol{z}}_0}\right) \\
&= \frac{\partial}{\partial \check{\boldsymbol{z}}_0}\left(\frac{\mathrm{d}\check{\boldsymbol{z}}}{\mathrm{d}t_\varepsilon}\right) \\
&= \frac{\partial \dot{\check{\boldsymbol{z}}}}{\partial \check{\boldsymbol{z}}}\frac{\partial \check{\boldsymbol{z}}}{\partial \check{\boldsymbol{z}}_0}, \\
\dot{\check{\boldsymbol{\Phi}}}\left(t_\varepsilon, t_{\varepsilon_0}\right) &= \check{\boldsymbol{A}}\left(t_\varepsilon\right)\check{\boldsymbol{\Phi}}\left(t_\varepsilon, t_{\varepsilon_0}\right).
\end{aligned} \tag{4.34}$$

where the initial STM is again the identity matrix $\check{\boldsymbol{\Phi}}\left(t_{\varepsilon_0}, t_{\varepsilon_0}\right) = \boldsymbol{I}$. The Jacobian matrix $\check{\boldsymbol{A}}$ is composed by submatrices as follows

$$\check{\boldsymbol{A}}\left(t_\varepsilon\right) = \left[\begin{array}{c|c} \dfrac{\partial \dot{\check{\boldsymbol{x}}}}{\partial \check{\boldsymbol{x}}} & \dfrac{\partial \dot{\check{\boldsymbol{x}}}}{\partial \check{\boldsymbol{\lambda}}} \\ \hline \dfrac{\partial \dot{\check{\boldsymbol{\lambda}}}}{\partial \check{\boldsymbol{x}}} & \dfrac{\partial \dot{\check{\boldsymbol{\lambda}}}}{\partial \check{\boldsymbol{\lambda}}} \end{array}\right] = \left[\begin{array}{c|c} \check{\boldsymbol{A}}_{\check{x}\check{x}} & \check{\boldsymbol{A}}_{\check{x}\check{\lambda}} \\ \hline \check{\boldsymbol{A}}_{\check{\lambda}\check{x}} & \check{\boldsymbol{A}}_{\check{\lambda}\check{\lambda}} \end{array}\right]. \tag{4.35}$$

The first subscript indicates the numerator, the second the denominator, where state variables are described by the vector $\check{\boldsymbol{x}}$ and adjoint ones by $\check{\boldsymbol{\lambda}}$.

Such a method allows taking into consideration potential discontinuities at boundaries in the variables. A generic discontinuity at the j-th boundary can be included both in the design vector $\check{\boldsymbol{z}}$ and in the STM $\check{\boldsymbol{\Phi}}$ by means of a relation vector $\check{\boldsymbol{h}}$ in the general form

$$\check{\boldsymbol{z}}_{j_+} = \check{\boldsymbol{h}} \cdot \check{\boldsymbol{z}}_{j_-} \tag{4.36a}$$

$$\check{\boldsymbol{\Phi}}\left(t_{\varepsilon_+}, t_{\varepsilon_0}\right) = \frac{\partial \check{\boldsymbol{h}}}{\partial \check{\boldsymbol{z}}_j}\check{\boldsymbol{\Phi}}\left(t_{\varepsilon_-}, t_{\varepsilon_0}\right). \tag{4.36b}$$

This is the reason for which the vector $\boldsymbol{s}$ in equation (4.27) does not show a distinction between $\check{\boldsymbol{y}}_{j_-}$ and $\check{\boldsymbol{y}}_{j_+}$ values, given that they are interdependent via the vector $\check{\boldsymbol{h}}$ and the constant quantities in vector $\check{\boldsymbol{c}}$.

Therefore the indirect OCP in the presented MPBVP fashion can be stated as in finding the optimal initial state $\boldsymbol{z}_0^*$ which allows the trajectory to evolve towards a desired final state $\check{\boldsymbol{z}}_f^*\left(\check{\boldsymbol{z}}_0^*\left(t_\varepsilon\right), t_\varepsilon\right)$ while satisfying all BCs $\boldsymbol{\chi}$. Such an operation is performed by integrating simultaneously the principal set of ODEs and all the STM equations, which are reported here for clarity:

$$\dot{\check{\boldsymbol{z}}} = \boldsymbol{f}\left(\check{\boldsymbol{z}}\left(t_\varepsilon\right), t_\varepsilon\right), \tag{4.37a}$$

$$\dot{\boldsymbol{\Phi}}\left(t_\varepsilon, t_{\varepsilon_0}\right) = \boldsymbol{A}\left(t_\varepsilon\right)\boldsymbol{\Phi}\left(t_\varepsilon, t_{\varepsilon_0}\right). \tag{4.37b}$$

The integration implements an implicit multistep numerical method with variable step size and order based on the Adams-Moulton formulations as described by Shampine and Gordon [113].

The use of the linear mapping via the STM induces errors during the iterative Differential Corrector (DC) process that may compromise the convergence of the method and induce divergences. Let $E_{max} = \max_i\left(\chi_i\right)$. In order to improve the procedure and increase its robustness, the following strategies have been implemented; first off, a correction factor is imposed during the update, namely the following equation holds true

$$\check{\boldsymbol{z}}_{r+1} = \check{\boldsymbol{z}}_r - \kappa_1 \cdot \left[\check{\boldsymbol{J}}\left(\check{\boldsymbol{\chi}}_r\right)\right]^{-1} \check{\boldsymbol{\chi}}_r, \tag{4.38}$$

where the relaxation parameter $\kappa_1 = 0.1 \div 1$ is usually suitable to guarantee the convergence. Lower values of κ_1 are suitable during the first raw guesses for unknown values, whereas higher values can be used when the solution is already in a reasonable neighborhood of the optimal solution. Moreover, a control on the subsequent error is performed with respect to the errors on the boundary conditions at the previous step,

$$E_{max,r+1} < \kappa_2 E_{max,r}, \tag{4.39}$$

where $\kappa_2 = 2 \div 3$ is usually suitable to aid the first step of the iterative process to converge even if the first couple of steps increase the maximum error while settling the correct optimality direction in the search space. If the equation does not hold true, a bisection is imposed on the correction κ_1 up to five times.

4.5 OCP for spacecraft trajectory optimization

The spacecraft dynamical system subject of optimization in this thesis is reported here for reference, from equation (2.2), omitting the neglected terms

$$\frac{\mathrm{d}\boldsymbol{r}}{\mathrm{d}t} = \boldsymbol{V} \tag{4.40a}$$

$$\frac{\mathrm{d}\boldsymbol{V}}{\mathrm{d}t} = \boldsymbol{g} + \frac{\boldsymbol{T}}{m} + \mathbf{a}_p \tag{4.40b}$$

$$\frac{\mathrm{d}m}{\mathrm{d}t} = -\frac{T}{c}\,. \tag{4.40c}$$

The OCT applied to the system of ODEs in equation (4.40) aims at finding the optimal control law $\boldsymbol{u}^*(t)$ that maximizes the final mass of the Spacecraft (SC) at the end of the trajectory. The Mayer formulation is preferred here (Section 4.2), thus $\Phi = 0$. The state vector $\boldsymbol{x}(t) \in \mathbb{R}^n$ is

$$\boldsymbol{x} = \begin{Bmatrix} r & \vartheta & \varphi & u & v & w & m \end{Bmatrix}^T, \tag{4.41}$$

where each state variable is associated with its corresponding adjoint variable, producing the augmented state vector $\boldsymbol{y}(t) \in \mathbb{R}^{2n}$

$$\boldsymbol{y} = \begin{Bmatrix} r & \vartheta & \varphi & u & v & w & \lambda_r & \lambda_\vartheta & \lambda_\varphi & \lambda_u & \lambda_v & \lambda_w & m & \lambda_m \end{Bmatrix}^T. \tag{4.42}$$

Therefore, the merit index is the value of the SC mass at the last arc ($j = n_p$)

$$\mathcal{J} = \varphi = m_f = m_{n_p}\,. \tag{4.43}$$

By explicitly expressing the system of ODEs in equation (4.40), as from the set of equations in (2.51), the Hamiltonian is therefore defined as

$$\begin{aligned}\mathcal{H} = \boldsymbol{\lambda}^T \boldsymbol{f} = \sum_{i=1}^{2n} \lambda_i f_i = \lambda_r u + \lambda_\vartheta \frac{v}{r\cos\varphi} + \lambda_\varphi \frac{w}{r} + \\ + \lambda_u \left[-\frac{\mu}{r^2} + \frac{v^2}{r} + \frac{w^2}{r} + \frac{T_u}{m} + (\mathrm{a}_p)_u \right] + \\ + \lambda_v \left[-\frac{uv}{r} + \frac{vw}{r}\tan\varphi + \frac{T_v}{m} + (\mathrm{a}_p)_v \right] + \\ + \lambda_w \left[-\frac{uw}{r} - \frac{v^2}{r}\tan\varphi + \frac{T_w}{m} + (\mathrm{a}_p)_w \right] + \\ - \lambda_m \frac{T}{c},\end{aligned} \tag{4.44}$$

or in compact form

$$\mathcal{H} = \boldsymbol{\lambda}_r^T \boldsymbol{V} + \boldsymbol{\lambda}_V^T \left(\frac{\boldsymbol{T}}{m} - \mu \frac{\boldsymbol{r}}{r^3} + \mathbf{a}_p \right) - \lambda_m \frac{T}{c}. \tag{4.45}$$

An alternative form of the equation (4.45) is provided by grouping all the terms multiplying the thrust-to-mass ratio in the coefficient $\mathcal{S}_\mathcal{F}$

$$\mathcal{H} = \boldsymbol{\lambda}_r^T \boldsymbol{V} + \boldsymbol{\lambda}_V^T \left(-\mu \frac{\boldsymbol{r}}{r^3} + \mathbf{a}_p \right) + \frac{T}{m} \mathcal{S}_\mathcal{F}, \tag{4.46}$$

where

$$\mathcal{S}_\mathcal{F} = \boldsymbol{\lambda}_V^T \frac{\boldsymbol{T}}{T} - \lambda_m \frac{m}{c}. \tag{4.47}$$

The control vector $\boldsymbol{u}(t)$ is composed of the thrust vector $\boldsymbol{T}$, namely its magnitude and direction. In accordance with the PMP, the optimal control $\boldsymbol{u}^*$ which maximizes the merit index for the trajectory, is the one that maximizes the Hamiltonian in equation (4.46).

The Hamiltonian is linear with respect to the thrust T. As seen in Section 4.2.2, this implies that a *bang-bang* control arises and the thrust must be maximized, $T = T_{max}$, when the switching function $\mathcal{S}_\mathcal{F} > 0$, while the thrust shall be null $T = 0$, when $\mathcal{S}_\mathcal{F} < 0$. Singular arcs, usually associated with atmospheric flight and requiring the computation of the time derivatives of the switching function, are excluded here.

For what concerns the thrust direction, a useful result is derived from the work of Lawden [86]; the optimal thrust direction that maximizes the $\mathcal{S}_{\mathcal{F}}$ in equation (4.47), which in turn maximizes the Hamiltonian in equation (4.46), is parallel to the adjoint velocity vector $\boldsymbol{\lambda}_V$, named *primer vector*

$$\boldsymbol{\lambda}_V = \begin{Bmatrix} \lambda_u \\ \lambda_v \\ \lambda_w \end{Bmatrix}, \qquad \lambda_V = \|\boldsymbol{\lambda}_V\| \,. \tag{4.48}$$

Given this information, equation (4.47) can be rewritten in its scalar form

$$\mathcal{S}_{\mathcal{F}} = \lambda_V - \lambda_m \frac{m}{c} \,. \tag{4.49}$$

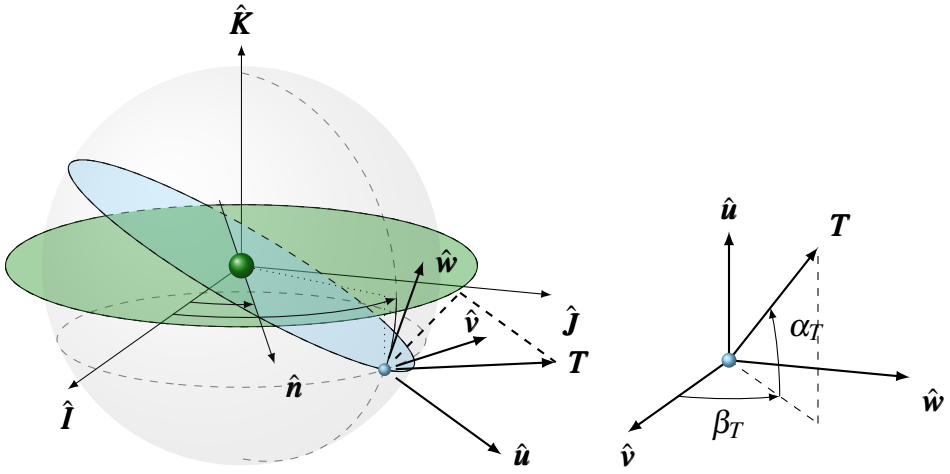

Fig. 4.4 Thrust angles in the SC ZEN RF

Figure 4.4 shows the thrust vector $\boldsymbol{T}$ with its characteristic thrust elevation angle α_T and heading angle β_T in the ZEN Reference Frame (RF), as seen in Section 2.3.1.

$$\boldsymbol{T} = \begin{Bmatrix} T_u \\ T_v \\ T_w \end{Bmatrix} = T \begin{Bmatrix} \sin\alpha_T \\ \cos\alpha_T \cos\beta_T \\ \cos\alpha_T \sin\beta_T \end{Bmatrix}, \qquad T = \|\boldsymbol{T}\| \,. \tag{4.50}$$

The optimal values for thrust angles are obtained by deriving the Hamiltonian in equation (4.44) with respect to the same angles, obtaining

$$\frac{\partial \mathcal{H}}{\partial \alpha_T} = 0 = \lambda_u \cos\alpha_T - (\lambda_v \cos\beta_T + \lambda_w \sin\beta_T)\sin\alpha_T \tag{4.51a}$$

$$\frac{\partial \mathcal{H}}{\partial \beta_T} = 0 = -\lambda_v \sin\beta_T + \lambda_w \cos\beta_T \,. \tag{4.51b}$$

With some mathematical manipulations, the set of equations (4.51) provides the following optimal directions

$$\sin\alpha_T = \frac{\lambda_u}{\lambda_V} \tag{4.52a}$$

$$\cos\alpha_T \cos\beta_T = \frac{\lambda_v}{\lambda_V} \tag{4.52b}$$

$$\cos\alpha_T \sin\beta_T = \frac{\lambda_w}{\lambda_V} \,, \tag{4.52c}$$

which are the cosine directors of the primer vector itself and incidentally are the same components of the thrust vector in equation (4.50). Therefore, the optimal thrust angles are found identically by computing the in-plane and out-of-plane angles via equations (4.52a) to (4.52c). The adjoint values are found via integration from the Euler-Lagrange equations, as seen in equation (4.11). Their problem-specific form is omitted here for brevity, but they are presented in Appendix C.

As posed, the problem would be completely defined. However, for highly-nonlinear dynamical systems and for the implemented high-fidelity model, complex gravitational interactions challenge the automatic computation of thrust ($\mathcal{S}_\mathcal{F} > 0$) and coast ($\mathcal{S}_\mathcal{F} < 0$) phases. Namely, if the $\mathcal{S}_\mathcal{F}$ in equation (4.49) happens to have small values fluctuating around the zero and changing multiple times their sign during the integration, numerical issues may arise; even small changes in the initial conditions, while performing the correction process depicted in Section 4.4, could abruptly shift the switching function, eliminating a desired thrust phase or including an unwanted coast phase. Even if this happens for a few steps during the integration, the resulting error gradients may be computed with scarce accuracy, and the solution may not converge. Handling thrust discontinuities is one of the main challenges in indirect optimization because they can create numerical problems in the evaluation of gradients. Several techniques have been used to deal with this

problem, such as smoothing techniques [6, 114, 115] or homotopy and continuation approach [116, 117]. More recently, new regularization techniques, such as uniform trigonometrization methods [118], and integrated control regularization methods [119], have also been introduced to handle thrust discontinuities and other kinds of path constraints.

In this analysis, a different approach is adopted. The switching structure (i.e., a suitable sequence of thrust and coast arcs) is specified *a priori*, and modified if PMP is violated. The simplest thrust-coast structure is initially assumed and eventually modified when required, according to the PMP. Each trajectory is divided into a number of distinct phases equal to the number of thrust and coast arcs specified, thus producing a MPBVP. The duration of each j-th phase, Δt_j, is unknown and subject to optimization. Additional boundary conditions specify that the switching function must be null at the switching points, where the thruster is turned on or off. This approach guarantees improved numerical accuracy and convergence speed and robustness compared to the alternative strategy of deciding the thrust level during integration, according to the instantaneous value of the switching function.

The following Chapters will extensively infer that the convergence speed also depends on the gravitational complexity in which the computation happens. A more complex dynamical interaction, for example close to the Earth-Moon system under the Sun's influence, would naturally require more computational time compared to trajectories far from the binary system. However, especially in situations with a higher level of gravitational complexity, the relative improvement in convergence speed from fixing the thrust structure is undeniable and becomes especially beneficial in ensuring a fast and accurate solution. On a standard 2.70 GHz CPU laptop, a reasonable initial guess (having at least the correct sign for the velocity adjoint vector, which in turn means having at least the knowledge if the SC should increase or decrease its velocity) produce a solution in less than 10 seconds per trajectory when close to the Earth-Moon, and less than 2 seconds when mainly under the Sun's influence, both within a 1×10^{-8} error tolerance. Additionally, the transition between two adjacent trajectories takes less than a second. These computational times are minimal, as expected with the use of indirect methods.

On the other hand, by fixing the switching structure, potential difficulties in convergence can be easily avoided, and in some cases, this may be one of the few improvements that can guarantee an automated solution (please refer to Figure 5.22

for a general overview). For instance, if a solution is on the border between a single-burn (thrust-coast) and a two-burn (thrust-coast-thrust-coast) structure, especially if the second thrust phase is very short, the switching function may oscillate indefinitely between a positive and a negative value without converging. The same applies if an optimal trajectory requires a very small final thrust arc in a three-leg solution (thrust-coast-thrust). By imposing the structure, the method becomes more robust and provides an immediate result, even if a portion of the switching function does not respect the PMP. Then, if the pre-defined thrust structure is correct, the PMP is respected and the solution is optimal. Otherwise, a simple inspection of the switching function can suggest how to modify the strategy, and a new solution can be readily obtained.

Chapter 5

Escape Trajectories from L_2 in the Hybrid 4-Body Problem

Chapter 5 describes all the resulting optimal escape trajectories deriving from the core analysis presented in the previous Chapters. All the trajectories are computed by using the *n*-Body Problem (NBP) Equations of Motion (EOMs) presented in Chapter 2. The dynamical body considers 4-body gravitation and is named here Four-Body Problem (4BP). A first part of the results is presented within the so-called Hybrid Four-Body Problem (H4BP); in this scenario, while the dynamical model is kept at high fidelity, the initial states are computed via approximate formulations as if the exact location of the Lagrangian Points (LPs) were still available. This operation happens both for the Lagrangian Point L_2 (L_2) in the vicinity of the Earth-Moon (EM) and Sun-Earth (SE) systems, named respectively Earth-Moon Lagrangian Point L_2 (EML_2) and Sun-Earth Lagrangian Point L_2 (SEL_2). Then, such trajectories are transitioned into higher-fidelity scenarios in which departures happen to be on specific Quasi-Periodic Orbit (QPO), computed in the NBP domain. There are multiple potential applications for these results. Beyond achieving desired terminal conditions at escape to target specific interplanetary destinations [14, 120–122], these escape trajectories also have significant practical applications from a space engineering point of view, including the design of efficient and cost-effective end-of-life disposal trajectories [123, 124] to reduce the space debris in those regions that will likely be heavily populated by satellites in the future.

5.1 Boundary conditions

5.1.1 Background

Many factors have to be considered when performing low-thrust Electric Propulsion (EP) trajectory computations. Even in very simple dynamical models, such as the Two-Body Problem (2BP) scenario, single-shooting methods find in the search space a solution that implies the Spacecraft (SC) should thrust in preferential directions; in a Low-Earth Orbit (LEO), for example, a SC has to thrust constantly in the tangential velocity direction in order to increase its energy and acquire enough kinetic energy to evade the primary gravitational pull. Depending on the orbital parameters, this may pose that the velocity shall be kept in the $\hat{\boldsymbol{v}}$ direction, for planar orbits, or with a specific projection in such Zenith-East-North (ZEN) Reference Frame (RF) for inclined orbits. However, the more complex the dynamical model is, the less obvious the search for the optimal thrust direction becomes. In the Circular Restricted Three-Body Problem (CR3BP), the gravitational bodies' influence induces gravitational effects that may guide a numerical method to find optimal solutions exploiting the combined gravitational pulls in unexpected behaviours. In the 4BP, such discrepancies increase both for the third-body perturbation and for other perturbative accelerations. Even if the implemented Indirect Method (IM) can compute optimal thrust angles to minimize the propellant request, the construction of suitable initial guesses is of utmost importance, as per Section 4.5, and so a thorough understanding of the dynamics behind simple escape trajectories has to be accomplished.

In the following Sections different scenarios will arise; escape trajectories will be computed in two different dynamical domains, the H4BP and the complete 4BP. In each of these scenarios, different departure conditions will change the main perturbation effects on the escape trajectories, namely those performed under the main influence of the Sun and the Earth, in the SE scenario, and under more complex gravitational interactions in the EM scenario. Indeed, in the latter case, even if the initial conditions will show that the combined Earth-Moon effect is predominant during the first phases of the escape, the same does not hold true while the SC gets farther away from the binary system, being strongly influenced by the Sun.

General conditions for the proposed problems are derived in this preface, stemming from approximate considerations from preliminary models.

5.1.2 Terminal conditions

Escape trajectories from L_2 or from QPOs in the vicinity of L_2, both in the SE and EM scenario, are considered complete when the SC reaches a finite, predetermined distance from the central body. Therefore, the "infinite distance" concept is converted in a distance greater than the principal body's Sphere Of Influence (SOI) radius. For SE and EM cases, the terminal distance is imposed to be $r_f = 3 \times 10^6$ km, about three times the Earth's SOI radius (Table 2.1). However, in the following Sections, the term SOI may be used simplistically to define the escape's boundary.

Considering that the terminal distance is finite, it is possible to compute an approximate upper boundary for the time to escape. Let the initial state correspond to a circular orbit with radius equal to the distance of the LP from Earth. A Hohmann ellipse to r_f in the 2BP approximation represents the minimum ΔV transfer to reach the final radius and is used to approximately evaluate the maximum escape time. The L_2 position is given from the radius of Hill's sphere r_{H_b}, evaluated by supposing that the mass of the smaller primary (Moon with respect to Earth or Earth with respect to Sun) is much smaller than the bigger primary. Here $b = \{\ell, E\}$ indicates that such value is computed with respect to the Moon or the Earth, respectively, so that

$$r_{H_b} = r_{12} \left(\frac{\mu_2}{3\mu_1} \right)^{1/3}. \tag{5.1}$$

The initial position for a SC with respect to (wrt) the Earth is

$$r_{0_{|\text{EML2}}} = r_{E\ell} + r_{H_\ell} = r_{E\ell} \left[1 + \left(\frac{\mu_\ell}{3\mu_E} \right)^{1/3} \right] = 4.459241 \times 10^5 \text{ km}, \tag{5.2a}$$

$$r_{0_{|\text{SEL2}}} = r_{H_E} = r_{Es} \left(\frac{\mu_E}{3\mu_s} \right)^{1/3} = 1.496559 \times 10^6 \text{ km}, \tag{5.2b}$$

and the Hohmann transfer semimajor axis and period $\mathscr{T}_h = \mathscr{T}/2$ are easily derived

$$\mathscr{T}_{h,max_{|\text{EML2}}} = \pi \sqrt{\frac{a^3_{h_{|\text{EML2}}}}{\mu_E}} = 130.25 \text{ days}, \tag{5.3a}$$

$$\mathscr{T}_{h,max_{|\text{SEL2}}} = \pi \sqrt{\frac{a^3_{h_{|\text{SEL2}}}}{\mu_E}} = 194.15 \text{ days}. \tag{5.3b}$$

These values are the upper bound quantities for the transfers, respectively for the EM and SE scenario. Such transfers reach r_f on an ellipse, therefore with an apogee-like velocity

$$V_{a_{|\text{EML2}}} = \sqrt{2\mu_E \left(\frac{1}{r_f} - \frac{1}{2a_{h_{|\text{EML2}}}} \right)} = 0.1854 \text{ km/s}, \tag{5.4a}$$

$$V_{a_{|\text{SEL2}}} = \sqrt{2\mu_E \left(\frac{1}{r_f} - \frac{1}{2a_{h_{|\text{SEL2}}}} \right)} = 0.2974 \text{ km/s}. \tag{5.4b}$$

However, given that at r_f the escape can be considered complete and such trajectories will be on an open path, these velocities do indeed approximate the hyperbolic excess velocities V_∞ computed by considering the remaining small specific potential energy. Such quantities are, therefore, the lower boundary for the desired V_∞ which, in turn, set the lower boundary for the approximate characteristic energy.

$$V_{\infty,min_{|\text{EML2}}} = 0.1854 \text{ km/s}, \qquad \mathscr{C}_{3f,min_{|\text{EML2}}} = 0.0344 \text{ (km/s)}^2, \tag{5.5a}$$

$$V_{\infty,min_{|\text{SEL2}}} = 0.2974 \text{ km/s}, \qquad \mathscr{C}_{3f,min_{|\text{SEL2}}} = 0.0884 \text{ (km/s)}^2. \tag{5.5b}$$

The conjunction of the upper boundary information regarding the time to escape in the set of equations (5.3) and the lower boundary values for the characteristic energy in the set of equations (5.5) help identify appropriate terminal conditions. The selected transfer times to escape are roughly half of the elliptical transfer values. Selected $\mathscr{C}_{3f}$ values of 0.2 and 0.5 $(\text{km/s})^2$, henceforth referred to as low- and high-energy escape conditions ($L\mathscr{C}_{3f}$ and $H\mathscr{C}_{3f}$), correspond to a $V_\infty = \{0.4472, 0.7071\}$ km/s, well beyond the benchmark ones. In a concise form, the reduced set of terminal boundary conditions $\boldsymbol{\chi}_f = \left\{ r_f \quad \Delta t \quad \mathscr{C}_{3f} \right\}^T$ is

$$\boldsymbol{\chi}_{f_{|\text{EML2}}} = \left\{ 3 \times 10^6 \text{ km} \quad 75 \text{ days} \quad \{0.2 \vee 0.5\} \text{ (km/s)}^2 \right\}^T, \tag{5.6a}$$

$$\boldsymbol{\chi}_{f_{|\text{SEL2}}} = \left\{ 3 \times 10^6 \text{ km} \quad 90 \text{ days} \quad \{0.2 \vee 0.5\} \text{ (km/s)}^2 \right\}^T. \tag{5.6b}$$

Such boundary conditions will be applied alternatively. While the final radius will be fixed throughout all the cases, two mission architectures arise, those at a fixed time to escape Δt and those at a fixed characteristic energy $\mathscr{C}_{3f}$.

5.1.3 Initial conditions

Even if in the H4BP the departure position lies in L_2, the Hill's sphere radius contains the distance among the two biggest gravitational bodies, which is time-dependent and retrieved from JPL's DE430 ephemerides. Therefore, both in the H4BP and in the 4BP domain, the departure epoch may heavily influence the escape performance. Specifically, the Moon's and Sun's states over time influence the evolution of a trajectory and different departure epochs with the same initial conditions will induce different behaviours. Five different cases are selected in this analysis; their departure epochs $\mathcal{E}(t)$, expressed in terms of their Coordinated Universal Time (UTC)[1] Modified Julian Day (MJD) values, are presented in Table 5.1.

Table 5.1 Selected departure epochs $\mathcal{E}$

		Epoch UTC	MJD	$r_{Em}(t)$ km
$\mathcal{E}_1$	●	2025/10/15 08:58:15.543	60963.374	384400.0
$\mathcal{E}_2$	●	2025/10/22 08:23:32.690	60970.350	405459.3
$\mathcal{E}_3$	●	2025/10/29 09:12:32.480	60977.384	392470.4
$\mathcal{E}_4$	●	2025/11/05 08:37:49.627	60984.360	357166.9
$\mathcal{E}_5$	●	2025/11/12 08:03:06.774	60991.335	384400.0

The reference departure date, $\mathcal{E}_1$, is October 15, 2025, when the Earth-Moon distance matches its average value of $r_{Em} = \ell^* = 384400$ km (please refer to Section 2.3 for characteristic quantities in the CR3BP). The analysis time is extended up to the point in which the instantaneous Earth-Moon distance is again at the average value, which happens on November 12, 2025, $\mathcal{E}_5$, roughly a sideral month further in time. The first four epochs allow studying how the Moon itself influences escape trajectories, given that its mean anomaly M would evolve of about 90° between each selected departure; case 5 completes one of the 13 lunar cycles per year, but more importantly, allows to notice the Sun's influence net of the Moon's one. Moreover, the selected epochs are chosen to have the Earth near its perihelion during the escape trajectory, making the solar perturbation more evident.

Therefore, as posed, initial conditions for the state variables are always defined and known. For the H4BP scenario, the initial position vector is provided by

[1] For the remainder of the thesis, the UTC format (YYYY/MM/DD HH:MM:SS.sss) is dropped in favor of a more straightforward DD/MM/YYYY, unless otherwise specified.

equation (5.2) for the radius and by placing the SC on the opportune polar coordinates in order to be in L_2. The initial velocity vector is selected to have the same angular velocity as the primaries' relative motion. Remember that planetary ephemerides are retrieved in Cartesian coordinates; position quantities are converted into polar ones and velocities in the ZEN RF. A correction factor that takes into account the time-dependent distance between the Earth and the scenario-specific other gravitational body, defined per each selected epoch, is introduced

$$\mathcal{K}_{\mathcal{E}}(\mathcal{E}) = \frac{\ell^*}{r_{Eb}(\mathcal{E})}. \tag{5.7}$$

Therefore the initial state vectors at each specific epoch are

$$\boldsymbol{x}_{0_{|\text{EML2}}}(\mathcal{E}) = \begin{Bmatrix} r_{0_{|\text{EML2}}} \\ \vartheta_{0_\ell} \\ \varphi_{0_\ell} \\ u_{0_\ell} \\ v_{\ell_0}\mathcal{K}_{\mathcal{E}} \\ w_{0_\ell}\mathcal{K}_{\mathcal{E}} \end{Bmatrix}, \qquad \boldsymbol{x}_{0_{|\text{SEL2}}}(\mathcal{E}) = \begin{Bmatrix} r_{0_{|\text{SEL2}}} \\ \vartheta_{0_s} + \pi \\ -\varphi_{0_s} \\ u_{0_s} \\ v_{0_s}\mathcal{K}_{\mathcal{E}} \\ -w_{0_s}\mathcal{K}_{\mathcal{E}} \end{Bmatrix}. \tag{5.8}$$

Please remember that the dynamical model is centered in the Earth Mean Equator and Equinox of Epoch J2000 (EME2000) RF, as discussed in Section 2.3, for both the EM and SE scenarios. Therefore, while EML_2 lies on the same line of the Moon, specifically in the same direction as seen from the Earth -and therefore EML_2 initial conditions are easily computed-, the Sun and SEL_2 at epoch do happen to be diametrically opposite. Therefore, the SEL_2 initial conditions, namely the L_2 state at epoch, require opportune symmetrical and specular mathematical manipulations.

From such considerations, it follows that the initial guesses to be provided to the IM are the ones referred to the adjoint variables $\boldsymbol{\lambda}_0(\mathcal{E})$, namely

$$\boldsymbol{\lambda}_0(\mathcal{E}) = \left\{ \lambda_r \quad \lambda_\vartheta \quad \lambda_\varphi \quad \lambda_u \quad \lambda_v \quad \lambda_w \right\}^T. \tag{5.9}$$

Reasonable guesses have to be provided to start the optimization procedure. While some of the adjoints have a decently intuitive evolution and influence on the performances, others show a less predictable behavior. Think about the velocity

adjoints as a combination of the pedals and steering wheel in a vehicle: the magnitude of the specific velocity adjoint indicates the relevance that the corresponding state velocity has at the same moment in time; the sign of the specific velocity adjoint implies the use of the accelerator pedal (thrust along that direction for positive values) or the brakes (thrust in the opposite direction for negative values). The greater the magnitude with respect to the others, the more relevant the specific adjoint is, implying that the subsequent thrust direction is important. The position adjoint variable, λ_r, is somehow a measure of how significant is the change of its associate state variable over time. A positive initial value is used here, since escape is required. The other two adjoint variables are less relevant; for example, $\dot{\lambda}_\vartheta$ contains only the influence of some perturbative terms (please refer to Appendix C) and no direct values from the EOMs. Therefore, small non-zero initial values can be imposed in the range $1 \times 10^{-4} \div 1 \times 10^{-6}$.

The last piece of the puzzle regards the Thrust Structure ($\mathrm{T_S}$), or the guess of the number of subarcs n_p in which a specific trajectory should be divided. Intuitively, the $\mathrm{T_S}$ should have an initial thrust phase, to depart from the initial location, and then can use a coast phase to reach the final destination. A theoretical insight to confirm such consideration comes from analyzing key terminal conditions, as shown in Section 4.2.2. For prescribed final positions and free velocity (fixed time to escape scenario), the final values of the velocity adjoint variables are all null, namely the terminal condition of the primer vector is $\boldsymbol{\lambda}_V = \mathbf{0}$. Therefore, from equation (4.47), close to the terminal epoch $\mathcal{S}_\mathcal{F}(\Delta t) < 0$ and the thruster should be turned off; moreover, initial values for the guessed adjoint velocity components should have a small magnitude, given that their evolution has to converge in a nullification. More complex structures will arise when terminal conditions on the velocities are imposed; sub-optimal solutions violating the Pontryagin's Maximum Principle (PMP) will be modified accordingly by introducing/removing thrust/coast phases, if needed.

In the computations, quantities are normalized by using Earth's ellipsoid major semiaxis $r_E = 6378.1363$ km and the corresponding circular velocity $\sqrt{\mu_E / r_E}$ as reference values, where $\mu_E = 398600.4415\ \mathrm{km}^3/\mathrm{s}^2$ is Earth's gravitational parameter. The normalized gravitational parameter of the Earth is equal to one.

5.1.4 Propellant consumption

In the dynamical model in equations (4.40), the last equation (4.40c) represents the propellant consumption over time due to the propulsive effort. This formulation shows a constant thrust T, which leads to the *bang-bang* control depicted in Section 4.5. Such a result holds by the assumption of considering as constant the available power at 1 AU, the specific impulse and, thus, the thrust at 1 AU. The available power and thrust are inversely proportional to the squared distance from the Sun r_{sSC}, assuming efficiency η_T and effective exhaust velocity c as constants:

$$T(r_{sSC}) = 2\frac{\eta_T}{c}P(r_{sSC}) = 2\frac{\eta_T}{c}\frac{P^*}{r_{sSC}^2} = \frac{T^*}{r_{sSC}^2}, \tag{5.10}$$

where P^* and T^* are the values at 1 AU and r_{sSC} is expressed in AU. Moreover, the effective exhaust velocity is proportional to the specific impulse I_{sp}, since $c = I_{sp}g_0$.

Depending on the mission scenario, two different EP thrusters are implemented. The propulsion system is based on the performance of the ArianeGroup RIT 2X [125] and its characteristics are presented in Table 5.2 below

Table 5.2 EP thrusters for the SEL2 and the EML2 scenarios

Quantity	Value	
	SEL2	EML2
	Ion	Hall
P^*	4.2 kW	4.2 kW
I_{sp}	3300 s	2000 s
η_T	0.625	0.625

Once the optimal trajectory is computed, the value of m_f is readily available. Therefore, by means of the Tsiolkovsky equation

$$m_f = m_0 e^{-\Delta V/c}, \tag{5.11}$$

the requested ΔV per each mission, distinguished by the appropriate choice of the thruster and, thus, function of the specific I_{sp}, is obtained as

$$\Delta V = -I_{sp}g_0 \ln\left(\frac{m_f}{m_0}\right). \tag{5.12}$$

5.2 Escape trajectories from Sun-Earth L_2

Escape trajectories computed from the SE Lagrangian point L_2 are analyzed here. These escape missions are characterized by a first thrust phase in which the Earth-Moon combined gravitational pull has to be superseded while the Sun is in opposition. During the escape, the Sun evolves in its (apparent) motion with respect to the Earth in the EME2000 RF, producing a varying over time perturbation. As anticipated in Section 2.6.1, the solar perturbation $\mathbf{a}_{sg}$, under simplifying assumptions, produces a net perturbing acceleration in the ZEN radial and tangential directions of the SC, reported here from equations (2.79a) and (2.79b) for clarity

$$(\mathbf{a}_{SCs} - \mathbf{a}_{Es}) \cdot \hat{\boldsymbol{u}} = \frac{3}{2} \frac{\mu_s}{r_{Es}^3} \{1 + \cos[2(\vartheta_s - \vartheta)]\}\,, \tag{5.13a}$$

$$(\mathbf{a}_{SCs} - \mathbf{a}_{Es}) \cdot \hat{\boldsymbol{v}} = \frac{3}{2} \frac{\mu_s}{r_{Es}^3} \sin[2(\vartheta_s - \vartheta)]\,. \tag{5.13b}$$

Equations (5.13a) and (5.13b) show that it is possible to enclose the perturbation effect dependence on the Sun-SC position in two proportionality terms [48, 126]

$$\sigma_u = 1 + \cos(2\Delta\vartheta)\,, \tag{5.14a}$$

$$\sigma_v = \sin(2\Delta\vartheta)\,, \tag{5.14b}$$

where $\Delta\vartheta$ is the angular difference between the Sun and the SC. A representation of the two proportionality terms is reported in Figure 5.1, where $\sigma = \sigma_u + \sigma_v$

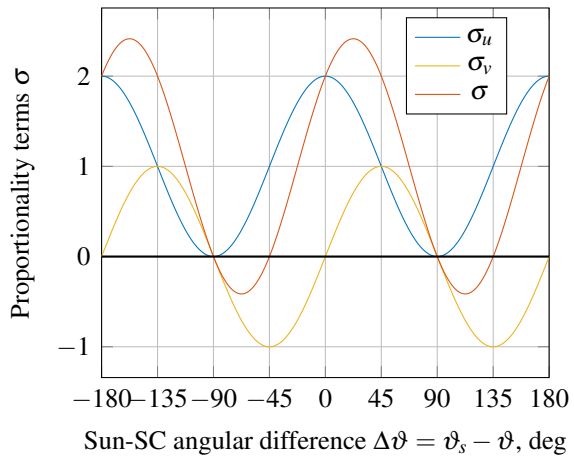

Fig. 5.1 Sun-SC solar gravitational perturbation proportionality terms

Figure 5.2 shows a polar view of the proportionality terms with respect to the SC-Earth line, where σ_u is normalized with a 1/2 coefficient to range from 0 to 1, while σ_v ranges from -1 to 1. The σ values sum the two contributions; negative values are identified by a dash-dot line, whereas positive ones are continuous.

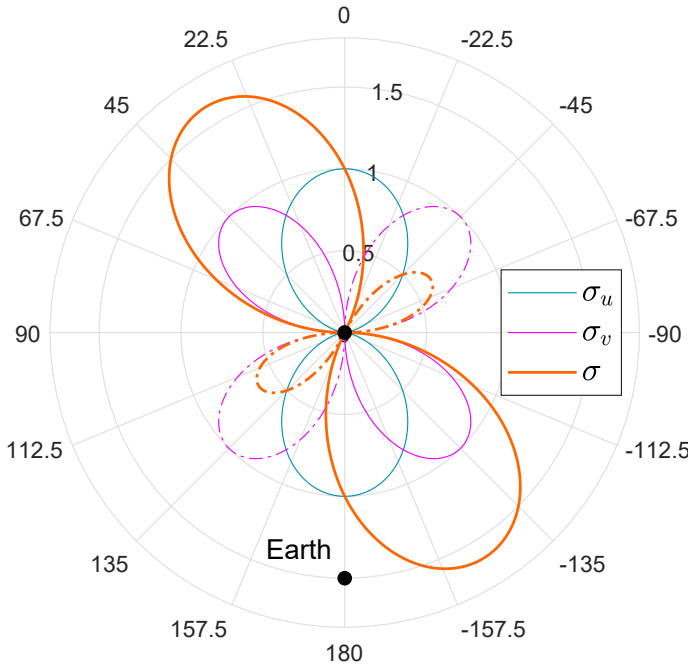

Fig. 5.2 Polar plot of σ_u, σ_v, and σ wrt $\Delta\vartheta = \vartheta - \vartheta_S$ in the SC-Earth rotating RF

In general, as discussed in Section 5.1, the SC energy is increased by the acceleration component along the SC direction in a closed orbit. Large positive values of σ_v provide a boost in the initial tangential velocity and tend to be intuitively more useful during the initial phase, whereas large σ_u should be preferred in the final phases, when the velocity tends to the radial direction (leaving the central body behind). However, for escape trajectories, and specifically in the SEL_2 scenario, the Sun is always at $\Delta\vartheta = 180^\circ$ at the departure epoch, and different results are expected. Both Figures 5.1 and 5.2 show that large σ_v values occur when the Sun is in the first ($0^\circ < \Delta\vartheta < 90^\circ$) or third ($-180^\circ < \Delta\vartheta < -90^\circ$) quadrant in the SC rotating frame, whereas other $\Delta\vartheta$ combinations may have a null or negative influence on the SC energy for trajectories continuously evolving outward. The radial acceleration, on the other hand, cannot produce a negative effect and has a maximum positive influence when the Sun is in between the fourth and first quadrants ($-45^\circ < \Delta\vartheta < 45^\circ$) or in between the second and the third quadrants ($\Delta\vartheta > 135^\circ$ and $\Delta\vartheta < -135^\circ$). In general, the combined effect of the two solar perturbation components has an overall

maximum positive effect on the SC energy when the Sun is either close to -157.5° or $+22.5^\circ$ with respect to the Earth-SC direction. The worst combinations happen when the Sun is almost in quadrature, namely around 112.5° or -67.5°.

Two simple coefficients are defined to assess how much the influence of the solar perturbation is acting favorably on an escape trajectory, $\eta_{sg,u}$ and $\eta_{sg,v}$. Such radial and tangential perturbation weights are introduced to evaluate the normalized contributions of solar perturbation along the whole trajectory. Let a generic trajectory be split into N uniform intervals of duration Δt_j, where the total time to escape $\Delta t = \sum_{j=1}^{N-1} \Delta t_j$. Therefore, $\eta_{sg,u}$ and $\eta_{sg,v}$ are evaluated as

$$\eta_{sg,u} = \frac{1}{2\Delta t_{max}} \left(\sum_{j=1}^{N-1} \frac{\sigma_{u,j} + \sigma_{u,j+1}}{2} \Delta t_j \right), \tag{5.15a}$$

$$\eta_{sg,v} = \frac{1}{\Delta t_{max}} \left(\sum_{j=1}^{N-1} \frac{\sigma_{v,j} + \sigma_{v,j+1}}{2} \Delta t_j \right). \tag{5.15b}$$

When a comparison between different trajectories has to be performed, the η_{sg} are normalized with respect to the longest mission among them, Δt_{max}. This strategy allows obtaining a general parameter that can also compare escape trajectories with different total duration. The 1/2 coefficient in $\eta_{sg,u}$ is introduced to make $\eta_{sg,u} = 1$ for maximum favorable effect, whereas $\eta_{sg,u} = 0$ corresponds to null effect, as it has already been done for the corresponding proportionality term σ_u. The values of $\eta_{sg,v}$, instead, range between -1 (most unfavorable) to 1 (most favorable) and do not undergo any changes, as per σ_v. The signed $\overline{\eta_{sg}}$ is simply the average value of $\eta_{sg,u}$ and $\eta_{sg,v}$.

5.2.1 Sun-Earth L_2 escapes with imposed mission duration Δt

Tentative guesses for the unknown initial adjoint variables are constructed as per Section 5.1.3. The solutions for the five departure dates show a common trend during the escape of $\Delta t = 90$ days. Figure 5.3 highlights a whole family of solutions (represented by the hundreds of subtle lines) with departures starting from case 1, on October 15, 2025 ($\mathcal{E}_1$), up to case 5, on November 12, 2025 ($\mathcal{E}_5$), whereas table 5.3 compares the performance of the reference cases depending on the departure date $\mathcal{E}_i$, showing that the solutions belong to the same family ($f = \mathrm{I}$) and have a 2-phase structure ($n_p = 2$). Please note that families are identified with roman numbers.

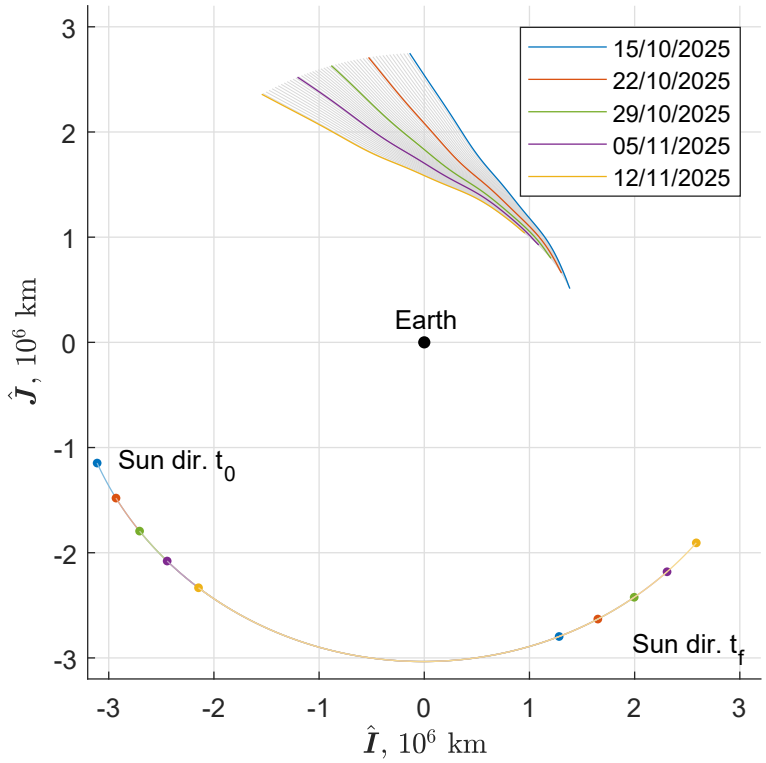

Fig. 5.3 SEL2 escape trajectories over a lunar month, fixed $\Delta t = 90$ days, free $\mathscr{C}_{3f}$, EME2000 RF

Table 5.3 SEL2 escape trajectories performance - fixed $\Delta t = 90$ days, free $\mathscr{C}_{3f}$

$\mathcal{E}$	f	n_p	$\eta_{sg,u}$	$\eta_{sg,v}$	$\overline{\eta_{sg}}$	ΔV m/s	$\mathscr{C}_{3f}$ $(\mathrm{km/s})^2$
1	I	2	0.975	0.208	0.592	30.676	0.1833
2	I	2	0.979	0.174	0.576	36.419	0.1931
3	I	2	0.978	0.178	0.578	55.369	0.2050
4	I	2	0.974	0.217	0.596	54.982	0.1956
5	I	2	0.976	0.210	0.593	33.572	0.1828

There are close similarities, and, at a first approximation, each curve seems simply rotated due to the different departure positions. Each trajectory is however different, mainly due to the Moon's position during flight, which changes with the departure date $\mathcal{E}$. The cost to escape is always small, but it shows remarkable changes (it is almost doubled in the most unfavorable case). Also the escape energy exhibits oscillation, to a lesser extent.

These selected five cases are henceforth highlighted with specific styles, as anticipated in Table 5.1. A family f collects solutions that can be found with a continuation approach; namely, converged solutions for the adjoint values $\boldsymbol{\lambda}(\mathcal{E}_i)$ are seeded as initial guesses at a neighbour epoch $t_0 = \mathcal{E}_i + \delta t$, with $i = 1, \ldots, 5$, and then the process repeats. If a forward-in-time continuation of a certain epoch merges with a backward-in-time continuation of a subsequent epoch, then all the trajectories found within them belong to the same family.

The SC is actually pulled towards the boundary of the SOI by the Sun, which has a large positive overall effect on the orbit energy. Its direction at the beginning and at the end of each selected escape is represented in the lower part of Figure 5.3. Thrust is therefore used to achieve a trajectory that maintains the Sun in a favorable position, maximizing the effect of its pull; indeed, the Sun moves from $\Delta\vartheta = 180^\circ$ to the third quadrant of the frame that rotates with the SC, where Sun's gravity acts to increase the orbit energy. The SC remains close to 180° and/or between -135° and -180° in the rotating frame, exploiting both tangential and radial perturbations.

In order to see the influence of the Moon, let two specific departure epochs be considered, $\mathcal{E}_1$ and $\mathcal{E}_3$. Figure 5.4 shows the evolution of the Sun-SC angle for these two departure dates. Please note that, henceforth, all Figures presenting a bolded portion (both continuous or piecewise-continuous) indicate that in that timeframe there is a thrust phase (T), if such information is relevant in the specific Figure.

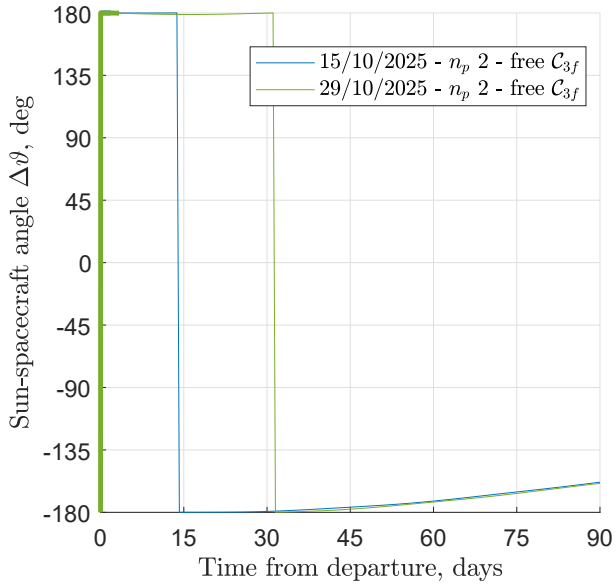

Fig. 5.4 SEL2 selected escape trajectories - time evolution of Sun-SC relative angle $\Delta\vartheta$

The two trajectories are separated by two weeks at departure. However, they evolve similarly to preserve the maximum positive effect of the Sun, both in the radial and tangential directions. For the SEL_2 scenario, it is way more favourable to exploit the positive radial perturbation initially, when the Sun is in opposition at $\Delta\vartheta(\mathcal{E}) = 180^\circ$ and acts weakening the Earth-Moon combined gravitational attraction. Such consideration is clearly visible even in the behavior adjoint variables have in their evolution, provided by the Euler-Lagrange equations (4.11), and in the corresponding optimal in-plane thrust angle α_T. Figure 5.5, on the left, shows the evolution of the optimal radial and tangential adjoint variables, λ_u and λ_v, as well as of the primer vector magnitude. The graph on the right shows the resulting optimal thrust angle $\alpha_T(t)$. Here non-bolded curves have no physical meaning, since thrust is not applied in coast arcs; they are included to better distinguish multiple cases.

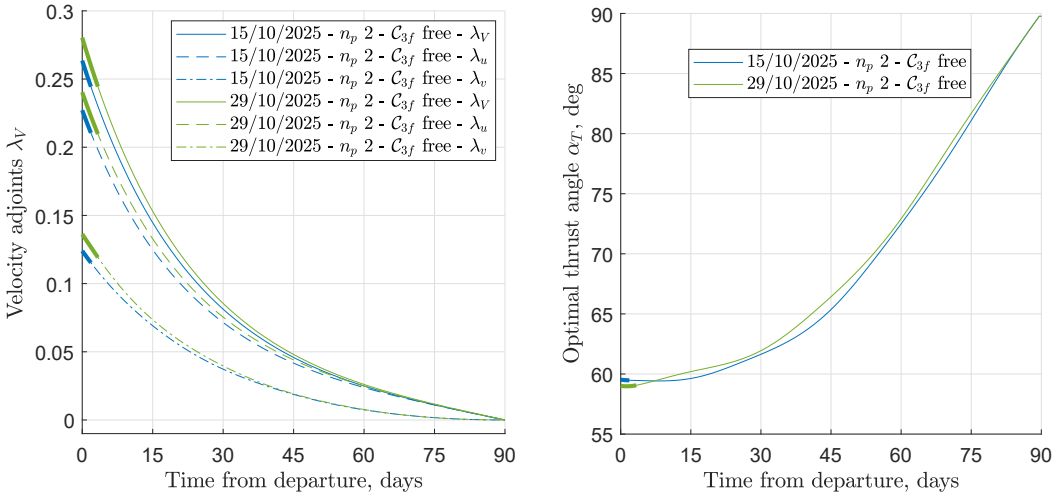

Fig. 5.5 SEL2 selected escape trajectories - time evolution of velocity adjoints λ_u, λ_v, and primer vector λ_V (left), optimal in-plane thrust angle α_T (right)

The optimal solution provides a $\lambda_{u,0} > \lambda_{v,0}$ (actually, a continuous $\lambda_u > \lambda_v$) for both the selected epochs (and, in practice, for all the others $\mathcal{E}_i$, $i = 1,\ldots,5$), and indeed the thrust direction at departure has already an in-plane thrust angle which favors the $\hat{\boldsymbol{u}}$ direction with an aperture of $\alpha_{T,0} \approx 60^\circ$. The optimality of the solution is visible, preliminarily, in the fulfillment of the Boundary Conditions (BCs); the mission has unbounded terminal velocity state variables that imply, from the optimality conditions in equation (4.10d), null terminal adjoint velocity components; $\lambda_V(\Delta t) = 0$, indeed. The optimality of the solution can also be proved by analyzing the switching function $\mathcal{S}_\mathcal{F}$ and understanding if PMP is fulfilled. Figure 5.6 shows

the $\mathcal{S}_\mathcal{F}$ for the two selected dates. The Thrust-Coast (T-C) switching structure, with

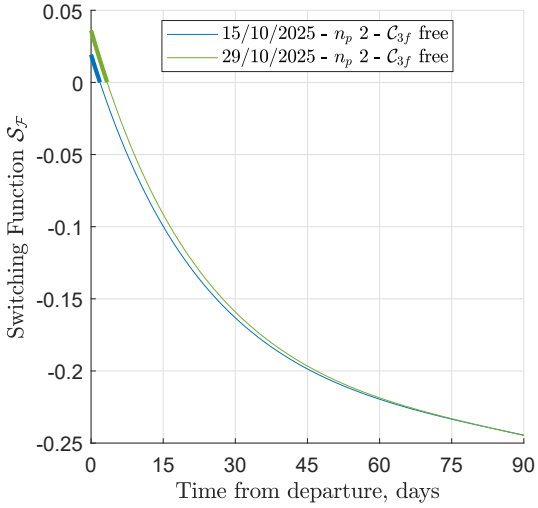

Fig. 5.6 SEL2 selected escape trajectories - time evolution of the switching function $\mathcal{S}_\mathcal{F}$

$n_p = 2$ arcs, is indeed optimal. Both the solutions start with $\mathcal{S}_\mathcal{F} > 0$, which, in order to maximize the Hamiltonian, implies a thrust phase in the first arc, accordingly to the *bang-bang* control. When $\mathcal{S}_\mathcal{F} < 0$, the thruster is turned off and the SC evolves under the sole gravitational perturbations. Therefore, the final characteristic energy, except for a minor thrust contribution at the beginning, is due to the solar perturbation, as presented in Figure 5.7.

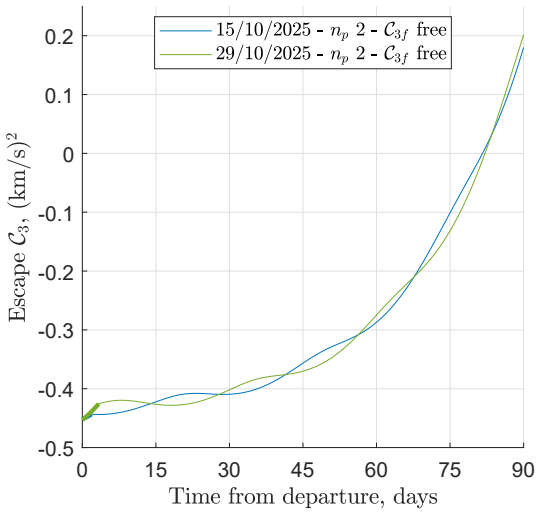

Fig. 5.7 SEL2 selected escape trajectories - time evolution of the characteristic energy $\mathscr{C}_3$

The Moon causes the fluctuations in the energy gain; since $\mathcal{E}_1$ and $\mathcal{E}_3$ are spaced apart by two weeks, the Moon revolves over roughly 180° among the two states, producing a specular oscillating perturbing acceleration. Figure 5.8 shows the lunisolar perturbative accelerations, $\mathbf{a}_{sg}$ and $\mathbf{a}_{\ell g}$, respectively due to the Sun (left) and the Moon (right), computed via equations (5.13a) and (5.13b).

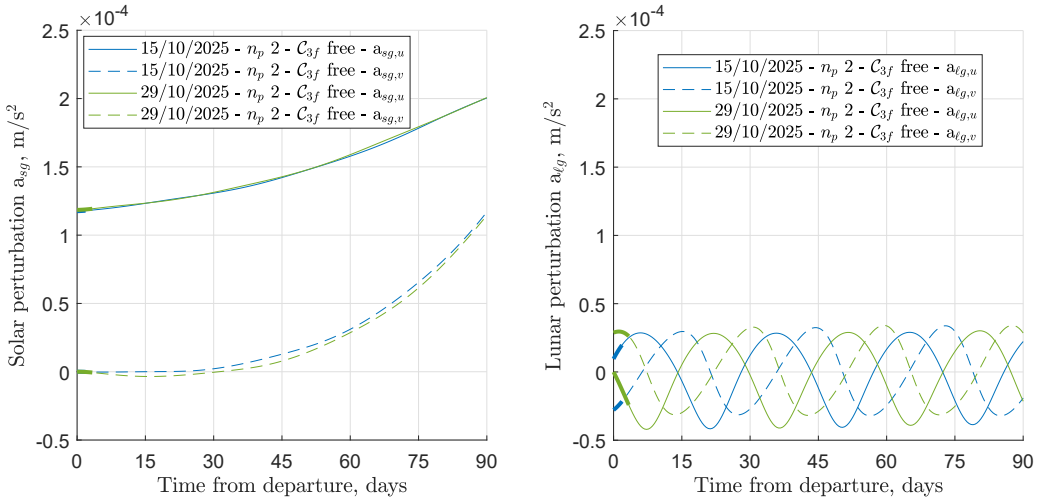

Fig. 5.8 SEL2 selected escape trajectories - time evolution of solar (left) and lunar (right) gravitational perturbation

The set of Figures 5.4 to 5.8 may seem to produce trivial results, with repeating quantities among different solutions. However, it is quite the opposite; the optimal solutions for the SE scenario prove that the overall state evolution of a SC is dependent on the positive perturbation of the Sun, whereas differences among neighbourhood solutions are due to the minor but decisive Moon's perturbation. The gravitational interactions and the boundary conditions of the fixed time to escape SEL_2 scenario indicate that no gravitational bodies are close enough to induce strong fluctuating perturbations, and the perturbation gradients evolve smoothly over time. For a comprehensive description of all the selected escape trajectories, Figures 5.9 and 5.10 show respectively the evolution over time of the characteristic energy $\mathscr{C}_3$ gain and the departure trajectories in the Sun-Earth synodic RF, centered on Earth. The resulting $\mathscr{C}_{3f}$ for all the selected departure dates revolves around the $\mathscr{C}_{3f} \approx 0.2\ (\mathrm{km/s})^2$ value, confirming that unbounded terminal energy trajectories do have an excess velocity resulting in heliocentric trajectories. Again, in a Sun-Earth synodic RF centered on Earth, all the trajectories evolve in the fourth quadrant and show evident similarities.

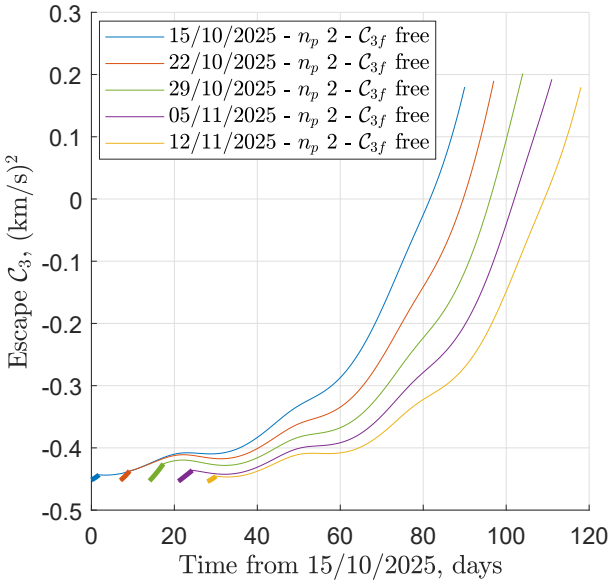

Fig. 5.9 SEL2 SC characteristic escape energy over time for reference departure dates

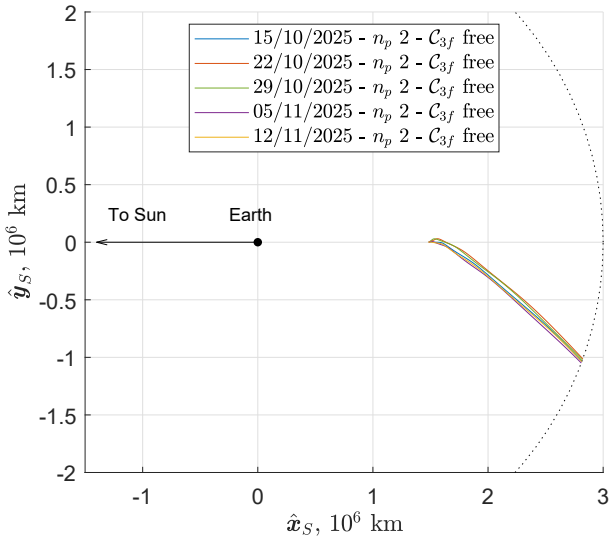

Fig. 5.10 SEL2 escape trajectories, Sun-Earth synodic RF

A more insightful representation of the Moon's perturbative effects on trajectories for the whole family of solutions is presented in Figure 5.11. On the left, the chart presents the trend of the propellant requests, and thus the ΔV, to reach an escape in 90 days with free final energy. The reference departure date (October 15, 2025) is in the region where ΔV and $\mathscr{C}_{3f}$ values are lowest. At $\mathcal{E}_1$, the Moon's angular position in the Sun-Earth synodic RF is around 120°, in the second quadrant; the SC is relatively far from the Moon, and Moon's gravity acts mainly on the Earth. The

initial geometry on the reference departure date shows that the Moon reduces the SC's geocentric energy by pulling the Earth; this perturbation modifies the Sun-Earth-SC geometry so that the Sun's pull on the SC is increased, and a lower propulsive effort is needed. The opposite happens after half lunar period. The final value of $\mathscr{C}_{3f}$ depends on the energy gain induced from thrusting and the perturbing bodies' overall effect, causing oscillations in the trajectory performance.

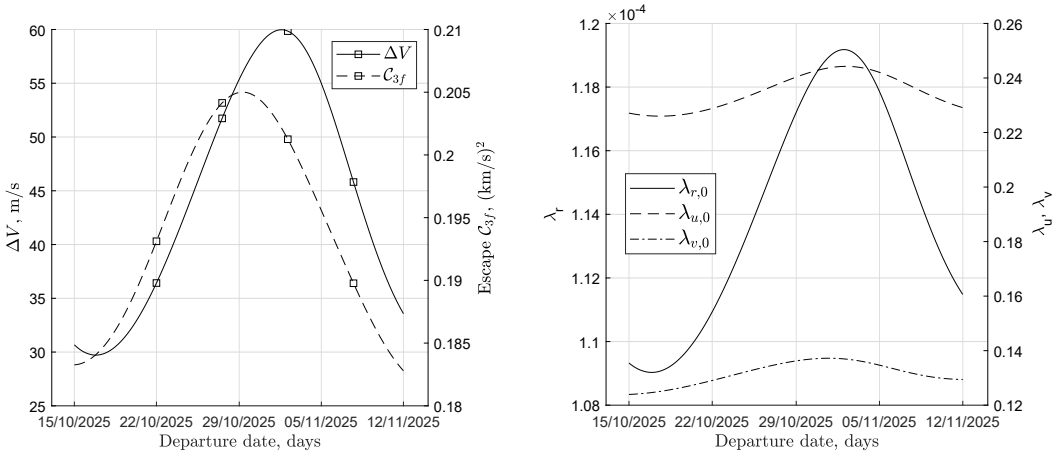

Fig. 5.11 SEL2 escape trajectories over a whole lunar month, fixed $\Delta t = 90$ days - trend over time of cost ΔV and free $\mathscr{C}_{3f}$ (left), adjoint variables $\lambda_{r,0}$, $\lambda_{u,0}$, $\lambda_{v,0}$ (right)

The converged optimal initial values for the velocity adjoints modify accordingly. The mission cost ΔV closely follows the position adjoint variable λ_r trend. The greater $\lambda_{r,0}$, the longer the thruster has to operate while changing the corresponding state variable, i.e. the position radius. The two in-plane velocity adjoint variables λ_u and λ_v, on the other hand, evolve accordingly to accommodate the longer thrust, but they do keep the same ratio, always thrusting at optimal initial angles around 60°.

However, the effect of Sun's pull is dominant, while oscillations are due to the Moon. Figure 5.12 shows the trend of these coefficients; again, SEL_2 escape trajectories exploit mostly the radial perturbation, with slight fluctuations of the tangential perturbation that, however, always acts favorably. Even though they are not an exact measure of solar effect, the η_{sg} coefficients, from equation (5.15), correctly match the actual propellant consumption trend, with minimum propellant requirements in the region between maximum $\eta_{sg,u}$ and $\eta_{sg,v}$.

Figure 5.13 represents two views of the same phase-space representation for the five escape trajectories pertaining to the same family I. The left Figure shows that despite minor differences at the beginning of the trajectories, depending on the

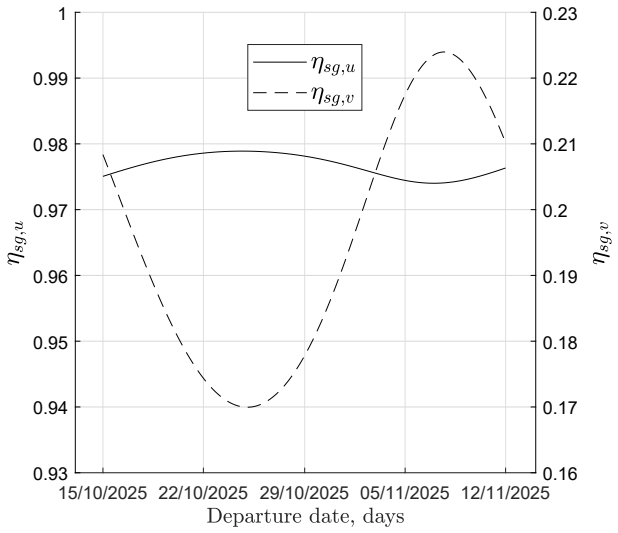

Fig. 5.12 SEL2 escape trajectories - radial and tangential overall perturbation effect over a lunar month

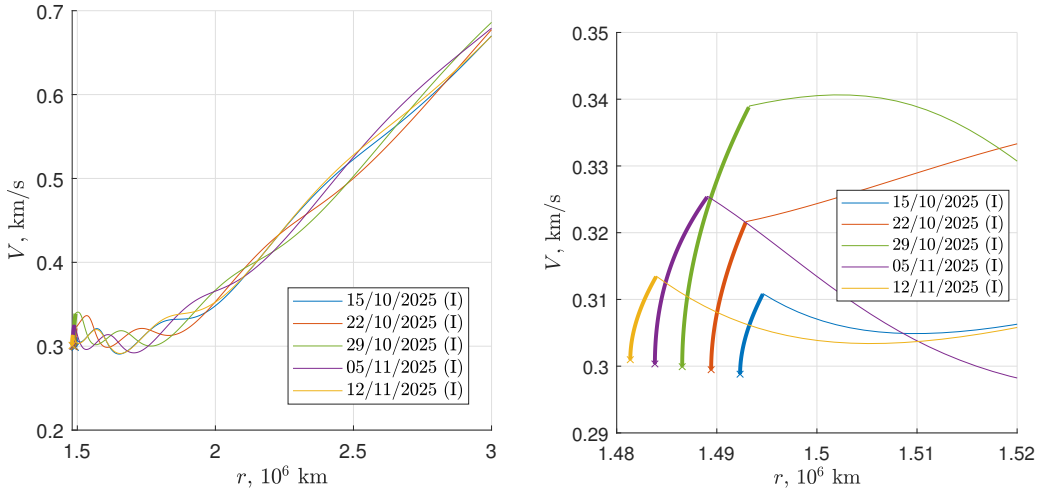

Fig. 5.13 SEL2 selected escape trajectories, fixed $\Delta t = 90$ days - phase-space representation (left), zoomed view (right)

SC initial state at epoch, every solution optimally finds a way to achieve a specific configuration to increase its energy while escaping thanks to the Sun perturbation. Please note that, given the similarities between this specific phase-space plot and the characteristic energy over time (Figure 5.7), this type of representation will not be proposed again in the following Sections. On the contrary, the right portion of Figure 5.13 allows appreciating the initial actions that each trajectory performs to achieve the same terminal conditions. All trajectories apply thrust in both the

(positive) tangential and radial directions, confirming the findings in the optimal thrust angle in Figure 5.5, and have a similar behavior, thus confining them in the same family. Again, the SEL_2 scenario may seem to provide trivial results, but it is very helpful in providing the right tools with more straightforward results for more complex cases.

5.2.2 Application: interplanetary trajectories from Sun-Earth L_2 towards Near-Earth Asteroids with imposed mission duration Δt

In a recent publication [48], fixed time-to-escape trajectories from SEL_2 in Section 5.2.1, departing on epoch $\mathcal{E}_1$, were used as tentative transfers to Near-Earth Asteroids (NEAs). Specifically, a set of 75 asteroids with small Minimum Orbit Intersection Distance (MOID) used in previous works [126, 127] was considered. As anticipated, when designing an interplanetary trajectory, preliminary analyses usually employ the patched-conic approximation. As recently carried out in two studies pertaining to the ARRM mission [128, 129], escape maneuvers and heliocentric transfers are often studied independently, and the results are then combined for a high-fidelity analysis of the whole transfer.

According to Figure 5.10, the escape direction for each of the free $\mathscr{C}_{3f}$ SEL_2 solutions has a specific orientation in the Sun-Earth system. Therefore, such escape trajectories should be suited to reach only the targets that require a similar orbit correction at the selected departure. Conversely, for each asteroid there is a departure date that maximizes the positive effect of the escape orientation. Departure from Earth's position with null $\mathscr{C}_{3f}$ on January 13, 2026 (i.e., $\mathcal{E}_1 + 90$ days) is assumed as the reference trajectory. The length of the heliocentric transfer to rendezvous with the asteroid is 3 years. The reference solutions are compared to trajectories with departure from the actual heliocentric position and velocity corresponding to the 90-day escape trajectory departing October 15, 2025.

In this example, escape from SEL_2 improves the reference trajectory for 21 out of 75 available targets. Propellant budget comparison for these solutions is shown in Table 5.4, ordered by percentage propellant saving. The difference in consumption with the reference trajectory is sometimes quite large. Note that 8 out of the first 10 asteroids have perihelion in the first quadrant, where the perihelion of the heliocentric

orbit at escape lies; the required change in orbital elements is reduced, explaining the saving. This general finding contains exceptions since the phasing constraint may affect the optimal rendezvous transfer which, in turn, may require different orbital adjustments.

Table 5.4 SEL2 escape trajectories - asteroid rendezvous propellant mass requirements

Asteroid	Reference m_p kg	90-day escape kg	% saving
2016 TB57	111.1	76.5	31.2
2013 XY20	82.4	59.7	27.5
2016 CF137	110.5	82.5	25.3
2017 BF29	88.9	66.8	24.8
2011 AA37	64.1	53.1	17.2
2012 BA35	185.7	152.8	17.7
2007 DD	185.3	152.6	17.6
2017 HK1	106.8	88.6	17.1
2015 TJ1	86.0	73.6	14.4
2014 EK24	80.0	69.6	13.0
2017 HZ4	123.4	108.9	11.8
2006 FH36	143.9	126.8	11.9
2015 BM510	88.6	78.8	11.0
2010 HA	76.5	68.3	10.8
2009 OS5	77.7	69.4	10.7
1996 XB27	70.3	63.6	9.6
2016 FY2	106.3	97.0	8.8
2015 VV	75.2	70.0	6.9
2001 QJ142	82.7	79.6	3.8
2013 EM89	66.3	64.9	2.1
2013 RV9	103.7	102.3	1.4

5.2.3 Sun-Earth L_2 escapes with constrained final energy $\mathscr{C}_{3f}$

Fixed-time escape trajectories can be observed under two different nuances. On the one hand, they do provide an optimal trajectory to reach a desired terminal position while achieving certain terminal energy, and such a framework may be the desired one for a specific mission. On the other hand, they prove to be extremely useful in the indirect method optimization; their convergence is more straightforward compared to problems with other terminal conditions. Indeed, as fixing the mission duration imposes that the Hamiltonian at the final time is free, also when final BCs on velocities are assumed, the corresponding adjoint velocity components are free. The whole optimization problem becomes more sensitive to the initial guesses $\boldsymbol{\lambda}_{V,0}$, and these are not guided anymore to converge to null values. Therefore, the optimal initial guess for the fixed time to escape scenario can be seeded as the tentative solution for the free-time, fixed-energy $\mathscr{C}_{3f}$ mission.

Optimizations on the final achieved energy at the escape boundary, therefore, are slightly more complex. For an interplanetary transfer, the escape leg is the first mission objective and specific values of escape energy and $\mathscr{C}_{3f}$ are sought. For example, in a recent publication [48], the three final velocities at r_f were used to start the interplanetary leg to rendezvous with specific NEAs; here, a different terminal condition is sought, namely the module of the terminal velocity and, thus, the $\mathscr{C}_{3f}$, leaving the direction free. Preliminary analysis has in fact shown that the cost of changing the escape velocity direction is usually very high (please refer to Section 5.2.2). If the final $\mathscr{C}_{3f}$ value is constrained, the escape trajectory is modified to change the overall effect of Sun's pull. Two case studies have been analyzed, by imposing the final $\mathscr{C}_{3f}$ equal to 0.2 (low-energy $L\mathscr{C}_{3f}$) and 0.5 (high-energy $H\mathscr{C}_{3f}$) $(\text{km/s})^2$.

Given the high sensitivity of the convergence process to the adjoint variables' initial values, both the exploration procedure to generate a family of solutions, and the passage from a solution with the same departure date to a new case with different final conditions, are particularly delicate. In a recent contribution [126], the author developed specifically tailored techniques on the $\mathcal{S}_{\mathcal{F}}$ to guarantee robustness of the method. Here a further improvement is implemented, namely an adaptive automated algorithm able to compute initial guesses with specific and robust recovery mechanisms, presented at the end of this Section, in the flowchart in Figure 5.22.

The first $\mathscr{C}_{3f}$-constrained converged solutions are the case studies with departing epochs $\mathcal{E}$ in the low-energy scenario. As presented in Table 5.3, the free $\mathscr{C}_{3f}$ achieved from the fixed-time solutions is very close to the desired $L\mathscr{C}_{3f}$, and thus such an optimal solution could be used as tentative ones for the present scenario. However, this set of low-energy tentative solutions has been built one-to-one on user experience, namely by imposing the initial thrust aligned with the velocity vector and with a simple 2-arc T-C T_S, and then verified with a continuation method from the fixed-time solutions. Intermediate epochs $\mathcal{E}_i < t < \mathcal{E}_{i+1}$, with $i = 1,\ldots,4$, have been found via an *ad hoc* continuation method. A gradual variation is imposed, starting from the free final $\mathscr{C}_{3f}$ solution towards the constrained one (or from $L\mathscr{C}_{3f}$ to $H\mathscr{C}_{3f}$) or using the closest available solution in terms of departure date as a tentative guess. If a forward search from an earlier date and a backward search from a later date do not end up at the same point, solutions belonging to different families f are found.

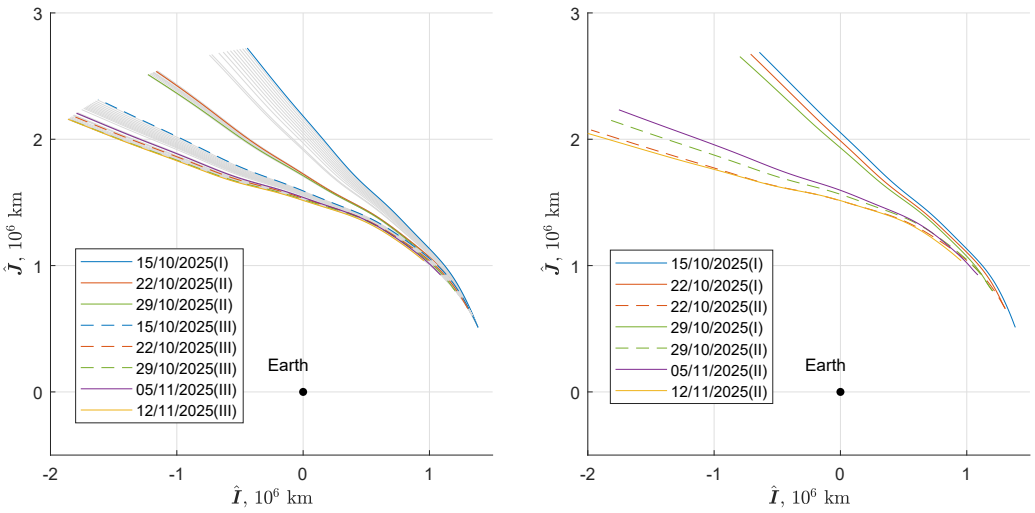

Fig. 5.14 SEL2 escape trajectories over a lunar month, fixed $L\mathscr{C}_{3f} = 0.2$ $(\mathrm{km/s})^2$ (left), fixed $H\mathscr{C}_{3f} = 0.5$ $(\mathrm{km/s})^2$ (right), free Δt, EME2000 RF

This bifurcation phenomenon is also visible in Figure 5.14 (left). Three families of solutions arise when solutions are forced to $\mathscr{C}_{3f} = 0.2$ $(\mathrm{km/s})^2$. Solutions for $\mathscr{C}_{3f} = 0.5$ $(\mathrm{km/s})^2$ evolve into two different families (Figure 5.14, right); trajectories belonging to family $f = \{\mathrm{I}, \mathrm{III}\}$ in the $L\mathscr{C}_{3f}$ case are transitioned into their corresponding $H\mathscr{C}_{3f}$ family, whereas those in family II merge into family I. Suboptimal solutions are found by forcing the $L\mathscr{C}_{3f}$ family II to preserve the orientation in the $H\mathscr{C}_{3f}$ case.

The first family has departure dates spanning between 15 October 2025 and 21 October 2025, with trajectories that tend to be radial and have short trip times when observed in the EME2000 RF. The second family is for departures between 18 October 2025 and 2 November 2025. The third family extends over the whole lunar month, and has trajectories with a more tangential velocity with respect to the other solutions. For example, $\mathcal{E}_1$ solutions in Figure 5.14 depart from the same location but bifurcate towards radial ($f = \text{I}$) and tangential ($f = \text{III}$) directions. Analogous considerations are shown in Figure 5.15 (left), in which all the trajectories reach the same final $\mathscr{C}_{3f}$ but with different costs and mission durations. Precise UTC limit epochs per each family are presented in Table 5.5.

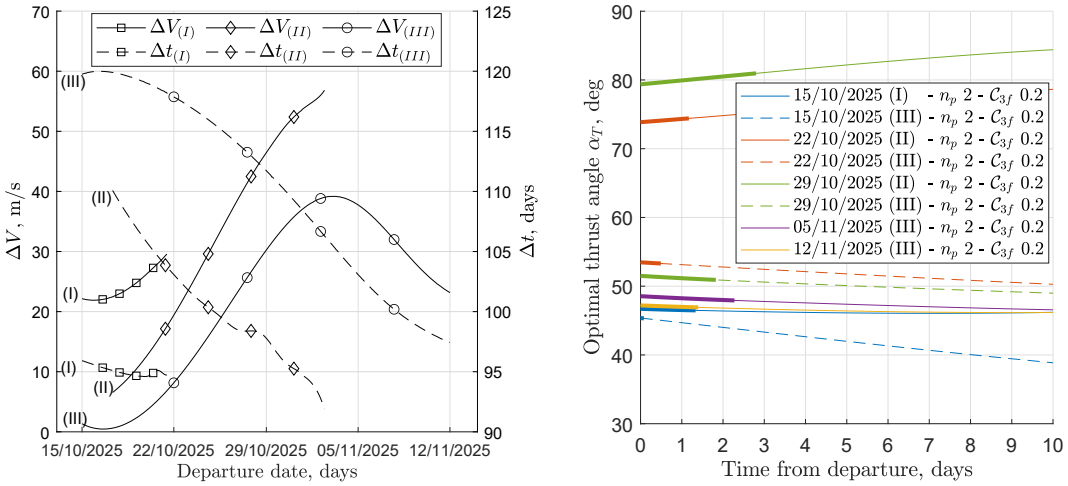

Fig. 5.15 SEL2 escape trajectories over a whole lunar month, fixed $L\mathscr{C}_{3f}$ - trend over time of cost ΔV and free Δt (left), optimal thrust angles α_T (right)

Table 5.5 SEL2 escape trajectories - epoch ranges for families of solutions

f	Epoch	
	Start	End
I	15/10/2025 08:58:15.543	21/10/2025 19:50:08.904
II	17/10/2025 16:46:41.259	02/11/2025 19:14:33.340
III	15/10/2025 08:58:15.543	12/11/2025 08:03:06.774

Figure 5.15, on the right, shows a zoomed portion of the departing optimal in-plane thrust angles α_T for all the selected solutions. Family I and III depart in a very similar way, almost equally distributing the thrust between the radial $\hat{\boldsymbol{u}}$ and tangential $\hat{\boldsymbol{v}}$ directions in the ZEN RF. However, $\alpha_{T,\mathcal{E}_{1(I)}} > \alpha_{T,\mathcal{E}_{1(III)}}$, namely the

departure thrust angle favours more the radial direction with a longer thrust arc in family I compared to the one in family III, showing that the SC is actively moving towards radial directions to acquire sooner a positive solar perturbation (thus the shorter trip times). On the other hand, the $\mathcal{E}_1$ family III solutions demonstrate that the minimal thrust at the beginning is used to depart from L_2, and then the longer coast arc is required to passively wait for the positive angular conjunction between the Sun and the SC. Family II solutions, instead, try to adapt to the family I strategy and thrust mainly in the $\hat{\boldsymbol{u}}$ direction. They perturb sooner the SC relative orientation with respect to the Sun, anticipating the arise of the solar tangential positive perturbation. Such longer initial thrust arc induces an initial slightly higher energy; then, the SC waits at almost constant energy while $\Delta\vartheta \to -135°$. The required energy for the escape is obtained later on during a more robust tangential perturbative coast arc. All these information are shown in Figures 5.16 and 5.17.

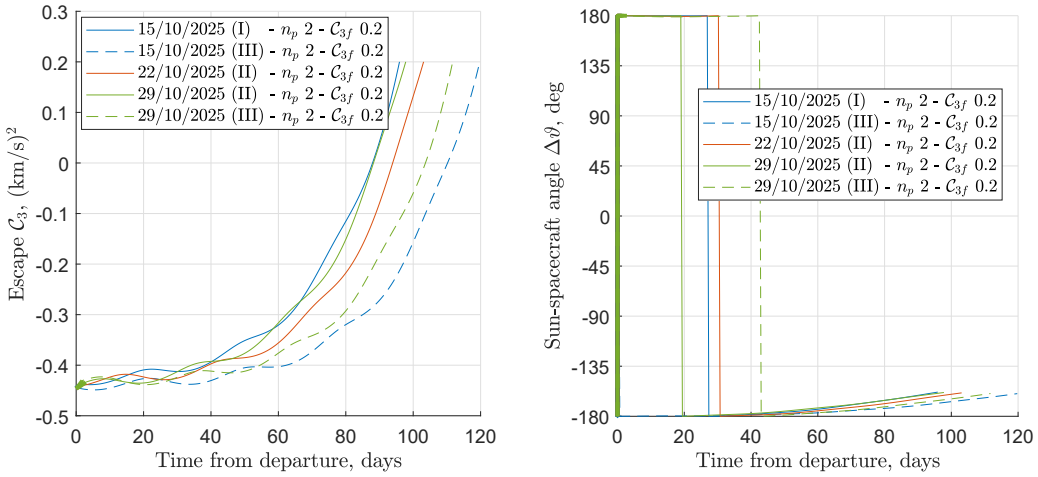

Fig. 5.16 SEL2 selected escape trajectories - time evolution of the characteristic energy $\mathcal{C}_3$ (left) and Sun-SC relative angle $\Delta\vartheta$ (right)

Figure 5.17 shows the phase-space representation of solutions for selected departure dates from Figure 5.14, for $\mathcal{C}_{3f} = 0.2$ (km/s)^2 on the left and $\mathcal{C}_{3f} = 0.5$ (km/s)^2 on the right. Both Figures show a zoomed portion of the initial departure stages. Again, here the families bifurcation phenomenon is clearly visible when more than one solution originates from the same initial point, which is represented for ease of visualization with a key-colored small cross. In Figure 5.17 (left), for example, solutions belonging to family II prefer a longer burn in the radial direction, thus increasing both position and velocity during the initial stages, whereas those in family III also include a tangential component, thus preserving a similar radius during the

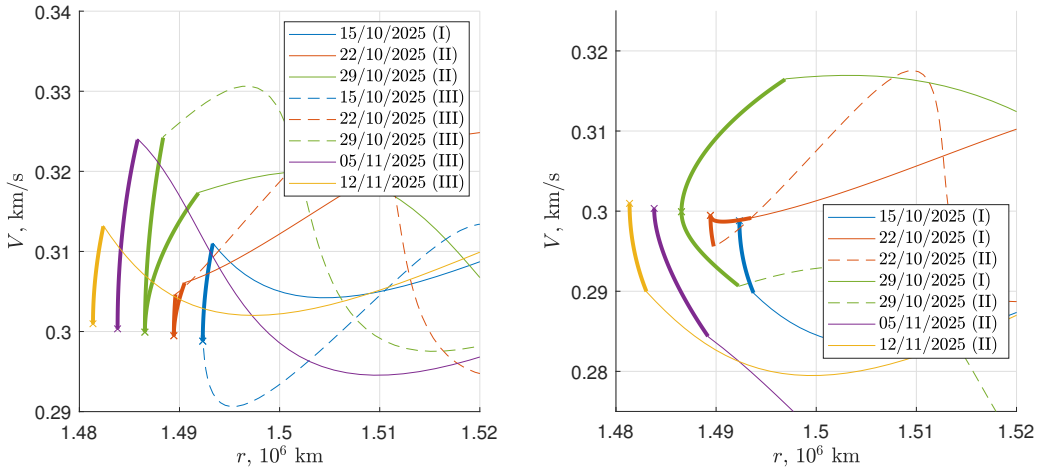

Fig. 5.17 SEL2 selected escape trajectories, phase-space representation with respect to Earth - fixed $L\mathscr{C}_{3f} = 0.2\ (\mathrm{km/s})^2$ (left), fixed $H\mathscr{C}_{3f} = 0.5\ (\mathrm{km/s})^2$ (right)

first burn, in agreement with the optimal thrust angles shown in Figure 5.15. Similarly, in the $H\mathscr{C}_{3f}$ case (Figure 5.17, right), the different behavior between family I and family II $\mathcal{E}_3$ solutions is evident, where both strategies favor an initial radial burn but in the accelerating and decelerating directions, respectively. Please note that the "family" concept should not lead to the misunderstanding that all solutions belonging to the same family must behave identically. On the contrary, solutions in the same family may have slightly different behaviors while still aiming for the same final result. For example, in the $L\mathscr{C}_{3f}$ scenario, the solution belonging to family III in $\mathcal{E}_1$ is the only one that decelerates. However, due to its initial state and the evolution of sun-SC perturbation during the escape, this maneuver is the optimal choice for a similar evolution and, therefore, it belongs to the same family.

Therefore, for the same departure date, it is possible to pick different strategies according to the specific needs; at the same time, it is clear that the improved code allows the indirect method to find various solutions without falling into the same local minima. In this case, family III is always the better solution for what concerns propellant consumption, but different constraints ($\mathscr{C}_{3f}$ value, additional time constraints) may change the scenario.

Figure 5.18 shows the trend of the spacecraft energy over time (left) and the Sun-SC relative angle (right) for the same departure epoch, $\mathcal{E}_1$, and for different terminal conditions. The $H\mathscr{C}_{3f}$ solution includes an evident second thrust arc after a coast arc, for a total of three phases in a T-C-T strategy. Instead of increasing

the duration of the first burn, the optimal solution reduces initial thrusting in favor of a longer terminal thrust arc, while the solar perturbation has a more substantial positive effect. The same considerations are depicted in Figure 5.19.

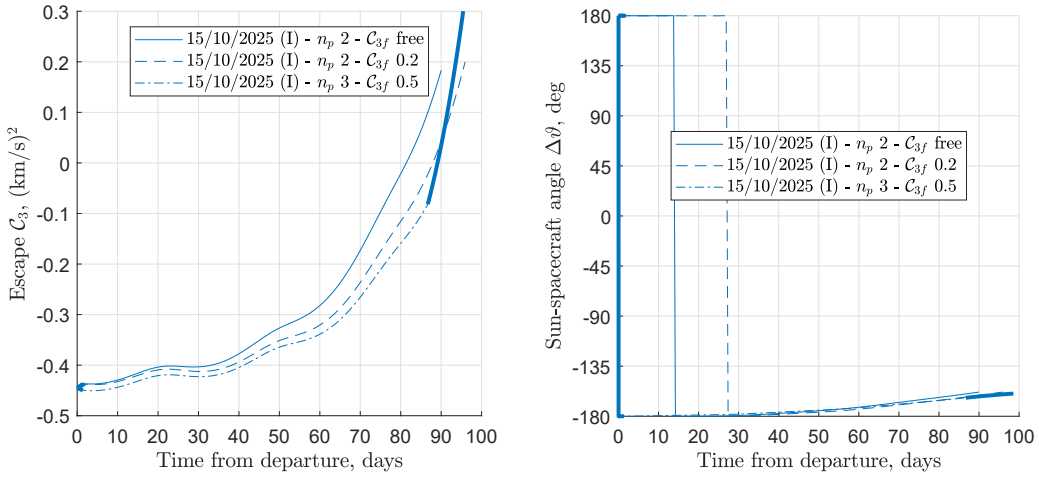

Fig. 5.18 SEL2 - SC energy over time (left), Sun-SC relative angle $\Delta\vartheta$ (right), comparison between free and fixed $\mathcal{C}_{3f}$

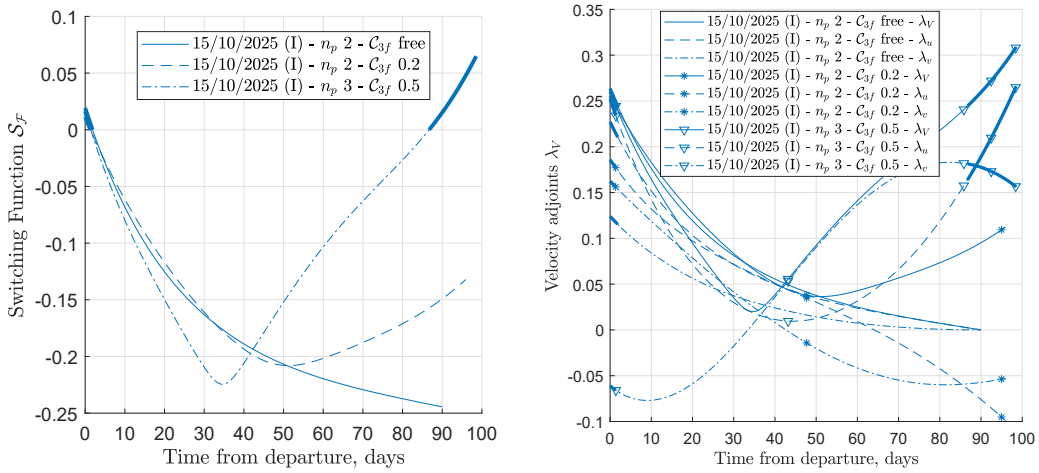

Fig. 5.19 SEL2 - switching function $\mathcal{S}_\mathcal{F}$ (left), velocity adjoints (right), comparison between free and fixed $\mathcal{C}_{3f}$

Here the $\mathcal{S}_\mathcal{F}$ (left) and the time-evolution of the planar adjoint velocity components, as well as the primer vector (right), are presented for these selected departures. While the free terminal energy scenario shows a monotonically decreasing $\mathcal{S}_\mathcal{F}$, with $\boldsymbol{\lambda}_V(\Delta t) = \mathbf{0}$, the $L\mathcal{C}_{3f}$ strategy shows a sign change in the $\mathcal{S}_\mathcal{F}$ derivative. This demonstrates that the requested propulsive effort is becoming more and more demanding, and for $\mathcal{C}_{3f} > L\mathcal{C}_{3f}$ it may be necessary to change the T_S. Indeed, for the

$H\mathscr{C}_{3f}$ case, the λ_V peaks again in the terminal phase of the trajectory, and to respect PMP a further thrust phase is requested, modifying the T_S.

Tables 5.6 and 5.7 show the solutions for the escape trajectories with fixed final energy. In the lower final energy scenario, multiple families of solutions arise; some trajectories exploit more consistently the solar perturbation whereas others use more propellant. In the scenario with higher final energy, a second consistent final burn is needed to reach the desired final energy with shorter radial trajectories in the first family and lengthier tangential ones in the second.

Table 5.6 SEL2 escape trajectories performance - fixed $\mathscr{C}_{3f} = 0.2$ $(\mathrm{km/s})^2$, free Δt

$\mathcal{E}$	f	n_p	$\eta_{sg,u}$	$\eta_{sg,v}$	$\overline{\eta_{sg}}$	ΔV m/s	Δt days
1	I	2	0.782	0.160	0.471	22.155	95.92
2	II	2	0.842	0.162	0.502	19.416	103.08
3	II	2	0.795	0.181	0.488	46.462	97.78
1	III	2	0.980	0.193	0.586	1.346	119.75
2	III	2	0.965	0.164	0.564	8.153	117.87
3	III	2	0.914	0.158	0.536	30.253	111.72
4	III	2	0.841	0.173	0.507	37.757	103.07
5	III	2	0.796	0.162	0.479	23.155	97.44

Table 5.7 SEL2 escape trajectories performance - fixed $\mathscr{C}_{3f} = 0.5$ $(\mathrm{km/s})^2$, free Δt

$\mathcal{E}$	f	n_p	$\eta_{sg,u}$	$\eta_{sg,v}$	$\overline{\eta_{sg}}$	ΔV m/s	Δt days
1	I	3	0.805	0.199	0.502	220.205	98.60
2	I	3	0.758	0.171	0.464	243.733	92.61
3	I	3	0.716	0.175	0.445	267.987	87.71
2	II	3	0.983	0.173	0.578	222.191	119.15
3	II	3	0.898	0.237	0.568	242.771	109.95
4	II	3	0.822	0.253	0.537	246.049	101.40
5	II	3	0.817	0.205	0.511	221.774	99.83

In order to verify that the trajectories do not end up in unwanted reentries in the Earth's gravitational influence, Figures 5.20 and 5.21 show the semimajor axes and the Sun-SC radius r_{sSC} of all the SEL_2 fixed-energy reference trajectories in the Heliocentric Ecliptic (HE) RF, on the left for the $L\mathscr{C}_{3f}$ case and on the right for

the $H\mathscr{C}_{3f}$ one. The integration is extended to 4 times the time to escape to show the SC evolution at later times. While for the $L\mathscr{C}_{3f}$ case this operation produces a simple extension of the final coasting phase, in the $H\mathscr{C}_{3f}$ scenario the appearance of a fictitious terminal fourth coasting phase is needed. All trajectories have similar trends with comparable costs, almost equal use of the solar perturbation and similar final energies. The escape directions are slightly different and therefore the orbital parameters show minor different trends. It is worth noting that small variations occur after the escape for the residual Earth's gravity influence. Nevertheless, departures spaced apart by one lunar month overlap again quite precisely.

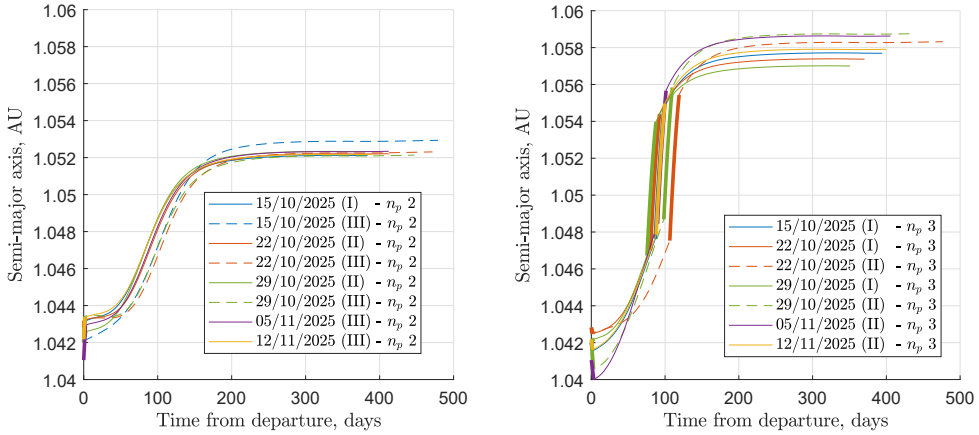

Fig. 5.20 SEL2 escape trajectories - fixed $L\mathscr{C}_{3f}$ (left), fixed $H\mathscr{C}_{3f}$ (right), semimajor axis in the HE RF

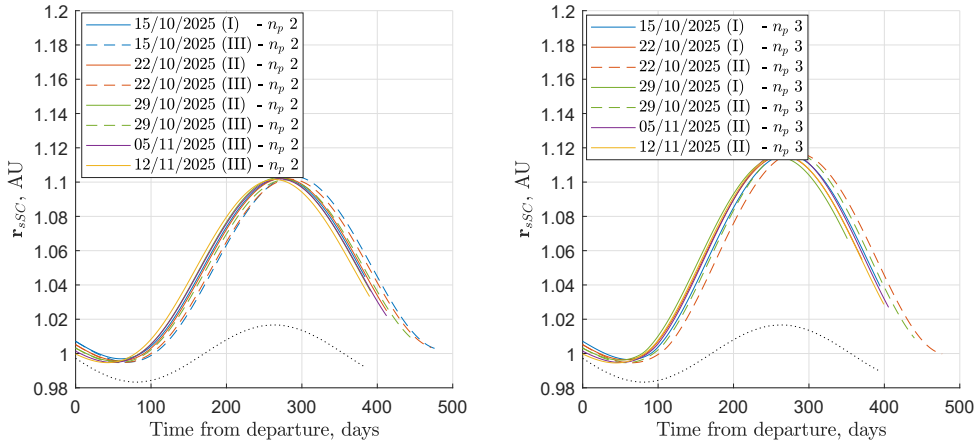

Fig. 5.21 SEL2 escape trajectories - fixed $L\mathscr{C}_{3f}$ (left), fixed $H\mathscr{C}_{3f}$ (right), Sun-SC position vector in the HE RF

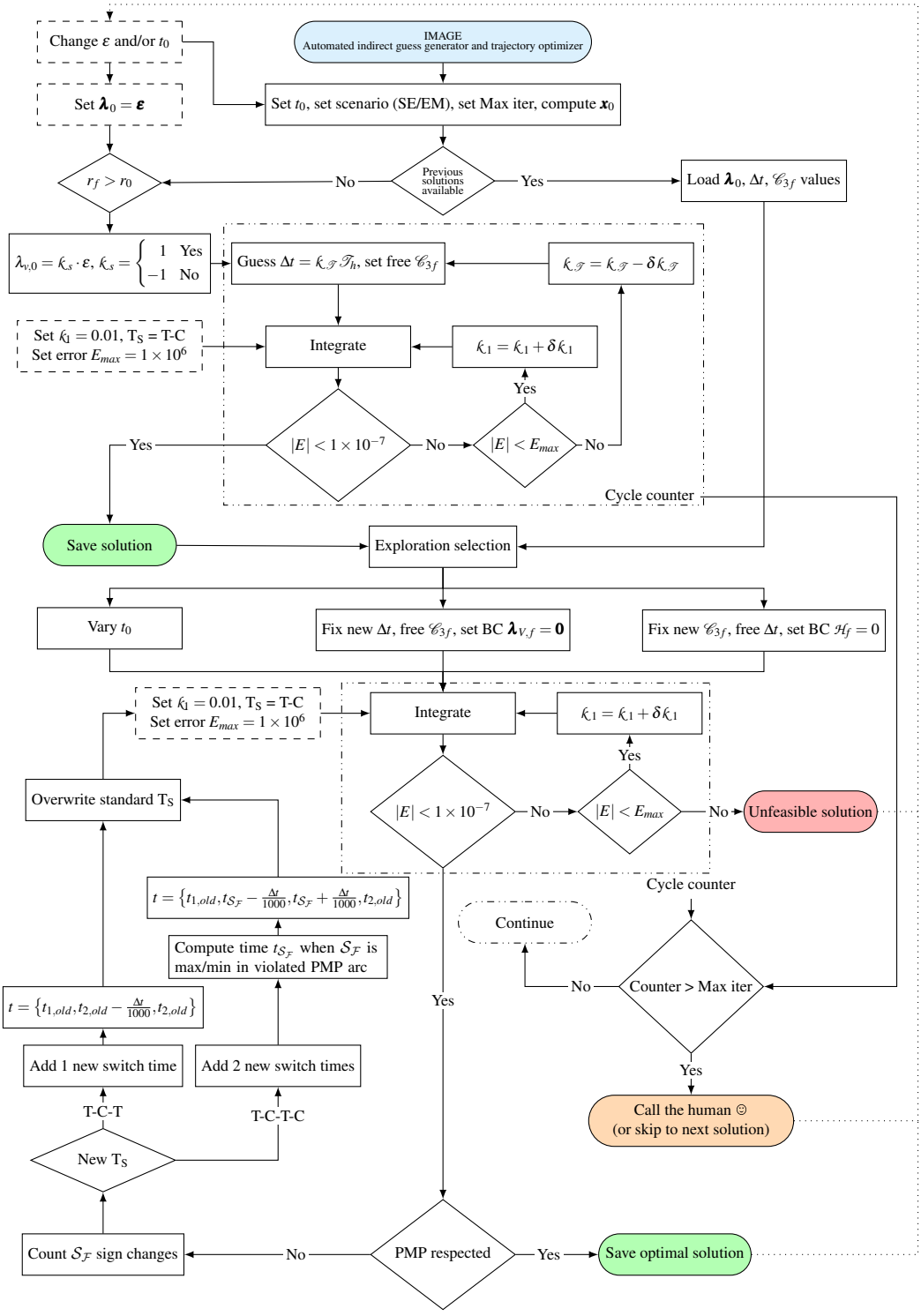

Fig. 5.22 IMAGE (Indirect Method Automated Global Exploration) automated continuation scheme algorithm - management of PMP compliance and automatic new T_S generations

Figure 5.22 shows the entire structure of the Indirect Method Automated Global Exploration (IMAGE) code, which is designed to autonomously search for low-thrust trajectories using an IM. It requires some basic input such as the maximum number of iterations and tolerance choices, as well as the dynamic system being explored. The code initially calculates the initial position in the synodic RF of a specific binary system, as per equation (5.2). Once this is done, the code has everything it needs to begin its work.

The exploration can begin immediately if a guess solution is already available at the correct or reasonable contiguous epoch or terminal condition. Otherwise, IMAGE only needs to know the boundary conditions to generate the correct guess values for the adjoint variables, specifically for $\lambda_{v,0}$ (positive for raising orbits, negative for reducing orbits), and a tentative time to escape based on the approximate information from the 2BP (equation (5.3)). The trajectory optimization code is then prompted with these initial guesses ($\boldsymbol{x}_0$ based on the scenario, and fixed mission duration). The number and size of the integration steps are generally small in the early stages, but if the final error is reduced, the step size can be slightly increased for the next run, ensuring significant robustness and improving the computational speed. If the error at the end of the procedure is beyond a specific threshold, a relaxation coefficient $0 < \mathcal{k}_{\mathcal{T}} < 1$ is applied to the estimated Δt, and the procedure is restarted until convergence or the maximum allowed number of iterations is reached. If the solution converges, it is saved and marked as potentially non-optimal. This information is essential because IMAGE has generated this solution almost "blindly" and it should be possible to overwrite this solution if a better one is found later.

At this point, a solution has been obtained, and initial values are available for the adjoint variables $\boldsymbol{\lambda}_0$ and the mission duration Δt. The user can then choose to either continue with a temporal exploration (same boundary conditions but different epochs), explore different mission durations, or different characteristic energies. If the user chooses to continue with temporal exploration, the guess solution is given to the integrator by specifying a different t_0. In the other two cases, the program automatically modifies the definition of the Optimal Control Problem (OCP) as described in Sections 4.2, 4.2.1 and 4.2.2.

The integration process continues as previously described, but with one key difference. If convergence is achieved, the solution is checked to see if it is PMP-compliant. If it is, the solution is saved as an optimal trajectory, labeled with a string

containing all necessary information for its identification (such as the binary system, starting epoch, EP thruster I_{sp}, boundary conditions, number of thrust phases, PMP compliance flag, and final mass). If the solution has converged but does not respect the PMP, a change in strategy is needed. Figure 5.22 shows the case where one or two thrust phases are added, but the code can also reduce the number of thrust phases if necessary. Whenever a thrust phase is added (or removed), an interior-point boundary condition is automatically inserted at the most appropriate point. If the code determines that an additional thrust phase may be needed near the end of the mission, it includes a very short thrust phase just before $t = \Delta t$. If a thrust phase is needed in the middle of a coasting phase (T-C $\rightarrow$ T-C-T-C), the value where the $\mathcal{S}_{\mathcal{F}}$ is maximum or minimum in the violated arc is selected as a midpoint, and two switching times are inserted immediately before and after. Finally, the T_S is overwritten and the integration process restarts, resetting the relaxation parameters. With the new T_S, the integration will try to fit these new phases appropriately and hopefully converge while following the PMP.

An internal routine also checks if the same initial conditions appear in two different saved solutions. If this is the case, the best solution may overwrite the other one if a) there are just minor changes in $\boldsymbol{\lambda}_0$ that provide a minimal improved solution, or b) the worst solution is not PMP-compliant and has a different T_S.

Obviously, like every code that is being developed and improved, there is still the "help" section in orange. Some unexplored edge cases or exceptions may still require fine-tuning to be effectively automated and are subject to future research.

On average, up to six different contiguous solutions can be found every minute. If a change of thrust structure is required, the number of solutions per minute is reduced to four; when a solution oscillates around a minimum $1 \times 10^{-7} < |E| < 1 \times 10^{-6}$, after a certain number of iterations the free variable (time to escape or final energy, depending on the scenario) is fixed to the current value to improve convergence. This tweak, although rare, reduces the automated computational time to roughly one new solution per minute.

5.2.4 Automated global exploration of Sun-Earth L_2 escape trajectories over a year

To demonstrate IMAGE capabilities, two different automated explorations are shown below by varying the departure epoch t_0 for the escape trajectories in the SEL_2 scenario over a whole year, from January 1, 2026 to January 1, 2027. Each trajectory has been computed automatically by the code with a time step $dt = 12$ hours. Figure 5.23 contains the whole family of solutions for escape trajectories at fixed $\Delta t = 90$ days; all solutions assume a T-C T_S and is evident the influence of the Earth distance from the Sun on performance. Here it may become more clear the reason behind the choice of the selected epochs in Section 5.1.3; during such lunar month, the ΔV required to escape is at its minimum due to the positive effect of the Sun's perturbation, and that has been selected purposely to show more evidently such effect.

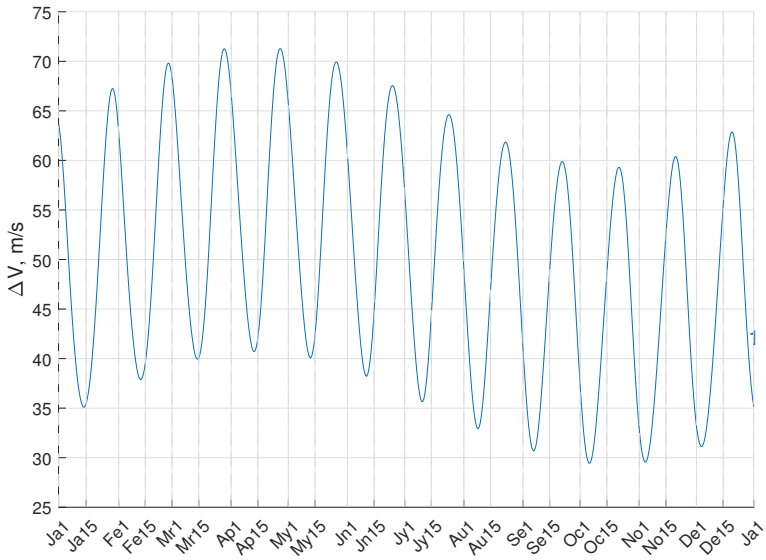

Fig. 5.23 SEL2 escape trajectories, fixed $\Delta t = 90$ days, free $\mathscr{C}_{3f}$ - trend over time of cost ΔV over one year - automated exploration from 01/01/2026 to 01/01/2027

With a closer inspection, the portion of solutions between October 15, 2026 and November 12, 2026 well match the performance presented in Figure 5.11, with slight differences due to the different years in which they are computed.

However, the powerful automated capabilities of IMAGE are even more evident in the constrained $L\mathscr{C}_{3f}$ scenario, in Figure 5.24. Here different families arise and the bifurcation among them is computed (and inferred) autonomously by accurately

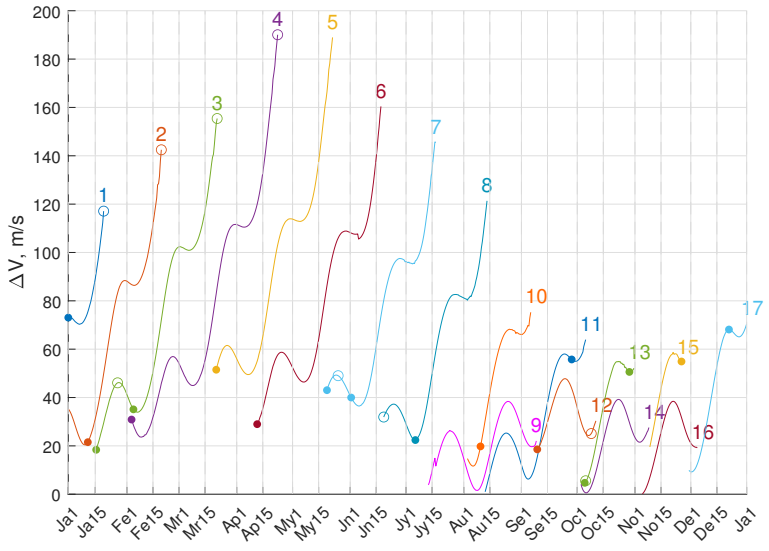

Fig. 5.24 SEL2 escape trajectories, fixed $\mathscr{C}_{3f} = 0.2\ (\mathrm{km/s})^2$, free Δt - trend over time of cost ΔV over one year - automated exploration from 01/01/2026 to 01/01/2027

noticing discontinuities in the initial adjoint vectors and mission durations. All families have a T-C T_S unless otherwise specified. Specifically, starting from January 1, 2026 and going forward in time up to January 1, 2027, if a trajectory passes from a two-burn, three-arcs strategy (T-C-T) to a single-burn strategy (T-C), then a small circle marker is added. If the opposite happens, a full dot marker is added. For example, family VII starts with a two-burn strategy around May 20, 2026 and preserves the same strategy up May 26, 2026, when the solution space switches to a single-burn scenario. On June 2, 2026, the optimal strategy changes again to a two-burn, up to the automated family cutoff around July 17, 2026.

It is clear that approximately every month, for all families that extend for that duration, there is a timeframe of reduced mission cost, happening when the Moon is reducing its distance from the Earth towards the minimum. The repetitive nature of this phenomenon is evident and extends to all families.

Families XII, XIII and XIV, specifically, match respectively families I, II, and III from Section 5.2.3, Figure 5.15 in a quite fascinating similar fashion. The part where the three families overlap is again around the beginning of the lunar month, around October 15, 2026 (corresponding to around October 22, 2025 in the selected cases).

5.3 Escape trajectories from Earth-Moon L_2

The dynamics in the vicinity of EML_2 is particularly complex even in the simpler CR3BP. The EM binary system is a very particular one, and humans can witness the binary system with the smallest primary-to-primary mass ratio, around 1:81 for Earth to Moon. There are more than 200 moons in the solar system, and each of them composes a binary system, under simplifying assumptions, with respect to their primary planet. For reference, Mars has two moons, Phobos and Deimos; 60 million Phobos or 320 million Deimos would be required to reach Mars' gravitational pull. Even the biggest Jupiter's moon, Ganymede, is in a 1:12000 mass ratio with respect to Jupiter itself. Therefore, while in all the other binary systems the simplifying assumptions of the CR3BP are very well respected, the EM scenario shows very complex gravitational interactions. The complexities intensify in the H4BP; the initial state for the SC is epoch-dependent as per equation (5.8) and may show a limited short-term stability. However, Moon's ephemerides make the Moon shift its position over time. At $\mathcal{E}_1$ and $\mathcal{E}_5$, the Moon has a positive gradient of its position vector, since it is moving from its mean average distance towards the maximum one (around $\mathcal{E}_2$, or $\mathcal{E}_5$ plus one week). At $\mathcal{E}_3$ the opposite happens, namely the Moon is lowering its position vector towards the minimum distance (around $\mathcal{E}_4$). Therefore, the initial pseudo-stability of the approximate (not anymore existent) L_2 location would see an approaching Moon, for $\mathcal{E}_1 \leq t_0 \leq \mathcal{E}_2$ and $\mathcal{E}_4 \leq t_0 \leq \mathcal{E}_5$, whereas the Moon would evolve detaching from the approximate L_2 position when $\mathcal{E}_2 \leq t_0 \leq \mathcal{E}_4$.

Such natural evolutions, in conjunction with all the perturbations deriving from the implementation of the H4BP, make the selection of the initial guesses for the unknown adjoint variables crucial and more challenging compared to the SE scenario.

The same specific five departure times in a lunar synodic period of the previous Section are again considered to explore the effect of the relative position of the Moon and the Sun on the escape maneuver. The first (October 15, 2025) and last (November 12, 2025) departures happen at times with the nominal Moon's mean orbital radius; a perturbed Moon orbit is considered so the positions in EME2000 are slightly different. The linearized L_2 distance is again used to define the spacecraft initial position, from equation (5.8). Like in the SEL_2 departure analysis, three scenarios are considered: the first with a fixed time to escape Δt and a free final energy, and other two with escape $\mathscr{C}_{3f}$ fixed at a lower (0.2 $(km/s)^2$) and higher (0.5 $(km/s)^2$) value with free time to escape.

5.3.1 Earth-Moon L_2 escapes with imposed mission duration Δt

As per the SEL_2 trajectories, single burn strategies are initially sought, with a T-C T_S. Figure 5.25 shows the manifold of departure trajectories over the whole lunar month, highlighting the selected departure epochs $\mathcal{E}$, whereas Table 5.8 shows the performance for the selected departure dates in each family.

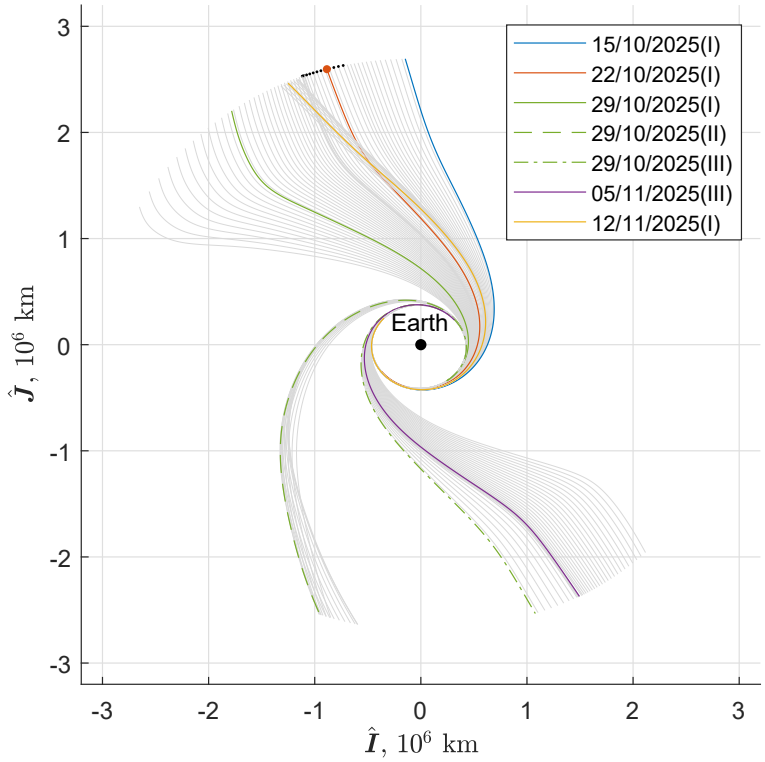

Fig. 5.25 EML2 escape trajectories over a lunar month, fixed $\Delta t = 75$ days, free $\mathscr{C}_{3f}$, EME2000 RF

Due to the greater dynamic complexity of the Earth-Moon system, even the trajectories with fixed final time and free final energy split into several families. Indeed, from $\mathcal{E}_1$ to $\mathcal{E}_5$, the Sun apparently revolves of $\approx 30°$ around the Earth, but the departure location, and thus the EML_2, moves with the Moon spanning 90° per departure. Such natural evolution of the Earth-Moon-Sun system changes the relative positioning of the SC at each departure epoch, producing different initial perturbative conditions. Due to these perturbative effects, there are also trajectories exploiting a second burn, distinguished by a small dot at the arc end in Figure 5.25. The switch from 2-arc to 4-arc solutions happens on 2025/10/20 17:19:38.689 UTC, and the *vice versa* happens on 2025/10/25 22:53:36.549 UTC.

Table 5.8 EML2 escape trajectories performance - fixed $\Delta t = 75$ days, free $\mathscr{C}_{3f}$

$\mathcal{E}$	f	n_p	$\eta_{sg,u}$	$\eta_{sg,v}$	$\overline{\eta_{sg}}$	ΔV m/s	$\mathscr{C}_{3f}$ $(\mathrm{km/s})^2$
1	I	2	0.833	0.064	0.448	48.763	0.3510
2	I	4	0.783	−0.429	0.177	61.183	0.1523
3	I	2	0.503	−0.712	−0.105	161.279	0.0026
3	II	2	0.434	0.750	0.592	20.476	0.4789
3	III	2	0.805	−0.106	0.349	17.412	0.3108
4	III	2	0.801	−0.376	0.212	38.572	0.1821
5	I	2	0.775	0.302	0.538	51.373	0.4430

Table 5.9 EML2 escape trajectories - epoch ranges for families of solutions

f	Epoch	
	Start	End
I	15/10/2025 08:58:15.543	31/10/2025 11:26:07.624
II	24/10/2025 17:35:41.049	02/11/2025 23:25:41.268
III	29/10/2025 02:13:59.266	11/11/2025 13:54:52.416
I	10/11/2025 08:36:56.916	12/11/2025 08:03:06.774

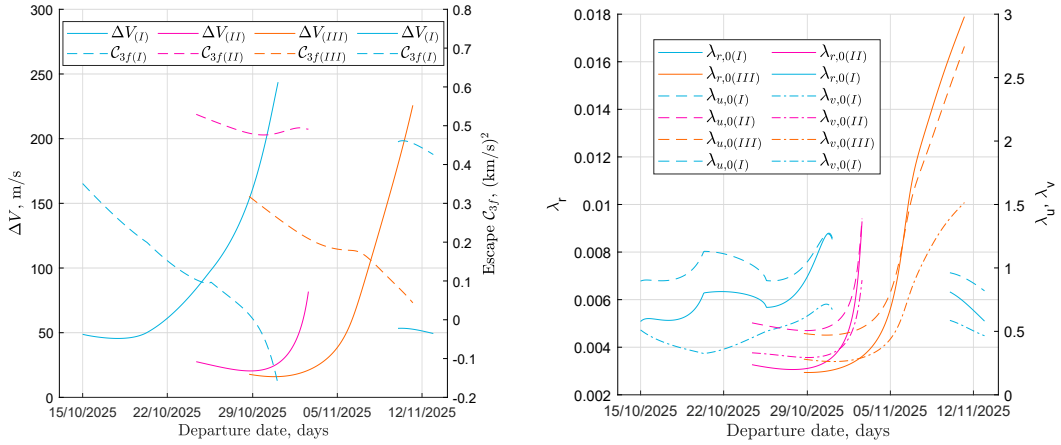

Fig. 5.26 EML2 escape trajectories over a whole lunar month, fixed $\Delta t = 75$ days - trend over time of cost ΔV and free $\mathscr{C}_{3f}$ (left), adjoint variables $\lambda_{r,0}$, $\lambda_{u,0}$, $\lambda_{v,0}$ (right)

Table 5.9 contains the epoch extremals dates for the families of solutions; please note that solutions pertaining to the second family I are the ones happening a lunar month after $\mathcal{E}_1$, therefore having the same overall strategy. Figure 5.26 shows the trend of propellant requests and achieved $\mathscr{C}_{3f}$ for the whole manifold of solutions over

the lunar month, with fixed time to escape $\Delta t = 75$ days. Family I covers departures between $\mathcal{E}_1$ and $\mathcal{E}_3$ and shows free $H\mathscr{C}_{3f}$ and minimal propellant consumption at $\mathcal{E}_1$, with a performance decrease towards $\mathcal{E}_2$; between $\mathcal{E}_2$ and $\mathcal{E}_3$ the propellant request becomes very high and the free $\mathscr{C}_{3f}$ shows negative values, suggesting that this specific escape maneuver may be not viable. Family II departures are located in the neighbourhood of $\mathcal{E}_2$ and have very high performance, with low propellant requests and very high free $\mathscr{C}_{3f}$. The third family covers departures from $\mathcal{E}_3$ almost to $\mathcal{E}_5$ and, as per family I, has higher performance at the lower end for both cost ΔV and achieved free $\mathscr{C}_{3f}$. Family I *bis*, around $\mathcal{E}_5$, retraces after a lunar month the performance of $\mathcal{E}_1$ solutions. Figure 5.26, on the right, shows the trend of the position adjoint variable $\lambda_{r,0}$ and the two in-plane velocity adjoints, $\lambda_{u,0}$ and $\lambda_{v,0}$; the worsening of performance, per each family, arises when the optimal adjoints gradient start peaking towards very high or very low values. At the same time, thrusting for longer periods does not directly imply achieving a greater terminal energy; if the Sun-SC relative positioning evolves towards very negative conditions, then even with longer thrust arcs only lower energy levels can be achieved. The relative Sun-SC angle for the case studies departure epochs, except for $\mathcal{E}_5$, is reported in Figure 5.27 (left), accompanied by the thrust angle configuration on the right. A supporting further representation in a polar view of the Sun-SC $\Delta\vartheta$ evolution is reported in Figure 5.28, where the solar perturbation coefficient σ presented in Figure 5.2 is superimposed to the $\Delta\vartheta$ Sun-SC evolution. The radial coordinate represents the Earth-SC position vector r_{ESC}; values are nondimensionalized ($r_0 = 0$, $r_f = 1$) and initial r_0 coordinates are separated by a small value for the sake of clarity.

The first reference departure case has a single-burn strategy with low propellant consumption. Its departure position starts at the rising of the positive tangential solar perturbation σ_v, and thrust is applied up to the point in which the radial perturbation σ_u aids the escape as well. Departures at $\mathcal{E}_3$ still have a single-burn T-C T_S, with different nuances in three families. The departure in family I is the least efficient among the three; this strategy tries to maximize σ_v during the first phase, showing an optimal thrust angle initially radial and evolving towards more tangential directions. By doing so, the SC does indeed exploit the positive tangential perturbation, but is forced to produce a long burn since it evolves for a long period (15 days $< t <$ 50 days) in the peak negative σ region, nullifying the propulsive effort. Even being PMP compliant, this strategy only represents a local optimum. Strategies II and III, instead, use a smaller thrust phase at the beginning, accepting to

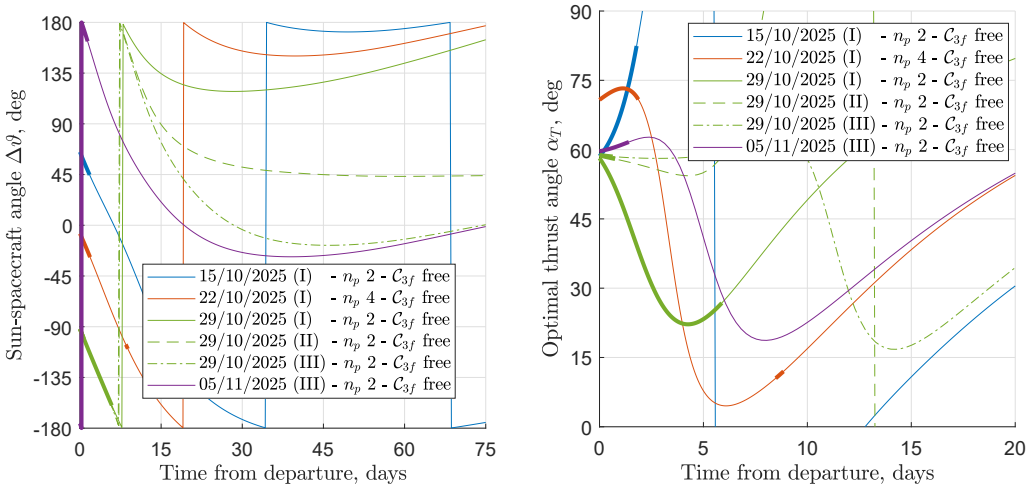

Fig. 5.27 EML2 selected escape trajectories, fixed $\Delta t = 75$ days - trend over time of Sun-SC relative angle $\Delta\vartheta$ (left), optimal thrust angles α_T (right)

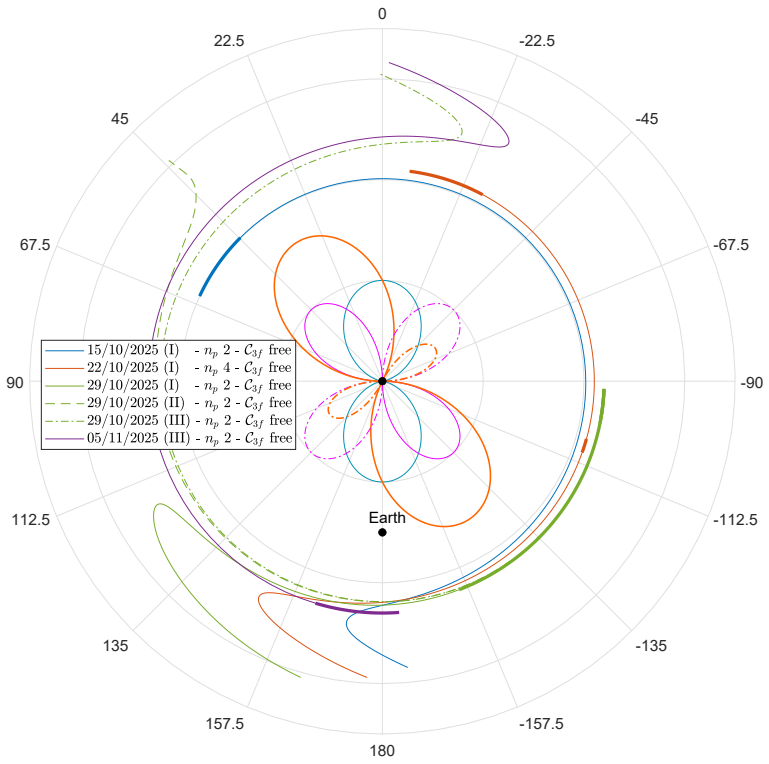

Fig. 5.28 EML2 selected escape trajectories polar view, fixed $\Delta t = 75$ days, free $\mathcal{C}_{3f}$, Earth-SC rotating RF

thrust only in the neutral perturbation condition $\Delta\vartheta \approx -90°$; however, such radial acceleration is enough to evade from L_2 and allows the SC to remain longer in the positive perturbative region and acquire enough velocity to overtake the region

rapidly with negative σ. This is a very useful example to understand the role of the solar perturbation with respect to the thrust itself; the more positive solar perturbations are exploited, the better the performance and the lower the propellant requests; on the other hand, the higher the propulsive effort in unfavourable zones, the higher the cost and the higher the loss in energy. The differences between $\mathcal{E}_3$ family II and III solutions derive from a slightly different thrust direction at the beginning; family III is slightly more radial than family II and applies the thrust for shorter times, thus experiencing a cumulative smaller σ_v, which affects the whole trajectory evolution. Please note that the presence of a significant radial component in α_T, for the EML_2 scenario, is highly likely to be a constant for all trajectories, since the SC has to separate consistently from the Moon after departure to avoid falling back towards it under its gravitational pull.

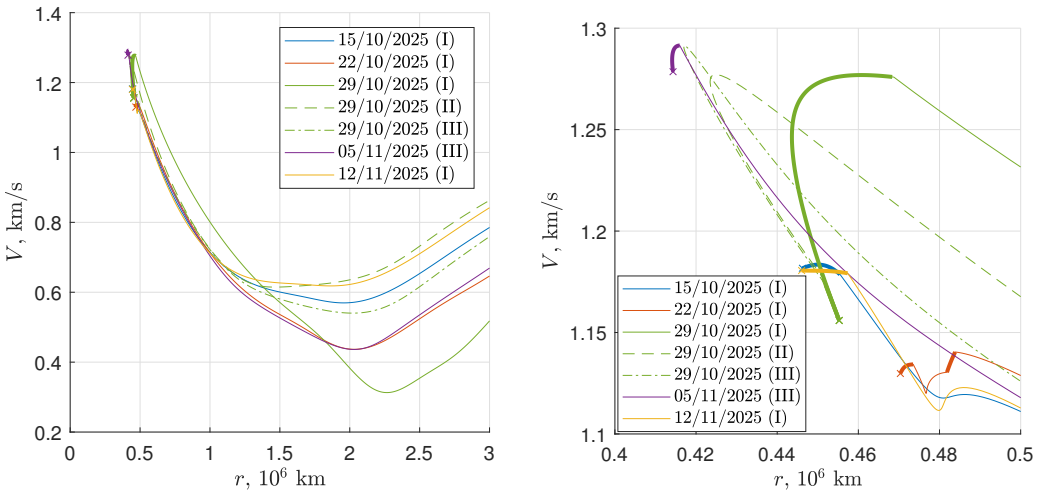

Fig. 5.29 EML2 selected escape trajectories, fixed $\Delta t = 75$ days - Earth-centered phase-space representation (left), zoomed view (right)

The same findings are presented in Figure 5.29. Family I solutions for all epochs adopt a significant increase of the radial distance with respect to a variation in velocity, except for $\mathcal{E}_3$ that requires an initial tangential burn to move the SC in a suitable configuration for such targeted condition. In turn, such long inefficient burn identifies an overall suboptimal trajectory, as confirmed in Figure 5.29 (left) where such solution provides the lowest terminal velocity -and, thus, characteristic energy- among all the others. The other solutions for $\mathcal{E}_3$ are generally more efficient; both trajectories perform a small burn that increases the velocity but also reduces the SC radius in what the author likes to call a *self swing-by*. Indeed, both get closer to the Moon, favorably exploiting its perturbation for the escape. The single selected case

for $\mathcal{E}_4$ is conveniently already placed at the initial time in the right spot to achieve a similar result.

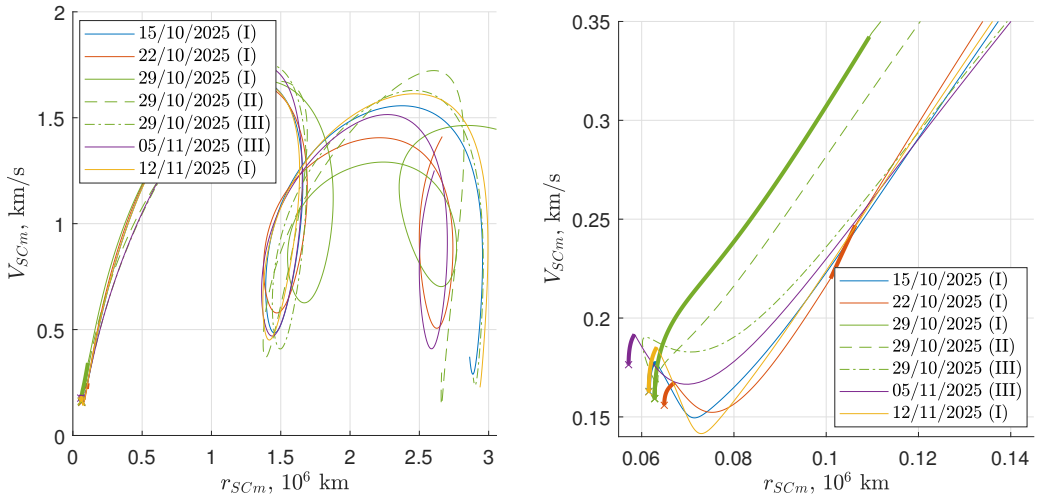

Fig. 5.30 EML2 selected escape trajectories, fixed $\Delta t = 75$ days - Moon-centered phase-space representation (left), zoomed view (right)

An even more insightful representation is provided in Figure 5.30 in which the phase-space representation of both the position and velocity quantities are computed with respect to the Moon's state over time. It is clear that all solutions accelerate tangentially in the direction of the Moon's velocity vector to escape, with some little differences in the radial configuration. For example, the trajectory departing at $\mathcal{E}_2$ has an overall radial optimal thrust angle Figure 5.27, and indeed departs more easily from the Moon, acquiring the highest portion of separation radius during the thrust phase -except for the suboptimal $\mathcal{E}_3$ family I trajectory-. Despite the characteristic evolution of all trajectories in the left representation, the *self swing-by* phenomenon is more clearly visible for the $\mathcal{E}_3$ solution, family III. While the $\mathcal{E}_3$ solution, family II, has an optimal thrust structure that allows achieving at minimum propellant expenditure the desired terminal conditions, the family III trajectory requires an additional "external aid" to compensate for the less favorable suboptimal thrusting. Indeed, its initial thrust phase provides a reduction of the SC-Moon distance while, however, preceding it; such configuration forces the SC to be pulled back by the Moon as if in a flyby, reducing its velocity temporarily but acquiring a locally more significant positive effect.

Figure 5.31 shows the energy evolution over time for the three strategies departing at $\mathcal{E}_3$, to further validate the above-mentioned considerations.

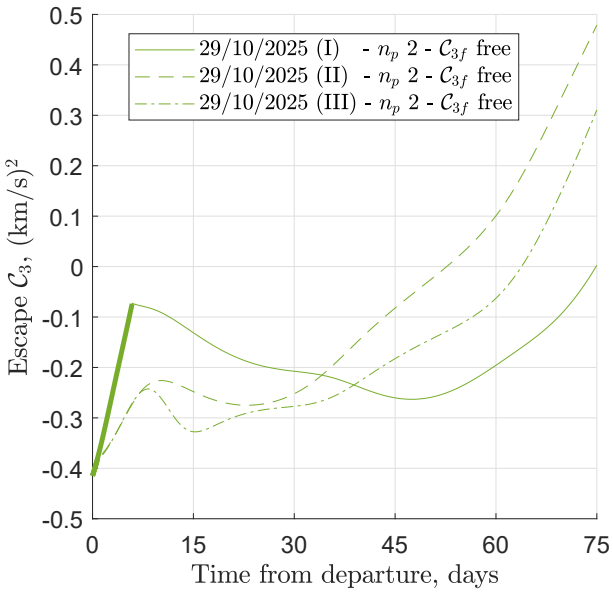

Fig. 5.31 EML2 escape trajectories - trend of escape energy over time, comparison between free and fixed $\mathscr{C}_{3f}$

The departure at $\mathcal{E}_4$ uses an initial consistent thrust arc to exploit the decreasing-over-time positive tangential perturbation and the peak of the radial perturbation. Optimal in-plane thrust angle and burn duration are selected precisely to eliminate thrust as soon as the relative Sun-SC angle reaches the negative tangential perturbation value. Note that, even if cases 3 and 4 from family III have departures separated by 90°, they tend to both end at $\Delta\vartheta \approx 0°$ to exploit the maximum positive radial perturbation during the terminal phase.

The departure at $\mathcal{E}_2$ shows a different T_S. To better understand how the change of strategy in the T_S for family I solutions arises, Figure 5.32 shows the $\mathcal{S}_\mathcal{F}$ for departures $\mathcal{E}_1$ and $\mathcal{E}_2$. The first one assumes a T-C T_S, but the $\mathcal{S}_\mathcal{F}$ is non monotonic and, around $t = 15$ days from departure, shows an almost non-negative peak. According to the PMP, the T_S should be modified in post-processing in the violated arcs, namely if the $\mathcal{S}_\mathcal{F}$ changes sign more times than expected.

When transitioning from $\mathcal{E}_1$ to $\mathcal{E}_2$ with a continuation approach ($\mathcal{E}_1 \rightarrow t \rightarrow \mathcal{E}_2$), the required propulsive effort increases; $\mathcal{S}_{\mathcal{F}_{\mathcal{E}_1}}$ starts upraising towards positive values, and transitions from the continuous blue curve to the continuous orange curve. Observing the bolded line in the zoomed portion, around 2.5 days after departure the 2-arc solution is tangent to the zero level and rises again towards positive values; the whole period $t \in [2.5, 18]$ days in which the $\mathcal{S}_\mathcal{F} > 0$ does not respect PMP and

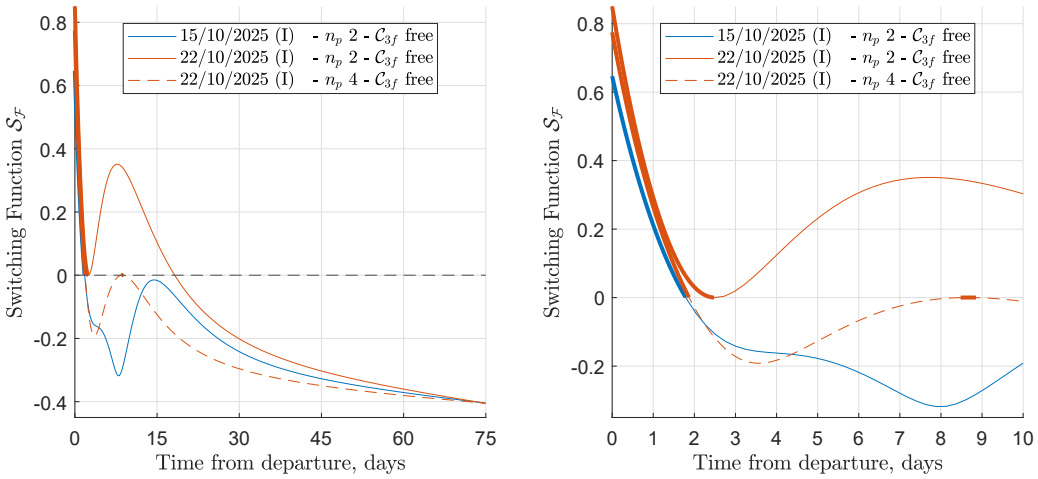

Fig. 5.32 SEL2 selected escape trajectories - Comparison of single-burn and two-burn thrust strategies and solution refinement (left), zoomed view (right)

suggests a change of strategy. An additional small thrust arc is inserted at the time from departure around the peak value of the non-optimal $\mathcal{S}_\mathcal{F}$, leading to a new guess $\mathrm{T_S}$ as $t_{\mathcal{S}_\mathcal{F}} = \{2.5, 7.5, 8, 75\}$ days in a new 2-burn, 4-arc T-C-T-C switching structure. When iterated, the $\boldsymbol{\lambda}_V$ tend to decrease overall and converge to a lower area under the λ_V curve. They are not shown here for the sake of conciseness, but clearly the λ_V trend matches the $\mathcal{S}_\mathcal{F}$ one, and the change in the initial guesses is clearly seen in Figure 5.26 (right), when the $\boldsymbol{\lambda}$ abruptly change in family I. Such a change of strategy leads to an improved optimal solution for $\mathcal{E}_2$ complying with PMP. For reference, the non-optimal solution required a $\Delta V = 67.772$ m/s, whereas the optimal one requires $\Delta V = 61.183$ m/s (Table 5.8), with a 10% improvement and with optimal switching times equal to $t_{\mathcal{S}_\mathcal{F}} = \{1.87, 8.48, 8.85, 75\}$ days. It is interesting to note that the improved strategy eliminates part of the thrust while the SC travels in the negative σ_v region, thus shortening this unfavorable phase, and applies the remaining propulsion again when $\Delta\vartheta \approx -100°$, with high positive σ_v and moderate σ_u (Figures 5.27 and 5.28).

Figure 5.33 shows the overall exploitation of the radial and tangential perturbation coefficients $\eta_{sg,u}$ and $\eta_{sg,v}$.

A different view is proposed in Figure 5.34, in which the same trajectories are represented in the Sun-Earth synodic RF centered on Earth. Departures at $\mathcal{E}_1$, $\mathcal{E}_2$, and $\mathcal{E}_3$ of family I occupy the first and fourth quadrants, favorably exploiting the radial component of Sun's perturbation in the final part of the escape. The SC always

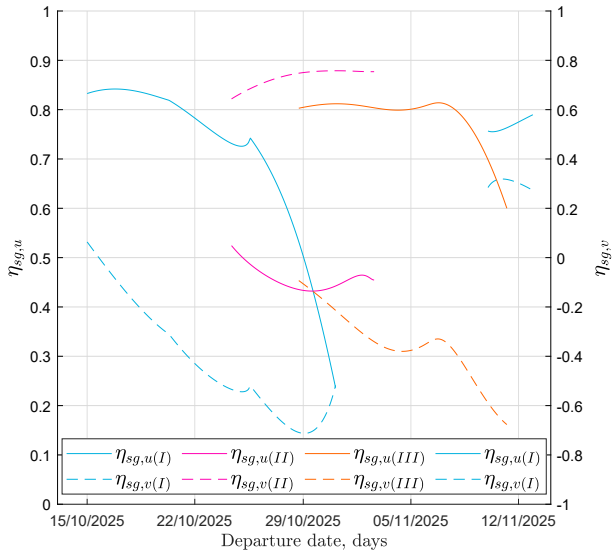

Fig. 5.33 EML2 escape trajectories - radial and tangential overall perturbation effect over a lunar month

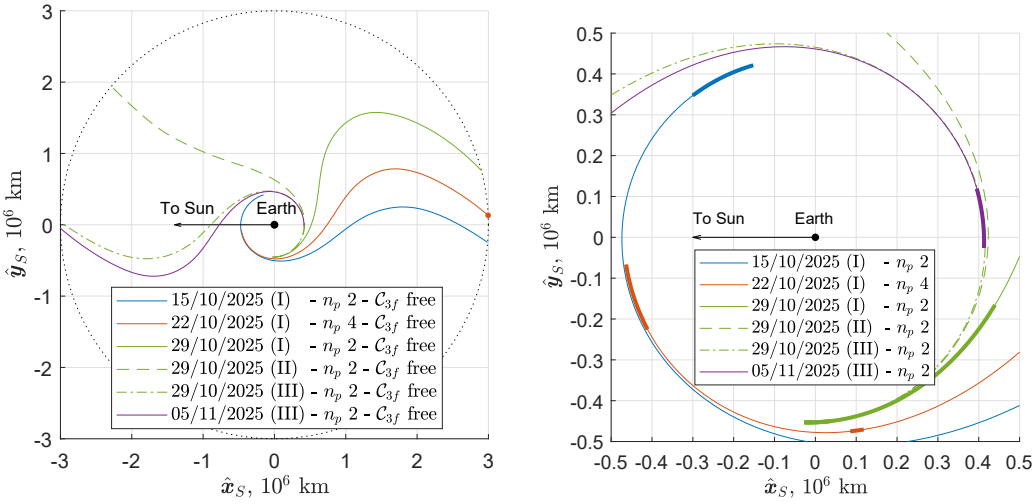

Fig. 5.34 EML2 selected escape trajectories, fixed $\Delta t = 75$ days, free $\mathcal{C}_{3f}$, SE synodic RF (left), zoomed view (right)

shows terminal $\Delta\vartheta$ close to 180°. However, the late departure of case 3 $\mathcal{E}_3$ forces a longer initial burn to achieve a similar result. The specular scenario, with departures $\mathcal{E}_{2(III)}$ and $\mathcal{E}_{3(III)}$, has escape points on the SEL1 side (i.e. between Earth and Sun). These trajectories occupy the second and third quadrants in the rotating RF, tending to null $\Delta\vartheta$, which, again, implies favorable radial perturbation. The single trajectory in the second quadrant, case 3 family II, exploits more substantially the tangential component with an escape tending to $\Delta\vartheta = 45°$. The last trajectory, case 5, repeats

the trend of family I solutions, being in particular very close, as expected, to the solution departing a lunar synodic month earlier, even though the different position of the Sun affects the trajectory details.

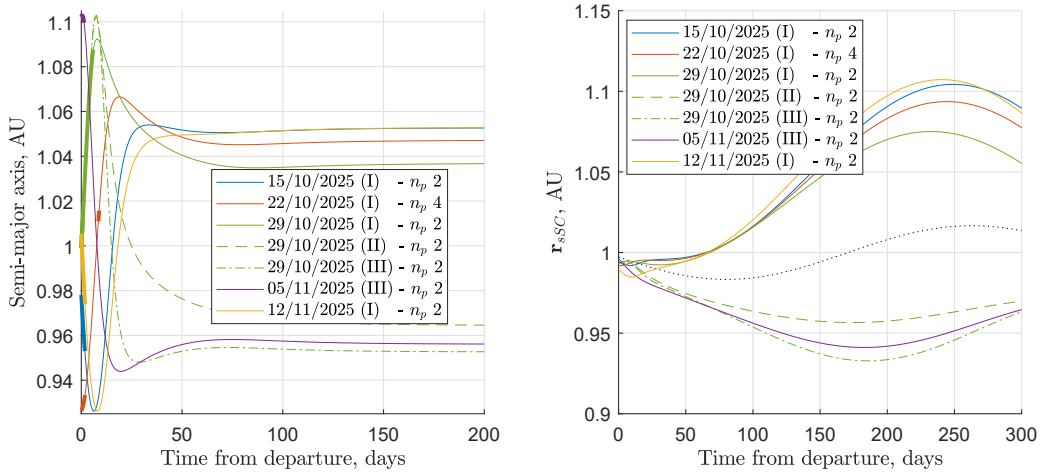

Fig. 5.35 EML2 escape trajectories - fixed $\Delta t = 75$ days, free $\mathscr{C}_{3f}$, semimajor axis (left) and Sun-SC position radius (right), HE RF

Figure 5.35 shows a zoomed view of the semimajor axis (left) and the trend of the SC's position vector wrt the Sun (right). The propagation times are four times the original ones. The different departure locations in the EML_2 produce different terminal conditions at r_f, thus inducing diverse escape directions in the HE RF. Trajectories escaping in between the first and fourth quadrant have a terminal V_∞ which produces a prograde change of apsis and composes positively with the Earth's heliocentric velocity vector, resulting in higher semimajor axis values and heliocentric trajectories above the Earth's orbit (depicted in the dotted black curve). The trajectories with terminal direction in between the second and the third quadrant, on the other hand, produce the opposite effect, resulting in lower semimajor axes and inner orbits.

It is noteworthy that the second family of solutions has a very low propellant consumption with a very high free final energy, implying that constrained final energy solutions, especially the ones fixed at lower values, will have to reduce somehow the spacecraft energy to achieve the desired boundary conditions. The same applies to part of family III solution and to case 5 (family I).

5.3.2 Earth-Moon L_2 escapes with constrained final energy $\mathscr{C}_{3f}$

Trajectories with $L\mathscr{C}_{3f}$ and $H\mathscr{C}_{3f}$ terminal conditions have been optimized with the same strategies implemented for the SEL_2 scenario for the continuation approach. The Moon's proximity and the lunisolar complex gravitational perturbation divide more evidently the families of solutions compared to the cases with free final energy. Figure 5.36 shows the manifold of solutions for the $L\mathscr{C}_{3f}$ (left) and $H\mathscr{C}_{3f}$ (right) scenario, whereas Tables 5.10 and 5.11 show the performance for the selected departure dates in their distinct families, for both cases. The families still have many solutions within them, but most of them tend to overlap in their final phase when the final energy is fixed.

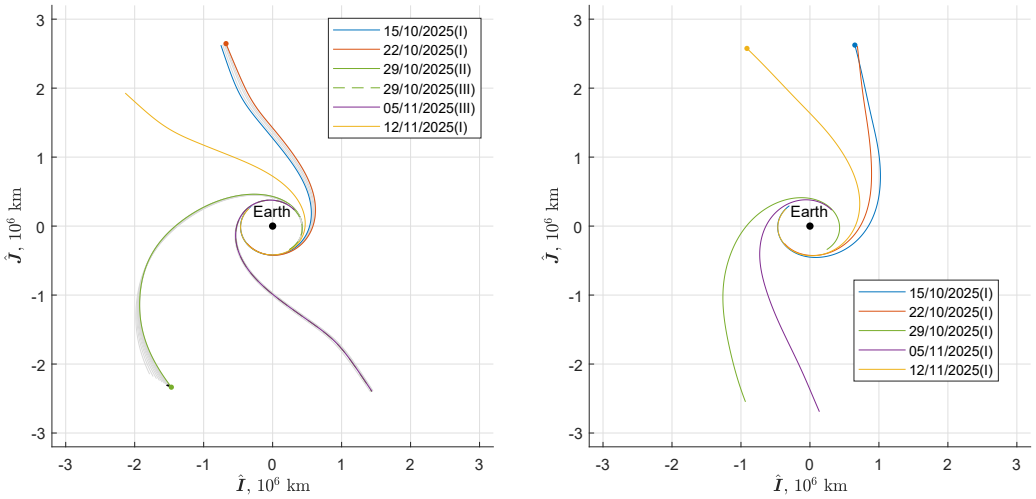

Fig. 5.36 EML2 escape trajectories over a lunar month, fixed $L\mathscr{C}_{3f} = 0.2$ $(\mathrm{km/s})^2$ (left), fixed $H\mathscr{C}_{3f} = 0.5$ $(\mathrm{km/s})^2$ (right), free Δt, EME2000 RF

Table 5.10 EML2 escape trajectories performance - fixed $\mathscr{C}_{3f} = 0.2$ $(\mathrm{km/s})^2$, free Δt

$\mathcal{E}$	f	n_p	$\eta_{sg,u}$	$\eta_{sg,v}$	$\overline{\eta_{sg}}$	ΔV m/s	Δt days
1	I	2	0.702	−0.274	0.214	46.297	78.59
2	I	4	0.711	−0.195	0.258	66.200	75.12
3	II	4	0.190	0.542	0.366	73.777	88.05
3	III	2	0.715	−0.241	0.237	17.354	80.81
4	III	2	0.678	−0.295	0.192	39.099	73.93
5	I	2	0.659	−0.314	0.172	49.933	78.43

Table 5.11 EML2 escape trajectories performance - fixed $\mathscr{C}_{3f} = 0.5$ $(\mathrm{km/s})^2$, free Δt

$\mathcal{E}$	f	n_p	$\eta_{sg,u}$	$\eta_{sg,v}$	$\overline{\eta_{sg}}$	ΔV m/s	Δt days
1	I	4	0.695	0.541	0.618	74.853	75.01
2	I	2	0.632	0.301	0.467	147.635	61.40
3	I	2	0.449	0.713	0.581	19.934	72.74
4	I	2	0.654	0.308	0.481	77.468	62.79
5	I	4	0.683	0.539	0.611	64.702	76.59

For the same considerations regarding negative perturbative effects due to the Sun perturbation in specific regions in space for those trajectories with departure epoch $\mathcal{E}_{2(II)}$, some single-burn solutions from the EML_2 free $\mathscr{C}_{3f}$ scenario assume the two-burn T-C-T-C structure when constrained to $L\mathscr{C}_{3f}$. However, all the case studies invert their optimal $\mathrm{T_S}$ when transitioned to their $H\mathscr{C}_{3f}$ counterpart, from 2 to 4 phases (T-C-T-C) or *vice versa*. Figure 5.37 shows the optimal thrust angle α_T for all the selected cases, for the $L\mathscr{C}_{3f}$ scenario on the left, and on the right for the $H\mathscr{C}_{3f}$ one, whereas Figure 5.38 shows the Sun-SC angles for all the trajectories in the same fashion.

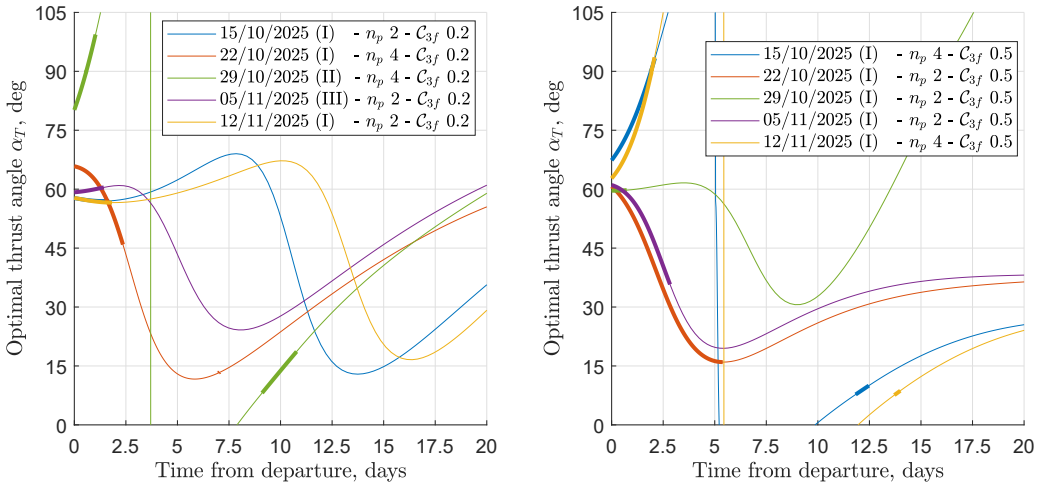

Fig. 5.37 EML2 selected escape trajectories - optimal thrust angle α_T in the $L\mathscr{C}_{3f}$ scenario (left) and $H\mathscr{C}_{3f}$ scenario (right)

Moreover, Figures 5.39 and 5.40 represent the polar projections of the escape trajectories as a function of their angular difference wrt their Sun-SC angle $\Delta\vartheta$.

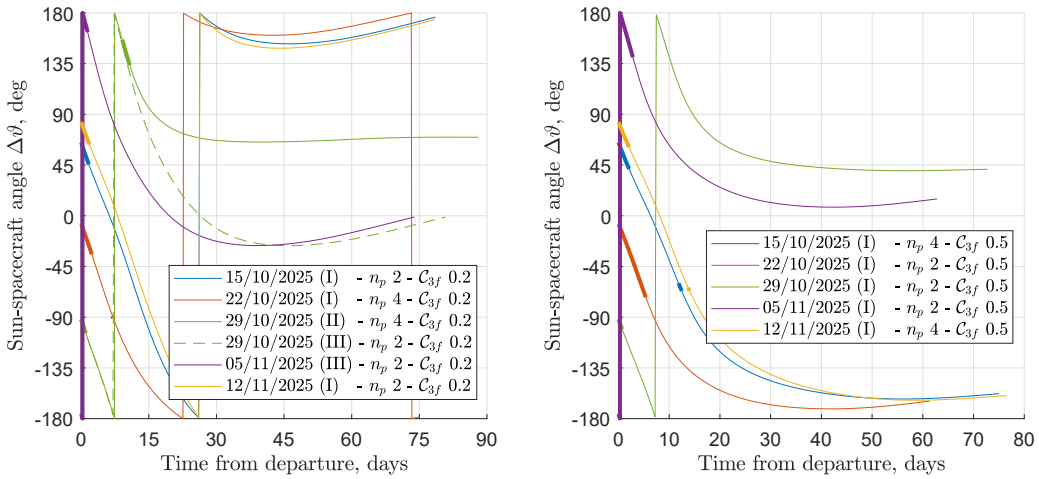

Fig. 5.38 EML2 selected escape trajectories - Sun-SC relative angle $\Delta\vartheta$ in the $L\mathcal{C}_{3f}$ scenario (left) and $H\mathcal{C}_{3f}$ scenario (right)

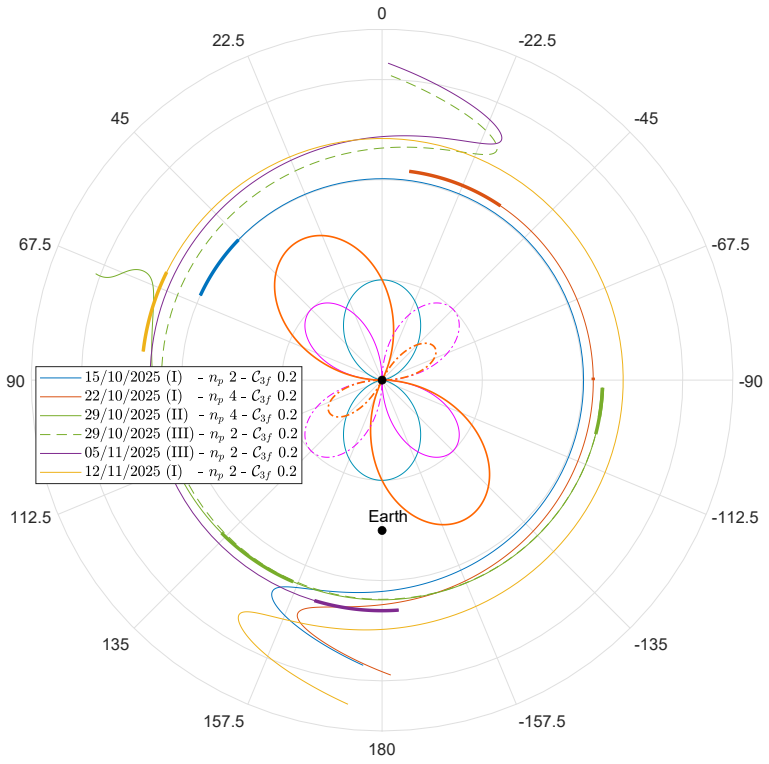

Fig. 5.39 EML2 selected escape trajectories polar view, fixed $L\mathcal{C}_{3f}$, free Δt, Earth-SC rotating RF

Starting from the low-energy scenario, while solution $\mathcal{E}_{2(I)}$, for example, follows the behaviour of its corresponding free $\mathcal{C}_{3f}$ scenario (Figure 5.28), applying a small adjustment as soon as the negative perturbative σ vanishes, trajectory $\mathcal{E}_{3(II)}$ changes

its strategy including a further thrust arc. The fixed-time scenario provided, for the same trajectory, a free $\mathscr{C}_{3f} = \{0.4789, 0.3108\}$ $(\mathrm{km/s})^2$, respectively for $\mathcal{E}_{3(II)}$ and $\mathcal{E}_{3(III)}$. Therefore, the $L\mathscr{C}_{3f}$ constraint actually forces the trajectory to be less efficient, and thus to lose its energy by remaining longer in the region in which the Sun's perturbation provides a negative effect by means of the additional thrust phase. Such behaviour is achieved by thrusting not only mainly in the radial direction, but at $\alpha_T > 90°$, therefore actually decelerating at the beginning of the trajectory; a lower passage close to the Moon guarantees enough energy to depart nonetheless, and the second thrust is performed accordingly. All the other trajectories maintain similar characteristics with their free-time counterparts, escaping at $\Delta\vartheta \approx \{0°, 180°\}$, depending on their starting position, thus grouping themselves towards favorable values of the solar perturbation.

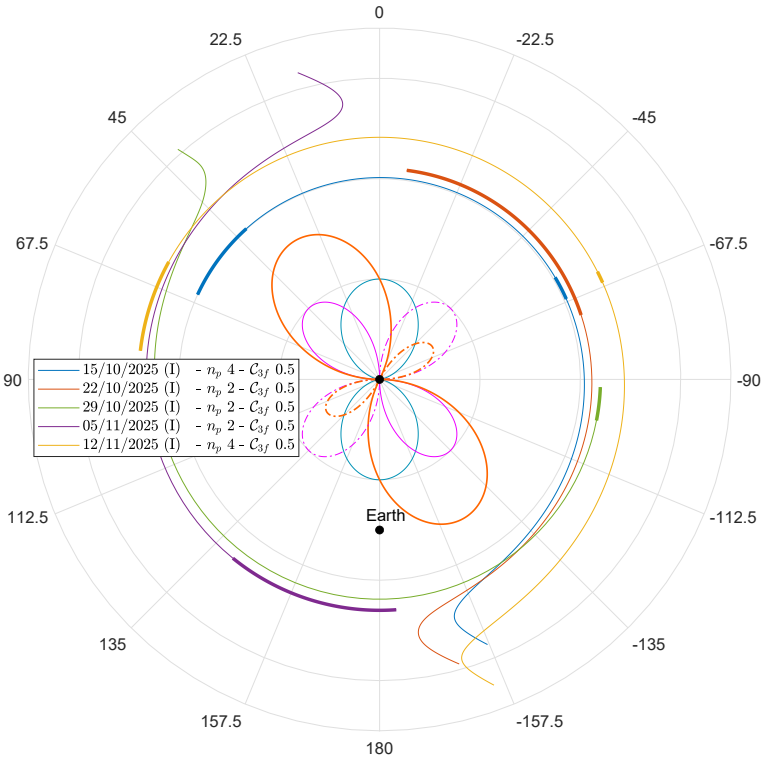

Fig. 5.40 EML2 selected escape trajectories polar view, fixed $H\mathscr{C}_{3f}$, free Δt, Earth-SC rotating RF

The high energy trajectories, on the other hand, show a perfect specular trend. Low single-burn and two-burn $L\mathscr{C}_{3f}$ solutions become two-burn and single-burn $H\mathscr{C}_{3f}$ trajectories. Solution $\mathcal{E}_1$ (and $\mathcal{E}_5$), for example, includes a second thrust arc when the negative solar perturbation coefficient σ is at its peak negative value,

and departs with radial to decelerating thrust angles, emulating the $L\mathscr{C}_{3f}$ $\mathcal{E}_{3(II)}$ behaviour. The $\mathcal{E}_2$ trajectory, on the other hand, eliminates the second thrust arc by continuously applying a propulsive force during the negative solar perturbation phase; this is performed to gain all the required energy before the $\Delta\vartheta$ reaches the positive σ_u condition at 180°. Note that solution $\mathcal{E}_4$ replicates $\mathcal{E}_2$'s solution, in order to achieve an escape close to $\Delta\vartheta \approx 0°$. Solution $\mathcal{E}_3$ simply increases the initial thrust by a sufficient amount to cover the small difference in terminal energy from the free-energy scenario.

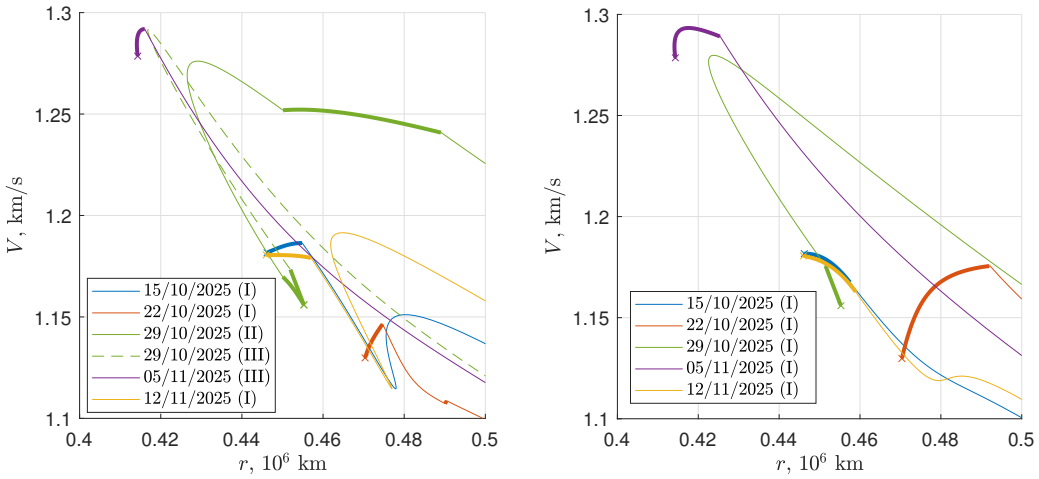

Fig. 5.41 EML2 selected escape trajectories, Earth-centered phase-space representation - fixed $L\mathscr{C}_{3f} = 0.2\ (\mathrm{km/s})^2$ (left), fixed $H\mathscr{C}_{3f} = 0.5\ (\mathrm{km/s})^2$ (right)

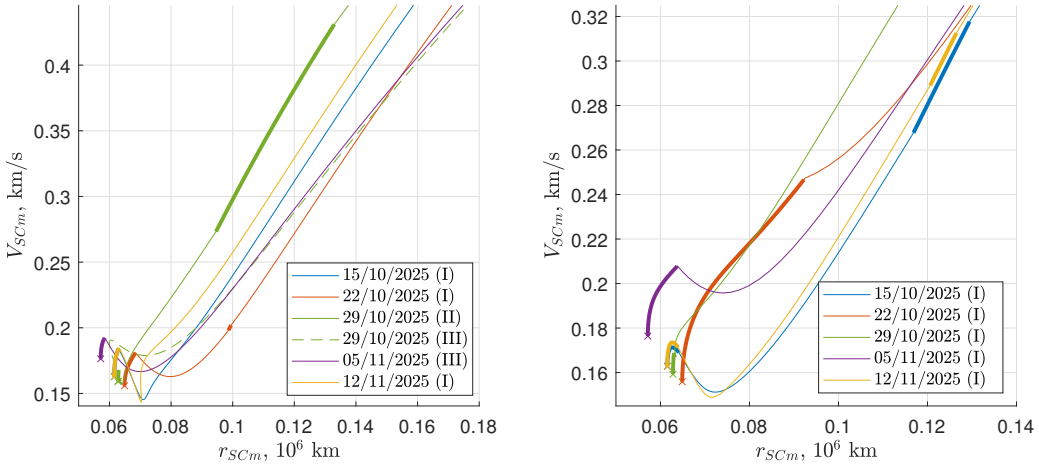

Fig. 5.42 EML2 selected escape trajectories, Moon-centered phase-space representation - fixed $L\mathscr{C}_{3f} = 0.2\ (\mathrm{km/s})^2$ (left), fixed $H\mathscr{C}_{3f} = 0.5\ (\mathrm{km/s})^2$ (right)

Figures 5.41 and 5.42 show the Earth-centered and Moon-centered phase-space representations for the selected escape trajectories, respectively, for both the low energy (left) and high energy (right) cases. Again, all the considerations are confirmed in this alternative analysis. In the Earth-centered view, for example, the $\mathcal{E}_{3(II)}$ $L\mathscr{C}_{3f}$ shows the energy reduction behaviour to achieve a lower terminal energy compared to the free one; indeed, after the small initial burn, a second burn is performed that counteracts the natural reduction in velocity that the SC would have achieved in a normal coasting phase. On the other hand, the bifurcations among families have again a clear representation; in the low-energy scenario, all family I solutions tend to have a more consistent radial thrust, the $\mathcal{E}_{3(II)}$ case presents an unique additional long thrust, whereas family III trajectories have a decise change in velocity compared to a quasi-stable initial position radius.

Figures 5.43 and 5.44 represents two sample cases, $\mathcal{E}_2$ and $\mathcal{E}_3$, selected to show low and high energy trajectories that must either increase or decrease the energy to achieve the fixed energy counterparts. In particular, case 2 from the free energy scenario has a very low final energy, whereas case 3 has a very high one. The 4-arc solution for case 2 slightly reduces its duration while increasing the first thrust phase to comply with the final energy increase and keep similar $\Delta\vartheta$ during the escape. This action eliminates the second burn making it a T-C trajectory. When forced to have the higher final energy, the optimal strategy keeps reducing the overall duration to escape, while increasing the thrust phase length; indeed, the solution forces the relative angle to stay in the third quadrant between -135° and -180°, where the solar perturbation acts more favorably.

With an opposite behavior, the single burn solution in the scenario with free final energy for case 3 has to reduce its overall energy to achieve the required lower C3. This increases the overall length of the trajectory with a strong reduction of the first burn phase, showing that the optimal strategy relies mainly on the solar perturbation to achieve the desired energy. Indeed, the majority of the escape, after the initial 30 days, remains in a region in which the Sun perturbation has a negative effect, retarding the energy increase.

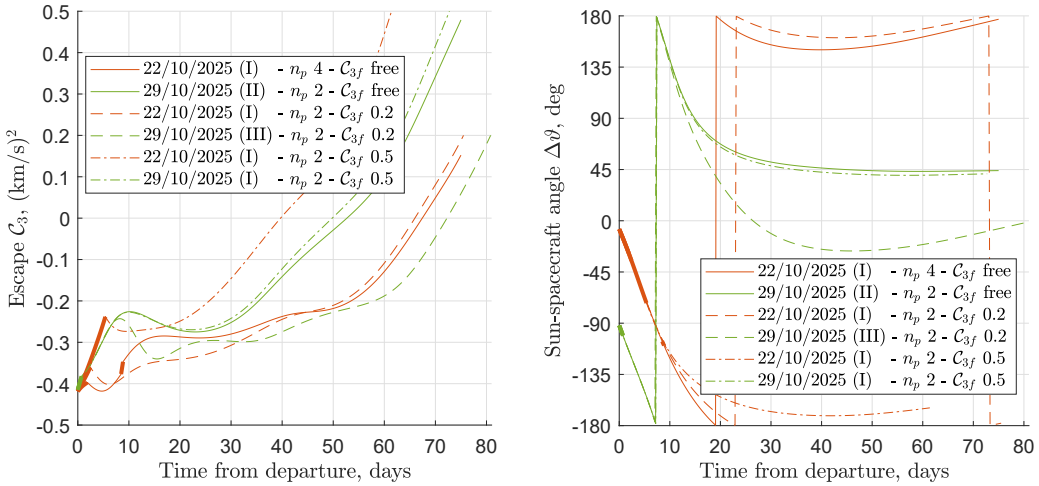

Fig. 5.43 EML2 selected escape trajectories - energy over time (left), Sun-SC angle (right), comparison between free and fixed $\mathcal{C}_{3f}$

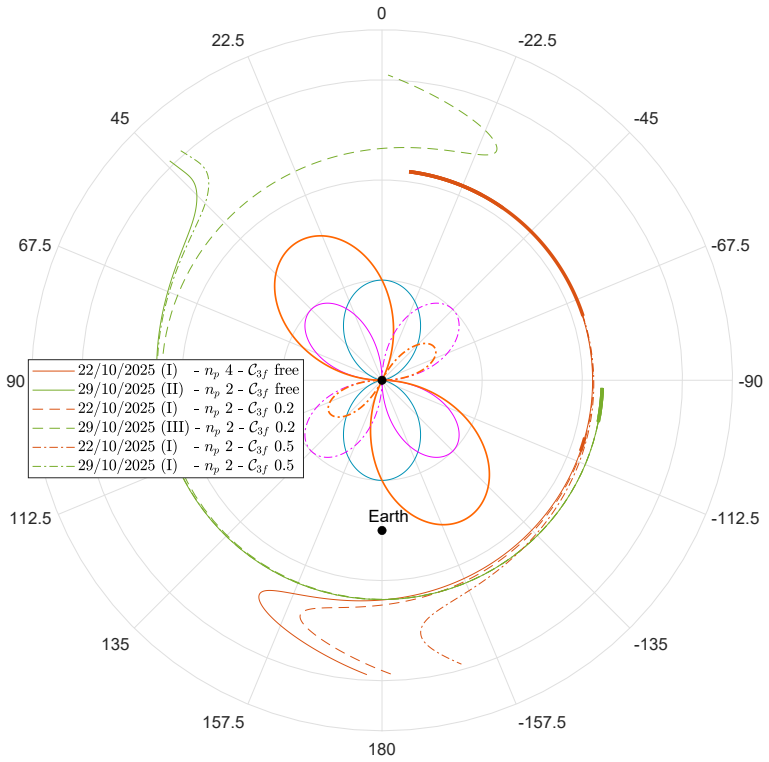

Fig. 5.44 EML2 selected escape trajectories polar view, comparison between free and fixed $\mathcal{C}_{3f}$, Earth-SC rotating RF

Chapter 6

Escape Trajectories from Quasi Periodic Orbits in the Ephemeris Model

Chapter 6 completes the analysis of optimal escape trajectories in the ephemeris model. Techniques in Chapter 3, as the Fixed-Time Differential Correction (FTDC) and Variable-Time Differential Correction (VTDC) are implemented to transition analytical approximate Periodic Orbits (POs) in the Circular Restricted Three-Body Problem (CR3BP) domain into medium fidelity POs. These orbits are then transitioned again into the higher fidelity model via a continuation approach, in order to account for the perturbation of all the desired additional gravitational bodies in the n-Body Problem (NBP) domain. Specifically, high-fidelity escape trajectories in the Four-Body Problem (4BP) from planar Quasi-Periodic Orbit (QPO) are here analyzed, with Spacecraft (SC) subject to the combined gravitational influence of the Sun, Earth, and Moon. The dynamical model also includes spherical harmonics, to account for the Earth's asphericity, and the Solar Radiation Pressure (SRP).

Section 1 briefly describes the Lyapunov Orbits (LOs) converged in the 4BP, identifying specific differences among them. Such QPOs serve as baseline trajectories from which the SC departs. Section 2 describes fixed-time, free terminal energy trajectories sought, whereas Section 3 deals with the counterpart scenario, in which such escape trajectories are constrained for their characteristic energy $\mathscr{C}_{3f}$.

6.1 Preface

A preliminary consideration regarding the characterization of Quasi-Periodic Lyapunov Orbits (QPLOs) is presented henceforth. LOs computed in the 4BP are strongly time-dependent for what concerns their shapes and quasi-periodicity characteristics. Following the algorithm presented in Section 3.4, Figure 3.18, the same initial analytical characteristic dimension, A_y, leads to very different geometries depending on the considered initial epoch $\mathcal{E}$. The same five different case studies of Chapter 4, Table 5.1, are reproposed here, with $\mathcal{E}_1$ on October 15, 2025 and $\mathcal{E}_5$ on November 12, 2025.

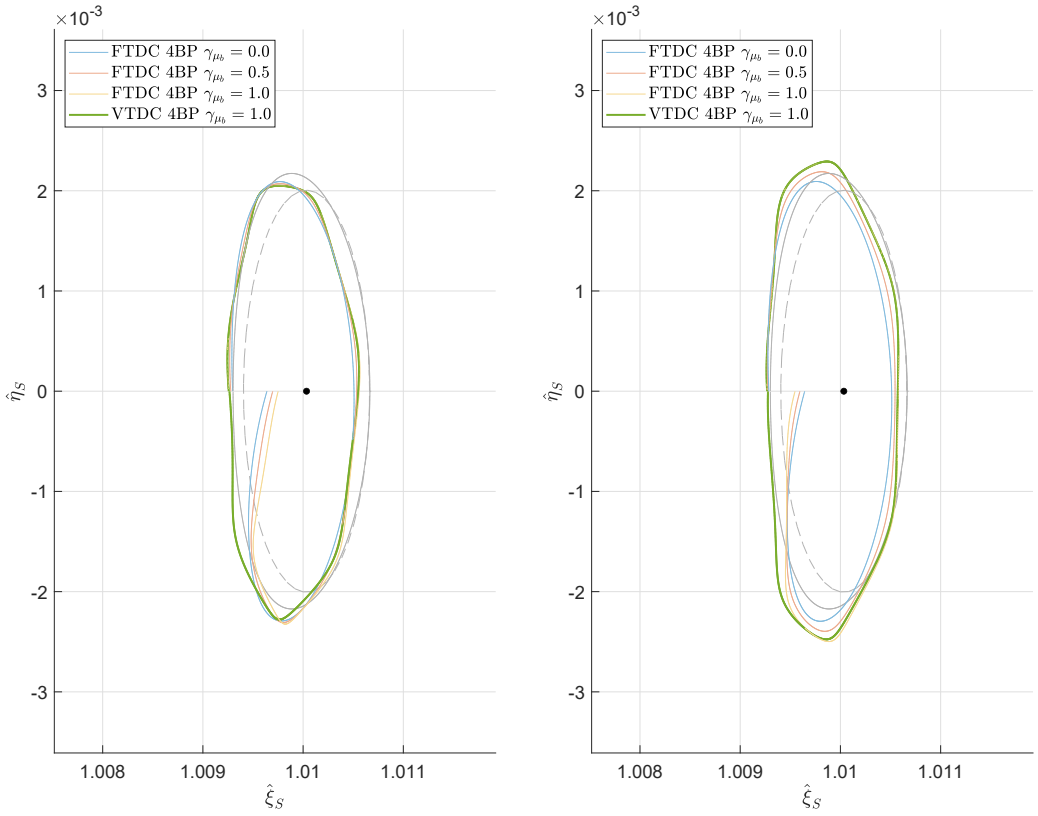

Fig. 6.1 SEL2 high-fidelity Lyapunov Orbits with initial analytic dimension $A_y = 3 \times 10^5$ km, departure epoch $\mathcal{E}_1$ (left), $\mathcal{E}_2$ (right), SE synodic RF

Figure 6.1 shows two converged LOs, starting with the same analytical characteristic dimension $A_y = 3 \times 10^5$ km and with departure date spaced apart just by one week; on $\mathcal{E}_1$, on the left, and $\mathcal{E}_2$, on the right. The analytical approximation and the CR3BP Non Linear (NL) integration are shown respectively with the dashed ellipse and the subtle gray line in transparency; the latter is used as the initial guess for the

NBP generation of the QPO, considering initially a null influence of further bodies, $\gamma_{\mu_b} = 0$. Slowly, with a step $\delta\gamma_{\mu_b}$, the QPO fidelity is increased by adding the other perturbative gravitational bodies up to when $\gamma_{\mu_b} = 1$. A step $\delta\gamma_{\mu_b} = 0.05 \div 0.2$ is usually suitable to guarantee the convergence, depending on the number of additional bodies included in the transition ($\delta\gamma_{\mu_b} = 0.2$ produces fast and robust results if only the Moon is added in the Sun-Earth Lagrangian Point L_2 (SEL_2) scenario, whereas by including all the planets of the solar system the lower boundary is preferred). The last step applies the VTDC, which ends up in the converged QPLO in green. Please note that, specifically for Figures in this Section, colors are not representative of specific epochs $\mathcal{E}$, contrarily to all the other occurrences. Those QPOs are placed in the vicinity of the (ideal) location of the Sun-Earth (SE) Lagrangian Point L_2 (L_2) point, and their departure epoch is located on the orbit intersection with the Sun-Earth-L_2 line of the nondimensional SE synodic Reference Frame (RF), $\hat{\boldsymbol{\xi}}_S$, on the Earth's side. They can be characterized by their Jacobi Constant $\mathscr{J}_C$, for fast referencing, and by their period; while the $\mathscr{J}_C$ concept relies on the autonomous characteristics of the CR3BP, and thus has the same value independetly on the departure epoch $\mathcal{E}$ and is a function of the QPO dimension, the period $\mathscr{T}$ is indeed epoch-dependent, as shown in Table 6.1.

Table 6.1 Lyapunov Quasi-Periodic Orbits in the Sun-Earth L_2 - Jacobi constant values, orbital periods

		Period $\mathscr{T} = f(\mathcal{E})$				
	$\mathscr{J}_C$ $(\text{km/s})^2$	$\mathscr{T}_{\mathcal{E}_1}$ days	$\mathscr{T}_{\mathcal{E}_2}$ days	$\mathscr{T}_{\mathcal{E}_3}$ days	$\mathscr{T}_{\mathcal{E}_4}$ days	$\mathscr{T}_{\mathcal{E}_5}$ days
SEL_2	3.000887	-	-	-	-	-
$Lyap_2$	3.000880	172.952	175.514	173.083	169.879	171.782
$Lyap_3$	3.000871	173.890	175.870	173.890	171.544	173.043
$Lyap_4$	3.000858	174.736	176.428	174.442	172.677	174.159
$Lyap_5$	3.000838	175.677	177.246	175.112	173.608	175.250
$Lyap_6$	3.000811	177.093	178.499	176.112	174.746	176.608
$Lyap_7$	3.000776	178.850	180.249	177.544	176.187	178.444
$Lyap_8$	3.000732	181.189	182.618	178.572	177.164	180.881

where the notation Lyap_j, with $j = 2, 3, \ldots, 8$ indicates the approximate analytical characteristic dimension from which the LO is derived, namely 2×10^5 km, 3×10^5 km, and so on.

QPOs' periods change over time among different epochs, but they show a monotonic increase dependent on the QPO shape. Different shapes and characteristics are due to the complex gravitational interactions happening between the Earth-Moon system and the Sun. Those QPOs computed with departures on $\mathcal{E}_2$ tend to have the highest periods, whereas two weeks later they show the shortest one. The reason behind this behaviour may be sought in the Moon's positioning rather than in the Earth's natural evolution along its orbit. On $\mathcal{E}_2$ (refer to Figure 5.34, for example, for a fast observation), the Moon is almost in conjunction between the Sun and the Earth, thus having a $\Delta\vartheta \approx 180°$ and pulling the Earth's in such a way that a SC in SEL_2 would experience a lower combined gravitational attraction, increasing the orbit shape. Instead, on $\mathcal{E}_4$, the Moon is in opposition and its gravitational influence is added to the Sun-Earth one, as seen from SEL_2. However, also the Earth is in the lowering phase of its orbit and therefore reduces its distance from the Sun between $\mathcal{E}_1$ and $\mathcal{E}_2$, which may explain the increasingly minor distance of the part of the QPO lying on the positive side of SEL_2 with respect to the negative side (the L_2 position, if still existent in the 4BP, would be closer to the Earth in this case).

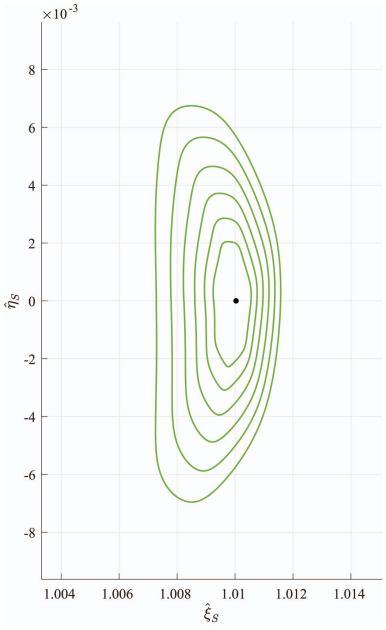

Fig. 6.2 SEL2 QPLOs with initial analytical $A_y = [3,8] \times 10^5$ km at $\mathcal{E}_1$, SE synodic RF

Figure 6.2 shows a manifold of converged QPLOs with the same departure epoch, $\mathcal{E}_1$, and initial analytical semimajor axis A_y from 3×10^5 km to 8×10^5 km, with a step of 1×10^5 km. The wider they are, the more similar they become to the NL

PO integration in the CR3BP. Given all the abovementioned considerations, it is more interesting to analyze the performance depending on the departure epoch $\mathcal{E}$ compared to the influence of the departing QPLO dimension. The reference departure dimension is chosen to be $A_y = 4 \times 10^5$ km in the analytical approximation.

To further validate this assumption, the following Figure 6.3 shows sample missions from QPLOs starting with $A_y = 2 \times 10^5$ km up to $A_y = 8 \times 10^5$ km, spaced apart by a step size of 2×10^5 km, all for the $\mathcal{E}_1$ departing epoch. All trajectories have initial states function of the specific QPLOs; the velocity components match the QPLO's ones, whereas the departure location is at the QPLO's $\hat{\boldsymbol{x}}_S$ axis intersection when $v_y > 0$, namely at the closest x_S coordinate with respect to the Earth.

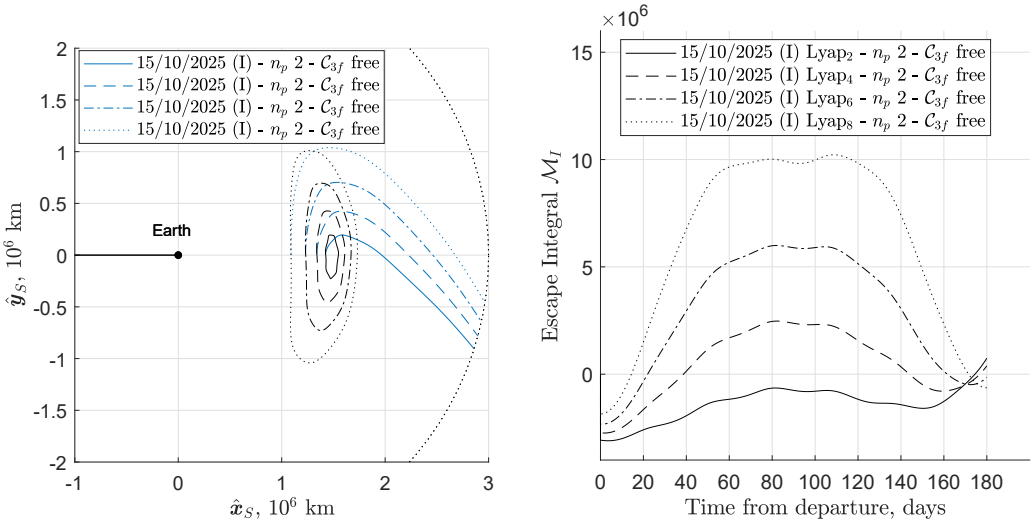

Fig. 6.3 SEL2 QPLOs escape trajectories with different departure LO size, SE synodic RF (left), escape warning (momentum integral) (right)

On the right, there is the momentum integral, or escape warning, introduced in equation (3.13), Section 3.1. The stability requirements to avoid influencing the escape due to unstable behaviours from the QPO itself are satisfied with larger orbits, which produce a non-positive value after a complete revolution. The smaller the QPO, the more a natural escape is probable. On the other hand, escape from larger QPOs shows a weak influence on the departure date. Therefore, the $A_y = 4 \times 10^5$ departing QPO is the best compromise between actual escape trajectories performed by thrusting and the potential to observe different behaviours at different epochs. Please note that the departing Lyapunov orbits will be omitted to avoid burdening the following graphs.

6.2 Escapes from Sun-Earth Quasi-Periodic Lyapunov Orbits with imposed mission duration Δt

This Section considers fixed-time $\Delta t = 90$ days and free terminal energy escape trajectories. An initial T-C Thrust Structure (T_S) is assumed and results from the Hybrid Four-Body Problem (H4BP) in Section 5.2.1 are seeded as guesses; convergence is readily obtained without the need to construct a new guess for the adjoint vector $\boldsymbol{\lambda}$.

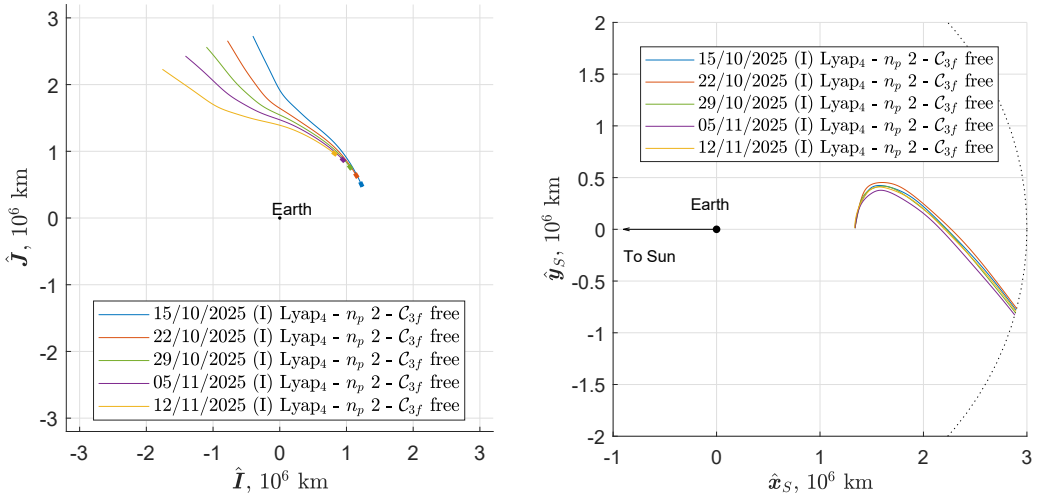

Fig. 6.4 SEL2 QPLOs escape trajectories over a lunar month, fixed $\Delta t = 90$ days, free $\mathscr{C}_{3f}$, EME2000 RF (left), SE synodic RF (right)

Table 6.2 SEL2 QPLOs escape trajectories performance - fixed $\Delta t = 90$ days, free $\mathscr{C}_{3f}$

$\mathcal{E}$	f	n_p	$\eta_{sg,u}$	$\eta_{sg,v}$	$\overline{\eta_{sg}}$	ΔV m/s	$\mathscr{C}_{3f}$ $(\mathrm{km/s})^2$
1	I	2	0.964	−0.203	0.380	34.916	0.0836
2	I	4	0.959	−0.236	0.361	34.822	0.0925
3	I	2	0.964	−0.203	0.380	34.541	0.1064
4	I	2	0.969	−0.167	0.401	34.489	0.0947
5	I	2	0.965	−0.201	0.382	34.448	0.0799

Figure 6.4 shows the optimal trajectory, per each departure epoch $\mathcal{E}$, in the Earth Mean Equator and Equinox of Epoch J2000 (EME2000) RF (left) and in the Sun-Earth synodic RF (right). The escape trajectories depart with the same initial

condition (at $y_S = 0$ and with $v_y > 0$), besides very minor differences in the departure location along the $\hat{\boldsymbol{x}}_S$ axis due to slightly different QPLOs at epoch. It is evident that all trajectories show almost exactly the same ΔV requirement with minimal differences in $\mathscr{C}_{3f}$, as described in Table 6.2 and in Figure 6.5.

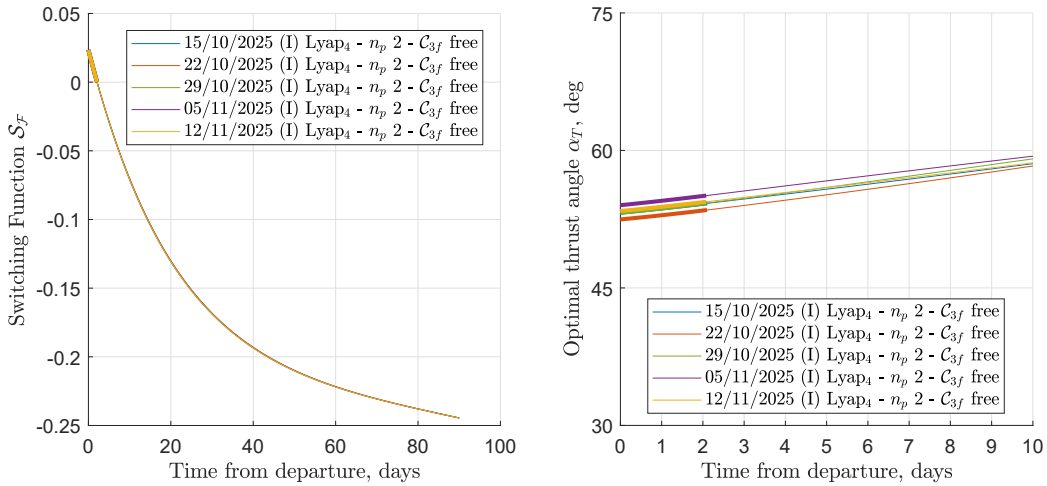

Fig. 6.5 SEL2 QPLOs switching function $\mathcal{S}_\mathcal{F}$ (left) and optimal thrust angle α_T (right)

The switching functions $\mathcal{S}_\mathcal{F}$, on the left, and the optimal thrust angles α_T, on the right, match almost perfectly in all cases. All these considerations are of utmost importance when compared to the results obtained in Section 5.2.1; in that framework, solutions differed consistently between $\mathcal{E}_1$ and $\mathcal{E}_5$, showing the optimal performance in terms of free $\mathscr{C}_{3f}$ at $\mathcal{E}_3$, but also the maximum cost ΔV. Here, the same applies to the best solution; $\mathcal{E}_3$ is still the one providing the highest free $\mathscr{C}_{3f}$ among all the others (see also Figure 6.6), but comes at no different cost and also while receiving a negative perturbative effect. Such a phenomenon arises because in the H4BP the approximate location of L_2 with respect to the actual position of the gravitational bodies had to be "actively corrected" with a propulsive effort, whereas in the 4BP here presented such perturbative effects are inherently contained in the converged QPLO. Please note, moreover, that all solutions departing from QPLOs show comparable but slightly lower ΔV than those from L_2 in the H4BP domain; therefore, solutions in the H4BP are conservative and can be used effectively to estimate the needs for preliminary interplanetary mission studies, as described in Section 5.2.2.

The optimal solution uses a minor mixed in-plane thrust angle, slightly favouring the radial direction, in order to evade from the QPO. The radial thrust direction is

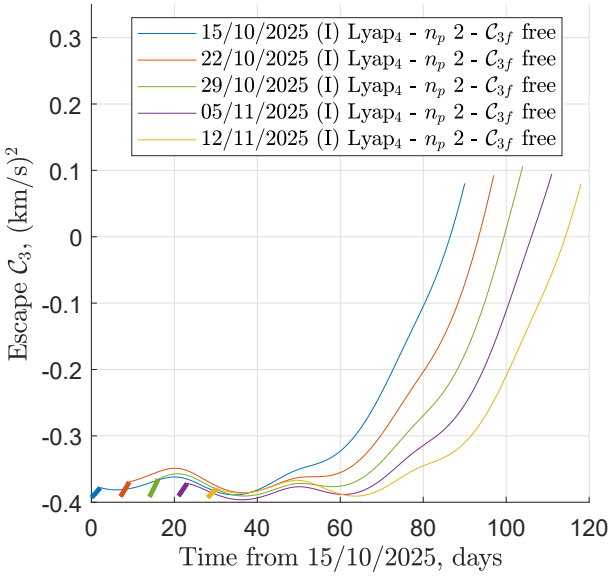

Fig. 6.6 SEL2 QPLOs energy over time, fixed $\Delta t = 90$ days, free $\mathscr{C}_{3f}$

preferred because it allows reaching the negative tangential perturbation σ_v at the right moment to naturally decelerate and start moving apparently in the opposite direction, towards the maximum positive perturbation coefficient σ. This retrograde behaviour is particularly visible in the QPO scenario because the SC travels with an initial velocity $v_0 > \left|-v_{s,0}\right|$, and is shown in the polar representation in Figure 6.7.

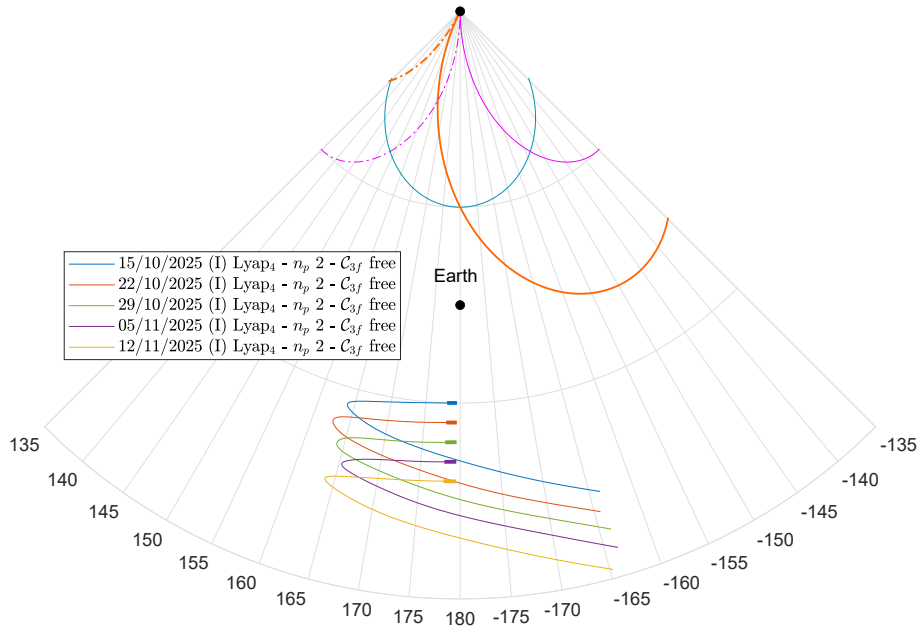

Fig. 6.7 SEL2 QPLOs escape trajectories polar view, fixed $\Delta t = 90$ days, free $\mathscr{C}_{3f}$

All trajectories exploit this behaviour and, even by trying to force the initial guesses to consider a tangential deceleration to accomplish the evasion, by posing a guess $\lambda_v < 0$, only very suboptimal solutions are found. Indeed, the optimal exploitation of the quasi-stability of the LO, and the greater intrinsic energy such orbit has with respect to departures from L_2 itself (please refer to Table 6.1 for $\mathscr{J}_C$ values), implies that the best strategy is to convey the QPO energy in an evasion path, instead of forcing the SC to abandon it completely. Such a scenario, instead, will arise in the next Section in specific bounded trajectories that will end up "skipping" the positive influence the QPO itself can provide.

6.3 Escapes from Sun-Earth Quasi-Periodic Lyapunov Orbits with fixed final energy $\mathscr{C}_{3f}$

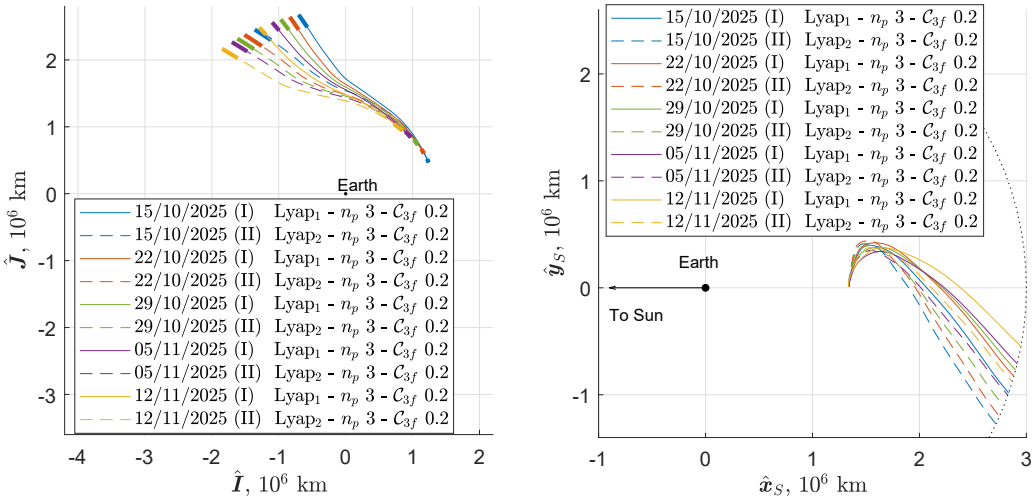

Fig. 6.8 SEL2 QPLOs escape trajectories over a lunar month, fixed $\mathscr{C}_{3f} = 0.2$ $(\mathrm{km/s})^2$, free Δt, EME2000 RF (left), SE synodic RF (right)

When transitioned from the free $\mathscr{C}_{3f}$ scenario to the $L\mathscr{C}_{3f}$ one, all trajectories equally bifurcate in two distinct families and acquire an additional thrust arc, for a T-C-T T_S. Figure 6.8 shows the manifold composed by the two families in the EME2000 RF (left) and in the SE synodic RF (right), and Table 6.3 outlines the escape trajectories performance.

Family I has short trip times whereas family II shows longer ones. Unexpectedly, higher costs are associated with longer missions. The interesting time-dependent

Table 6.3 SEL2 QPLOs escape trajectories performance - fixed $\mathscr{C}_{3f} = 0.2$ $(\mathrm{km/s})^2$, free Δt

$\mathcal{E}$	f	n_p	$\eta_{sg,u}$	$\eta_{sg,v}$	$\overline{\eta_{sg}}$	ΔV m/s	Δt days
1	I	3	0.808	−0.123	0.343	103.279	99.72
2	I	3	0.747	−0.156	0.297	113.391	92.24
3	I	3	0.707	−0.132	0.287	108.169	86.70
4	I	3	0.667	−0.108	0.279	105.502	81.18
5	I	3	0.615	−0.134	0.241	116.341	75.02
1	II	3	0.949	−0.082	0.358	109.316	118.81
2	II	3	0.908	−0.123	0.392	121.443	113.68
3	II	3	0.863	−0.110	0.376	118.164	106.95
4	II	3	0.813	−0.092	0.361	115.059	99.82
5	II	3	0.764	−0.127	0.318	123.745	93.77

characterization implies that the later on the departure epoch $\mathcal{E}$, the better the propulsive efficiency and the reduction in the propellant request.

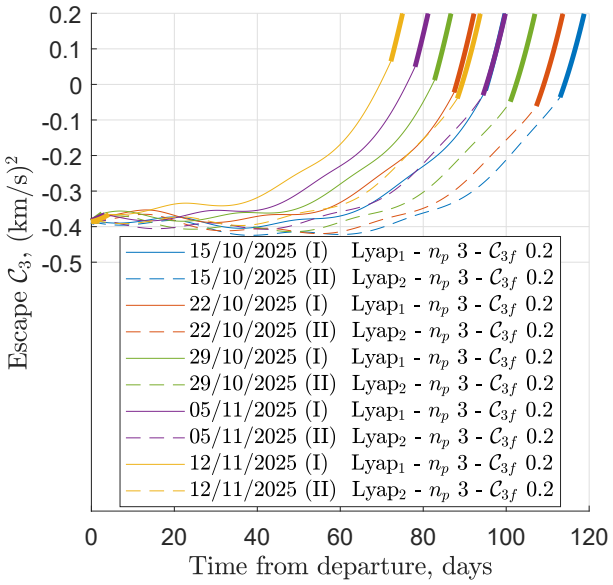

Fig. 6.9 SEL2 QPLOs escape trajectories energy over time

Figure 6.9 shows the trend of the energy over time for the SC; trajectories belonging to the first family appear in reverse order, with the shortest trip time for $\mathcal{E}_{5(I)}$ and the longest one for $\mathcal{E}_{1(I)}$. Family II, conversely, starts with a finely overlapping $\mathcal{E}_{4(II)}$ solution matching graphically $\mathcal{E}_{1(I)}$, as well as $\mathcal{E}_{5(II)}$ with $\mathcal{E}_{2(I)}$; they are indeed the "same" solution, for what concerns the indirect method optimization, and the

minor differences are due to the departure point on the epoch-dependent QPO. As noticeable from the performance results, both families I and II tend to reduce the positive radial perturbation while delaying the departure epoch from $\mathcal{E}_1$ to $\mathcal{E}_2$. A lower mean perturbation coefficient $\overline{\eta_{sg}}$, in this particular case, produces shorter trip times and almost equal performance. Again, such a result must be found in the QPOs departure points. Figure 6.10 can help visualize the results influences due to the solar perturbations, as well as with Figure 6.11, representing the optimal thrust angle.

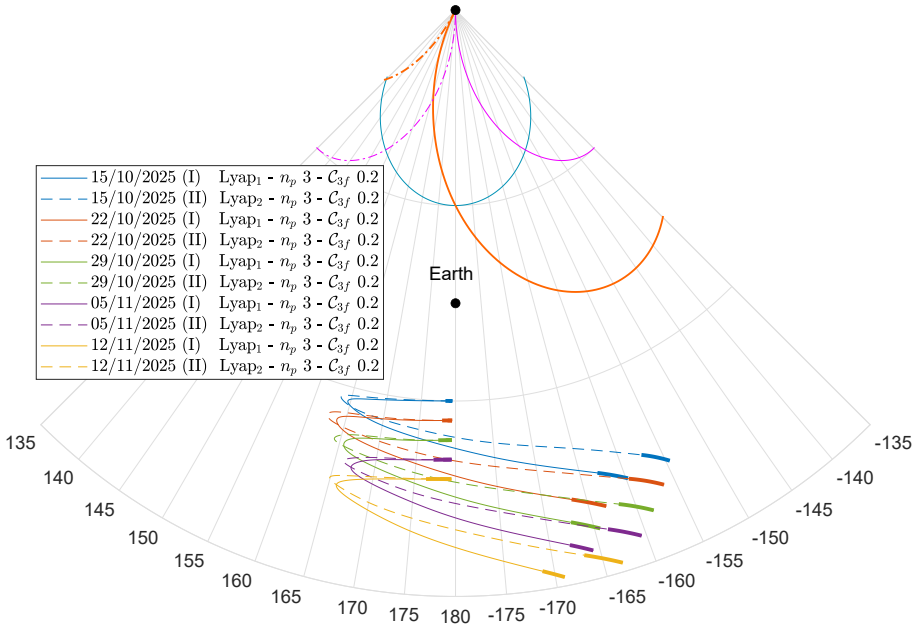

Fig. 6.10 SEL2 QPLOs escape trajectories polar view, fixed $\mathscr{C}_{3f} = 0.2\ (\mathrm{km/s})^2$, free Δt

All solutions thrust substantially in the radial direction, with $\alpha_T > 65^\circ$ in all the first thrust arcs, but family I missions prefer a slightly higher tangential component. Longer burns happen tangentially, whereas shorter ones radially; family I, in essence, exploits the QPO energy to evade, perturbing its quasi-stable state and diverging from the orbit itself. Family II, instead, has solutions that "jump off" the Lyapunov, acquiring less velocity in the tangential direction and thus apparently reverting back, with respect to the Sun, in the $\Delta\vartheta < 160^\circ$ region, which implies a negative tangential perturbation. Therefore, family II may be considered a "sub-optimal" solution.

The reason for which later departures require shorter trip times may be explained by the escape direction. While in the synodic RF all trajectories appear to escape in the fourth quadrant, actual heliocentric escape trajectories are almost all happening in the prograde/outward direction, producing a precession of the line of apsides.

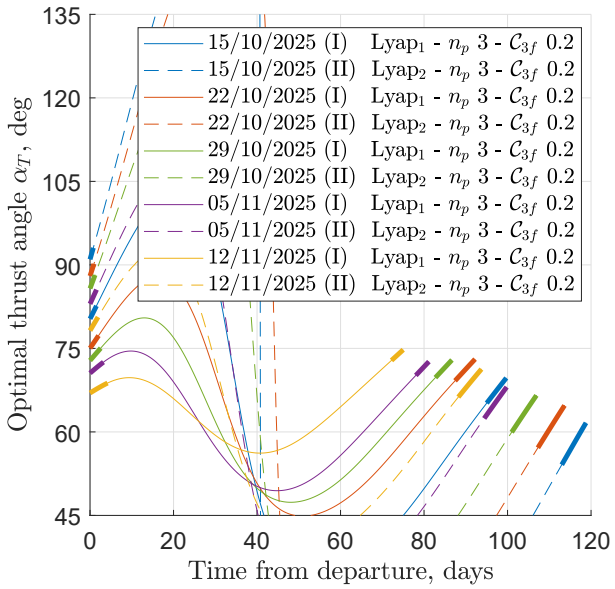

Fig. 6.11 SEL2 QPLOs escape trajectories optimal trust angle α_T, fixed $\mathscr{C}_{3f} = 0.2$ $(\mathrm{km/s})^2$, free Δt

Figure 6.12 shows the resulting heliocentric semimajor axis for free $\mathscr{C}_{3f}$ solutions, on the left, and constrained $L\mathscr{C}_{3f}$ trajectories, on the right. As per the other cases, integration times are extended by a factor equal to four per each individual mission duration, and whereas a thrust arc completes the trajectory, an additional fictitious fourth coast arc is introduced.

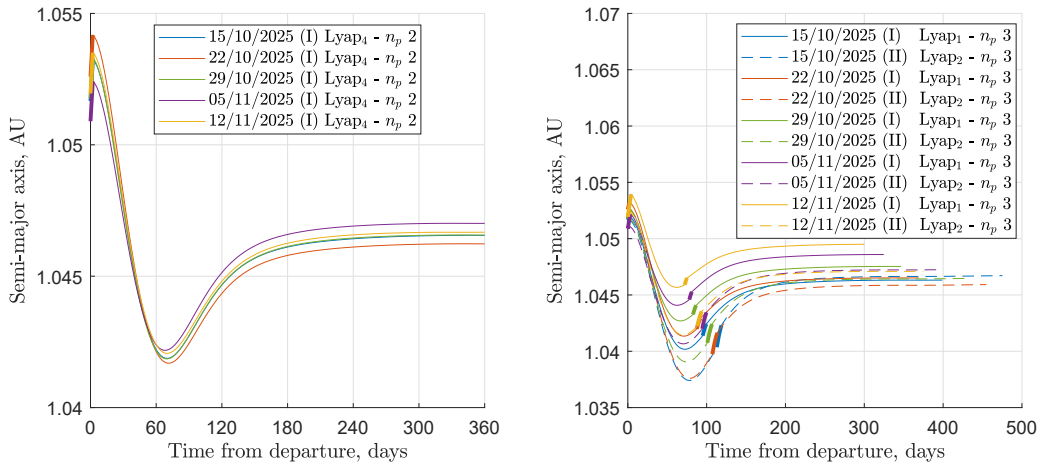

Fig. 6.12 SEL2 QPLOs escape trajectories semimajor axis, free $\mathscr{C}_{3f}$ fixed $\Delta t = 90$ days (left), fixed $\mathscr{C}_{3f} = 0.2$ $(\mathrm{km/s})^2$ free Δt (right), HE RF

Accepting longer escape trajectories, strategies to accomplish evasions from the Earth-Moon gravitational pull from QPOs can come at little to no cost, provided the correct optimal thrust angle is applied. In this thesis, escape trajectories are sought and, therefore, the *always* favorable solar perturbation, in the SEL_2 scenario just analyzed, straightforwardly reaching the heliocentric phase. On the other hand, this is the reason for which delicate stationkeeping strategies have to be implemented for Lyapunov orbits and Halo orbits, given that the opposite behaviour is less frequent, namely, no perturbation can come from the L_2 point in the SE scenario to bring the SC back to the Earth-Moon system.

Chapter 7

Concluding Remarks

The current interest in the Lagrangian Points (LPs) requires viable methods for the analysis of trajectories to and from these regions. In this context, the focus of the present discussion was the space trajectory optimization of low-thrust electric propulsion escapes in a high-fidelity model. In particular, escape trajectories in the Sun-Earth (SE) and Earth-Moon (EM) binary systems were considered, in a dynamical model including 4-body gravitation, Solar Radiation Pressure (SRP), and spherical harmonics for the Earth's asphericity.

Indirect methods were considered suitable for this purpose and exploited in this work. Extensive discussion regarding the Optimal Control Theory (OCT) and the Multi-Point Boundary Value Problem (MPBVP) was outlined in Chapter 4, identifying the indirect numerical method as the best candidate for resolving comprehensively the Hamiltonian Boundary Value Problem (HBVP) arising from the application of the OCT to the space trajectory optimization problem. Necessary and optimality conditions were derived, and powerful theoretical insights were outlined to guide the control law's evolution toward its optimal configuration. The derivation of optimality conditions for the definition of the MPBVP, and the analysis of solutions, allowed for an extensive understanding of the escape strategies. This knowledge, in turn, was extremely useful for the definition of suitable switching structures and initial guesses. The delicacy of the indirect method was tackled with specifically tailored strategies, such as the introduction of the multipoint approach and the *a priori* definition of a thrust structure to limit numerical issues in the switching function evolution. The automatic generation of tentative guesses significantly contributed to the analysis's

development. Invaluable post-processing operations were enabled with the application of the Pontryagin's Maximum Principle (PMP) to the problem, allowing to change a converged solution when the Thrust Structure (T_S) was violating, in some arcs, the PMP. The approach has proved successful, making the method extremely powerful and flexible. Moreover, the method's effectiveness was demonstrated by its ability to find local optima efficiently, with low computational effort. These features allow for the confident identification of the most relevant local optima and the subsequent identification of the global optimum among them. The characteristic speed of the indirect approach allows for rapid evaluation of different escape scenarios. The SE scenario provided a comprehensive understanding of the solar gravitational perturbation, with the exceptional performance of the indirect method in finding the best strategy to exploit every single bit of the positive perturbation to allow escape trajectories at little cost. On the other hand, the EM scenario extensively demonstrated the strong influence of both the Moon and the Sun on escapes, in preferential escape directions for the first and with specific coast phases to accommodate better perturbation for the latter.

In this work, a method to find Quasi-Periodic Orbits (QPOs) in a higher fidelity model was developed; a set of algorithms at increasing fidelity levels were sequentially operated to transition from elliptical analytical approximations, to Periodic Orbits (POs) computed via nonlinear numerical integration in the Circular Restricted Three-Body Problem (CR3BP) and then, finally, transitioned in the ephemeris model.

The transition to high-fidelity escape maneuvers from LPs to departures from QPOs was a straightforward process, proving that the simpler analysis in the Hybrid Four-Body Problem (H4BP) was a very suitable seeding tool for higher fidelity trajectory optimizations. A comparison of the results shows similar characteristics, but the changes related to the departure date appear less critical for the QPOs case due to their intrinsic higher stability. Escape trajectories from LPs, however, provide a good preliminary approximation of escape maneuvers starting for practical orbits around/in the vicinity of LPs.

7.1 Future research

The objectives of this work have been successfully obtained. The indirect optimization approach was applied to escape trajectories from LPs, solving the issues related

to the handling of thrust discontinuities with the multipoint approach and proper use of PMP. Suitable tentative solutions are found with the proposed automated search and continuation approaches. The developed tools have led to understanding the characteristics of escape trajectories from Sun-Earth Lagrangian Point L_2 (SEL_2) and Earth-Moon Lagrangian Point L_2 (EML_2) and orbits around these points. Due to their speed, they represent a valuable means for extensive analysis of escape trajectories.

The space domain is vast; therefore, many additional topics would have been analyzed in more detail in a more extended research period.

The useful insights that each analyzed scenario provided suggest the generation of additional case studies to understand further the perturbation influences that may help or prevent escape trajectories. First, an analysis of the influence of the departure point on the starting QPO can be easily performed by using the current solutions (with a departure on the $\hat{\boldsymbol{x}}_S$-axis) as a tentative guess and a continuation approach. Such an operation would allow understanding if preferential locations exist to exploit the intrinsic energy and general long-term instability of the QPO, and how to redirect them towards a more efficient escape.

Different QPOs can also be considered with similar approaches. Quasi-Periodic Near Rectilinear Halo Orbits (QPNRHOs) in the vicinity of the EM system, especially the Near Rectilinear Halo Orbit (NRHO) with 9:2 synodic resonance with the Moon, are of particular interest. The introduction of these three-dimensional vertical orbits may require suitable changes in both the algorithm structure and method; a multi-shooting algorithm could be beneficial to tackle the numerical issues at the periselenium during the escape optimization, whereas an improved QPO construction algorithm may be needed to construct such high-fidelity QPNRHOs.

The indirect approach presented here can also be extended to consider different transfers to and from LPs or orbits in their vicinity. The easier extension is to analyze capture maneuvers, which are symmetrical to escape ones. Change in the final boundary condition can be used to consider transfers to/from Earth or Moon parking orbits. Similarly, trajectories from (and to) the SE or EM Lagrangian Point L_1 (L_1) could be explored to outline the specular dynamic differences due to having initial or terminal conditions in between the two main gravitational bodies. Again, multiple shooting techniques and a careful definition of tentative guesses may be required, but the framework outlined in this thesis seems well-suited for this task. The tools here

developed and currently available are powerful and fast means for analysis of escape maneuvers. They could be used to rapidly build a database of achievable escape conditions and related costs as a function, for instance, of departure/escape date. These data can be coupled with the analysis of the interplanetary leg to a specified target body with an approach similar to the one described in [128] and adopted in the preliminary definition and optimization of the ARRM trajectory [129].

References

[1] Edgard. Y. Choueiri. A Critical History of Electric Propulsion: The First 50 Years (1906-1956). *Journal of Propulsion and Power*, 20(2):193–203, 2004. doi: 10.2514/1.9245.

[2] John T. Betts. *Practical Methods for Optimal Control and Estimation Using Nonlinear Programming*. Advances in Design and Control, 2010. ISBN 978-0-89871-688-7. doi: 10.1137/1.9780898718577.

[3] Stefano Campagnola, Rüdiger Jehn, and Carlos Corral Van Damme. Design of Lunar Gravity Assist for the BepiColombo Mission to Mercury. In *Proceedings of the AIAA/AAS Astrodynamics Specialist Conference*, 2004. AAS 04-130.

[4] J. Basset, Y. Xu, and O. A. Yakimenko. Computing Short-Time Aircraft Maneuvers Using Direct Methods. *Journal of Computer and System Sciences International*, 49:481–513, 2010. doi: 10.1134/S1064230710030159.

[5] Ryan J. Whitley, Cesar A. Ocampo, and Jacob Williams. Performance of an Autonomous Multi-Maneuver Algorithm for Lunar Trans-Earth Injection. *Journal of Spacecraft and Rockets*, 49(1), 2012. doi: 10.2514/1.52710.

[6] R. Bertrand and R. Epenoy. New Smoothing Techniques for Solving Bang-Bang Optimal Control Problems - Numerical Results and Statistical Interpretation. *Optimal Control Applications and Methods*, 23(4):171–197, 2002. doi: 10.1002/oca.709.

[7] Lorenzo Casalino. Singular Arcs During Aerocruise. *Journal of Guidance, Control, and Dynamics*, 23(1), 2000. doi: 10.2514/2.4494.

[8] Morris Handelsman. Optimal Free-Space Fixed-Thrust Trajectories Using Impulsive Trajectories as Starting Iteratives. *AIAA Journal*, 4(6):1077–1082, 1966. doi: 10.2514/3.3607.

[9] John E. Prussing and Jeng-Hua Chiu. Optimal Multiple-Impulse Time-Fixed Rendezvous Between Circular Orbits. *Journal of Guidance, Control, and Dynamics*, 9(1):17–22, 1986. doi: 10.2514/3.20060.

[10] European Space Agency. The Vigil mission, 2022. URL https://www.eoportal.org/satellite-missions/vigil. (Retrieved: 2023-01-03).

[11] European Space Agency. The "no name" Space Weather mission, 2020. URL https://www.esa.int/Safety_Security/The_no_name_space_weather_mission. (Retrieved: 2023-01-03).

[12] European Space Agency. PLATO: Revealing Habitable Worlds Around Solar-Like Stars. Technical report, 2017. URL https://sci.esa.int/web/plato/-/59252-plato-definition-study-report-red-book. Definition Study Report, ESA-SCI(2017)1. (Retrieved: 2023-01-03).

[13] European Space Agency. Euclid: Mapping the Geometry of the Dark Universe. Technical report, 2011. URL https://sci.esa.int/web/euclid/-/48983-euclid-definition-study-report-esa-sre-2011-12. Definition Study Report, ESA/SRE(2011)12. (Retrieved: 2023-01-03).

[14] Alessia De Iuliis, Luigi Mascolo, Stefano De Santi, and Lorenzo Casalino. Asteroid Rendezvous Missions with Departure From Earth-Sun L4 and L5. In *Proceedings of the 2020 AAS/AIAA Astrodynamics Specialist Conference*, 2020.

[15] European Space Agency. The Comet Interceptor mission, 2019. URL https://www.cosmos.esa.int/web/comet-interceptor/home. (Retrieved: 2023-01-03).

[16] European Space Agency. The Atmospheric Remote-sensing Infrared Exoplanet Large-survey (ARIEL) mission, 2020. URL https://www.cosmos.esa.int/web/ariel. (Retrieved: 2023-01-03).

[17] ESA Earth Observation Portal (eoPortal). Lunar Gateway of NASA's Artemis Program. URL https://www.eoportal.org/other-space-activities/lunar-gateway. (Retrieved: 2023-01-03).

[18] S. Fuller, E Lehnhardt, C. Zaid, and K. Halloran. A Critical History of Electric Propulsion: The Frist Fifty Years (1906-1956). In *Proceedings of the 72nd International Astronautical Congress*, 2021. Iafastro; IAC-21,A3,2B,13,x66240.

[19] NASA. The Artemis Plan. URL https://www.nasa.gov/sites/default/files/atoms/files/artemis_plan-20200921.pdf. NASA's Lunar Exploration Program Overview, Technical Report NP-2020-05-2853-HQ. (Retrieved: 2023-01-03).

[20] M. Matsumoto. Deep Space Transportation System Using the Sun-Earth L2 Point. In *Proceedings of the 20th International Symposium on Space Flight Dynamics*, 2007.

[21] Yang Gao. Near-Earth Asteroid Flyby Trajectories from the Sun-Earth L2 for Chang'e-2's Extended Flight. *Acta Mechanica Sinica*, 29:123–131, 2013. doi: 10.1007/s10409-013-0011-8.

[22] P. Machuca, J. P. Sánchez, Josep J. Masdemont, and Gerard Gómez. High-Fidelity Trajectory Design to Flyby Near-Earth Asteroids using CubeSats. *Acta Astronautica*, 167:146–163, 2020. doi: 10.1016/j.actaastro.2019.09.041.

[23] Michael A. Patterson and Anil V. Rao. *A General-Purpose MATLAB Software for Solving Multi-Phase Optimal Control Problems*, 2016. Version 2.3.

[24] Yoshiaki Kawajir, François Margot, Carl Laird, Stefan Vigerske, and Andreas Wätcher. *Introduction to* IPOPT*: A tutorial for downloading, installing, and using* IPOPT, 2015. Version 3.11, Revision: 2567.

[25] F. Bernelli Zazzera, F. Topputo, and M. Massari. Assessment of Mission Design Including Utilization of Libration Points and Weak Stability Boundaries. Technical report, European Space Agency, 2004. Ariadna ID: 03/4103, C/N 18147/04/NL/MV.

[26] E. Canalias, G. Gomez, M. Marcote, and J. J. Masdemont. Assessment of Mission Design Including Utilization of Libration Points and Weak Stability Boundaries. Technical report, European Space Agency, 2004. Ariadna ID: 03/4103, C/N 18147/04/NL/MV.

[27] K. Tanaka and J. Kawagughi. Escape Trajectories from the L_2 Point of the Earth-Moon System. *Japan Society for Aeronautical and Space Sciences*, 57 (4):238–244, 2014. doi: 10.2322/tjsass.57.238.

[28] Victor Szebehely. *Theory of Orbits: The Restricted Problem of Three Bodies*. Academic Press Inc., 1967. ISBN 978-0-12412-431-8. doi: 10.1016/B978-0-12-395732-0.X5001-6.

[29] Roger R. Bate, Donald D. Mueller, and Jerry E. White. *Fundamentals of Astrodynamics*. Dover Publications, New York, 1971. ISBN 978-0-48660-061-1.

[30] John E. Prussing and Bruce A. Conway. *Orbital Mechanics*. Oxford University Press, 1993. ISBN 978-1-56347-157-9. doi: 10.2514/3.12179.

[31] David A. Vallado. *Fundamentals of Astrodynamics and Applications*. McGraw-Hill Companies, Space Technology Series, 1997. ISBN 0-07-066829-9.

[32] Richard H. Battin. *An Introduction to the Mathematics and Methods of Astrodynamics*. AIAA Education Series, 1999. ISBN 978-1-60086-154-3. doi: 10.2514/4.861543.

[33] Oliver Montenbruck and Eberhard Gill. *Satellite Orbits: Models, Methods, Applications*. Springer, 2000. ISBN 978-3-642-58351-3.

[34] Archie E. Roy. *Orbital Motion*. CRC Press, 2004. ISBN 978-0-75031-015-4.

[35] Hanspeter Shaub and John L. Junkins. *Analytical Mechanics of Space Systems*. AIAA Education Series, 2018. ISBN 978-1-62410-657-6. doi: 10.2514/4.105210.

[36] William E. Wiesel. *Modern Astrodynamics*. CreateSpace, 2nd edition, 2010. ISBN 978-145378-1470.

[37] Giorgio Fasano and János D. Pintér. *Modeling and Optimization in Space Engineering*. Springer, 2013. ISBN 978-1-4614-4469-5. doi: 10.1007/978-1-4614-4469-5.

[38] Howard D. Curtis. *Orbital Mechanics for Engineering Students*. Butterworth-Heinemann, Elsevier, 4th edition, 2020. ISBN 978-0-12824-025-0. doi: 10.1016/C2016-0-02107-1.

[39] Alessandro Dei Tos Diogene. *Trajectory Optimization of Limited Control Authority Spacecraft in High-Fidelity Models*. PhD thesis, Politecnico di Milano, 2017.

[40] Jet Propulsion Laboratory Solar System Dynamics. JPL Planetary and Lunar Ephemerides: Export Information, 2020. URL https://ssd.jpl.nasa.gov/planets/eph_export.html. (Retrieved: 2023-01-03).

[41] National Aeronautics and Space Administration. Report Concerning Space Data System Standards - Navigation Data - Definitions and Conventions. Technical report, National Aeronautics and Space Administration, 2019. Informational Report, CCSDS 500.0-G-D, Green Book.

[42] Lorenzo Casalino. *Ottimizzazione energetica di manovre orbitali aeroassistite*. PhD thesis, Politecnico di Torino, Facoltà di Ingegneria, 1998.

[43] Alejandro M. Leiva and Carlos B. Briozzo. The Earth-Moon CR3BP: a Full Atlas of Low-Energy Fast Periodic Transfer Orbits. 2006. doi: 10.48550/arXiv.astro-ph/0612386. arXiv Astrophysics. (Retrieved: 2023-01-03).

[44] Daniel J. Grebow. Generating Periodic Orbits in the Circular Restricted Three-Body Problem with Applications to Lunar South Pole Coverage. Master's thesis, Purdue University, 2013.

[45] Thomas A. Pavlak. *Trajectory Design and Orbit Maintenance Strategies in Multi-Body Dynamical Regimes*. PhD thesis, Purdue University, 2013.

[46] Joseph-Louis Lagrange. Essai sur le Problème des Trois Corps. *Oeuvres de Lagrange*, 6:229–331, 1772. URL http://sites.mathdoc.fr/cgi-bin/oeitem?id=OE_LAGRANGE__6_229_0. (Retrieved: 2023-01-03).

[47] Dennis B. Westra. Lagrangian Points, 2017. URL https://www.mat.univie.ac.at/~westra. Physics and Mathematics. (Retrieved: 2023-01-03).

[48] Luigi Mascolo and Lorenzo Casalino. Optimal Escape from Sun-Earth/Earth-Moon L2 with Electric Propulsion. *Aerospace*, 9(4), 2022. doi: 10.3390/aerospace9040186.

[49] Francesco Simeoni, Lorenzo Casalino, Alessandro Zavoli, and Guido Colasurdo. Indirect Optimization of Satellite Deployment into a Highly Elliptic Orbit. *International Journal of Aerospace Engineering*, 20:389–404, 2012. doi: 10.1155/2012/152683.

[50] Camilla Colombo. Long-Term Evolution of Highly-Elliptical Orbits: Luni-Solar Perturbation Effects for Stability and Re-Entry. *Frontiers in Astronomy and Space Sciences*, 6(34), 2019. doi: 10.3389/fspas.2019.00034.

[51] Jean A. Kéchichian. Analytic Expansions of Luni-Solar Gravity Perturbations along Rotating Axes for Trajectory Optimization: Part 1: The Dynamic System. *Acta Astronautica*, 68(11):1947–1963, 2011. ISSN 0094-5765. doi: 10.1016/j.actaastro.2010.12.001.

[52] Jean-Baptiste Thevenet and Richard Epenoy. Minimum-Fuel Deployment for Spacecraft Formations via Optimal Control. *Journal of Guidance, Control, and Dynamics*, 31(1):101–113, 2008. doi: 10.2514/1.30364.

[53] Jason C. H. Chuang, Troy D. Goodson, and John Hanson. Multiple-Burn Families of Optimal Low- and Medium-Thrust Orbit Transfers. *Journal of Spacecraft and Rockets*, 36(6):866–874, 1999. doi: 10.2514/2.3505.

[54] R. C. Domingos, R. Vilhena de Moraes, and A. F. Bertachini De Almeida Prado. Third-Body Perturbation in the Case of Elliptic Orbits for the Disturbing Body. *Mathematical Problems in Engineering*, 2008, 2008. doi: 10.1155/2008/763654.

[55] Martin Lara. On Perturbation Solutions in the Restricted Three-Body Problem Dynamics. *Acta Astronautica*, 195:596–604, 2022. ISSN 0094-5765. doi: 10.1016/j.actaastro.2022.01.022.

[56] National Geospatial-Intelligence Agency (NGA). Earth Gravitational Model EGM2008, 2008. URL https://earth-info.nga.mil/. (Retrieved: 2023-01-03).

[57] Nikolaos K. Pavlis, Simon A. Holmes, Steve C. Kenyon, and John K. Factor. The Development and Evaluation of the Earth Gravitational Model 2008 (EGM2008). *Journal of Geophysical Research*, 117:1–38, 2012. ISSN B04406. doi: 10.1029/2011JB008916.

[58] Robert W. Farquhar. *The Control and Use of Libration-Point Satellites*. PhD thesis, Goddard Space Flight Center, 1966. NASA Technical Report, ID: NASA TR R-346.

[59] Mihai Popescu and Vladimir Cardoş. The Domain of Initial Conditions for the Class of Three-Dimensional Halo Periodical Orbits. *Acta Astronautica*, 36 (4):193–196, 1995. ISSN 0094-5765. doi: 10.1016/0094-5765(95)00107-B.

[60] Emily M. Zimovan-Spreen, Kathleen C. Howell, and Diane C. Davis. Near Rectilinear Halo Orbits and Nearby Higher-Period Dynamical Structures: Orbital Stability and Resonance Properties. *Celestial Mechanics and Dynamical Astronomy*, 132, 2020. doi: 10.1007/s10569-020-09968-2.

[61] Stefania Soldini, Gerard Gómez, Joseph J. Masdemont, Camilla Colombo, and Scott Walker. Solar Radiation Pressure Assisted Transfers Between Lissajous Orbits of the Sun-Earth System. In *Proceedings of the 67th International Astronautical Congress*, 2016. IAC-16.C1.6.13.

[62] Brian P. McCarthy and Kathleen C. Howell. Trajectory Design Using Quasi-Periodic Orbits in the Multi-Body Problem. In *Proceedings of the AIAA/AAS Astrodynamics Specialist Conference*, 2019. AAS 19-329.

[63] Brian P. McCarthy and Kathleen C. Howell. Leveraging Quasi-Periodic Orbits for Trajectory Design in Cislunar Space. *Astrodynamics*, 5:139–165, 2021. doi: 10.1007/s42064-020-0094-5.

[64] Wang Sang Koon, Martin W. Lo, Jerrold E. Marsden, and Shane D. Ross. *Dynamical Systems, the Three-Body Problem, and Space Mission Design*. Marsden Books, 2006. ISBN 978-0-615-24095-4. doi: 10.1142/9789812792617_0222.

[65] John V. Breakwell and John V. Brown. The "Halo" Family of 3-Dimensional Periodic Orbits in the Earth-Moon Restricted 3-Body Problem. *Celestial Mechanics*, 20:389–404, 1979. doi: 10.1007/BF01230405.

[66] Ettore Perozzi and Sylvio Ferraz-Mello. *Space Manifold Dynamics*. Springer, 2010. ISBN 978-1-4419-0348-8. doi: 10.1007/978-1-4419-0348-8.

[67] David L. Richardson. Periodic and Quasi Periodic Halo Orbits in the Earth-Sun/Earth-Moon Systems. Technical report, 2010. FDSS Contract #NNG10CP02C, Subtask 1 of Task Order 31: Advanced Mission Design.

[68] Jeffrey S. Parker and Rodney L. Anderson. *Low-Energy Lunar Trajectory Design*. Wiley, 2014. ISBN 978-1-118-85531-7. doi: 10.1002/9781118855065.

[69] Davide Guzzetti, Emily Zimovan, Kathleen Howell, and Diane Davis. Stationkeeping Analysis for Spacecraft in Lunar Near Rectilinear Halo Orbits. In *Proceedings of the 2017 AAS/AIAA Astrodynamics Specialist Conference*, 2017.

[70] Marta Ceccaroni, Alessandra Celletti, and Giuseppe Pucacco. Bifurcations Thresholds of Halo Orbits. In Gerard Gómez and Josep J. Masdemont, editors, *Astrodynamics Network AstroNet-II*, pages 35–44, Cham, 2016. Springer International Publishing. ISBN 978-3-319-23986-6.

[71] Kathleen C. Howell and J. V. Breakwell. Almost Rectilinear Halo Orbits. *Celestial Mechanics*, 32:29–52, 1982. doi: 10.1007/BF01358402.

[72] David E. Lee. White Paper: Gateway Destination Orbit Model: A Continuous 15 Year NRHO Reference Trajectory. Technical report, National Aeronautics and Space Administration, 2019. Report/Patent Number JSC-E-DAA-TN72594.

[73] NASA Space Science Data Coordinated Archive (NSSDCA). Moon Fact Sheet, 2021. URL https://nssdc.gsfc.nasa.gov/planetary/factsheet/moonfact.html. (Retrieved: 2023-01-03).

[74] Ryan J. Whitley, Diane C. Davis, Laura M. Burke, Brian P. McCarthy, Rolfe J. Power, Melissa L. McGuire, and Kathleen C. Howell. Earth-Moon Near Rectilinear Halo and Butterfly Orbits for Lunar Surface Exploration. In *Proceedings of the AIAA/AAS Astrodynamics Specialist Conference*, 2018. AAS 18-406.

[75] Advanced Concepts Team, Mission Analysis. 1st global trajectory optimization competition (gtoc). URL https://www.esa.int/gsp/ACT/projects/gtoc_1/gtoc1wrkprog/. (Retrieved: 2023-01-03).

[76] David Morante, Manuel Sanjurjo Rivo, and Manuel Soler. A Survey on Low-Thrust Trajectory Optimization Approaches. *Aerospace*, 8(3), 2021. ISSN 2226-4310. doi: 10.3390/aerospace8030088.

[77] John T. Betts. Survey of Numerical Methods for Trajectory Optimization. *Journal of Guidance, Control, and Dynamics*, 21(2):193–207, 1998. doi: 10.2514/2.4231.

[78] A. V. Rao. A Survey of Numerical Methods for Optimal Control. In *Proceedings of the AAS/AIAA Astrodynamics Specialist Conference*, August 2010. AAS 09-334.

[79] B. A. Conway. Survey of Methods Available for the Numerical Optimization of Continuous Dynamic Systems. *Journal of Optimization Theory and Applications*, 152(2):271–306, 2012. doi: 10.1007/s10957-011-9918-z.

[80] Abolfazl Shirazi, Josu Ceberio, and Jose A. Lozano. Spacecraft Trajectory Optimization: A Review of Models, Objectives, Approaches and Solutions. *Progress in Aerospace Sciences*, 102:76–98, 2018. ISSN 0376-0421. doi: 10.1016/j.paerosci.2018.07.007.

[81] Greg Johnson and Sebastian Munoz. *COPERNICUS*, a Generalized Trajectory Design and Optimization System. Technical report, The University of Texas at Austin, 2003. Engineering Communication ASE 333T, Dr. Jennifer Lehman.

[82] Steven P. Hughes, Rizwan H. Qureshi, Steven D. Cooley, and Joel J. Parker. Verification and Validation of the General Mission Analysis Tool (GMAT). In *Proceedings of the AIAA/AAS Astrodynamics Specialist Conference*, August 2014. doi: 10.2514/6.2014-4151. AIAA 2014-4151.

[83] Erik Gallesio. *STK Reference Manual*, 1999. Version 4.0.

[84] V. Coverstone-Carroll, J.W. Hartmann, and W.J. Mason. Optimal Multi-Objective Low-Thrust Spacecraft Trajectories. *Computer Methods in Applied Mechanics and Engineering*, 186(2):387–402, 2000. ISSN 0045-7825. doi: 10.1016/S0045-7825(99)00393-X.

[85] H. J. Oberle and W. Grimm. BNDSCO*: A Program for the Numerical Solution of Optimal Control Problems*. PhD thesis, Institute for Applied Mathematics, University of Hamburg; Institute for Flight System Dynamics, German Aerospace Research Establishment DLR, Oberpfaffenhofen, 2001.

[86] Derek F. Lawden. *Optimal Trajectories for Space Navigation*. Butterworths & Co. (Publishers) Ltd., 1963. Suggested U. D. C. number: 629.7.086. Paper hard-cover personal copy.

[87] Derek F. Lawden. Minimal Rocket Trajectories. *Journal of the American Rocket Society*, 29:360–367, 1953. doi: 10.2514/8.4642.

[88] Derek F. Lawden. Fundamentals of Space Navigation. *Journal of the British Interplanetary Society*, 13:87–101, 1954.

[89] Derek F. Lawden. Optimal Powered Arcs in an Inverse Square Law Field. *Journal of the American Rocket Society*, 31:566–568, 1954.

[90] Placido Cicala and Angelo Miele. Generalized Theory of the Optimum Thrust Programming for the Level Flight of a Rocket-Powered Aircraft. *Journal of Jet Propulsion*, 26(6):443–455, 1956. doi: 10.2514/8.7047.

[91] W. G. Melbourne and C. G. Sauer Jr. Optimum Thrust Programs for Power-Limited Propulsion Systems. *Astronautica Acta*, 8:205–227, 1962.

[92] Christopher L. Ranieri and Cesar A. Ocampo. Indirect Optimization of Three-Dimensional Finite-Burning Interplanetary Transfers Including Spiral Dynamics. *Journal of Guidance, Control, and Dynamics*, 32(2):445–455, 2009. doi: 10.2514/1.38170.

[93] Camilla Colombo, Massimiliano Vasile, and Gianmarco Radice. Optimal Low-Thrust Trajectories to Asteroids through an Algorithm based on Differential Dynamic Programming. *Celestial Mechanics and Dynamical Astronomy*, 105: 75–112, 2009. doi: 10.1007/s10569-009-9224-3.

[94] D. Pérez-Palau and R. Epenoy. Indirect optimal control for minimum-fuel low-Thrust earth-moon transfer. *Advances in the Astronautical Sciences*, 161: 499–518, 2017.

[95] Yang Wang. *Efficient Indirect Optimization of Low-Thrust Trajectories with Interior-Point Constraints*. PhD thesis, Politecnico di Milano, 2022.

[96] Guido Colasurdo. Optimal Finite-Thrust Spacecraft Trajectories. In *Proceedings of the Astrodynamics Conference*, 1992. doi: 10.2514/6.1992-4510.

[97] Guido Colasurdo and Dario Pastrone. Indirect Optimization Method for Impulsive Transfers. In *Proceedings of the Astrodynamics Conference*, 1994. doi: 10.2514/6.1994-3762.

[98] Lorenzo Casalino, Guido Colasurdo, and Dario Pastrone. Optimal Three-Dimensional Trajectories for Manned Mars Missions. In *Proceedings of the Astrodynamics Conference*, 1996. doi: 10.2514/6.1996-3612.

[99] Lorenzo Casalino, Guido Colasurdo, and Dario Pastrone. Indirect Approach for Minimum-Fuel Aeroassisted Transfers. In *Proceedings of the Astrodynamics Conference*, pages 192–200, 1996. doi: 10.2514/6.1996-3592.

[100] Lorenzo Casalino, Guido Colasurdo, and Dario Pastrone. Optimization Procedure for Preliminary Design of Opposition-Class Mars Missions. *Journal of Guidance, Control, and Dynamics*, 21(1):134–140, 1998. doi: 10.2514/2.4209.

[101] Lorenzo Casalino, Guido Colasurdo, and Dario Pastrone. Optimization of ΔV Earth-Gravity-Assist Trajectories. *Journal of Guidance, Control, and Dynamics*, 21(6):991–995, 1998. doi: 10.2514/2.4336.

[102] Francesco Simeoni. *Cooperative Deployment of Satellite Formation into Highly Elliptic Orbit*. PhD thesis, Politecnico di Torino, 2013.

[103] Donald E. Kirk. *Optimal Control Theory: An Introduction*. Dover Publications, Inc., 1975. ISBN 978-0-48643-484-1. doi: 10.1002/aic.690170452.

[104] Arthur E. Jr. Bryson and Yu-Chi Ho. *Applied Optimal Control; Optimization, Estimation, and Control*. Taylor & Francis Group, 1975. ISBN 978-1-31513-766-7. doi: 10.1201/9781315137667.

[105] David Burghes and Alexander Graham. *Control and Optimal Control Theories with Applications*. Horwood Publishing Limited, Published in 1980, Reprinted in 2004, 2004. ISBN 978-1-904275-01-5.

[106] Bruce A. Conway. *Spacecraft Trajectory Optimization*. Cambridge University Press, 2010. ISBN 978-0-51177-802-5. doi: 10.1017/CBO9780511778025.

[107] Emmanuel Trélat. Optimal Control and Applications to Aerospace: Some Results and Challenges. *Journal of Optimization Theory and Applications*, 154:713–758, 2012. doi: 10.1007/s10957-012-0050-5.

[108] Daniel Liberon. *Calculus of Variations and Optimal Control Theory*. Princeton University Press, 2012. ISBN 978-1-40084-264-3. doi: 10.1515/9781400842643.

[109] John A. Burns. *Introduction to the Calculus of Variations and Control with Modern Applications*. Chapman & Hall/CRC Applied Mathematics & Nonlinear Science. Taylor & Francis, 2013. ISBN 978-1-46657-139-6.

[110] Leonhard Euler. Elementa Calculi Variationum, 1766. URL https://scholarlycommons.pacific.edu/euler-works/296/. Euler Archive. Retrieved (2023-01-13).

[111] Leonhard Euler. Integral Calculus, vol. III (*Institutionum Calculi Integralis Volumen Tertium*), 1770. URL https://scholarlycommons.pacific.edu/euler-works/385/. Euler Archive. Retrieved (2023-01-13).

[112] J. P. McDanell and W. F. Powers. Necessary Conditions Joining Optimal Singular and Nonsingular Subarcs. *SIAM Journal on Control*, 9(2):161–173, 1971. doi: 10.1137/0309014.

[113] Lawrence F. Shampine and Marilyn Kay Gordon. *Computer Solution of Ordinary Differential Equations: the Initial Value Problem*. W. H. Freeman and Company, 1975. ISBN 9780716704614.

[114] C. Silva and E. Trélat. Smooth Regularization of Bang-Bang Optimal Control Problems. *IEEE Transactions on Automatic Control*, 55(11):2488–2499, 2010. doi: 10.1109/TAC.2010.2047742.

[115] Ehsan Taheri and John L. Junkins. Generic Smoothing for Optimal Bang-Off-Bang Spacecraft Maneuvers. *Journal of Guidance, Control, and Dynamics*, 41(11):2467–2472, 2018. doi: 10.2514/1.G003604.

[116] Z. Gao and H. Baoyin. Using Homotopy Method to Solve Bang–Bang Optimal Control Problems. *Optimization, Simulation, and Control*, 76:243–256, 2013. doi: 10.1007/978-1-4614-5131-0_15.

[117] Z. Gao and H. Baoyin. Solving Fuel-Optimal Low-Thrust Orbital Transfers with Bang-Bang Control Using a Novel Continuation Technique. *Acta Astronautica*, 137:98–113, 2017. doi: 10.1016/j.actaastro.2017.03.032.

[118] Kshitij Mall, Michael J. Grant, and Ehsan Taheri. Uniform Trigonometrization Method for Optimal Control Problems with Control and State Constraints. *Journal of Spacecraft and Rockets*, 57(5):995–1007, 2020. doi: 10.2514/1.A34624.

[119] Thomas Anthony and Michael J. Grant. Path Constraint Regularization in Optimal Control Problems using Saturation Functions. In *Proceedings of the 2018 AIAA Atmospheric Flight Mechanics Conference*, 2018. doi: 10.2514/6.2018-0018. AIAA 2018-0018.

[120] Daniel García Yárnoz, Joan-Pau Sanchez, and Colin R. McInnes. *Opportunities for Asteroid Retrieval Missions*, pages 479–505. Springer Berlin Heidelberg, Berlin, Heidelberg, 2013. ISBN 978-3-642-39244-3. doi: 10.1007/978-3-642-39244-3_21.

[121] Gustavo Gargioni, David Alexandre, Marco Peterson, and Kevin Schroeder. Multiple Asteroid Retrieval Mission from Lunar Orbital Platform-Gateway Using Reusable Spacecrafts. In *2019 IEEE Aerospace Conference*, pages 1–13, 2019. doi: 10.1109/AERO.2019.8741985.

[122] D. Perna, M. Pajola, L. Casalino, S. Ivanovski, M. Lavagna, M. Zannoni, M. Bechini, A. Capannolo, A. Colagrossi, G. Cremonese, E. Dotto, A. Lucchetti, E. Mazzotta Epifani, J. Prinetto, E. Simioni, P. Tortora, and G. Zanotti. The "Asteroid Nodal Intersection Multiple Encounters" (ANIME) CubeSat Mission: Science and Planetary Protection. In *Proceedings of the 7th IAA Planetary Defense Conference*, April 2021. IAA-PDC-21-08-06.

[123] Camilla Colombo, Elisa Maria Alessi, Willem van der Weg, Stefania Soldini, Francesca Letizia, Massimo Vetrisano, Massimiliano Vasile, Alessandro Rossi,

and Markus Landgraf. End-of-life disposal concepts for Libration Point Orbit and Highly Elliptical Orbit missions. *Acta Astronautica*, 110:298–312, 2015. ISSN 0094-5765. doi: 10.1016/j.actaastro.2014.11.002. Dynamics and Control of Space Systems.

[124] Greta De Marco and Camilla Colombo. End-of-Life Disposal Design for Spacecraft at Libration Point Orbits and an Interpretation of Their Probability of Earth Return. In *Proceedings of the 69th International Astronautical Congress*, 2018. IAC-18.C1.

[125] ArianeGroup. Electric Ion Space Propulsion Systems and Thrusters. URL https://www.ariane.group/en/equipment-and-services/satellites-and-spacecraft/rit-2x-series/. (Retrieved: 2023-01-03).

[126] Luigi Mascolo, Alessia De Iuliis, and Lorenzo Casalino. Fast and Accurate Estimation of Fuel-Optimal Trajectories to Near-Earth Asteroids. *Acta Astronautica*, 188:49–56, 2021. ISSN 0094-5765. doi: 10.1016/j.actaastro.2021.07.013.

[127] A. Mereta and D. Izzo. Target Selection for a Small Low-Thrust Mission to Near-Earth Asteroids. *Astrodynamics*, 2:249–263, 2018. doi: 10.1007/s42064-018-0024-y.

[128] Raymond G. Merrill, Min Ou, Mattew A. Vavrina, Christopher A. Jones, and Jacob Englander. Interplanetary Trajectory Design for the Asteroid Robotic Redirect Mission Alternate Approach Trade Study. In *Proceedings of the AIAA/AAS Astrodynamics Specialist Conference*, 2014. doi: 10.2514/6.2014-4457. AIAA 2014-4457.

[129] Lorenzo Casalino and Gregory Lantoine. Design of Lunar-Gravity-Assisted Escape Trajectories. *The Journal of the Astronautical Sciences*, 67:1374–1390, 2020. doi: 10.1007/s40295-020-00229-w.

Appendix A

CR3BP State Transition Matrix

First and second pseudopotential $\mathscr{U}$ partial derivatives

$$
\begin{aligned}
\frac{\partial \mathscr{U}}{\partial \xi} &= \frac{\partial}{\partial \xi}\left\{\frac{1}{2}\left(\xi^2+\eta^2\right)+\frac{1-\mu}{\left[(\xi+\mu)^2+\eta^2+\zeta^2\right]^{\frac{1}{2}}}+\frac{\mu}{\left[(\xi-1+\mu)^2+\eta^2+\zeta^2\right]^{\frac{1}{2}}}\right\} \\
&= \xi-\frac{(1-\mu)(\xi+\mu)}{\left[(\xi+\mu)^2+\eta^2+\zeta^2\right]^{\frac{3}{2}}}-\frac{\mu(\xi-1+\mu)}{\left[(\xi-1+\mu)^2+\eta^2+\zeta^2\right]^{\frac{3}{2}}} \\
&= \xi-(1-\mu)\frac{(\xi+\mu)}{\rho_{13}^3}-\mu\frac{(\xi-1+\mu)}{\rho_{23}^3} \\
\frac{\partial \mathscr{U}}{\partial \eta} &= \eta-(1-\mu)\frac{\eta}{\rho_{13}^3}-\mu\frac{\eta}{\rho_{23}^3} \\
\frac{\partial \mathscr{U}}{\partial \zeta} &= -(1-\mu)\frac{\zeta}{\rho_{13}^3}-\mu\frac{\zeta}{\rho_{23}^3}
\end{aligned}
\tag{A.1}
$$

$$A_{41} = \mathscr{U}_{\xi\xi} = 1 - \frac{(1-\mu)}{\rho_{13}^5}\left[\rho_{13}^2 - 3(\xi+\mu)^2\right] - \frac{\mu}{\rho_{23}^5}\left[\rho_{23}^2 - 3(\xi-1+\mu)^2\right] \tag{A.2a}$$

$$A_{42} = \mathscr{U}_{\xi\eta} = 3\eta\left[\frac{(1-\mu)}{\rho_{13}^5}(\xi+\mu) + \frac{\mu}{\rho_{23}^5}(\xi-1+\mu)\right] \tag{A.2b}$$

$$A_{43} = \mathscr{U}_{\xi\zeta} = 3\zeta\left[\frac{(1-\mu)}{\rho_{13}^5}(\xi+\mu) + \frac{\mu}{\rho_{23}^5}(\xi-1+\mu)\right] \tag{A.2c}$$

$$A_{51} = \mathscr{U}_{\eta\xi} = \mathscr{U}_{\xi\eta} \tag{A.2d}$$

$$A_{52} = \mathscr{U}_{\eta\eta} = 1 - \frac{(1-\mu)}{\rho_{13}^5}\left[\rho_{13}^2 - 3\eta^2\right] - \frac{\mu}{\rho_{23}^5}\left[\rho_{23}^2 - 3\eta^2\right] \tag{A.2e}$$

$$A_{53} = \mathscr{U}_{\eta\zeta} = 3\eta\zeta\left[\frac{(1-\mu)}{\rho_{13}^5} + \frac{\mu}{\rho_{23}^5}\right] \tag{A.2f}$$

$$A_{61} = \mathscr{U}_{\zeta\xi} = \mathscr{U}_{\xi\zeta} \tag{A.2g}$$

$$A_{62} = \mathscr{U}_{\zeta\eta} = \mathscr{U}_{\eta\zeta} \tag{A.2h}$$

$$A_{63} = \mathscr{U}_{\zeta\zeta} = -\frac{(1-\mu)}{\rho_{13}^5}\left(\rho_{13}^2 - 3\zeta^2\right) - \frac{\mu}{\rho_{23}^5}\left(\rho_{23}^2 - 3\zeta^2\right) \tag{A.2i}$$

$$\boldsymbol{A} = \begin{bmatrix} 0 & 0 & 0 & 1 & 0 & 0 \\ 0 & 0 & 0 & 0 & 1 & 0 \\ 0 & 0 & 0 & 0 & 0 & 1 \\ \mathscr{U}_{\xi\xi} & \mathscr{U}_{\xi\eta} & \mathscr{U}_{\xi\zeta} & 0 & 2 & 0 \\ \mathscr{U}_{\eta\xi} & \mathscr{U}_{\eta\eta} & \mathscr{U}_{\eta\zeta} & -2 & 0 & 0 \\ \mathscr{U}_{\zeta\xi} & \mathscr{U}_{\zeta\eta} & \mathscr{U}_{\zeta\zeta} & 0 & 0 & 0 \end{bmatrix} \tag{A.3}$$

Appendix B

NBP State Transition Matrix

Second U partial derivatives

The general dimensional formulation is

$$\ddot{\boldsymbol{r}}_{ki} = -\frac{\mu_i + \mu_k}{r_{ki}^3}\boldsymbol{r}_{ki} + \sum_{\substack{j=1 \\ j\neq i,\ k}}^{n} \mu_j \left(\frac{\boldsymbol{r}_{ij}}{r_{ij}^3} - \frac{\boldsymbol{r}_{kj}}{r_{kj}^3} \right) \tag{B.1}$$

Following the example in the CR3BP scenario, the Right-Hand Side (RHS) is already the first derivative of the potential. Therefore, by projecting in the inertial directions

$$\ddot{x}_{ki} = -\frac{\mu_i + \mu_k}{r_{ki}^3}x_{ki} + \sum_{\substack{j=1 \\ j\neq i,\ k}}^{n} \mu_j \left(\frac{x_{ij}}{r_{ij}^3} - \frac{x_{kj}}{r_{kj}^3} \right) \tag{B.2a}$$

$$\ddot{y}_{ki} = -\frac{\mu_i + \mu_k}{r_{ki}^3}y_{ki} + \sum_{\substack{j=1 \\ j\neq i,\ k}}^{n} \mu_j \left(\frac{y_{ij}}{r_{ij}^3} - \frac{y_{kj}}{r_{kj}^3} \right) \tag{B.2b}$$

$$\ddot{z}_{ki} = -\frac{\mu_i + \mu_k}{r_{ki}^3}z_{ki} + \sum_{\substack{j=1 \\ j\neq i,\ k}}^{n} \mu_j \left(\frac{z_{ij}}{r_{ij}^3} - \frac{z_{kj}}{r_{kj}^3} \right) \tag{B.2c}$$

(please note that there are null partial derivatives for r_{kj}, given they are ephemeris data)

$$A_{41} = \frac{\partial U_x}{\partial x} = U_{xx} = \frac{\partial}{\partial x}\left[-\frac{\mu_i+\mu_k}{r_{ki}^3}x_{ki} + \sum_{\substack{j=1\\ j\neq i,\ k}}^{n} \mu_j\left(\frac{x_{ij}}{r_{ij}^3} - \frac{x_{kj}}{r_{kj}^3}\right)\right]$$

$$= -\frac{\mu_i+\mu_k}{r_{ki}^3} - \frac{\mu_i+\mu_k}{r_{ki}^5}x_{ki}\left(-3x_{ki}\right) + \sum_{\substack{j=1\\ j\neq i,\ k}}^{n} \mu_j\left[\frac{1}{r_{ij}^3} + \frac{x_{ij}}{r_{ij}^5}\left(-3x_{ij}\right)\right]$$

$$A_{41} = \frac{\mu_i+\mu_k}{r_{ki}^5}\left(3x_{ki}^2 - r_{ki}^2\right) - \sum_{\substack{j=1\\ j\neq i,\ k}}^{n} \frac{\mu_j}{r_{ij}^5}\left(3x_{ij}^2 - r_{ij}^2\right) \tag{B.3a}$$

$$A_{42} = \frac{\partial U_x}{\partial y} = U_{xy} = \frac{\partial}{\partial y}\left[-\frac{\mu_i+\mu_k}{r_{ki}^3}x_{ki} + \sum_{\substack{j=1\\ j\neq i,\ k}}^{n} \mu_j\left(\frac{x_{ij}}{r_{ij}^3} - \frac{x_{kj}}{r_{kj}^3}\right)\right]$$

$$= 0 - \frac{\mu_i+\mu_k}{r_{ki}^5}x_{ki}\left(-3y_{ki}\right) + \sum_{\substack{j=1\\ j\neq i,\ k}}^{n} \mu_j\left[0 + \frac{x_{ij}}{r_{ij}^5}\left(-3y_{ij}\right)\right]$$

$$A_{42} = \frac{\mu_i+\mu_k}{r_{ki}^5}\left(3x_{ki}y_{ki}\right) - \sum_{\substack{j=1\\ j\neq i,\ k}}^{n} \frac{\mu_j}{r_{ij}^5}\left(3x_{ij}y_{ij}\right) \tag{B.3b}$$

$$A_{43} = \frac{\partial U_x}{\partial z} = U_{xz} = \frac{\mu_i+\mu_k}{r_{ki}^5}\left(3x_{ki}z_{ki}\right) - \sum_{\substack{j=1\\ j\neq i,\ k}}^{n} \frac{\mu_j}{r_{ij}^5}\left(3x_{ij}z_{ij}\right) \tag{B.3c}$$

$$A_{51} = \frac{\partial U_y}{\partial x} = U_{xy} \tag{B.3d}$$

$$A_{52} = \frac{\partial U_y}{\partial y} = U_{yy} = \frac{\mu_i+\mu_k}{r_{ki}^5}\left(3y_{ki}^2 - r_{ki}^2\right) - \sum_{\substack{j=1\\ j\neq i,\ k}}^{n} \frac{\mu_j}{r_{ij}^5}\left(3y_{ij}^2 - r_{ij}^2\right) \tag{B.3e}$$

$$A_{53} = \frac{\partial U_y}{\partial z} = U_{yz} = \frac{\mu_i+\mu_k}{r_{ki}^5}\left(3y_{ki}z_{ki}\right) - \sum_{\substack{j=1\\ j\neq i,\ k}}^{n} \frac{\mu_j}{r_{ij}^5}\left(3y_{ij}z_{ij}\right) \tag{B.3f}$$

$$A_{61} = \frac{\partial U_z}{\partial x} = U_{xz} \tag{B.3g}$$

$$A_{62} = \frac{\partial U_z}{\partial y} = U_{yz} \tag{B.3h}$$

$$A_{66} = \frac{\partial U_z}{\partial z} = U_{zz} = \frac{\mu_i+\mu_k}{r_{ki}^5}\left(3z_{ki}^2 - r_{ki}^2\right) - \sum_{\substack{j=1\\ j\neq i,\ k}}^{n} \frac{\mu_j}{r_{ij}^5}\left(3z_{ij}^2 - r_{ij}^2\right) \tag{B.3i}$$

Appendix C

Euler-Lagrange equations for the adjoint variables

$$\dot{\boldsymbol{\lambda}} = -\frac{\partial \mathcal{H}}{\partial \boldsymbol{x}} \tag{C.1}$$

$$\begin{aligned}\dot{\lambda}_r = \frac{1}{r^2}\Bigg[&\lambda_\vartheta \frac{v}{\cos\varphi} + \lambda_\varphi w + \lambda_u\left(-\frac{2\mu}{r} + v^2 + w^2\right) + \lambda_v\left(-uv + vw\tan\varphi\right) \\ &+ \lambda_w\left(-uw - v^2\tan\varphi\right)\Bigg] - \lambda_u\frac{\partial\left(\mathrm{a}_p\right)_u}{\partial r} - \lambda_v\frac{\partial\left(\mathrm{a}_p\right)_v}{\partial r} - \lambda_w\frac{\partial\left(\mathrm{a}_p\right)_w}{\partial r} - S_F\frac{\partial T}{\partial r}\end{aligned} \tag{C.2a}$$

$$\dot{\lambda}_\vartheta = -\lambda_u\frac{\partial\left(\mathrm{a}_p\right)_u}{\partial\vartheta} - \lambda_v\frac{\partial\left(\mathrm{a}_p\right)_v}{\partial\vartheta} - \lambda_w\frac{\partial\left(\mathrm{a}_p\right)_w}{\partial\vartheta} + S_F\frac{\partial T}{\partial\vartheta} \tag{C.2b}$$

$$\begin{aligned}\dot{\lambda}_\varphi = &\frac{1}{r\cos^2\varphi}\left(-\lambda_\vartheta v\sin\varphi - \lambda_v vw + \lambda_w v^2\right) \\ &- \lambda_u\frac{\partial\left(\mathrm{a}_p\right)_u}{\partial\varphi} - \lambda_v\frac{\partial\left(\mathrm{a}_p\right)_v}{\partial\varphi} - \lambda_w\frac{\partial\left(\mathrm{a}_p\right)_w}{\partial\varphi} + S_F\frac{\partial T}{\partial\varphi}\end{aligned} \tag{C.2c}$$

$$\dot{\lambda}_u = \frac{1}{r}\left(-\lambda_r r + \lambda_v v + \lambda_w w\right) \tag{C.2d}$$

$$\dot{\lambda}_v = \frac{1}{r}\left[-\lambda_\vartheta\frac{1}{\cos\varphi} - 2\lambda_u v + \lambda_v\left(u - w\tan\varphi\right) + 2\lambda_w v\tan\varphi\right] \tag{C.2e}$$

$$\dot{\lambda}_w = \frac{1}{r}\left(-\lambda_\varphi - 2\lambda_u w - \lambda_v v\tan\varphi + \lambda_w u\right) \tag{C.2f}$$

$$\dot{\lambda}_m = \frac{T}{m^2}\lambda_V - \lambda_u\frac{\partial\left(\mathrm{a}_p\right)_u}{\partial m} - \lambda_v\frac{\partial\left(\mathrm{a}_p\right)_v}{\partial m} - \lambda_w\frac{\partial\left(\mathrm{a}_p\right)_w}{\partial m} \tag{C.2g}$$